Devices for satellite-assisted quantum networks

by

Youn Seok Lee

A thesis
presented to the University of Waterloo
in fulfillment of the
thesis requirement for the degree of
Doctor of Philosophy
in
Physics (Quantum Information)

Waterloo, Ontario, Canada, 2021

Examining Committee Membership

The following served on the Examining Committee for this thesis. The decision of the Examining Committee is by majority vote.

External Examiner:	Todd Pittman Professor, Department of Physics, University of Maryland, Baltimore County
Supervisor(s):	Thomas Jennewein Associate Professor
Internal Member:	Kevin Resch Professor
Internal-External Member:	Na Young Kim Associate Professor
Other Member(s):	Kyung Soo Choi Assistant Professor

Author's Declaration

I hereby declare that I am the sole author of this thesis. This is a true copy of the thesis, including any required final revisions, as accepted by my examiners.

I understand that my thesis may be made electronically available to the public.

Abstract

Quantum networks, quantum nodes interconnected by quantum channels, offer powerful means of secure communications and quantum computations. They are crucial elements in a broad area of quantum technologies including quantum simulations and metrologies. In particular, quantum links with satellites take the network into a global or greater scale, extending the capability of transmitting information. It also provides experimental platforms of testing quantum physics in a relativistic regime. The realization of satellite-assisted quantum networks requires devices that are interfaced with quantum optical channels to satellites. This thesis discusses the development of four essential devices, three of which are in line with Canada's Quantum Encryption and Science Satellite (QEYSSat) mission.

First, polarization-entangled photon sources are developed to transmit one of the paired photons over ground-based fiber-optic networks and the other over ground-to-satellite free-space links. A practical and versatile interferometric scheme is designed and demonstrated, which allows constructing highly non-degenerate sources with only conventional polarization optics. A method of directly producing entangled photon-pairs from optical fibers without interferometers is studied with thorough numerical analysis to show feasibility of experimental demonstration. An entangled photon source for the QEYSSat mission is conceptually designed, and several key parameters to fulfill a set of performance requirements are theoretically studied and experimentally verified.

Secondly, this thesis presents two characterization platforms for optical components that are designed and implemented for the QEYSSat mission. One is to precisely measure transmitted wavefronts of large optics including telescopes. A proof-of-principle experiment is conducted with accurate modelling of measurement apparatus via three-dimensional ray-tracing, and quantitative agreement between the experiment and simulations validates our methodology. The other provides polarization characterizations for a variety of optical components including lenses, mirrors, and telescopes with consistent precision. A detailed description of subsystems including calibrations and test procedures is provided. Polarization-test results of several components for the QEYSSat are discussed.

Third, quantum frequency transducers are developed for single-photon quantum key distributions with QEYSSat links. The devices are designed to translate the wavelength of single-photons emitted from quantum dot single-photon sources to QEYSSat channel wavelength via four-wave mixing Bragg-scattering process. Two optical media are concerned: a silicon nitride ring resonator and a photonic crystal fiber. Thorough numerical simulations are performed to estimate the device performance for both cases. A proof-of-principle demonstration of the frequency translation is conducted with a commercial photonic crystal fiber.

Finally, a quantum simulator, serving as a quantum node in satellite-assisted quantum networks, is designed in a silicon nitride nanophotonic platform with cesium atoms. The designed photonic structure tailors electromagnetic vacuum such that photon-mediated forces between atoms causes collective motions mediating site-selective SU(2) spin-spin interactions. A coherent spin-exchange rate between atoms and collective dissipation rate of atoms are precisely estimated via finite-element time domain simulations. Furthermore, two schemes of trapping atoms in the vicinity of the designed structure are studied with calculations of potential energies and phonon tunneling rates. Experimental progress toward realization of the proposed system is summarized.

The presented research activities of designing, analyzing, and implementing devices demonstrates the readiness of satellite-assisted quantum networks. This work contributes to creating quantum channels by entanglements with interfaces of various quantum systems in line with a broader scope of establishing a global quantum internet and quantum space exploration.

Acknowledgements

First and foremost, I would like to thank my supervisor, Prof. Thomas Jennewein, for all his support and advice during my study at Quantum Photonic Laboratory (QPL). I greatly appreciate the freedom he offered to choose and pursue my research. Under his generous supervision, I have truly enjoyed my graduate studies and been able to keep a sustainable pace without burning out.

I would also like to thank Prof. Kyung Soo Choi for his support and guidance during my study at Ultracold Quantum Matter and Light (UQML). I learned so much in doing experimental physics from very basics with machining and building electronics to in-depth design and analysis with advanced computational tools.

I also wish to thank my Advisory Committee, Prof. Kevin Resch, Prof. Na Young Kim, and Prof. Norbert Lütkenhaus. I thank Prof. Todd Pittman for joining my Examining Committee.

I express my sincere gratitude to Mike and Ophelia Lazaridis Fellowships for the four-year financial support to my graduate study at University of Waterloo.

I would like to acknowledge Dr. Brendon Higgins, Dr. Katanya Kuntz, Dr. Dogan Sinar, Dr. Sara Hosseini, Ramy Tannous for their proof reading on part of my thesis.

I would like to gratefully acknowledge Steve Weiss and Matt Cooper for their IT supports and guidance.

My colleagues in the QPL have motivated, inspired, and encouraged me over the journey of Ph.D. program. Foremost, I thank my officemates, Ramy Tannous and Sebastian Slaman, for their warm welcome with open arms and having so much fun time with me in the lab and squash court. Dr. Jean-Philippe Bourgoin provided his generous guidance during my initial work at the QPL. Dr. Brendon Higgins has taught me by example the thorough approach to physical problems. I also appreciate Dr. Katanya Kuntz for always filling the group with positive energy and cheers. I thank Kimia Mohammadi and Lindsay Babcock for sharing the joyful time with me in the lab. I appreciate Jisu Kwon for all the administrative support. Finally, I would like to acknowledge Brian Moffat for his management of various projects with the generosity.

I would like to thank my colleagues at the UQML. I thank Dr. Chang Liu for fruitful scientific and technical discussions. I thank Hyeran Kong, an amazingly hard worker with full of passions, for sharing experiences in the design and implementation of UHV systems. I thank Sainath Motlakunta for so much fun time in the lab and kindly introducing me of the Linux world.

Sports have been my life stabilizer during my graduate study. I would like to thank Andrew Cameron and Carl Tutton for enjoying squash with me. Also, I thank Dong Seob Chung, Hyunwoo Choi, Maria Joo, Hyunjae Lee, Danny Kun, and Ramy Tannous for playing tennis with me. I thank Hyeonghwa Yu and Joo Hyung Ryu for introducing me of the joy of rock climbing. Without you guys, I would not have kept hard works while maintaining heathy mental and physical condition.

I must thank my parents (Sung Uk Lee and Gyoung Hee Cho) and sister (Si Won Lee) for their unconditional love and support. I would lilke to thank Pan Liu who has always been with me and has given me endless supports, encouragement, and love.

Dedication

To graduate students.

Table of Contents

List of Tables

List of Figures

Chapter 1

Introduction

1.1 My history at University of Waterloo

Over the past five years of my graduate study at University of Waterloo, I have been given ample opportunity to pursue my research at two different groups: Ultracold Quantum Matter and Light (UQML) led by Prof. Kyung Soo Choi and Quantum Photonics Laboratory (QPL) led by Prof. Thomas Jennewein. My time at the UQML was full of experiences to deepen my knowledge about fundamental atomic physics with lots of inputs about cutting-edge technologies in experimental atom and molecular optical (AMO) physics, e.g., ultra-cold atomic gases in extreme-high vacuum. My research at the QPL broadened the horizon of my knowledge in quantum optics and photonics as well as technical skills of developing devices for practical applications, e.g., versatile quantum light sources and optical characterization tools, from conceptual designs to their prototyping.

In September 2016, I joined the UQML as a visiting scholar and started building electronics for Waveguide QED Lab. With circuit designs provided by my colleagues, Hyeran Kong and Dr. Chang Liu, from Rydberg Lab, my role was to turn them into working devices that power up and control external cavity diode lasers. In January 2017, I started my master program and continued my research activities in the Waveguide QED Lab at the UQML under the supervision of Prof. Kyung Soo Choi. My main responsibility was to develop AMO experimental hardware, such as ultra-high vacuum (UHV) system, lasers, and electromagnets. Hyeran Kong and Dr. Chang Liu shared their technical expertise with me during the development. From the middle of 2017 to November, I was lucky to work with Dr. Ying Dong and involved in designing and analyzing photonic crystal waveguides to support his proposed waveguide QED scheme. Sainath Motlakunta introduced me Linux

systems and helped me debugging numerical simulation tools during the designing acitivities. Prof. Kyung Soo Choi supported my first round of training sessions for fabrications of the designed photonic devices in Quantum-Nano Fabrication and Characterization facility, which was completed in February 2018. As experiments in the Rydberg Lab advanced and needed more hands, I supported developments of laser systems with spectroscopies to frequency- and phase-lock lasers in the Rydberg Lab. I completed my research activities at the UQML and my master program was transferred to the Ph.D. program in April 2018.

In May 2018, I joined the QPL and participated in hardware developments for ground stations in Canada's Quantum Encryption and Science Satellite (QEYSSat) mission. The research activities consist of various projects of designing, prototyping, and characterizing photonic devices. From May to October 2018, I worked on the proof-of-principle demonstration for wavefront and polarization characterizations of various telescopes under the guidance of Dr. Jean-Philippe Bourgoin and Dr. Brendon Higgins. The automation of characterization platforms using a six-axis robot arm was completed in May 2019, and Lindsay Bobcock and I initiated the operations of polarization tests on various optics including commerically available telescopes and mirrors. I led polarization characterizations supporting the development of optical components for the QEYSSat satellite payload led by our industry team, Honeywell Canada Aerospace until March 2020. Kimia Mohammadi joined in January 2020 and contributed to refinement of the characterization platform. Kimia Mohammadi and I upgraded wavefront and polarization characterization systems in early 2021, and use them to test a quantum transmitter telescope in April 2021.

I supported the development of fiber-based photon-pair source led by a visiting scholar in the QPL, Mengyu Xie, from May 2018 to March 2019. Based on her characterizations of photon pairs generated from polarization-maintaining fibers, I developed an entangled photon source with a new interferometric scheme. With Ramy Tannous's assistance, the demonstration and characterization of the source was completed in December 2019. In November 2019, Prof. Thomas Jennewein and I conceived the idea of using the new interferometer for an entangled photon source for the QEYSSat mission. A conceptual design for photon generations and detailed designs including detection schemes were completed in March 2020. Implementation of the designed source has been mainly led by my colleague, Paul Oh, since May 2020.

In the QPL, my main thesis work was to develop a frequency transducer to interface quantum dot single-photon sources with the QEYSSat link. This project was proceeded in collaboration with Dr. Robin Williams's group at National Research Council Canada (NRC). In March 2019, I visited the NRC team to learn fabrication and characterization processes. Dr. Khaled Mnaymneh provided me with a training session about various equipments in the NRC nanofabrication facility. I designed ring resonators using numerical

simulations of electromagnetism, which was completed in January 2020. From March to September 2020, Covid-19 outbreak shut down all lab activities and also prevented me from proceeding with the fabrication of the designed ring resonator at NRC. The laboratory reopened in October 2020, and I carried out frequency translation experiments with alternative media, i.e., photonic crystal fibers. My experimental activities ended in June 2021.

I note that I will use "we" rather than "I" just as a convention in the remaining chapters. I remark the statement of contributions at the beginning of every chapter to avoid the ambiguity of credits.

1.2 Quantum networks

Quantum networks, quantum devices or objects interconnected through quantum channels, play a crucial role for scientific investigations and technological advancements in a broad range of applications, including quantum computing, communications, metrology, and fundamental scientific explorations. It was first conceptualized as a platform for quantum transmission of information [62], and proof-of-principle demonstrations of basic building blocks have been performed with atoms and lasers in laboratories from late 1990's to early 2000's [156]. Over the past few decades, there have been several directions in the development of quantum networks. On the one hand, through significant advances in quantum communications and quantum memories, the networks with longer distances of quantum links have been pursued for secure communciations and enhancing quantum computations [302]. On the other hand, considerable endeavors have been made to achieve complex network connectivity in nanoscopic quantum networks to explore high-dimensional quantum many-body dynamics [76]. This thesis concerns these two extrema of quantum networks: primarily with enhancing ground-to-satellite quantum links for a global quantum internet and the other with strongly interacting atoms applicable to a fully programmable spin network. These two sectors of quantum networks have emerged with their own motivations and potential applications, as illustrated in Figure 1.1 and in the text that follows.

Current quantum technology is capable of constructing small-scale devices with limited capacity for dedicated tasks. For example, superconducting qubits and trapped ion systems can perform quantum computing with tens of qubits and reasonabe connectivity, surpassing the performance of conventional devices [242]. However, inevitable noise in quantum gates limits the size of quantum circuits to 50–100 qubits, while more practical

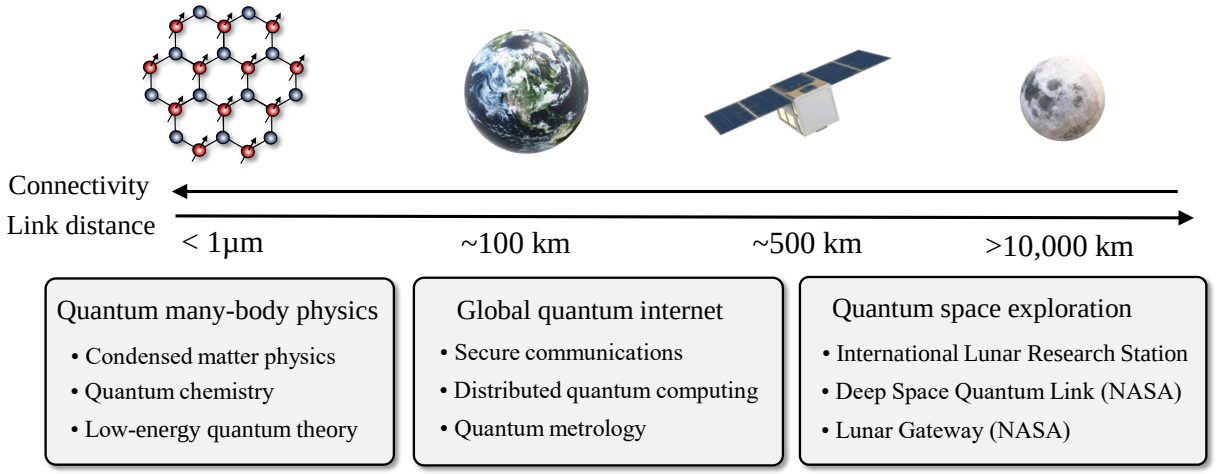

Figure 1.1: Quantum networks in different length scales with applications and potential opportunities.

applications requires millions of qubits with fault-tolerant architecture [39]. In this so-called Noisy Intermediate-Scale Quantum (NISQ) era, one of the approaches to establish a larger scale and multi-functional quantum device is to form a network of such NISQ devices by coherently interconnecting them with quantum links. Technological advances in quantum communciations and memories may provide reliable quantum links between distant locations on Earth. As opposed to classical links, the computational space scales exponentially with the number of quantum links, which may be leveraged by distributing computing tasks over multiple quantum nodes [290, 51, 48]. Conversely, remote users may access centralized quantum processors via quantum-secured communications, forming a quantum computing cloud infrastructure.

The networks formed with ground-satellite or inter-satellite links may provide a new avenue of standardization of units as well as scientific tools to explore quantum phenomena in space. For example, a global quantum network of atomic clocks may be formed with inter-satellite links, serving as an united clock with quantum-limited precision and quantum-secured accessbility from anywhere on Earth [160]. Also, the capability of transmitting information over noisy channels allows extending the baseline of telescopes [105]. To this limit, the quantum network may be established with even further space objects such as the Moon mainly for scientific purposes of testing the quantum theory in a relativistic scale [250]. One of the feasible and near-term experiments is a Bell test with entangled photon pairs under different gravitational fields. It is expected to witness entanglement decoherence induced by gravitational field, originally proposed by Timoth C Ralph. Re-

cently, such a Bell test between Earth and Moon has been conceived with entangled photon sources placed at Lagrangian points [53].

The quantum network can also be established in a nanoscopic scale with natural quantum objects such as atoms and ions. With quantum links created by coherent atom-light interactions, the network effectively forms a quantum spin-network whose connectivity can be engineered by active controls over the individual atom-light interactions. The controllable spin-network can then be used to efficiently emulate a complex many-body system under investigation. Such an analogue quantum simulator has already been successfully applied to solve problems in condensed matter physics [108, 61], and opened up a new paradigm of engineering matters and probing deeply into the properties of exotic materials. On the one hand, the concept of "photons engineered by matter and matter dressed with photons" has been a principal theme to describe exotic quantum states of light and matter. On the other hand, quantum information has become a key ingredient to describe the nature of blackholes and spacetime from the perspective of low-energy theory, which may provide insights toward a grand unified theory. Also, this small-scale yet flexible quantum network provides powerful scientific tools to tackle practical but computationally challenging problems such as electronic states of molecules in the subject of quantum chemistry.

Broad impacts of quantum networks with a variety of applications has recently stimulated the involvement of industry and government agencies [216]. Over the past several years, quantum technology has been gradually transferred from laboratory to industry. Several countries have already established metropolian quantum networks and industrial quantum computers outperformed classical computers, i.e., quantum supremacy [17]. Furthermore, collaborations between industries and academia has been pushing the limits of the experimental capability to explore science with unprecedented complexity and physical scale. This active and collective development of quantum technologies is often referred to as the quantum revolution.

1.2.1 Quantum key distribution

Quantum key distribution (QKD) is the first quantum application and demonstrates point-to-point quantum links using photons as quantum information carriers. It provides means of sharing secret keys between two remote parties with information-theoretic security based on quantum mechanical principles. Generally, secret key information is encoded in quantum states of individual photons that are expected to be preserved throughout photon transmission from one party to the other. Based on the superposition principle, the photons arrived at the other party inherently contains the information about the presence of

eavesdroppers because measurements on photons inevitably disturb their original states and leave traces. In the following, we briefly describe two of the most famous QKD protocols. For more quantitative analysis of the two protocols, see reference [257].

BB84 protocol

The first QKD protocol was proposed by Charles Bennett and Gilles Brassard in 1984 [29], namely the BB84 protocol. In the protocol, Alice sends Bob a photonic qubit which is randomly prepared in one of the four states in two non-orthogonal bases, e.g., horizontal, vertical, diagonal and anti-diagonal polarization states. Bob performs measurements with randomly chosen basis of the qubits and record the qubit states. After the photon transmission is completed, the two parties reveal the sequence of their bases used for the qubit preparation and measurement through public communication channels, and keep the results only when they used the same bases (i.e., sifting procedure), which results raw keys. Then, Alice and Bob compare the portions of their raw keys to estimate the quantum bit error rate (QBER), defined as a ratio of the error rate to the total photon-detection rate, which represents the amount of information leaked to other channels including eavesdroppers. If the QBER is above a certain threshold value, the channel is aborted and the raw keys are discarded. Otherwise, the two parties proceed with classical error corrections and privacy amplifications to extract final secret keys.

The implementation of the standard BB84 protocol requires true single-photon sources to transmit the qubits, while attenuated lasers are much preferable in practice, i.e., weak coherent pulses. However, the attenuated lasers inherently produces more than one photon in each wavepacket. The multiphotons opens a way for an eavesdropper to obtain the qubit information without leaving errors in the Bob's measurements, such as a photon-number splitting attack. Accounting such information leakage in the post-processing results significant reduction of the secure key size at the end of the protocol, which also limits the distance between the two parties.

In 2003, Hwang proposed employing decoy states to overcome the photon-number splitting attack. The decoy states were used to randomize the placement of the signal pulses, which forces eavesdroppers to obtain information probabilistically. The idea was further analyzed by Lo *et al.* in 2005 [185], and the formulated protocol is often called a decoy-state BB84 protocol. The protocol introduces the decoy-state pulses to randomize the mean-photon numbers of the pulse chain for the purpose of detecting the presence of eavesdroppers. Meanwhile, the key generation is performed by following the original BB84. The decoy-state method allows maintaining a high key-generation rate with attenuated lasers as in the case of using true single-photon sources. The decoy-state BB84 has been one of

the most popular QKD schemes and the decoy-state method has been applied for other protocols such as twin-field QKD [107].

BBM92 protocol

The above BB84 protocol is often categorized into a prepare-and-measure scheme where one of the two parties (Alice) encodes the information and transmit it to the other (Bob) who performs measurements. The correlation of the secret key between the two parties imposed by the state-preparation process at Alice or a third party. Such a correlation can also arise from directly distributing entangled pairs shared between Alice and Bob. In 1992, Bennett *et al.* proposed a QKD scheme, namely a BBM92 protocol [30], where the photon-exchange process is performed by the measurements on the entangled photon pairs at the two parties. The protocol is essentially equivalent to the BB84 protocol. The photonic state preparation is achieved by projecting one of the entangled pairs onto one of the four states via measurements of the other.

In 2003, Masato Koashi and John Preskill proved that the QKD with a source whose average states are basis independent performs the same secure key rate as in the case of using single-photon sources [158]. More concretely, a basis-independent source produces the output states that are invariant under the basis rotation. Remarkably, most of practical entangled photon sources including parametric down-conversions produces basis-independent photonic states. Based on their proof, the BBM92 protocol with practical entangled photon sources was further analyzed by Ma *et al.* in 2007 [196]. The analysis showed that the entanglement-based QKD can tolerate higher channel losses than the decoy-state BB84 protocol.

Secret key rate, quantum bit error rate (QBER), and devices for quantum key distributions

Generally, the secret key rate $K = Rr$ is the product of the raw key rate R and the secret fraction r [257]. Roughly speaking, the raw key rate and the secret fraction represents the efficiency and accuracy of transmitting photons from one (Alice) to the other (Bob), respectively. The raw key rate $R = \nu\eta$ is mainly determined by the photon production rate ν and the channel transmittance η. The secret fraction is mainly affected by the QBER, and the low secret fraction means that photon-transmission channel is corrupted by either noises or eavesdroppers (Eves). Mathematically, it is expressed as $r = I(A:B) - I_E$ where $I(A:B) = H(A) + H(B) - H(AB) = H(A) - H(A|B)$ is the mutual information of the

raw keys A and B. Here I_E is Eve's information on the raw key of Alice or Bob and H is Shannon entropy.

In the BB84 protocol, we assume that Alice uses a perfect single photon source (no multiphotons, i.e., $g^{(2)} = 0$) with the photon-production rate ν and a quantum random number generator to prepare a sequence of polarization states. Then, the entropy of the raw key is $H(A) = H(B) = 1$. Any imperfaction of the correlation $H(A|B)$ of Alice's and Bob's raw keys is characterized by binary entropy $h(\text{QBER})$ of the QBER, which also estimates the Eve's information $I_E = h(\text{QBER})$. Therefore, the secret key rate can be written as

$$K = (\nu/2)\eta(1 - 2h(\text{QBER})). \tag{1.1}$$

Here a factor of $1/2$ accounts the sifting process.

The QBER is a key parameter in the implementation of any QKDs since it measures the amount of the information leakage to other channels during photon-transmission process. As discussed in the above example of the BB84 protocol, the QBER directly impacts the length of the attainable secret key at the end of the protocol; the higher QBER results the shorter secret key. The QBER resulting no keys $K = 0$ is called a threshold QBER which depends on the protocols. The higher threshold QBER means better tolerance of the protocol to the systematic errors. The threshold QBER for the BB84 protocol in Equation 1.1 is around 11 %.

Any systematic errors in the preparation and measurement of photonic states contribute to the increment of QBER. The measurement error includes dark-count rate of photon detectors and other background noises. Therefore, for a given channel loss, the achievable distance of quantum links highly depends on the performance of devices used in the photon-exchange process. In polarization-encoded QKDs, as an example, the degree of polarizations of the initially prepared state is the baseline of the QBER. The polarization-extinction ratio of measurement devices and the misalignment of polarization axes can increase the QBER. Also, if photon transmitters or receivers are lossy, the random errors from the detector's intrinsic noise can contribute to the QBER and dominate over the signal. Therefore, the devices for the QKD is generally required for producing highly pure states of photons and measuring them with minimal errors. Also, the high photon-production rate is preferred to obtain a long distance of quantum links.

1.2.2 Quantum communications with satellites

One critical drawback of using photons in QKDs is the loss; the information simply disappears, which limits the maximum distance between two parties. For example, typical

propagation loss 0.2 dB/km [1] of optical fibers limits the photon-transmission distance up to about one or two hundreds of kilometers. Satellites have been considered as a necessary piece to combat the limitations of existing terrestrial technology for quantum networks in a global scale. This is mainly because the transmission loss scales quadratically with the distance in space as opposed to the exponential scaling in optical fibers; once the photons are outside of atmosphere, the transmission loss is only limited by diffraction because there is no media to scatter the photons. Also, satellites orbiting around Earth are accessible from anywhere on the ground, which makes it a promising candidate as global quantum nodes interconnecting world-wide quantum devices.

Using satellites to mediate the quantum information exchange between distant nodes on Earth has been conceived since the late 1990's. One of the major-initiative investigations is Space QUEST project in 2004 funded by European Space Agency. In 2007, entangled photons were distributed over 144 km–distant parties through free-space channel across islands [288], reaching distance longer than the thickness of atmospheric layers, which clearly showed the feasibility of quantum communications using satellites. In 2016 August, China's Quantum Experiments at Space Scale (QUESS) mission successfully launched the first quantum communication satellite, named Micius satellite, and demonstrated QKDs in down-link configuration [179]. With the Micius satellite, the QUESS mission has further accomplished the entanglement distribution over 1200 km [310], ground-to-satellite quantum state teleportation [249], entanglement-based QKD between ground and satellite [311] as well as between two 1120 km–distant nodes on the ground [312].

The global quantum network will ultimately be formed with a constellation of satellites that are interconnected via photon exchange while mediating long-distance information transmissions on the ground. According to the recent analysis by Brito *et al.* [42], a number of satellites (>100) in conjunction with hubs features a notion of forming a robust and scale-free network which allows the entanglement distribution between any two nodes with only a few entanglement swappings. Such mass production of satellites requires cost-effective development of small satellites such as micro satellites or CubeSats. There have been a number of world-wide projects for miniaturized QKD satellites, as summarized in references [28, 263].

1.2.3 Quantum Encryption and Science Satellite (QEYSSat)

In Canada, Quantum Encryption and Science Satellite (QEYSSat) mission funded by Canada Space Agency (CSA) has been developing a set of technologies enabling quantum key distributions between a micro satellite quantum receiver and ground stations [142, 259,

238, 237]. Our QEYSSat Science Team at the QPL has been developing quantum light sources together with a quantum optical ground station to be located at the University of Waterloo. In parallel, our industry partner, Honeywell Canada Aerospace, has been responsible for designing and constructing quantum payload hardware on the satellite as well as an optical quantum ground station to be located at the CSA. The QEYSSat mission is scheduled to launch in 2022.

The objectives of the QEYSSat mission are long-distance QKDs using a low-earth orbit (LEO)-based satellite as a trusted node and long-distance entanglement tests. The QKD will be performed with the well established BB84 and BBM92 protocols in an uplink configuration where photons are sent from the ground to satellite. This reduces the onboard complexity tremendously, resulting in a simple key distribution orbital node. Also, the uplink allows testing various quantum sources on the ground with the satellite quantum link. For example, our recent indoor-experimental study showed that quantum dot single-photon sources performs better with satellite links than weak coherent pulse sources in BB84 QKD protocol [55]. The comparison of quantum dot entangled photon sources with conventional spontanous parametric down-conversions would also be an interesting subject to study in terms of efficient entanglement distributions and quantum state teleportations [14].

It is worth noting that the QEYSSat spacecraft carries a secondary payload for high-speed optical communications in addition to the primary QKD payload [259, 237]. Developed by Honeywell, the secondary payload is mainly motivated by market needs for LEO constellation optical inter-satellite links. Thus, it is designed to compliant with low-cost mass production methods while providing full duplex 10Gbps communication at inter-satellite distances exceeding 6000 km. The secondary payload will support the QEYSSat primary mission with a classical optical communication link to the ground.

1.2.4 Devices for quantum networks

In the context of global quantum internet, it has been conceived that quantum information is not encoded to traveling photons due to inevitable photon loss unlike classical fiber-optic communication where each optical pulse carries one bit via its intensity level. Instead, the information is transmitted by a quantum state teleporation scheme where a Bell-state measurement on one of the entangled qubits and a message qubit "teleports" the information to the other qubit of the entangled pair [40, 51]. Then, two bits of classical information will be used to reconstruct the original qubit by local unitary operations. This also allows faithful transmission of fragile quantum information over noisy channel via entanglement purification schemes. Therefore, the entanglement is the key resource of

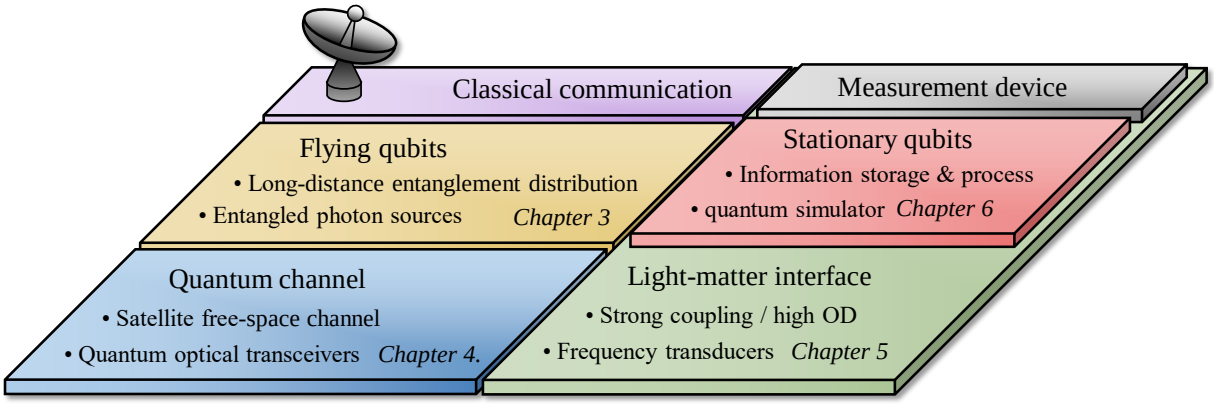

Figure 1.2: Devices for quantum networks with corresponding thesis Chapters. The detailed description of each device is provided in the main text.

qauntum information transmission and processing tasks. The deterministic or on-demand distribution of these resources with the ability of local storage and information processing is a crucial technology in the development of quantum networks.

A fully functional quantum node is formed with multiple quantum devices that are possibly built upon various physical platforms of stationary qubits. Photonic quantum information can be coherently mapped to and read-out from the stationary matter qubits, and it is commonly accepted that the quantum links will be formed by photon-transmission channels. The whole assembly will eventually interface with optical quantum channels and classical communications, as illustrated in Figure 1.2. The contents of this thesis may be viewed as development of key devices for satellite-assisted quantum networks. Although the quantum network is not completely realized here, the presented research tackles some of major challenges in the pursuit of longer distance of quantum channels and higher complexity of quantum networks for nodes. The thesis is organized in a way that each chapter discusses one device with its own motivations and challenges.

Entangled photon sources

Entanglement is a key resource of quantum channels, and efficient entanglement distribution over long distances is a very first step to establishing a global quantum network. Every qubit transmission consumes an entangled pair, hence the production rate of the entangled pairs is directly connected to the qubit transmission rate. Therefore, entangled photon sources must be optimized for the best transmission of entangled pairs through

optical channels. Also, practical and cost-effective implementations may be equally important for scalability. There are commercial products, e.g., OZoptics and NuCrypt, that are operational with fiber-optic networks. Recently, chip-scale entangled photon sources have rapidly progressed with CMOS-compatible fabrications [224, 106, 60].

Chapter 2 discusses two distinct and practical schemes for polarization-entangled photon sources: one is based on a versatile interferometric setup and the other is a direct production of entangled photon-pairs without any interferometers. Both were motivated to distribute the entanglement over long distances using satellites. Theoretical analysis and experimental demonstrations for both schemes are discussed. This chapter also presents a conceptual design for an entangled photon source developed for the QEYSSat mission. As an analysis for the designed system, the key experimental parameters was numerically optimized to meet the required specifications.

Photonic transceiver

It is crucial to engineer quantum channels to preserve photonic quantum information and to minimize the transmission loss of flying qubits. To be specific, photon transceivers must be designed and constructed according to channel characteristics. In fiber-optic channels, the photon loss is a pre-determined factor by the properties of manufactured optical fibers, and much attention has been paid to enhance transmission bandwidths with wavelength-division multiplexing scheme while suppressing Raman noises [81]. In free-space channels, the photon loss is a variable or function of a geometry of photon transceivers and other parameters. For example, one can reduce the loss by carefully designing and optimizing transceiver telescopes and pointing systems. The development of an optical assembly especially for ground-to-satellite free-space channels requires sophisticated designing and testing process.

Chapter 3 describes our characterization infrastructure for optical components developed for the QEYSSat mission. Two critical properties of light for efficient transmission of quantum information over free-space channels, i.e., wavefronts and polarizations, are characterized. Fully automated, the wavefront measurement platform is capable of identifying the error at the precision better than 0.01λ over a 20 cm aperture. The polarization testbed is robotized for versatility of performing tests on various optical elements including lenses, prisms, mirrors, and telescopes. In-depth discussions on the design of both testbeds are provided with theoretical analysis and experimental verifications. The infrastructure supported the development of hardware for a quantum satellite payload as well as optical ground stations.

Frequency transducers

Quantum frequency transducers are a necessary element to interface quantum nodes with optical channels in a technology-independent manner. Photon sources and detectors sometimes do not operate at channel wavelengths. Also, the photon-acceptance wavelengths and bandwidths of matter qubits are usually determined by the nature of materials being used. For example, it is well known that room temperature single-photon detectors perform much better at visible and near infrared wavelengths (500 nm to 800 nm) than telecom wavelength (1320 nm to 1580 nm). Also, InAsP/InP quantum-dot single-photon sources operate at the wavelengths from 890 nm to 985 nm and solid-state quantum memeories operate at distinct wavelengths ranging from 580 nm to 740 nm [318, 19]. Moreover, interfacing superconducing qubits with optical photons has lately been an active research topic.

The interface of flying qubits with stationary matter qubits via quantum frequency translations plays an important role to create a global quantum internet. In particular, quantum repeaters that are linked with satellites significantly enhance the capability of distributing entanglements. Recent analysis showed that several entangled photon sources on LEO satellites with realistic quantum memories (90 % storage-retrieval efficiency) on the ground could provide the entanglement between two distant nodes over 20 000 km [36].

In Chapter 4, the design of quantum frequency transducers with silicon nitride ring resonators is described with ambition of single-photon quantum communications with satellites in the QEYSSat mission. Theory of optical frequency translation with four-wave mixings is formulated to study optimal conditions in optical waveguides and ring cavities. A full package of numerical simulation program is described for thorough performance assessment of the designed device. In addition, as an alternative approach, the four-wave mixing process using photonic crystal fibers is theoretically studied and experimentally demonstrated to perform the wavelength translation from 985 nm to 785 nm.

Interface between flying and stationary qubits

Local storage and processing of quantum information requires efficient interfacing of flying qubits with stationary matter qubits. The coherent information exchange between the two qubits is obtained by conditioning strong light-matter interaction. Two common approaches to enhance the interaction strength are to employ an optical cavity for longer interaction time and to increase an optical depth of an ensemble of the matter qubits. The cavity-assisted interaction may be understood as the modified electromagnetic vacuum

stimulating the absorption or emission of photons with the quantum information embedded in a specific mode or spin state. On the other hand, the ensemble of matter qubits may collectively interact with electromagnetic quanta, and its interaction strength scales with the square root of the number of the matter qubits. The former method tends to be more commonly used for addressing the qubit-to-qubit information exchange in the scope of the global quantum internet [221] whereas the latter has been popular in quantum metrology to exaggerate the properties of the matter to be mapped onto photons such as in optical lattice clocks [277].

With advanced techniques of engineering light-matter interactions in a unique nanophotonic platform, Chapter 5 discusses the development of a programmable quantum spin network. A novel waveguide QED system with neutral atoms in a photonic crystal waveguide is proposed as an analogue quantum simulator for universal Hamiltonians [76, 70]. An air-slotted photonic crystal waveguide is designed to support the proposed system, and numerical simulations estimate atomic spin-spin interaction rate as well as system dissipation rates at various experimental parameters, e.g., laser field detuning. Although the main motiviation in Chapter 5 is to explore quantum many-body physics, the developed quantum device can readily serve as a universal quantum processor.

1.2.5 Free-space channel for ground-to-satellite quantum link

In the development of devices for satellite-assisted quantum internet, it is essential to understand properties of free-space quantum channels and to set guidelines for designing accordingly. Photonic degrees of freedom must be carefully chosen to diminish decoherence based on the channel properties. Also, the link budget is determined by the transmission loss together with the production rate of photon sources and background noises [18]. Moreover, an orbiting satellite causes limited contact time for exchanging photons and the amount of background noises must be analyzed to keep a high signal-to-noise ratio during the operation. The characteristics of free-space channels particularly for ground-to-satellite links are briefly described in the following, while a comprehensive review in more general free-space optics can be found in other literature [284].

Preferred photonic degrees of freedom

In 1969, D. H. Höhn reported experimental observations on polarizations of He-Ne laser light after its propagation through atmosphere over 4.5 km [120]. The researcher injected linearly polarized laser beam (1.2 mm beam diameter, extinction ratio $> 10^7$) and measured the degree of depolarization while monitoring intensity variations associated to the

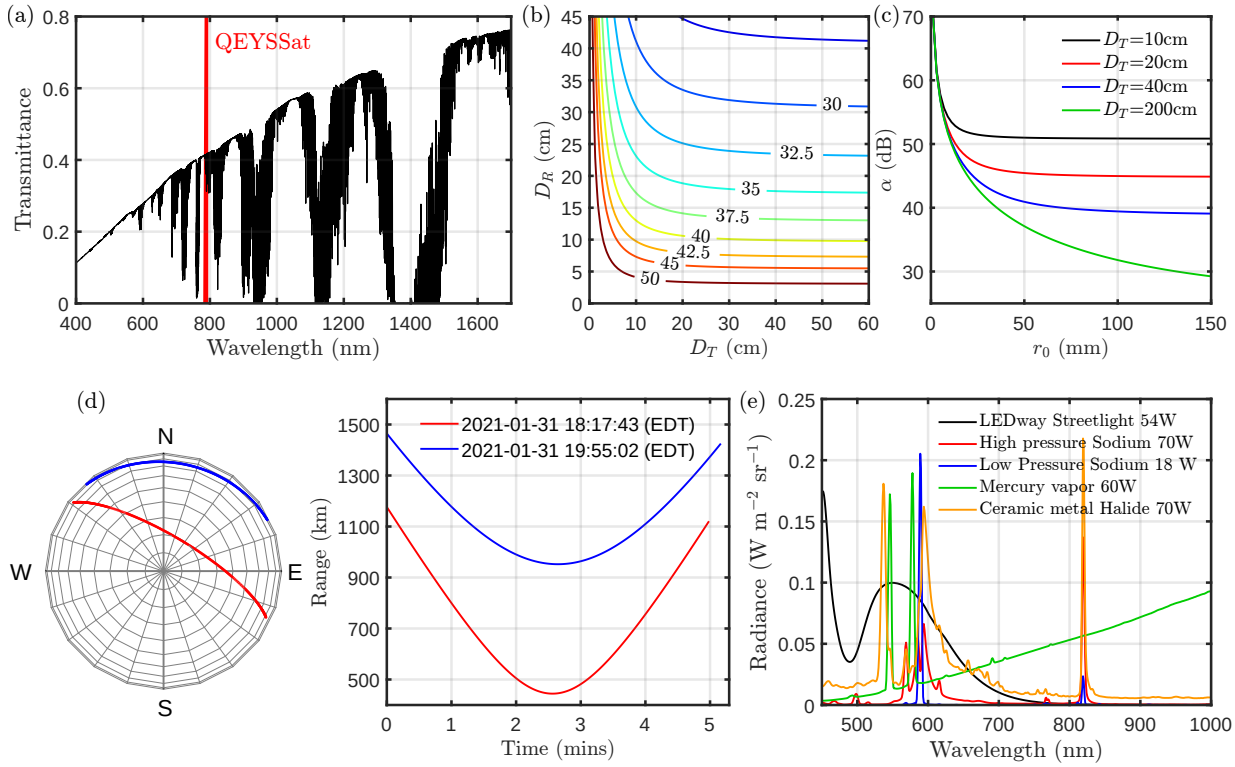

Figure 1.3: Characteristics of optical free-space channels for ground-to-satellite quantum link. (a) Atmospheric transmission spectrum at a typical rural location for propagation at zenith simulated by LibRadTran with average 30 % Earth albedo and 5 km visibility. (b) Contour plots of free-space uplink attenuation in decibels as a function of diameters of photon-transmitter D_T and reciever telescopes D_R. (c) The uplink attenuation α as a function of Fried's parameter r_0. (d) Exemplary trajectories of International Space Station (ISS) simulated by SGP4 algorithm with Two-line element (TLE) provided by North American Aerospace Defense Command (NORAD). (e) Spectra of various artificial light sources; the data were obtained from http://ngdc.noaa.gov/eog/night_sat/spectra.html.

atmospheric turbulence. The results showed surprisingly small depolarization ($< 10^{-5}$) in the regime of "intermediate" turbulence, indicating that atmosphere is a nearly isotropic optical medium. Indeed, the polarizations of photons have been one of the most popular photonic degrees of freedom in free-space quantum communications. In our QEYSSat mission, as well as other satellite missions (e.g. Micius), QKD and entanglement test is planned to be conducted by the exchange of polarized light.

Recently, there have been experimental demonstrations of using other photonic degrees of freedom for free-space quantum communications such as orbital angular momentums [266] and time bins of light [144]. Especially, unlike polarization (spin) states, the arrival time of photons can be viewed as an external degree of freedom directly coupled to reference frames or spacetime curvatures via Lorentz transformations, which may be leveraged for fundamental tests of quantum mechanics with satellite-assisted quantum networks [250]. In 2016, Vallone *et al.* conducted an experiment where time-bin encoded laser pulses were sent to and retroreflected from orbiting satellites named Ajisai and Stella, and measured kinematic phases from single-photon interferences [289]. Although the experiment did not show general relativistic effects due to technical limitations, the attempt to probe phase information from single-photon interference in large scale may be viewed as a milestone toward a full realization of the famous Colella-Overhauser-Werner experiment [68, 321].

Transmission loss

Transmission loss is one of the most critical and limiting factors for long-distance quantum links. There are mainly three contributions in free-space channels: atmospheric scattering, atmospheric turbulence, and light diffraction. The first two factors are determined by intrinsic properties of the atmosphere and the last one is due to the nature of electromagnetic wave. Note that the dominant factors to limit the link distance are the atmospheric scattering and turbulence in ground-based free-space optical communications, whereas in ground-to-satellite or inter-satellite links, the diffraction plays an equally important role as the vacuum-propagation distance becomes longer in space. Furthermore, it is a tunable parameter by the geometric settings of photon transceivers; the divergence angle of diffraction-limited light $\theta_T = \lambda/D_T$ at wavelength λ is determined by incident aperture diameter D_T.

Figure 1.3(a) shows an exemplary atmospheric transmission as a function of wavelength. This is calculated by open-source library of radiative transfer simulations (LibRadTran) for propagation at zenith in a typical rural location with 5 km visibility and 30 % Earth albedo. The overall tendency of higher transmission at longer wavelength stems from Rayleigh scattering and the fine structure originates from various absorption by mainly oxygens and water molecules. Obviously, the channel wavelength must avoid those absorption lines. In consideration with single-photon detection efficiency and light diffraction, the wavelength range of quantum communications in the QEYSSat mission is chosen from 780 nm to 795 nm [38].

In addition to the scattering process, the propagating light through the atmosphere

experiences phase shifts across the transverse electric field profile. Irregular thermal distribution and winds vary local atmospheric density, and thus individual segmants of the optical wavefront experience different phase shifts that are time-dependent. In the far field, this causes beam scintilation and deflections which acts as additional losses. This randomization of the wavefront can be modelled as the reduction of (averaged) spatial coherence characterized by the so-called Fried parameter r_0. Then, the additional loss may be treated as diffraction of the reduced effective aperture with a diameter r_0, i.e., additional divergence angle $\theta_{\text{atm}} = \lambda/r_0$ caused by atmospheric turbulence.

After accounting for the atmospheric turbulence and the diffraction of incident light, the link attenuation factor α for propagation distance L as the ratio of power measured at transmitter and receiver telescopes may be expressed as [18]

$$\alpha = \frac{L^2\,(\theta_T^2 + \theta_{\text{atm}}^2)}{D_R^2}\,\frac{1}{T_T\,(1-L_P)\,T_R}\,10^{\frac{\alpha_{\text{atm}}}{10}}, \tag{1.2}$$

where D_R and α_{atm} are the diameter of the aperture at receiver and the attenuation of the atmosphere in decibels, respectively. Here, the transmittance of optical terminals at the transmitter T_T and receiver T_R is included and the L_P denotes additional losses due to pointing errors.

Figure 1.3(b) shows contour plots of the link attenuation factors as a function of the transmitter and receiver apertures for an exemplary ground-to-satellite link under nominal conditions of L =500 km, $T_T = T_R = 0.8$, $L_P = 0.2$, r_0 =9 cm, α_{atm} =4 dB. With transmitter and receiver aperture of $D_R \sim D_T \sim 20$ cm, the link attenuation factor is found to be around 35 dB. This means that, if a source emits photons at a 1 GHz rate from the ground, the photon-detection rate at the satellite would be around 1 MHz which is far beyond the typical dark-counting rate of silicon-based single-photon detectors. Another interesting observation is that the increment of transmitter aperture diameter does not improve the photon transmission after a certain value for a fixed receiver aperture. For example, for a receiver with D_R=25 cm the link attentuation factor becomes nearly constant at α =32.5 dB when the transmitter diameter is larger than 30 cm. This is mainly attributed to the atmospheric turbulence effectively reducing the transmitter aperture to a constant value. The dependency of the attenuation factor to the Fried parameter r_0 for a fixed receiver telescope D_R =25 cm is shown in Figure 1.3(c).

The turbulence-induced loss could be mitigated by employing adaptive optics. It is one of the active research areas in free-space quantum communications and some of the applications are QKDs in daylight [102] and interference-based QKDs such as measurement device independent QKDs [52]. This topic is beyond the scope of this thesis, and theoretical

analysis on the advantages of using adaptive optics in ground-to-satellite links is provided in reference [244].

Contact time

It is worth emphasizing that satellite quantum links exhibit a finite operating time. It highly depends on satellite orbits and passages. For example, when satellites are out of sight, the links are simply not available. Also, in some cases, e.g., bad weather, low elevation angle may cause too high loss for the link to be operational for QKDs. Figure 1.3(d) shows two passages of International Space Station (ISS) that were observable from University of Waterloo on the same day. The trajectories were calculated from Two-Line Element via SGP4 propagator provided by North American Aerospace Defense Command. The two ISS passages represent good and bad cases of the orbits in the QEYSSat mission. The satellites were within the line-of-sight only for about 5 minutes. Also, when the satellite appears at low-elevation angles, the closest distance between the transmitter and satellite becomes almost twice as long as when it appears at zenith.

Background noise

For operations at night, the main source of background noises in photon detections is artificial light on Earth. In the QEYSSat mission, a telescope at a satellite payload has a 0.3° field-of-view [237]. Assuming that the satellite is 500 km away from the transmitter, the telescope would recieve light from a circular region with radius around 2.6 km on Earth. Although it is collimated, the quantum signal is vary faint compared to street light, and therefore great care must be taken in selecting the location of transmitters. Also, the spectral windows of quantum signal must be chosen to avoid a potential overlap with the spectral radiance of aritifical lights, as shown in Figure 1.3(e). It was found that most of commonly used lights, e.g., LED street lights and Sodium vapour lamps, are not bright in the QEYSSat channel wavelength (780 nm to 795 nm). Nonetheless, one must verify the darkness near ground stations with experimental measurements.

Chapter 2

Polarization-entangled photon sources for ground-to-satellite quantum links

In this chapter, we design and demonstrate practical and phase-stable polarization-entangled photon sources for distributing entanglements over ground-to-satellite quantum links. We develop a novel interferometric setup which is suitable for highly non-degenerate photon sources without requiring customization of polarization optics and exhibits an excellent phase stability. We also investigate directly producing polarization-entangled photons from conventional optical fibers. At the end of this chapter, we present our conceptual design of the source to be used for the QEYSSat mission.

The content of this chapter was published in Quantum Science and Technology and Optics Express:

1. Youn Seok Lee, Mengyu Xie, Ramy Tannous, and Thomas Jennewein. Sagnac-type entangled photon source using only conventional polarization optics. Quantum Sci. Technol. **6** 025004 (2021) [171]

2. Mengyu Xie, Youn Seok Lee, Ramy Tannous, Guilu Long, and Thomas Jennewein. Roles of fiber birefringence and Raman scattering in spontaneous four-wave mixing process through birefringent fiber. Opt. Express **29**(20), 31348-31363 (2021) [308]

I am allowed by the policies of Quantum Science and Technology, Optics Express, and by permision from my co-authors to republish this work here.

Statement of contributions

- **Polarization-entangled photon source using only conventional polariation optics**
  Prof. Thomas Jennewein and I conceived the idea of the interferometric scheme. I performed the theoretical analysis as well as experimental demonstration. Ramy Tannous and Mengyu Xie contributed to generating photon pairs from polarization-maintaining fibers.

- **Polarization-entangled photon source without optical interferometer**
  Prof. Thomas Jennewein and I conceived the idea. I performed the theoretical analysis as well as experimental demonstration.

- **Toward ground-to-satetllite entanglement distribution**
  Prof. Thomas Jennewein and I conceived the conceptual design of the polarization-entangled photon source for the QEYSSat mission. I carried out theoretical analysis and developed the Matlab code to estimate absolute pair-emission rates as well as optimal beam waists in nonlinear crystals.

2.1 Introduction

Polarization-entangled photon source (PPS) is a quantum optical device which has contributed to many scientific advances in quantum information science. It played a central role in merging quantum optics with information science, and provided an experimental tool for many proof-of-principle demonstrations for quantum computational gates and quantum communication protocols. Also, it enabled experimental demonstrations that the quantum theory is incompatible with local realism via the violation of Bell's inequality [260, 98], which offered insights to on-going discussions in the interpretations of the quantum mechanics [153]. PPSs have been an important item in laboratories studying discrete-variable quantum optics. Many of the key components are nowadays commercially available, and the practical implementation with minimal budget is an important aspect in the field.

Recently, PPSs have also been taken outside of the well regulated environment optical labs and utilized in outdoor experiments. This is mainly motivated by two ambitions: testing quantum entanglement in gravity and free-space quantum communications. It requires sophisticated designing and precise engineering of the source for its high robustness and reliable operation with proper packages to protect the internal optomechanical setup. In 2016, researchers at Institute for Quantum Optics and Quantum Information in Vienna has

placed a PPS in the free fall and rotation of the crate for entanglement tests in accelerated reference frame [89]. In the same year, researchers at Centre of Quantum Technologies in Singapore reported an assembly technique that made a photon-pair source survive from the explosion of a rocket [280]. In 2020, the same group demonstrated the polarization entanglement in an orbiting nano-satellite [294].

With the growing interest of entanglement distributions over free-space channels, we summarize some of the preferred settings of PPSs. First, optical polarization is a good photonic degrees of freedom for encoding quantum information due to its minimal decoherence [120]. Most of the reported experimental demonstrations as well as proposals for quantum links between satellites and ground stations utilized the polarization of photons [263]. Secondly, the wavelength of one of the pairs which is sent through free-space channels is preferred to be from 780 nm to 810 nm. This wavelength range was found to be an optimal zone in our previous study [38], which was mainly deduced from the trade-off between photon loss by Rayleigh scattering and light diffraction as well as photon-detection efficiency of silicon-based single-photon detectors. Additionally, the narrow spectral bandwidth is desired to efficiently filter out the unwanted stray light from various objects such as Sun, Moon, and street light. Finally, high generation rate and device throughput are required for long-distance links, which is applicable for fiber-optic channels as well.

2.2 Polarization-entangled photon source using only conventional polariation optics

2.2.1 Motivation

The main motivation of the work presented in this section is to develop a PPS which can directly distribute polarization-entangled photons over both ground-to-satellite quantum link and optical fiber-based network. As stated before, the photon transmission for free-space quantum channels is optimal at near-infrared (780 nm to 810 nm) [38] wavelengths, whereas telecom wavelengths (1310 nm to 1550 nm) are optimal for optical fiber channels. This poses the requirement of highly non-degenerate PPSs, which have been implemented with various nonlinear materials and schemes, such as a dispersion-shifted fiber in Michelson-interferometer [177], periodically poled potassium titanyl phosphate in a so-called sandwich configuration [233, 129] and in a Sagnac-interferometer [119], and periodically poled lithium niobate in a Sagnac-interferometer [256].

Sagnac-type entangled photon sources (Sagnac-EPS), as depicted in Figure 2.1(a), have

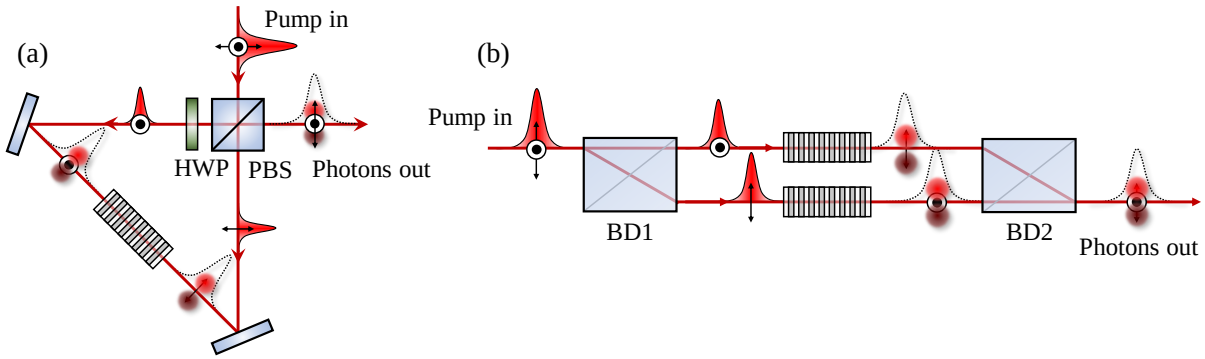

Figure 2.1: A schematic diagram of two existing interferometric schemes for polarization-entangled photon sources: (a) Sagnac-type entangled photon source (Sagnac-EPS) and (b) Mach-Zehnder-type entangled photon source (MZ-EPS); PBS, polarization beam splitter; HWP, half-waveplate; BD, beam displacers. Both interferometers superpose two orthongonally polarized pair-generation processes, producing polarization entangled photons. We consider spontaneous parametric down conversion process with a type-I phase-matching condition as an example. The HWP and PBS are required to operate at two or three distinct wavelengths (i.e., pump field and photon pairs) in Sagnac-EPS. In the MZ-EPS, the two orthogonally polarized pair-production processes are spatially saparated.

been one of the most popular methods due to their intrinsic phase stability and versatility [155]. A variety of nonlinear optical media including nonlinear optical fibers, photonic crystal fibers, bulk- and waveguide-type periodically poled nonlinear crystals, and atomic vapour cells have been employed [176, 86, 85, 94, 180, 16, 292, 207, 229]. However, a typical Sagnac-EPS requires polarization optics working in at least two, sometimes three, very distinct wavelengths, i.e., pump and photon pairs. The customization of polarization optics for highly non-degenerate photon pairs is technically demanding and costly, and its performance typically limits the quality of the polarization-entanglement. Sauge *et al.* [256] demonstrated a non-degenerate entangled photon source by unfolding the Sagnac loop into two different loops: one for pump (532 nm) and idler (1550 nm) photons and the other for signal (810 nm) photon. This unfolded Sagnac scheme, which is originally proposed by Fiorentino *et al.* [91], provides flexibility in the choice of the wavelength without the customization of polarization optics. Recently, the unfolded Sagnac-like entangled photon source was implemented for the randomness extraction from Bell violation [261]. However, the scheme loses the intrinsic phase stability of an original Sagnac-EPS due to the separate optical paths for the signal and idler photons. On the other hand, Hentschel *et al.* [119] demonstrated an original Sagnac-EPS by replacing a polarization beam split-

ter and a half-waveplate with a Glan-Thompson polarizer and a periscope, respectively. In their setup, a custom-designed Glan-Thompson polarizer is required to avoid angular dispersions and the optical alignment is relatively tedious.

Mach-Zehnder-type entangled photon sources (MZ-EPS) with two beam displacers have recently become popular [90, 84, 260, 123, 187]. The main advantages of this design are the simple alignment procedure and the compactness, while the monolithic configuration exhibits a high phase stability, as shown in Figure 2.1(b). In addition, the MZ-EPS takes full advantage of the high polarization extinction ratio of beam displacers over a wide range of wavelengths. However, since the photon-pair production processes occur in two different optical paths, one may have to prepare two identical nonlinear materials or miniaturize the waveplates used. More importantly, the MZ-EPS cannot be easily adapted for fiber- or waveguide-based nonlinear media due to the requirement of their guided modes to be matched.

In this section, we develop a new interferometer configuration for PPSs which is suitable for various optical nonlinear materials over a wide wavelength range without the need for customized polarization optics. The interferometer is configured such that a Sagnac loop is placed inside a Mach-Zehnder interferometer that is formed by two beam displacers. The polarization states of the pump and photon pairs are split and recombined by two beam displacers as in MZ-EPS, and at the same time, two pair-production processes are kept in a common optical path as in Sagnac-EPS. Thus, the designed entangled photon source, which we call a beam displacement Sagnac-type entangled photon sources (BD-Sagnac-EPS), takes advantage of both an original Sagnac-EPS and MZ-EPS. We demonstrate the designed interferometer with the pulsed generation of polarization-entangled photon pairs at the wavelengths of 764 nm and 1221 nm via spontaneous four-wave mixing (SFWM) in a commercial-grade polarization-maintaining fiber (PMF) by using only standard commercial optical elements.

2.2.2 Conceptual design of the BD-Sagnac-EPS

The conceptual design of the novel BD-Sagnac-EPS is depicted in Figure 2.2. Two beam displacers (BD1 and BD2) form a Mach-Zehnder interferometer; one (BD1) is for the input port of pump light and the other (BD2) is for the output port of the generated photon pairs. The diagonally polarized pump light enters the interferometer, and the BD1 converts the two orthogonal polarizations into two parallel optical paths, $|H\rangle_P$ and $|V\rangle_P$. By connecting one path to the other, the Sagnac loop is formed inside the Mach-Zehnder interferometer (blue path: clockwise and red path: counterclockwise). The optical

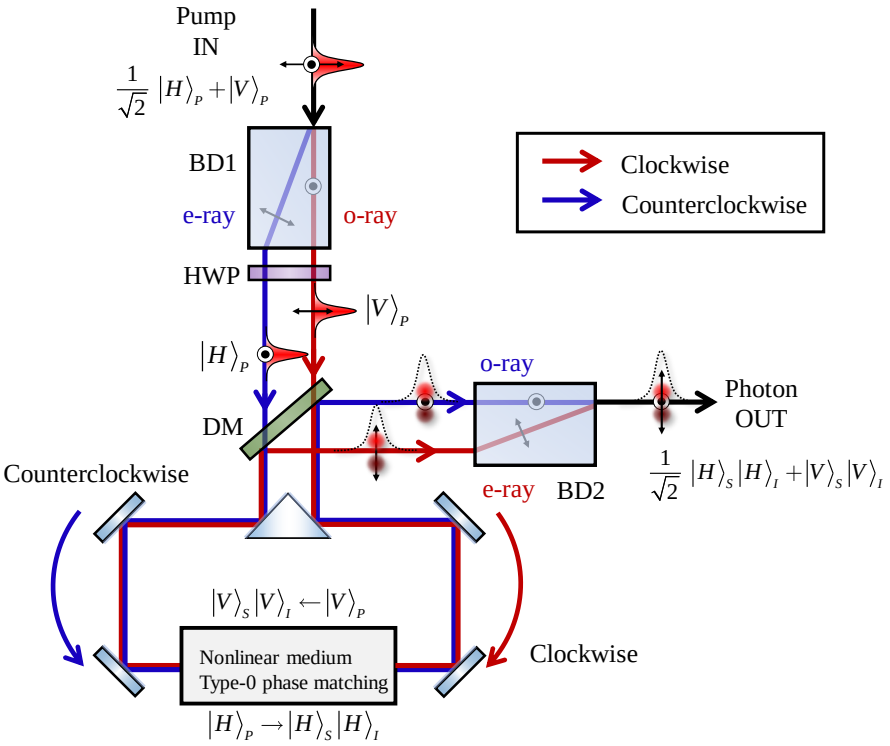

Figure 2.2: A schematic drawing of the conceptual design for beam displacement Sagnac-type entangled photon source; BD, beam displacers; HWP, half-waveplate; DM, dichroic mirror; o-ray, ordinary ray; e-ray, extraordinary ray. Here, we consider a type-0 phase-matching condition as an example of the pair-generation process. The implementations for type-1 and type-2 phase-matching conditions are discussed in the main text.

nonlinear medium is placed at the center of the Sagnac loop where the correlated photon pairs (namely, signal and idler) are generated via a spontaneous parametric amplification process, e.g., a spontaneous parametric down-conversion and four-wave mixing. As an example, we consider the medium where type-0 phase-matching conditions are satisfied in two orthogonal polarization axes: $|V\rangle_P \rightarrow |V\rangle_S|V\rangle_I$ (clockwise) and $|H\rangle_P \rightarrow |H\rangle_S|H\rangle_I$ (counterclockwise) [1]. Here, the subscripts P, S, and I stand for the pump, signal, and

[1]The phase-matching condition in two orthogonal polarization directions can be implemented in various ways. One example is to place two identical nonlinear crystals that are cross-oriented to each other [274]. Also, one may utilize nonlinear media which naturally satisfy the phase-matching condition in both polarization axes such as an atomic ensemble [229]. As for the fiber-based or pigtailed media, the two ends of the fiber can be twisted such that the two pump polarizations are aligned to the phase-matching directions

idler photons, respectively. As the wavelengths of the generated photons are different from that of the pump, the two orthogonally polarized photon pairs are spectrally filtered out using a dichroic mirror which in our case was implemented with a standard bandpass filter, and exit the Sagnac loop [2]. Then, the BD2 recombines the two photon pairs into a single spatial mode. The superposition of two pair-production processes yields the polarization-entangled state, $|\Phi^+\rangle = (|V\rangle_S |V\rangle_I + |H\rangle_S |H\rangle_I)/\sqrt{2}$.

Beam displacers are made of uniaxial birefringent materials where refractive indices between ordinary and extraordinary rays are different. The refractive index discrepancy for a few centimeter beam displacer yields an optical path length difference that is large enough to timely separate the photons' wavepackets of two polarization modes, i.e., a temporal walk-off. To make the optical path lengths balanced within the interferometer, the temporal walk-off caused by the BD1 must be compensated at the BD2. In this example of the type-0 phase-matching condition, a half-waveplate is introduced after the first beam displacer in order to flip the pump polarization such that ordinary/extraordinary ray at the first beam displacer experiences the extraordinary/ordinary path at the second beam displacer. Note that for the type-1 phase-matching condition, the interferometer is balanced without the half-waveplate in Figure 2.2.

However, for non-degenerate entangled photon sources, the three photons, i.e., pump, signal, and idler, for each polarization mode propagate through the beam displacer at different speeds and refraction angles due to its chromatic dispersion. This causes additional spatial and temporal walk-offs that must be compensated before or after the interferometer appropriately. As illustrated in Figure 2.3, the spatial walk-off decreases the fiber-coupling efficiency of the entangled photon pairs and the temporal walk-off degrades the entanglement quality due to the imperfect overlap between the photon wavepackets in the ordinary and extraordinary paths [189]. Furthermore, the phase shifts caused by the temperature variation are different for the three photons due to the chromatic dispersion, which may impact the stability of the interferometer significantly. In the following, we estimate the walk-offs and the temperature-dependent phase shift of the entangled state, for different uniaxial birefringent crystals.

First, we estimate the spatial walk-off $\Delta d_{S(I)}$ by calculating the refraction angles ψ

at both ends.

[2] This could also be realized by a standard notch filter centered at the pump's wavelength. In this case, the incident pump light is reflected and the generated photon pairs are transmitted. Note that a precise spectral filter or dichroic mirror is not required because the pump wavelength is usually far apart from the photon-pair's wavelengths in parametric down-conversion and four-wave mixing process.

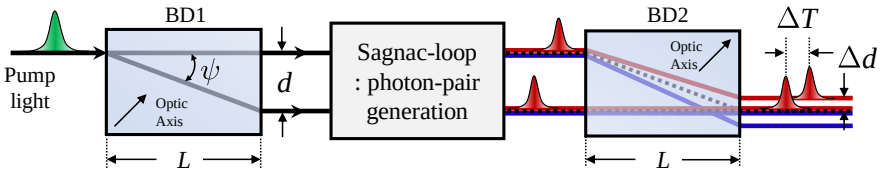

Figure 2.3: Spatial and temporal walk-off due to the chromatic dispersion of beam displacers (BD1 and BD2). The photons generated from an optical nonlinear medium in the Sagnac loop have different wavelengths from the incident pump light, and therefore they pass through the BD2 with different refractive angles and group velocities.

between ordinary and extraordinary rays in the beam displacers [222], as expressed by

$$\tan(\psi) = \frac{(n_e^2 - n_o^2)\cos(\theta)\sin(\theta)}{n_e^2\cos^2(\theta) + n_o^2\sin^2(\theta)}, \tag{2.1}$$

where θ is the angle between the optical axis and the wavevector of the incident light. Here, n_o and n_e are denoted as the ordinary and extraordinary refractive indices, respectively. From the Sellmeier equation for different birefringent materials, the spatial walk-off is calculated for the optical axis aligned at the angle of 45° with respect to the wavevector of incident light:

$$\Delta d_{S(I)} = L\tan(\psi_P) - L\tan\left(\psi_{S(I)}\right), \tag{2.2}$$

where L is the length of beam displacers and $\psi_{P(S,I)}$ is the refraction angle of the pump, signal, and idler photons, respectively.

Secondly, to estimate the temporal walk-off $\Delta T_{S(I)}$, we consider the arrival time of the photon pairs at the end of the BD2 after traveling through the ordinary and extraordinary paths of the interferometer. These arrival times for signal and idler photons are referenced from when the pump pulse departed the front of the BD1 and can be expressed as

$$T_{\mathrm{S(I)},o(e)} = \frac{l_{e(o)}(\lambda_{\mathrm{P}})}{v_{g,e(o)}(\lambda_{\mathrm{P}})} + \frac{l_{o(e)}(\lambda_{\mathrm{S(I)}})}{v_{g,o(e)}(\lambda_{\mathrm{S(I)}})}, \tag{2.3}$$

where $l_{e(o)} = L/\cos(\psi)$ is the physical optical path length for the extraordinary (ordinary) light of the beam displacer and $v_{g,e(o)}(\lambda_{P(S,I)})$ is the group velocity of the extraordinary (ordinary) light at the wavelength of the pump, signal, and idler photons, respectively. Note that the group velocity for the extraordinary ray was calculated from the effective refractive index n_{eff}, defined as

$$\frac{1}{n_{\mathrm{eff}}^2} = \frac{\sin^2(\theta_e)}{n_e^2} + \frac{\cos^2(\theta_e)}{n_o^2}, \tag{2.4}$$

where $\theta_e = \psi + \theta$ is the angle between the optic axis and the wavevector of the extraordinary ray. Then, the temporal walk-off can be calculated by the arrival time difference between ordinary and extraordinary light,

$$\Delta T_{S(I)} = T_{\mathrm{S(I)},o} - T_{\mathrm{S(I)},e}. \tag{2.5}$$

Finally, the temperature-dependent phase shift is estimated for the entangled state which can be written as

$$|\Phi^+\rangle = \frac{1}{\sqrt{2}} \left(|V\rangle_S |V\rangle_I + e^{i\phi(\lambda,T)} |H\rangle_S |H\rangle_I \right). \tag{2.6}$$

Here, the $\phi(\lambda, T)$ is the relative phase between the clockwise and counterclockwise optical paths. As for the optical elements that lie inside the Sagnac loop, the temperature-dependent phase shift can be negligible due to the self-compensation effect [119] and we ignore the phase shift due to the waveplate after the first beam displacer because of its thickness. Then, the relative phase can be expressed as

$$\begin{aligned} \phi(\lambda, T) &= 2\phi_e(\lambda_P) + \phi_o(\lambda_S) + \phi_o(\lambda_I) - (2\phi_o(\lambda_P) + \phi_e(\lambda_S) + \phi_e(\lambda_I)) \\ &\equiv 2\Delta\phi(\lambda_P) - \Delta\phi(\lambda_S) - \Delta\phi(\lambda_I). \end{aligned} \tag{2.7}$$

Here, the factor of two for the pump's phase shift comes from the fact that in the four-wave mixing process two pump photons are converted to the signal and idler photons. It is worth to note that the phase shift difference between the ordinary and extraordinary rays $\Delta\phi(\lambda) = \phi_e(\lambda) - \phi_o(\lambda)$ for signal and idler photons are compensated by the pump-photon. This is the manifestation of the self-compensating effect of the Saganc-interferometer [119]. In fact, our designed interferometer can be viewed as an unfolded Sagnac interferometer: a polarized beam splitter is replaced by two beam displacers, and it maintains the inherent stability of the Sagnac interferometer. The temperature-dependent phase shift is characterized by the derivative of the phase shift with respect to the temperature $\partial\phi/\partial T$. Each term can be expressed in terms of the thermo-optic coefficient and the thermal expansion coefficient as

$$\frac{\partial\phi}{\partial T} = \frac{2\pi}{\lambda} L(T) \left[\frac{\partial n(\lambda, T)}{\partial T} + n(\lambda, T)\alpha \right], \tag{2.8}$$

where α is a thermal expansion coefficient. Again, the thermo-optic coefficient for the extraordinary ray is derived from the formula of the effective refractive index 2.4.

$$\frac{\partial n}{\partial T} = \frac{\frac{\partial n_o}{\partial T} n_e + n_o \frac{\partial n_e}{\partial T}}{\sqrt{n_o^2 \sin^2(\theta_e) + n_e^2 \cos^2(\theta_e)}} + n_o n_e \frac{2n_o \frac{\partial n_o}{\partial T} \sin^2(\theta_e) + 2n_e \frac{\partial n_e}{\partial T} \cos^2(\theta_e)}{(n_o^2 \sin^2(\theta_e) + n_e^2 \cos^2(\theta_e))^{3/2}} \tag{2.9}$$

Table 2.1: The spatial, temporal walk-off, and temperature-dependent phase shift caused by chromatic dispersions from different materials for two beam displacers in BD-Sagnac-EPS. The Sellmeier equations $n_{o(e)}$, thermo-optic coefficient dn/dT, and thermal expansion coefficient α for calcite and α-BBO are obtained from [228]. Those parameters for YVO_4 were from [255]. Note that in [255] the thermo-optic and thermal expansion coefficients are available at the wavelength of 0.9 µm, 1.1 µm, and 1.3 µm. We applied a linear interpolation and extrapolate to obtain the values at the wavelength of 764 nm, 940 nm, and 1221 nm.

Material	$\Delta T_S, \Delta T_I$ (ps)	$\Delta d_S, \Delta d_I$ (mm)	$\partial\phi/\partial T$ (°/K)
Calcite	-0.20, 0.06	-0.07, 0.09	-7.00
α-BBO	-0.18, 0.15	-0.01, -0.01	-0.97
YVO_4	1.35, -0.93	0.07, -0.06	-0.86

It is worth noting that one can design the beam displacers by cascading two or more complementary birefringent materials with the carefully chosen length ratio such that the first-order temperature-dependence of the phase shift vanishes [72]. However, in our analysis, we restrict our scope to the two beam displacers with the same length and birefringent material for the practical implementation of the BD-Sagnac-EPS.

We demonstrate our design by generating photon pairs at 764 nm and 1221 nm via SFWM driven by the pump light at 940 nm. The spatial ΔT_I, temporal walk-off ΔT_S, and the temperature-dependent phase shift $\partial\phi/\partial T$ are calculated for three common birefringent materials, i.e., calcite, α-BBO, and YVO_4, for 40 mm–long beam displacers at the wavelengths of the photon pairs. The results are summarized in Table. 2.1. We found that the temperature-dependence of the phase shift is less than 0.04π/K for the three materials and the YVO_4 is the most promising candidate in terms of thermal stability. As the temporal walk-off is relatively easy to compensate by birefringent materials in comparison with the spatial walk-off, the α-BBOs is also a good choice. However, in our demonstration, we used two calcite beam displacers due to the availability of these components at our facilities.

After accounting for the spatial and temporal walk-off, as well as the temperature-dependent phase shift, here we summarize the main advantages of the BD-Sagnac-EPS. First, the setup does not require any customized polarization optics because pump and photon pairs do not share any common polarization optics. In fact, our demonstration consists of all commercial off-the-shelf optical elements. Protected-silver coated mirrors have a nominal reflectivity of greater than 97 % for wavelengths between 0.450 µm to 7 µm while the two identical calcite beam displacers exhibit extinction ratios of 100,000:1 over wavelengths between 0.200 µm to 3.5 µm, which makes the setup suitable for highly non-

degenerate polarization-entangled photon pairs. Secondly, the interferometer is symmetric and the optical path lengths are balanced for two orthogonal polarization states by the Sagnac loop, and therefore pulsed operation can be readily achieved. Third, the alignment procedure is easier than for typical Sagnac-type sources due to the fact that the optical path of the incident pump light and the emitted photon pairs can be individually controlled, meaning that the optical paths for the pump and photon pairs do not have to be on the same plane. Finally, our design is applicable for as broad range of optical nonlinear media as with typical Sagnac-EPS, including an optical nonlinear bulk crystal, nonlinear optical fibers, and periodically poled nonlinear waveguides. Furthermore, our design is not limited to the type-0 phase-matching condition described above, as type-1 and type-2 phase-matching conditions can also be implemented with minor modifications. For example, the type-1 condition can be easily implemented by removing the half-waveplate. For the type-2 condition, one may add one or two more beam displacers to rearrange the polarization components at the output, as demonstrated in other works [260, 123].

2.2.3 Experimental setup

We experimentally implement our design and generate non-degenerate polarization-entangled photon pairs via SFWM in a commercially available PMF (HB800G, Thorlabs). A schematic of the experimental setup is presented in Figure 2.5. Diagonally polarized pump light from a mode-locked laser, operating at a wavelength of 940 nm with a pulse duration of 3 ps and the repetition rate of 76 MHz, is split into two optical paths with horizontal- and vertical-polarization by 40 mm-long calcite beam displacer. The pump light passes through a bandpass filter (940 nm, FWHM = 10 nm) and enters the Sagnac loop. A 20 cm-long PMF is used as the optical nonlinear medium. The PMF is twisted by 90° such that its slow axes of each end are aligned to two counter-propagating pump polarizations. Correlated photon pairs are generated at wavelengths of 764 nm and 1221 nm via SFWM, and the phase-matching condition is assisted by the birefringence of slow- and fast-axis of PMF [86, 269]. The PMF has neither any active temperature stabilization nor thermal insulation. The generated photons are reflected by the bandpass filter centered at the pump's wavelength, and then recombined into a single spatial mode by the identical calcite beam displacer. The signal and idler photons are separated by a dichroic mirror, coupled into single-mode fibers, and then detected by a Silicon-based single-photon detector (Excelitas, SPCM-AQ4H, Detection Efficiency $\approx 55\,\%$) and superconducting nanowire single-photon detector (Quantum Opus, Opus One, Detection Efficiency $\approx 80\,\%$), respectively. Note that we used bandpass filters for the signal (770 nm, FWHM = 10 nm) and idler (1220 nm, FWHM = 25 nm) in front of the each single-mode fibers in order to block stray lights such

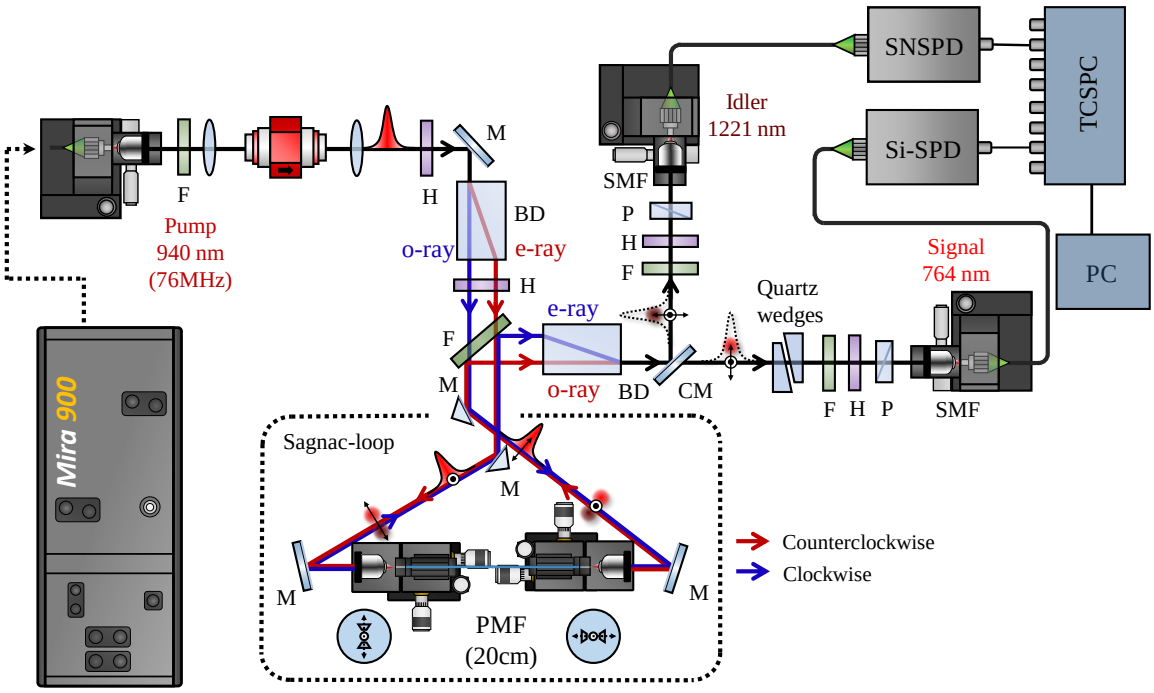

Figure 2.4: A schematic drawing of the experimental setup for the demonstration of the new interferometer design. Correlated photon pairs are generated at the wavelength of 764 nm and 1221 nm from 20 cm-long PMF that is pumped by a mode-locked picosecond pulse laser (940 nm, 76 MHz, 3 ps). The PMF is placed at the center of Sagnac loop and twisted by 90°, such that the slow-axis is aligned to pump polarizations. The generated photon pairs exit the Sagnac loop upon the reflection by a spectral bandpass filter; BD, 40 mm-long calcite beam displacer; F, bandpass filter; H, half-wave plate; P, linear polarizer; M, protected-silver-coated mirror; DM, dichroic mirror; SMF, single-mode fiber; SNSPD, superconducting nanowire single-photon detector; Si-SPD, Silicon-based single-photon detector; TCSPC, time-correlated single-photon counter.

as Raman-scattered lights. The polarization correlations are analyzed by half-waveplates and linear polarizers. The pair production rate and heralding efficiencies are characterized by single and coincidence counting rates.

As shown in Table. 2.1, we estimated the spatial walk-off for signal and idler photon to be 0.07 mm and 0.09 mm, respectively. We model the photon's spatial modes in clockwise and counterclockwise paths as two Gaussian beams $F_1(x, y)$ and $F_2(x, y)$ with the beam diameter (1/e) of 1.1 mm. The corresponding spatial amplitude overlap factor $\int F_1 \cdot F_2 \, dx \, dy$

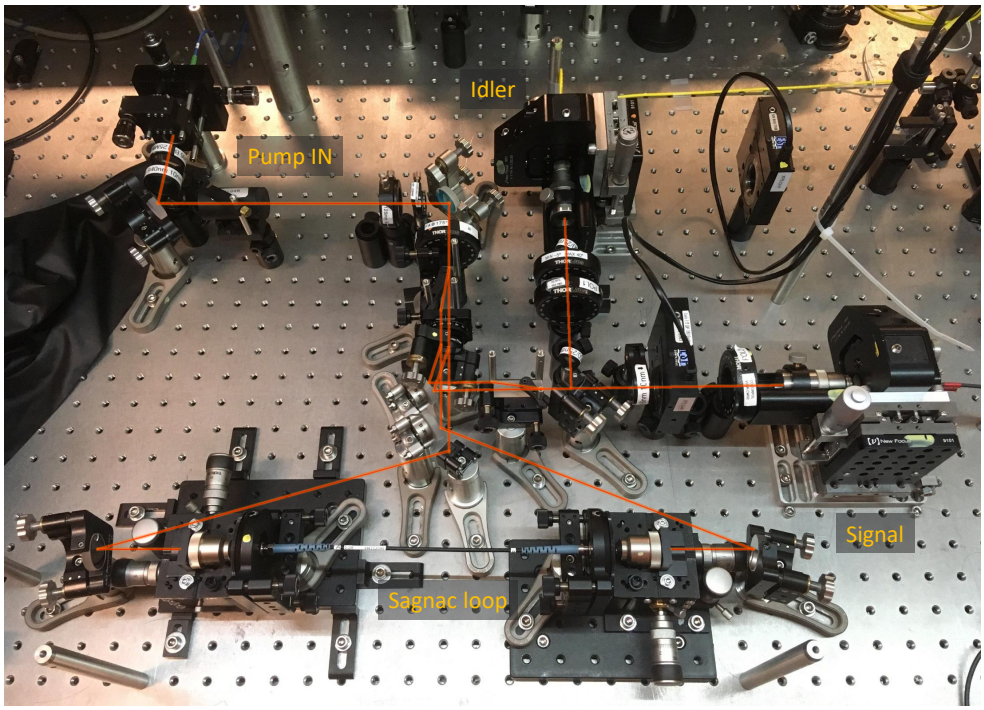

Figure 2.5: A photograph of the experimental setup for proof-of-principle demonstration of a BD-Sagnac-EPS in October 2019.

between the two modes is calculated to be higher than 99 % for both signal and idler wavelengths. Therefore, in this experiment, it is expected that the fiber-coupling efficiency drop due to the spatial walk-off is negligible [152]. On the other hand, from the measured spectral full width at half maximum (FWHM) of the signal (0.8 nm) and idler photons (2.0 nm), we model the photon's amplitude temporal wavepacket with a Gaussian function whose temporal width (1/e) is 1.3 ps for both signal and idler photons. Similarly, the amplitude overlap factors between the wavepackets are calculated to be 97.3 % and 99.8 % for the signal and idler photons, respectively. Therefore, in this experiment, we introduced a 1.6 cm–thick quartz crystal in the signal arm to compensate for the temporal walk-off of signal photons.

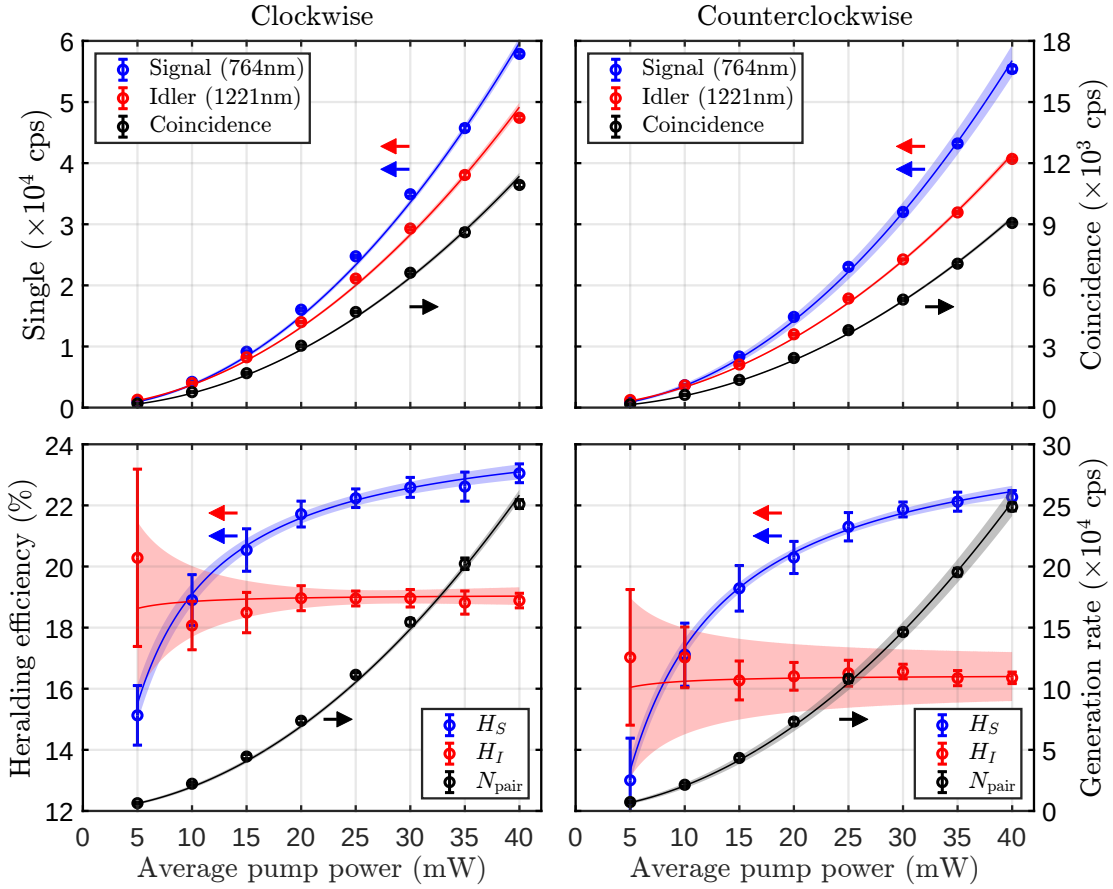

Figure 2.6: Photon-pair generation rate for the clockwise (left) and counterclockwise (right) paths of the Sagnac loop. The circles are the mean values of ten separate measurements of single and coincidence counting rates with the standard deviations as the error bars. The solid curves are fits to the model 2.10, and the shaded regions represent the 95 % confidence interval for the fitting curve.

2.2.4 Results

Correlated photon-pair generation from a polarization-maintaining optical fiber

We measure the single and coincidence counting rates for the clockwise and counterclockwise paths with a coincidence window Δt_C of 1 ns, as shown in Figure 2.6. After subtracting the detector's dark counts from the single counting rate, we calculate the mean values for the single and coincidence counting rates over five separate measurements. The measured

single $N_{S(I)}$ and coincidence N_C counting rates are used to estimate the heralding efficiencies, $H_{S(I)} = N_C/N_{I(S)}$, and the pair generation rate, $N_{\text{Pair}} = (N_S N_I)/N_C$. The quadratic scaling of the counting rates with the incident pump power shows that the pair production process is governed by the third-order optical nonlinear process. Therefore, it is rational to quantify the pair generation rate per pulse in units of cps/mW^2, which is estimated to be $2.1(2) \times 10^{-6}$ cps/mW^2 per pulse for our experiment.

In Figure 2.6, it is notable that the heralding efficiency for the signal photons varies as a function of pump power while that of the idler photons stays relatively constant. This feature is not typically observed in the spontaneous parametric down-conversion process. To study this behavior, we modeled the single and coincidence rate with the inclusion of the Raman-scattered photons from the PMF. In particular, we assumed that the incoherent Raman-scattering plays a major role as background noise in our experiment which scales linearly with pump power [41]. The modeled single and coincidence counting rates are expressed as

$$\begin{aligned}
N_S &= \eta_S N_{\text{Pair}} P^2 + N_{D,S} + \eta_S N_{\text{Raman,S}} P, \\
N_I &= \eta_I N_{\text{Pair}} P^2 + N_{D,I} + \eta_I N_{\text{Raman,I}} P, \\
N_C &= \eta_S \eta_I N_{\text{Pair}} P^2 \\
&\quad + \eta_S N_{\text{Pair}} P^2 (N_{D,I} + N_{\text{Raman,I}} P \eta_I) \Delta t_C \\
&\quad + \eta_I N_{\text{Pair}} P^2 (N_{D,S} + N_{\text{Raman,S}} P \eta_S) \Delta t_C \\
&\quad + (N_{D,I} + \eta_I N_{\text{Raman,I}} P)(N_{D,S} + \eta_S N_{\text{Raman,S}} P) \Delta t_C,
\end{aligned} \tag{2.10}$$

where $\eta_{S(I)}$ is the total detection efficiencies of signal(idler) photons including fiber-coupling efficiency, photon loss by imperfect optics, and detection efficiency. N_{Pair} is the pair generation rate of SFWM process, $N_{\text{Raman,S(I)}}$ is the Raman-scattering rates at the signal(idler) wavelengths, $N_{D,S(I)}$ is the dark counts for the signal(idler) photon detectors, and P is the average pump power.

We applied the least-squares method to perform a global fitting of the model 2.10 to the experimental data of $\{N_S, N_I, N_C, H_S, H_I\}$ with the shared fitting parameters of $\{N_{\text{Pair}}, N_{\text{Raman,S}}, N_{\text{Raman,I}}, \eta_S, \eta_I\}$. Then, we used the optimized parameters to estimate the pair generation rate $N_S N_I / N_C$, as shown in Figure 2.6. In Figure 2.6, the symbols represent the experimentally obtained values from the measured single and coincidence count rate after the subtraction of the dark counts of each detector. The solid lines are a curve fit based on the model and the shaded regions represent the 95 % confidence interval for the fitting. The fit parameters for the clockwise (counterclockwise) path are obtained to be $\{N_{\text{Pair}} = 149.71(141.97),\ N_{\text{Raman,S}} = 18.61(0),\ N_{\text{Raman,I}} = 450.39(615.96),$

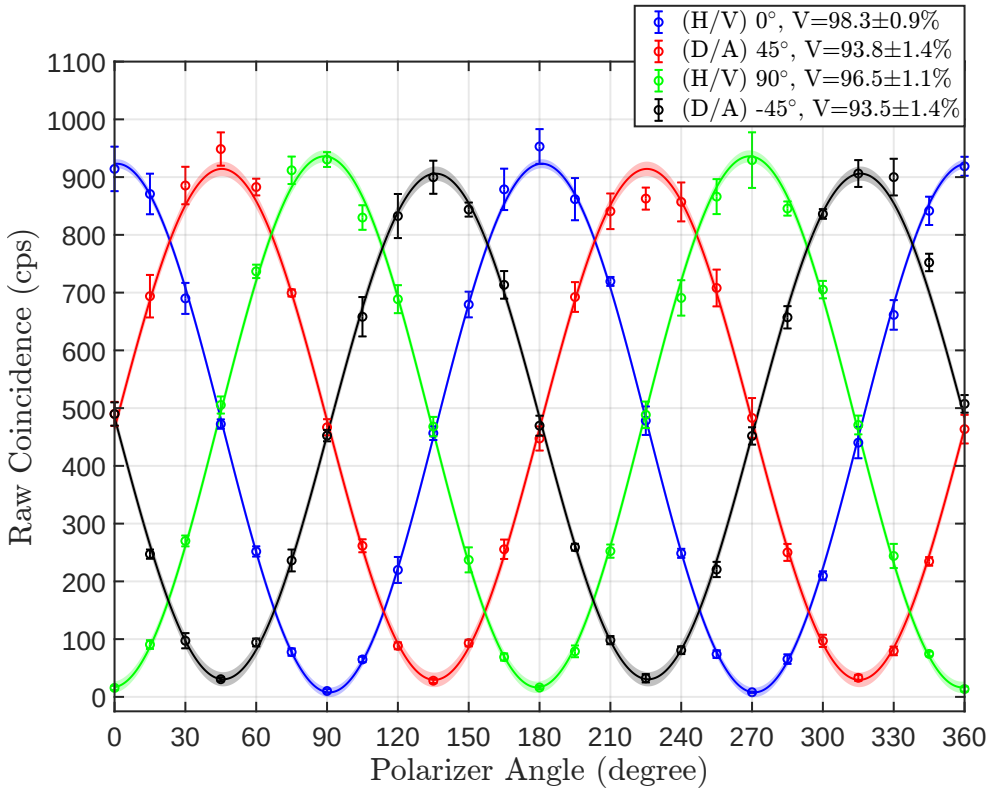

Figure 2.7: Measurement of polarization entanglement: the circles are experimental data with the standard deviation calculated over five separate measurements. The solid curves are sinusoidal fits, and the shaded regions represent the 95 % confidence interval for the sinusoidal fits. The visibilities are calculated from raw coincidence counts without any background subtraction.

$\eta_S = 0.25(0.25)$, $\eta_I = 0.19(0.16)\}$, which agrees with the fact that the incoherent Raman-scattering dominates in longer wavelength. It is worth noting that the difference in the heralding efficiencies for the signal photons is negligible whereas there is a 3 % discrepancy for the idler photons. This may be attributed to the polarization-dependent detection efficiencies of the superconducting nanowire single-photon detector. From our model, we interpret that the varying heralding efficiency is due to the fact that the incoherent Raman noise dominates in idler arm for the low pump power regime. Thus, a click on the idler detector has a low probability of heralding the presence of a photon in the signal arm.

Polarization-entangled photon pairs

Polarization entanglement produced by the BD-Sagnac-EPS was characterized by performing polarization-correlation measurements. We measured the coincidence counting rates as a function of the rotation angle of a polarizer in the signal arm while the polarization measurement bases for the idler photons are fixed to horizontal (H, 0°), vertical (V, +90°), diagonal (D, +45°), and antidiagonal (A, -45°), as shown in Figure 2.7. The measurement was performed under the average pump power of 20 mW with a coincidence window of 0.6 ns. For each polarization setting, the mean values and standard deviations are calculated over five separate measurements of the single and coincidence counting rates. The single counting rates of the signal and idler photons remained constant at around 13 000 cps and 8000 cps, respectively, during all four polarization-correlation measurements. A linear least-squares method was applied to perform a sinusoidal fit to the 2π-rotation of polarization-correlation measurement.

The visibilities, $\mathrm{V} = (\max\{N_C\} - \min\{N_C\}) \,/\, (\max\{N_C\} + \min\{N_C\})$, calculated from raw coincidence counting rates for the idler's polarization bases at H, V, D, A are $(98.3 \pm 0.9)\,\%$, $(96.5 \pm 1.1)\,\%$, $(93.8 \pm 1.4)\,\%$, and $(93.5 \pm 1.4)\,\%$, respectively with the averaged value of $\mathrm{V_{avg}} = (95.5 \pm 0.6)\,\%$. To verify the polarization entanglement, we performed the CHSH inequality test [63] with the measured coincidence rates in Figure 2.7. The inequality is expressed as

$$S = |E(\theta_1, \theta_2) - E(\theta_1, \theta_2') + E(\theta_1', \theta_2) + E(\theta_1', \theta_2')| \leq 2, \tag{2.11}$$

where θ_i is the rotation angles of the linear polarizers for signal and idler photons. Here, the polarization-correlation coefficient $E(\theta_1, \theta_2)$ is expressed as

$$E(\theta_1, \theta_2) = \frac{N_C(\theta_1, \theta_2) - N_C(\theta_1, \bar{\theta}_2) - N_C(\bar{\theta}_1, \theta_2) + N_C(\bar{\theta}_1, \bar{\theta}_2)}{N_C(\theta_1, \theta_2) - N_C(\theta_1, \bar{\theta}_2) - N_C(\bar{\theta}_1, \theta_2) + N_C(\bar{\theta}_1, \bar{\theta}_2)}, \tag{2.12}$$

where $N_C(\theta_1, \theta_2)$ is the coincidence counting rate between the signal and idler photon detections with the two linear polarizers set to θ_1 and θ_2, and $\bar{\theta} = \theta + 90°$ denotes the orthogonal setting of linear polarizers. We obtained the parameter $S = 2.70 \pm 0.04$ from the raw coincidence counting rate recorded for the polarizers' settings at $\theta_1 = 0°$, $\theta_2 = 22.5°$, $\theta_1' = 45°$, and $\theta_2' = 67.5°$, which is in good agreement with the expected experimental value $S_{\mathrm{exp}} = 2\sqrt{2}\mathrm{V_{avg}}$. The strong violation of the CHSH inequality by 17.5 standard deviations is a direct indication of the polarization entanglement. Based on the above model for counting rates together with the analysis on the spatial and temporal walk-off, the reduced entanglement quality was mainly attributed to spontaneous Raman scattering in PMF at idler wavelength and the uncompensated temporal walk-off for the idler photons.

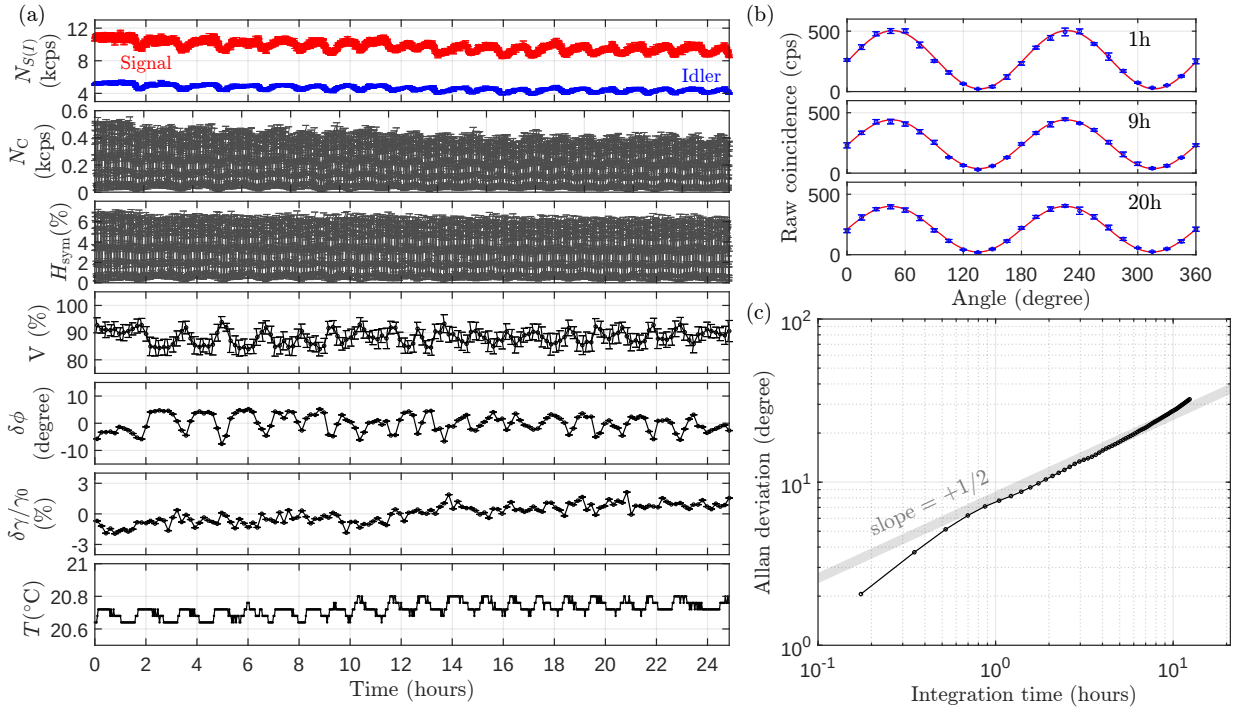

Figure 2.8: The phase-stability measurement of the BD-Sagnac-EPS. (a) Polarization-correlation measurement for over 24 hours. Single and coincidence counting rates are measured as a function of the rotation angle of the polarizer at signal arm while the polarization basis of the idler photons is fixed to the diagonal state (D, +45°). The visibility V, the variation of the phase $\delta\phi$, and the relative amplitude fluctuation $\delta\gamma/\gamma_0$ ($\gamma_0 = 1/\sqrt{2}$) are extracted by fitting the model 2.13 to the symmetric heralding efficiency. The temperature of our laboratory T was monitored during the measurement (see text for a detailed analysis). (b) The magnified plot of raw coincidence counts for different measurement times. (c) Allan phase deviation as a function of the integration time. Block dots denote experimental data and a gray area represents lines with the slope +1/2.

Phase stability

In order to characterize the phase stability of the BD-Sagnac-EPS, we performed the polarization-correlation measurement for over 24 hours without active phase stabilization, as shown in Figure 2.8. The temperature of the laboratory environment was regulated within a peak-to-peak value of 0.16°C. We performed a full 2π-rotation of the signal polarization basis at a period of ten minutes while the idler polarization basis is fixed to the

diagonal basis (D, +45°). The coincidence measurements are averaged over five separate measurement events at each rotation angle setting. We observed that the variation of the visibility V remains within the range of 83.9 % to 93.9 %, as shown in Figure 2.8(a).

To extract the phase information from the measured data, we model the coincidence rate N_C in terms of the phase and amplitude of the produced entangled state. We assume that the entangled state is a pure state $|\Phi\rangle = \gamma\,|HH\rangle + \sqrt{1-\gamma^2}e^{i\phi}\,|VV\rangle$ and ignore the contributions from the Raman-scattering and the detector's dark counts. With the idler polarization basis fixed at a diagonal state $|M_S\rangle = 1/\sqrt{2}\big(|H\rangle + |V\rangle\big)$ while rotating the signal basis $|M_I\rangle = \cos\theta\,|H\rangle + \sin\theta\,|V\rangle$, the coincidence counting rate can be expressed as

$$\begin{aligned} N_C &= N_\Phi \eta_S \eta_I |\,\langle M_S M_I|\,\Phi\rangle\,|^2 \\ &= \frac{N_\Phi \eta_S \eta_I}{2}\big(\gamma^2\cos^2\theta + (1-\gamma^2)\sin^2\theta + \gamma\sqrt{1-\gamma^2}\sin 2\theta\cos\phi\big). \end{aligned} \tag{2.13}$$

Here N_Φ denotes a photon pair production rate of the entangled state which equals the double of the pair production rate N_{Pair} of SFWM discussed in Section 2.2.4. Note that single counting rates for signal and idler are constant values $N_{S(I)} = \eta_{S(I)}N_\Phi/2$ over a full 2π-rotation of the signal polarization basis. The amplitude γ and phase ϕ can be replaced with their mean values and their fluctuation; $\gamma \to 1/\sqrt{2} + \delta\gamma$ and $\phi \to \delta\phi$. Then, the second-order Taylor expansion simplifies the above expression 2.13 as

$$N_C \approx N_\Phi \eta_S \eta_I \frac{1}{4}\big[1 + \sin(2\theta + \sin^{-1}\big(2\sqrt{2}\delta\gamma\big)\big)\cos\delta\phi\big]. \tag{2.14}$$

The amplitude $\delta\gamma$ and phase fluctuation $\delta\phi$ appear in the polarization-correlation measurement as a phase shift and visibility drop, respectively. Therefore, one can extract them by fitting the model to the measured coincidences with the fitting parameters of γ and ϕ. However, the coincidence counting rate N_C depends not only the systematic errors γ and ϕ of the entangled state caused by the instability of the interferometer, but it also reflects the instability of the other instrument such as the pump laser, i.e., the pair generation rate N_Φ. In fact, we observed considerable fluctuations in single counting rates, as shown in Figure 2.8(a). Since our interest is the phase stability of the designed interferometer, we take a symmetrized heralding efficiency $H_{\text{sym}} = N_C/\sqrt{N_S N_I}$ as a more appropriate parameter that is not affected by the fluctuating pair generation rate. Then, we fit the model to the heralding efficiency calculated from the raw single and coincidence rates for every full rotation of the signal polarizer, and obtain 143 values of the amplitude γ and phase ϕ of the entangled state, as shown in Figure 2.8(a).

In Figure 2.8(a), we observed that the standard deviation of the phase fluctuation is 3.17° under the temperature variation of 0.04°C, which is ten times larger than our

estimation in Section 2.2.2. Since the robustness of the BD-Sagnac-EPS to the temperature variation is inherently obtained from its geometric Sagnac configuration, we stress that this unexpected instability does not originate from the intrinsic property of the design as well as the components used. We believe that the instability may be attributed to a combination of multiple external factors, e.g., pump wavelength drift, a temperature-dependent phase-matching condition in PMF, and the fiber-coupling efficiency fluctuation. For example, Figure 2.8(a) shows that the visibility variation is correlated with the single counting rates. One possible explanation for this is that the spectral instability of our mode-locked pump laser causes a slight wavelength-shift which may impact the relative phase $\phi(\lambda, T)$ of the entangled state. In our setup, the quartz crystal compensates only for the signal's temporal walk-off. In this case, the pump wavelength-dependent phase shift is estimated to be 1.01 rad/nm [3], which corresponds to the 5.8° phase shift due to 0.1 nm pump wavelength-shift. The other reason may be the instability of the fiber coupling efficiencies in two polarization modes. In our demonstration, the 20 cm-long PMF located at the center of the Sagnac loop was kept straight in order to minimize the bending losses experience by the idler. The footprint of our experimental setup is about 70 cm×50 cm and the distance between the one end of the PMF to the tip of each single-mode fiber is approximately 80 cm. As each of the two orthogonally polarized photons is produced from one end of the PMF, any temperature variation and mechanical noise can cause the imbalanced fiber coupling efficiencies between the two polarization modes. These effects are not fully captured in our model 2.13 with the pure entangled state $|\Phi\rangle$. The origin of the instability will be further investigated in the future.

To quantify the long-term phase stability of the interferometer, we calculate the Allan deviation with the extracted phases ϕ [8]. The Allan deviation with respect to the integration time T is defined as

$$\sigma(T = N\tau) = \sqrt{\frac{1}{2}\left\langle(\Delta\phi)^2\right\rangle} = \sqrt{\frac{1}{2(N_{\text{tot}} - N)}\sum_{i=1}^{N_{\text{tot}}-N}(\phi_{i+N} - \phi_i)^2}. \tag{2.15}$$

The overall integration time, $T = N\tau$, is divided into N samples with the time interval $\tau =$ 10 minutes and the total number of samples $N_{\text{tot}} = 143$. We observed the Allan deviation of 8° over the integration time of 1 hour, as shown in Figure 2.8(c). Note that the optical path length from the first beam displacer to the second beam displacer in our setup is approximately 1.3 m. The 8° phase uncertainty corresponds to the relative length deviation of 2.1×10^{-8} per hour. This phase stability is comparable with the results obtained from a

[3] If the temporal walk-off is compensated for both signal and idler photons, the pump wavelength-dependent phase shift is estimated to be 0.48 rad/nm.

typical Sagnac interferometer with strong laser light [209]. Finally, it is worth noting that the Allan deviation allows us not only to quantify the phase stability but also to identify the source of noises by its scaling behavior [251]. In Figure 2.8(c), the measured Allan deviation follows the square-root scaling which indicates that the random-walk noise plays a major role in the long-term phase instability.

Our prototype demonstration can be further optimized in the future. In particular, the phase stability can improved by thermal insulation of the setup and the miniaturization of the interferometer. For example, the polarization-maintaining fiber used in our demonstration can be replaced with other fibers which exhibit the less bending loss over a wide wavelength range such as endlessly single-mode photonic crystal fibers, which simplifies the Sagnac loop with the fiber-optic coil. Also, as the two beam displacers and the spectral filter are relatively insensitive to the misalignment, they can be readily packaged into a small pigtailed fiber-bench or integrated on a piece of the pre-aligned plate. On the other hand, the entanglement quality can be substantially improved by reducing the Raman noise. This could be implemented by either using narrower spectral filters or cooling the fiber. Despite the remaining issues to be addressed in the future, we believe that this stable, practical, and versatile source is a useful scientific research tool and will be a promising candidate for industrial applications in quantum communication, sensing, and information processing.

2.3 Polarization-entangled photon source without optical interferometer

2.3.1 Motivation

In the previous section, we presented a practical and versatile interferometric scheme for PPSs. The interferometer superposed orthogonally polarized pump fields each of which drives photon-pair generation process in a certain propagation direction, e.g., clockwise or counterclockwise path. This is because the nonlinear medium satisfies the phase-matching condition in a specific polarization and propagation direction of the pump field. In this section, we consider removing the optical interferometric setup and single-pass of the pump field through an (nearly) isotropic $\chi^{(3)}$ nonlinear medium where the phase-matching condition is satisfied in both orthogonal pump polarizations.

The single-pass pump configuration has been studied and experimentally demonstrated in several different schemes. First, before interferometric setups were spotlighted, PPSs

in early stages were based on a birefringent medum, e.g., beta-barium borate, driven by a strong pump light at a specific polarization state. By carefully aligning the incident angle of the pump field, one can find and select two spatial modes producing polarization-entangled photons [164]. Secondly, two periodically poled nonlinear media were cross-oriented and placed in series. The timely distinguishable two pair-production processes were compensated by birefringent media before and/or after the generation process [233, 129, 273, 167]. Both methods, i.e., birefringent phase matching and walk-off compensation, require birefringent materials which must be carefully designed with a certain cut-axis and desired length, and these are usually custom-designed and hence costly. One other notable approach for the non-interferometric entangled photon source is to cross-splice two highly birefringent optical fibers [208, 234].

In this section, we present a PPS which does not require an interferometer and walk-off compensation. The setup becomes much simpler and naturally phase stable. All we need for the source is a single-mode optical fiber and two orthogonally polarized pump fields. The idea is to utilize a dual-pump four-wave mixing process in an isotropic optical nonlinear medium which conserves the total angular momentum where the polarization correlation between the generated photon pair arises. Since the pair generation processes are symmetric under the rotation of polarization states, the output state of the paired photon is polarization-entanged. This idea was first proposed by Lin *et al.* in 2007 [181]. However, all optical fibers are either weakly or highly birefringent in practice and the birefringence is wavelength dependent. Our solution is to utilize principal states of polarization [239] and the presented analysis is focused on the preservation of pump polarizations.

2.3.2 Vectorial quantum theory of spontaneous four-wave mixing

We present a vectorial quantum theory of photon-pair generations via SFWM. The theoretical framework for describing SFWM with scalar fields is provided in references [133, 77], and here we adopt the formalism for the case with vector fields. The system of interest is depicted in Figure 2.9. Two orthogonally polarized pump lights (ω_{P1} and ω_{P2}) are coupled into a single-mode fiber and polarization-entangled photon pairs named signal (ω_{S}) and idler (ω_{I}) are produced from the fiber. This parametric vacuum-amplification process is achieved by placing zero-dispersion wavelength (ω_{ZD}) near the center of the four wavelengths to satisfy the phase matching condition $\omega_{\mathrm{P1}}+\omega_{\mathrm{P2}} = \omega_{\mathrm{I}}+\omega_{\mathrm{S}}$ and $\beta_{\mathrm{P1}}+\beta_{\mathrm{P2}} = \beta_{\mathrm{I}}+\beta_{\mathrm{S}}$. Here, β and ω are the propagation constant and angular frequency of optical fields, respectively. For now, we assume the fiber is perfectly an isotropic medium and our goal is to derive the polarization states of the generated photons at the output of the fiber.

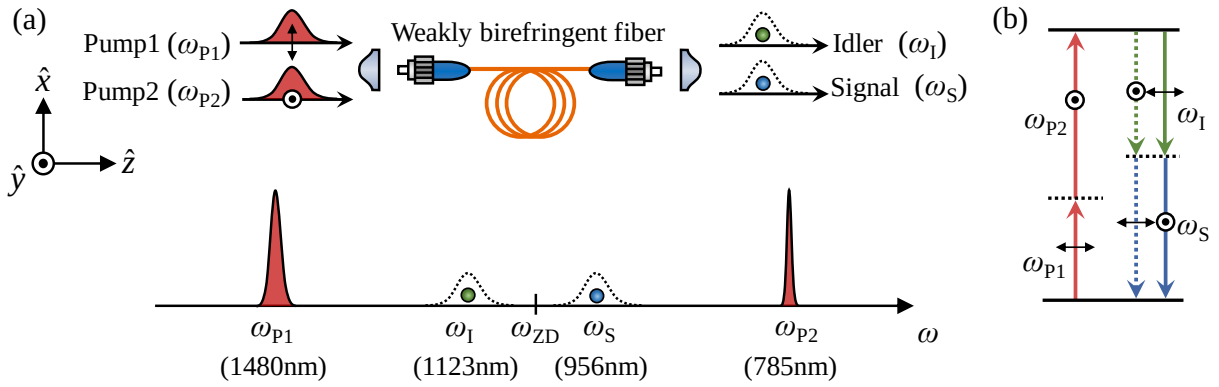

Figure 2.9: Direct generation of polarization-entangled photons from a single-mode fiber via dual-pump spontaneous four-wave mixing process. (a) Two orthogonally polarized pump fields (ω_{P1} and ω_{P2}) are coupled into a single-mode fiber and polarization-entangled photon pairs named signal (ω_S) and idler (ω_I) are produced from the fiber. This parametric vacuum amplification process is achieved by placing zero-dispersion wavelength (ω_{ZD}) near the center of the four wavelengths. (b) A schematic diagram of energy-level configurations of the four optical fields.

SFWM is microscopically photon-photon interactions mediated by an optical nonlinear dielectric medium. It is fundamentally dispersive light-matter interactions and the famous Kramers-Kronig relation, i.e., causality, ties it with the dissipation of light to environment, i.e., photon loss, which means the system Hamiltonian is not conserved during the time evolution. The self-consistent description for SFWM process requires the quantization of electromagnetic fields in the presence of dielectrics, which we discuss in Chapter 5. For now, we assume that the medium is lossless and it is simply characterized by the macroscopic quantities such as dielectric constant. Following the discussion in reference [133], we write electric field operators in guided modes as

$$\hat{\mathbf{E}}(\mathbf{r},t)=\sum_{j=x,y}\left(F(x,y)\sqrt{\frac{\hbar}{2\epsilon_0 c}}\frac{1}{\sqrt{2\pi}}\int \mathrm{d}\omega\sqrt{\frac{\omega}{n(\omega)}}\hat{a}_j(\omega,z)e^{-i\omega t}+\mathrm{H.c.}\right)\mathbf{e}_j, \tag{2.16}$$

where $F(x,y)$ and $n(\omega)$ are the transverse mode function of electric fields and the refractive index of the medium, respectively. The photonic annihilation operators satisfy the bosonic equal-space commutation relations $\left[\hat{a}_i(\omega),\hat{a}_j^\dagger(\omega')\right]=\delta(\omega-\omega')\delta_{ij}$ with Dirac delta function $\delta(\omega-\omega')$ and Kronecker delta function δ_{ij}. As for the guided mode in optical fibers, the transverse modal distribution $F(x,y)$ is independent from the propagation distance z, and therefore we integrate it over the transverse plane and normalize by the effective mode

area $A_{\text{eff}} = 1/\left[\iint |F(x,y)|^4 \mathrm{d}x\mathrm{d}y\right]$ to simplify the dynamical variable

$$\begin{aligned}\hat{\mathbf{E}}(z,t) &= \sum_{j=x,y}\left(\int \mathrm{d}\omega \sqrt{\frac{\hbar\omega}{4\pi\epsilon_0 c A_{\text{eff}} n_j(\omega)}}\hat{a}_j(\omega,z)e^{-i\omega t} + \text{H.c.}\right)\mathbf{e}_j \\ &\equiv \hat{\mathbf{E}}^{(+)}(z,t) + \hat{\mathbf{E}}^{(-)}(z,t).\end{aligned} \tag{2.17}$$

The evolution of the photons over the propagation distance z is governed by the Heisenberg equation

$$\frac{\partial \hat{a}_j(\omega,z)}{\partial z} = \frac{i}{\hbar}\left[\hat{a}_j(\omega,z), \hat{G}(z)\right], \tag{2.18}$$

where the momentum generator $\hat{G}(z)$ is given by the intergration of the momentum flow over the effective mode area A_{eff} during the quantization time T [133]:

$$\hat{G}(z) = \int_{A_{\text{eff}}} \mathrm{d}S \int_0^T \mathrm{d}t \hat{\mathbf{D}}^{(-)}(z,t)\cdot\hat{\mathbf{E}}^{(+)}(z,t) + \text{H.c.}. \tag{2.19}$$

The local density and speed of the momentum flow is governed by the dispacement field operator $\hat{\mathbf{D}}(z,t) = \epsilon_0\hat{\mathbf{E}}(z,t) + \hat{\mathbf{P}}(z,t)$. Here, the induced polarization $\hat{\mathbf{P}}(z,t)$ can be Taylor-expended as in classcial nonlinear optics. Since our fiber is assumed to be an isotropic medium where the second-order nonlinearity vanishes, we can rewrite the displacement field operator in terms of the electric field operators as

$$\hat{\mathbf{D}}(z,t) = \epsilon_0\hat{\mathbf{E}}(z,t) + \epsilon_0\overleftrightarrow{\chi}^{(1)}(\omega)\hat{\mathbf{E}}(z,t) + \epsilon_0\overleftrightarrow{\chi}^{(3)}\vdots\hat{\mathbf{E}}(z,t)\hat{\mathbf{E}}(z,t)\hat{\mathbf{E}}(z,t), \tag{2.20}$$

where $\overleftrightarrow{\chi}^{(n)}$ is the nth-order medium susceptibility tensors. For isotropic media $\overleftrightarrow{\chi}^{(1)}(\omega) = \chi^{(1)}(\omega) = n^2(\omega) - 1$, the third-order susceptibility tensor can be expressed in terms of three independent elements as $\chi^{(3)}_{ijkl} = \chi_{1111}\left(\delta_{ij}\delta_{kl} + \delta_{ik}\delta_{jl} + \delta_{il}\delta_{jk}\right)$ [6]. Then, each polarization component of the displacement field operator is expressed as

$$\begin{aligned}\hat{D}_i(z,t) &= \epsilon_0 n(\omega)^2\hat{E}_i(z,t) + \epsilon_0\chi_{1111}\sum_{jkl}\left[\left(\delta_{ij}\delta_{kl} + \delta_{ik}\delta_{jl} + \delta_{il}\delta_{jk}\right)\hat{E}_j(z,t)\hat{E}_k(z,t)\hat{E}_l(z,t)\right] \\ &\equiv \hat{D}_i^{(l)}(z,t) + \hat{D}_i^{(nl)}(z,t).\end{aligned} \tag{2.21}$$

Here, we split $\hat{D}_i(z,t)$ into the linear $\hat{D}_i^{(l)}(z,t)$ and the nonlinear $\hat{D}_i^{(nl)}(z,t)$ terms. First, we substitute the linear term $\hat{D}_i^{(l)}(z,t)$ to the Equation 2.19. After the rearrangement of

the coefficients and using the definition of the effective mode area, we find

$$\hat{G}_l(z) = \sum_j \int \mathrm{d}\omega \frac{\hbar\omega}{c} n(\omega)\hat{a}_j^\dagger(\omega, z)\hat{a}_j(\omega, z). \tag{2.22}$$

The solution of the Heisenberg equation $\hat{a}_j(\omega, z) = \hat{a}_j(\omega, z = 0)e^{-i\beta(\omega)z}$ with $\beta(\omega) = n(\omega)\omega/c$ simply describes the linear propagation of the electric field operator with the preservation of the polarization state.

Now we turn our attention to the nonlinear dynamics. For simplicity, we assume that the electric field operator consists of four distinct fields whose central frequencies are ω_{P1}, ω_{P2}, ω_{S}, and ω_{I}. Also, we assume two monochromatic pumps and take their bandwidth to be the frequency step $2\pi/T$. Since the self- and cross-phase modulation can be treated classically, we ignore the modulation terms for now and only keep the four-wave mixing term. Following the algebra similar to the reference [77], we find the nonlinear momentum generator

$$\begin{aligned}\hat{G}_{nl}(z) = \frac{2\pi}{T^2}\frac{\hbar^2\chi^{(3)}_{1111}}{\epsilon_0 c^2 A_{\mathrm{eff}}}\sum_{ijkl}(\delta_{ij}\delta_{kl} + \delta_{ik}\delta_{jl} + \delta_{il}\delta_{jk})\Bigg[\sqrt{\frac{\omega_{\mathrm{P1}}\omega_{\mathrm{P2}}}{n(\omega_{\mathrm{P1}})n(\omega_{\mathrm{P2}})}} \\ \int \mathrm{d}\omega\sqrt{\frac{\omega\left(\omega_{\mathrm{P1}} + \omega_{\mathrm{P2}} - \omega\right)}{n(\omega)n(\omega_{\mathrm{P1}} + \omega_{\mathrm{P2}} - \omega)}}\hat{a}_j(\omega_{\mathrm{P1}}, z)\hat{a}_k(\omega_{\mathrm{P2}}, z)\hat{a}_l^\dagger(\omega, z)\hat{a}_i^\dagger(\omega_{\mathrm{P1}} + \omega_{\mathrm{P2}} - \omega, z)\Bigg].\end{aligned} \tag{2.23}$$

We substitute the derived momentum generators into Equation 2.18. In the rotating frame by taking $\hat{a}_j = \hat{\tilde{a}}_j(\omega, z)e^{i\beta(\omega)z}$, we obtain the Heisenberg equation for the slowly varying field

$$\begin{aligned}\frac{\partial\hat{\tilde{a}}_j(\omega, z)}{\partial z} = i\frac{2\pi}{T^2}\frac{\hbar\chi^{(3)}_{1111}}{\epsilon_0 c^2 A_{\mathrm{eff}}}\sqrt{\frac{\omega_{\mathrm{P1}}\omega_{\mathrm{P2}}\omega(\omega_{\mathrm{P1}} + \omega_{\mathrm{P2}} - \omega)}{n(\omega_{\mathrm{P1}})n(\omega_{\mathrm{P2}})n(\omega)n(\omega_{\mathrm{P1}} + \omega_{\mathrm{P2}} - \omega)}}e^{i\Delta\beta(\omega)z} \\ \Bigg[\sum_{i=x,y} A_i(\omega_{\mathrm{P1}}, z)\hat{\tilde{a}}_i^\dagger(\omega_{\mathrm{P1}} + \omega_{\mathrm{P2}} - \omega, z)A_j(\omega_{\mathrm{P2}}, z) \\ + \sum_{i=x,y} A_i(\omega_{\mathrm{P2}}, z)\hat{\tilde{a}}_i^\dagger(\omega_{\mathrm{P1}} + \omega_{\mathrm{P2}} - \omega, z)A_j(\omega_{\mathrm{P1}}, z) \\ + \sum_{i=x,y} A_i(\omega_{\mathrm{P1}}, z)A_i(\omega_{\mathrm{P2}}, z)\hat{\tilde{a}}_j^\dagger(\omega_{\mathrm{P1}} + \omega_{\mathrm{P2}} - \omega, z)\Bigg],\end{aligned} \tag{2.24}$$

with the phase mismatching term $\Delta\beta = \beta_i(\omega_{\mathrm{P1}}) + \beta(\omega_{\mathrm{P2}}) - \beta(\omega) - \beta(\omega_{\mathrm{P1}} + \omega_{\mathrm{P2}} - \omega)$. The strong pump fields were taken to be classical $\hat{\tilde{a}}_j(\omega_{\mathrm{P1(P2)}}, z) = A_j(\omega_{\mathrm{P1(P2)}}, z)$ and undepleted

$|A_j((\omega_{\mathrm{P1(P2)}}, z)|^2 = |A_j((\omega_{\mathrm{P1(P2)}}, 0)|^2$. To further simplify the Equation 2.24, we define the nonlinear coefficient $\gamma(\omega)$ and the pump power P_j as

$$\begin{aligned}\gamma(\omega) &= \frac{3\chi^{(3)}_{1111}\sqrt{\omega(\omega_{\mathrm{P1}}+\omega_{\mathrm{P2}}-\omega)}}{2\epsilon_0 c^2 A_{\mathrm{eff}}\sqrt{n(\omega_{\mathrm{P1}})n(\omega_{\mathrm{P2}})n(\omega)n(\omega_{\mathrm{P1}}+\omega_{\mathrm{P2}}-\omega)}},\\ P_j(\omega, z) &= \frac{\hbar\omega \times N(z)}{T} = \frac{2\pi\hbar\omega}{T^2}|A_j(\omega, z)|^2.\end{aligned} \tag{2.25}$$

Then, we set two pumps to be orthogonally and linearly polarized ($A_y(\omega_{\mathrm{P1}}, z) = 0$ and $A_x(\omega_{\mathrm{P2}}, z) = 0$), and decompose the polarization state of the generated photons in terms of x- and y-polarization bases as $\hat{\tilde{a}}_j = \cos(\theta)\hat{\tilde{a}}_x + \sin(\theta)\hat{\tilde{a}}_y$. The evolution of the signal and idler photons via SFWM process is described by

$$\begin{aligned}\frac{\partial\hat{\tilde{a}}_j(\omega, z)}{\partial z} &= \frac{\partial}{\partial z}\big(\cos\theta\hat{\tilde{a}}_x(\omega, z) + \sin\theta\hat{\tilde{a}}_y(\omega, z)\big)\\ &= i\frac{2\sqrt{P_x(\omega_{\mathrm{P1}})P_y(\omega_{\mathrm{P2}})}}{3}\gamma(\omega)e^{i\Delta\beta(\omega)z}\\ &\times\big(\sin\theta\hat{\tilde{a}}^\dagger_x(\omega_{\mathrm{P1}}+\omega_{\mathrm{P2}}-\omega, z) + \cos\theta\hat{\tilde{a}}^\dagger_y(\omega_{\mathrm{P1}}+\omega_{\mathrm{P2}}-\omega, z)\big).\end{aligned} \tag{2.26}$$

As clearly seen in the above expression, the polarization state-independent correlation arises between the generated photon pairs. The underlying physics is the angular momentum conservation provided by the rotational symmetry of the isotropic medium which correlates the polarization states of the signal and idler fields. The initial angular momentum is set to null by two orthogonally polarized pumps, which opens all possibilities of the polarization states of photonic excitations, thereby producing polarization-entanglement of the paired photons.

We calculate the joint spectral function and the pair generation rate. By integrating over the propagation distance $z = L$ with $\theta = 0$, we obtain the output state

$$\hat{\tilde{a}}_x(\omega, L) = \hat{\tilde{a}}_x(\omega, 0) + i\frac{2\sqrt{P_x(\omega_{\mathrm{P1}})P_y(\omega_{\mathrm{P2}})}}{3}\gamma(\omega)L\mathrm{sinc}\left(\frac{\Delta\beta L}{2}\right)\hat{\tilde{a}}^\dagger_y(\omega_{\mathrm{P1}}+\omega_{\mathrm{P2}}-\omega, z). \tag{2.27}$$

The joint spectral density function can be calculated by the probability of detecting the paired photons at the orthogonal polarization basis $|\psi\rangle = |0\rangle_{S,x}|0\rangle_{I,y}$:

$$\begin{aligned}n_d(\omega, L) &= \langle\psi|\hat{\tilde{a}}^\dagger_x(\omega, L)\hat{\tilde{a}}_x(\omega, L)|\psi\rangle\\ &= \frac{4P_x(\omega_{\mathrm{P1}})P_y(\omega_{\mathrm{P2}})}{9}\gamma^2(\omega)L^2\mathrm{sinc}^2\left(\frac{\Delta\beta(\omega)L}{2}\right).\end{aligned} \tag{2.28}$$

The photon-pair generation rate can be calcuated by integrating the joint spectral density function over the entire frequency range.

$$N_{\text{pair/sec}} = \int \mathrm{d}\omega n_d(\omega, L) = \frac{4P_x(\omega_{\text{P1}})P_y(\omega_{\text{P2}})}{9} L^2 \int \mathrm{d}\omega \gamma^2(\omega) \mathrm{sinc}^2\left(\frac{\Delta\beta(\omega)L}{2}\right) \tag{2.29}$$

2.3.3 Low-birefringent fiber, principal states of polarization, nonlinear polarization rotations

We have studied that the polarization-entangled state are generated by injecting two orthogonally polarized pump lights into ideal optical fibers. However, in reality there is no such thing. The initial polarization states are always rotated or even depolarized over the propagation due to various reasons, e.g., non-uniform cylindrical structure of the fiber cross section, stress-induced birefringence, thermal gradient, etc. One might naively think that, even if the fiber's birefringence rotates incident polarization states of the four fields, the polarization correlation may still be maintained because the global rotation of the four polarizations would keep the "relative distance" between the states intact. However, it turns out that this would be true only if the birefringence is constant over the wavelength range. Since the birefringence is generally a function of wavelength, the polarization states of the four fields are rotated differently, and therefore the pump polarizations are not orthogonal to each other. Here, we investigate the conditions to maintain the orthogonality of pump polarizations in weakly birefringent fibers.

Principal states of polarization

Inspired by the observation of the perservation of two orthogonal polarizations over a 5 km–long single-mode fiber in 1981 [197], Poole *et al.* showed that for any linear optical transmission medium without polarization-dependent losses or gains there exist two mutually orthogonal polarizations for which the corresponding output states are independent of frequency to first order. The pair of polarization states are referred to as the principal states of polarization (PSP) [239]. To be specific, polarization rotations due to medium birefringence can be described by a complex transfer matrix $T(\omega)$. If we assume that there is no polarization-dependent loss, then $T(\omega)$ takes the form

$$T(\omega) = e^{-\alpha - i\beta(\omega)} U(\omega) \tag{2.30}$$

where $\beta(\omega)$ is the propagation constant and $U(\omega)$ is a unitary matrix

$$U(\omega) = \begin{bmatrix} u_1(\omega) & u_2(\omega) \\ -u_2^*(\omega) & u_1^*(\omega) \end{bmatrix} \tag{2.31}$$

with $|u_1(\omega)|^2 + |u_2(\omega)|^2 = 1$. Then, the PSP is obtained by the eigenvectors of the unitary matrix in Equation 2.31

$$\hat{\mathbf{e}}_\pm = \left[\left(\frac{\partial u_2(\omega)}{\partial \omega} - ik_\pm u_2(\omega)\right)/D_\pm, \left(\frac{\partial u_1(\omega)}{\partial \omega} - ik_\pm u_1(\omega)\right)/D_\pm\right]^{\mathrm{T}}, \tag{2.32}$$

where the $k_\pm$ and $D_\pm$ are expressed as

$$\begin{aligned} k_\pm &= \pm\sqrt{\left|\frac{\partial u_2(\omega)}{\partial \omega}\right|^2 + \left|\frac{\partial u_2(\omega)}{\partial \omega}\right|^2} \\ D_\pm &= \sqrt{2k_\pm\left(k_\pm - \mathrm{Im}\left[u_1^*(\omega)\frac{\partial u_1(\omega)}{\partial \omega} + u_2^*(\omega)\frac{\partial u_2(\omega)}{\partial \omega}\right]\right)}. \end{aligned} \tag{2.33}$$

PSP has been a useful tool to characterize the polarization-mode dispersion (PMD) of single-mode fibers [240] because the group delay between the two eigenstates is mainly caused by second- or higher-order dispersion. Also, the PSP plays an important role to define an axis in Stokes space where we describe the state evolution within a birefringent medium [276]. In this study, we hope to take advantage of using PSP to maintain the orthogonality of two pump polarizations over the length of a weakly birefringent fiber. Since the generation of signal and idler photons are equally probable over the whole polarization states, we expect that the polarization states of the paired photons are coherently superposed over the propagation. Then, the output state can be decomposed in terms of the PSP and the relative phase shift can be compensated by waveplates after the fiber.

Nonlinear polarization rotations

The polarization states of the pumps and photon pairs are rotated by the mere presence of two strong pump fields even in perfectly cylindrical fibers via self- and cross-phase modulations. This is purely due to the third-order nonlinear effect and is always present, and therefore must be characterized before conducting experiments. The four fields can be treated classically and expressed as complex vectors $|A\rangle_{i=\mathrm{P1,P2,S,I}} = [A_x^i, A_y^i]^{\mathrm{T}}$ normalized by the power $|A_x^i|^2 + |A_y^i|^2 = P_i$. Then, the nonlinear polarization rotation (NPR) of the four vector fields reads

$$\begin{aligned} \frac{d\vec{S}_{\mathrm{P1(2)}}}{dz} &= \frac{2\gamma}{3}\left[(\vec{S}_{\mathrm{P1(2)}} + 2\vec{S}_{\mathrm{P2(1)}})_2\hat{e}_2 - 2\vec{S}_{\mathrm{P2(1)}}\right] \times \vec{S}_{\mathrm{P1(2)}}, \\ \frac{d\vec{S}_{\mathrm{S(I)}}}{dz} &= \frac{4\gamma}{3}\left[(\vec{S}_{\mathrm{P1}} + \vec{S}_{\mathrm{P2}})_2\hat{e}_2 - (\vec{S}_{\mathrm{P1}} + \vec{S}_{\mathrm{P2}})\right] \times \vec{S}_{\mathrm{S(I)}}, \end{aligned} \tag{2.34}$$

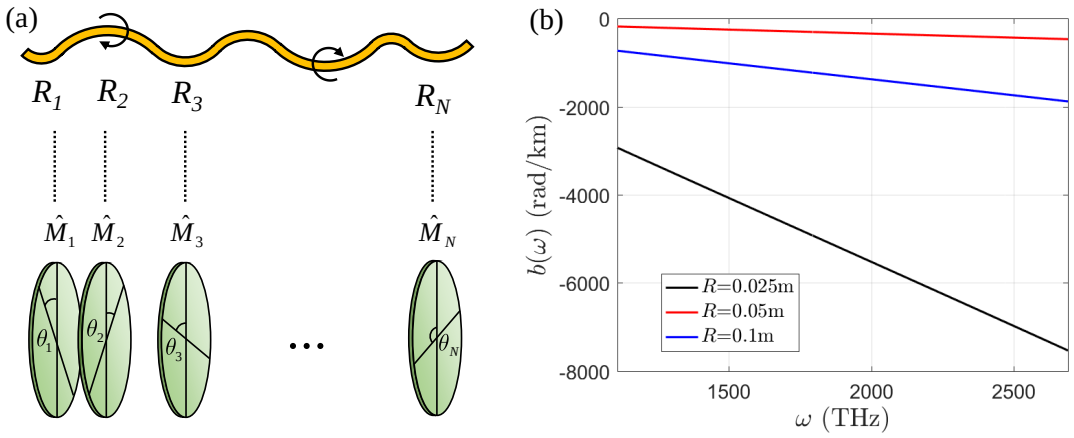

Figure 2.10: Theoretical modeling of a weakly birefringent fiber with a concatenation of phase retarders. (a) A weakly birefringent fiber is modeled as a concatenation of a short fibers with its bending radius R. Each short fiber is viewed as a waveplate. The birefringence is calculated by the analytic formula in Equation 2.36. (b) Typical bending-induced birefringence of an optical fiber (125 µm cladding diameter). The birefringence is wavelength-dependent and it is mostly linear with respect to the angular frequency.

where the Stokes vector $\vec{S} = \left[S_1, S_2, S_3\right] = \langle A|\vec{\sigma}|A\rangle$ represents the polarization states with the Pauli vector $\vec{\sigma} = \sigma_1\mathbf{e}_1 + \sigma_2\mathbf{e}_2 + \sigma_3\mathbf{e}_3$. Here, σ_j are the Pauli matrices

$$\sigma_1 = \begin{bmatrix} 0 & 1 \\ 1 & 0 \end{bmatrix}, \sigma_2 = \begin{bmatrix} 0 & -i \\ i & 0 \end{bmatrix}, \sigma_3 = \begin{bmatrix} 1 & 0 \\ 0 & -1 \end{bmatrix}. \tag{2.35}$$

The full derivation of the Equation 2.34 is provided in reference [182]. The first equation describes the variation of incident pump polarization states. It is obtained by the cross product with either the state itself, i.e., self-phase modulation, and/or the other pump polarization state, i.e., cross-phase modulation. Interestingly, the second equation shows that the signal and idler polarization states can be preserved when the two pump are orthogonal, i.e., $\vec{S}_{\mathrm{P1}} = -\vec{S}_{\mathrm{P2}}$. It is worth noting that our photon-pair generation process lies in the low-gain regime $\gamma PL \ll 1$ to reduce the multi-pair generations, which may also make the NPR negligible.

Coupled nonlinear Schrödinger equations and low-birefringent fiber model: a series of randomly varying phase retarders

Here, we present our numerical analysis with randomly varying birefringence of a fiber to investigate the feasibility of experimental demonstration. We model a low-birefringent fiber with the concatenation of birefringent plates $\hat{M}_i$, as depicted in Figure 2.10(a). Each plate represents a segmant of the fiber at a given orientation and bending radius. The bending-induced birefringence can be calculated by a simple formula according to the reference [286]:

$$b(\omega) = 0.25k(\omega)n_{\text{eff}}^3(\omega)(p_{11} - p_{12})(1+\nu)\frac{r^2}{R^2}, \tag{2.36}$$

where k is the wave vector, r is the fiber diameter, and R is the bending radius. For fused silica, $\nu = 0.17, (p_{11} - p_{12}) = -0.15$. The effective refractive index $n_{\text{eff}}(\omega)$ is calculated by solving the eigenvalue equation for transverse electric fields derived from the Maxwell's equation in a cylindrical coordinate system [6]. The Equation 2.36 shows that the birefringence is wavelength dependent and mostly linear with respect to the angular frequency ω. Examplary plots are shown in Figure 2.10(b).

We evaluate the polarization states of the output fields by solving coupled nonlinear Schrödinger equations (CNLSE) via Runge-Kutta fourth order interaction picture (RK4IP) method [317]. The CNLSE was originally derived by Curtis R. Menyuk in 1987 [206] and has been used for performance estimation for optical nonlinear processes such as supercontinuum generation [285]. We share our source code in Appendix B.

For the complex vector of slowly varying amplitudes $\mathbf{A} = [A_x(z,t), A_y(z,t)]^{\mathrm{T}}$, the linear and nonlineaer dynamics is described by the CNLSE

$$i\frac{\partial \mathbf{A}}{\partial z} + b\Sigma\mathbf{A} + ib'\Sigma\frac{\partial \mathbf{A}}{\partial t} - \frac{1}{2}\beta'\frac{\partial^2 \mathbf{A}}{\partial t^2} + \gamma\left[|\mathbf{A}|^2\mathbf{A} - \frac{1}{3}\big(\mathbf{A}^\dagger\sigma_2\mathbf{A}\big)\sigma_2\mathbf{A}\right] = 0. \tag{2.37}$$

In our model, the linear interaction between the two polarization components can be described by the birefringence of the modeled fiber

$$\Sigma = \hat{M}_N\hat{M}_{N-1}\cdots\hat{M}_3\hat{M}_2\hat{M}_1 \tag{2.38}$$

with each plate expressed by a Jones matrix

$$\hat{M}_i = \begin{bmatrix} e^{-ib_i(\omega)\delta z/2}\cos^2(\theta_i) + e^{ib_i(\omega)\delta z/2}\sin^2(\theta_i) & (e^{-ib_i(\omega)\delta z/2} - e^{ib_i(\omega)\delta z/2})\cos(\theta_i)\sin(\theta_i) \\ (e^{-ib_i(\omega)\delta z/2} - e^{ib_i(\omega)\delta z/2})\cos(\theta_i)\sin(\theta_i) & e^{-ib_i(\omega)\delta z/2}\sin^2(\theta_i) + e^{ib_i(\omega)\delta z/2}\cos^2(\theta_i) \end{bmatrix}. \tag{2.39}$$

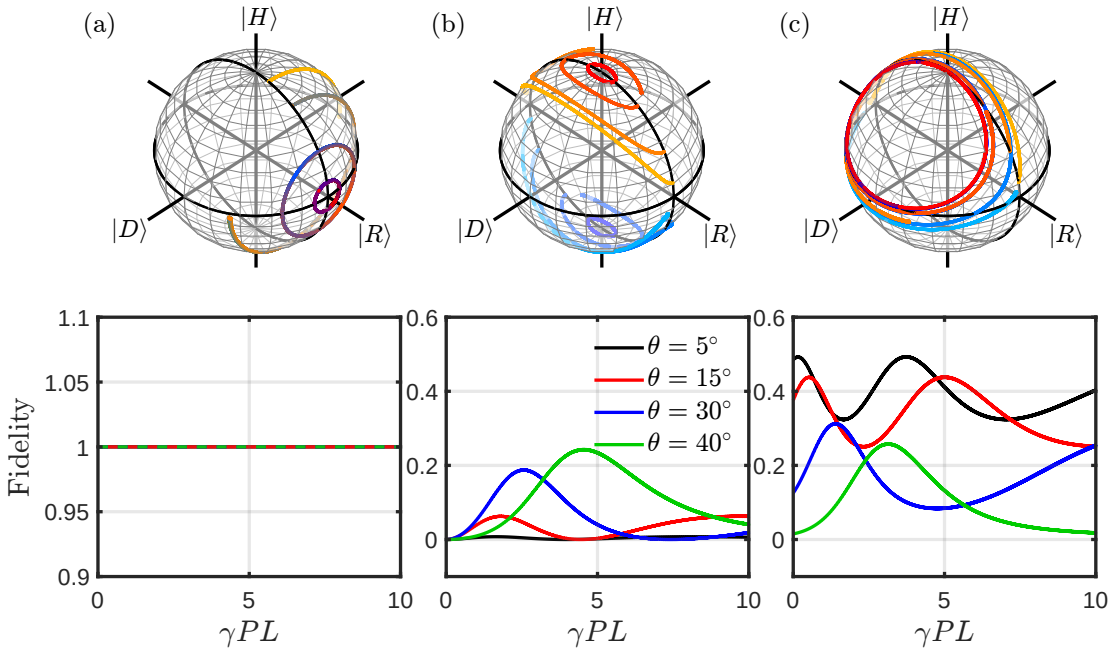

Figure 2.11: Nonlinear polarization rotations in the absence of externally induced birefringence. We solved the CNLSE for the incident pump polarization states of (a) $|A_{\mathrm{P1}}\rangle = |\alpha\rangle$ and $|A_{\mathrm{P2}}\rangle = |\alpha\rangle$, (b) $|A_{\mathrm{P1}}\rangle = |\alpha\rangle$ and $|A_{\mathrm{P2}}\rangle = |\beta\rangle$, and (c) $|A_{\mathrm{P1}}\rangle = |\alpha\rangle$ and $|A_{\mathrm{P2}}\rangle = 1/\sqrt{2}\,(|\alpha\rangle + |\beta\rangle)$ with $|\alpha\rangle = [\cos(\theta), i\sin(\theta)]^{\mathrm{T}}$ and $|\beta\rangle = [i\sin(\theta), i\cos(\theta)]^{\mathrm{T}}$. The quantum state fidelity $|\langle A_{\mathrm{P1}}|A_{\mathrm{P2}}\rangle|^2$ between two output pump polarization states are calculated as a function of the nonlinear interaction strength γPL.

Here, the birefringence $b_i(\omega)$ and the orientation of the plate θ_i are the random variables with the fixed plate thickness δz. The nonlinear interaction between the two polarization components is described by the last two terms. In this simulation, we assume that all the input fields are monochromatic such that the group delay between the two eigenpolarizations is ignored.

Numerical analysis

In our experiment, we use an endlessly single-mode photonic crystal fiber (ESPhCF) with the zero-dispersion wavelength λ_{ZDW} =1050 nm. The dispersion satisfies the phase-matching condition with the pumps at $\lambda_{\mathrm{P1}} = 780$nm and $\lambda_{\mathrm{P2}} = 1480$nm for the generated photon pairs at $\lambda_{\mathrm{S}} = 920$nm and $\lambda_{\mathrm{I}} = 1160$nm. The ESPhCF was modeled as a conven-

tional single-mode fiber with extraordinarily small cladding refractive index. This corresponds to the fact that the cladding is made of air-holes in ESPhCFs, which effectively reduce the cladding refractive index. The fiber is modeled with the 5.0 µm core diameter and the core–to–cladding index difference $\Delta n = 0.12$.

Figure 2.11 shows the evolution of pump polarizations via NPR in the absence of birefringence. We evaluated the quantum state fidelity between the output polarization states to estimate their relative distance at various input settings. Note that we set two pump powers to be equal. We found that the pump polarization states rotate together when the incident states were identically prepared. On the other hand, the orthogonally prepared states do not maintain their orthogonality, and the variation gets greater as the initial states differ from the horizontal and vertical states. We verified the orthogonally prepared state maintains the fidelity less than 1 % with $\gamma PL < 0.4$. For a 5 m–long ESPhCF with $\gamma \sim 10\mathrm{W}^{-1}\,\mathrm{km}^{-1}$, the $\gamma PL \sim 0.4$ corresponds to the incident single-pump power $P_{\mathrm{P1}} = P_{\mathrm{P1}} \sim 8\mathrm{W}$.

We now investigate the evolution of the PSP during the propagtion over the modeled birefringent fiber. We first verify the wavelength independency of the preservation of PSP by launching a coherent and broadband pulse light into the fiber and calculate the intensity spectra at the non-orthogonal basis, as shown in Figure 2.12(a). We model the 50 m–long fiber with eight thousands birefringent plates whose phase retardences are randomized with the bending radius R =30 cm. We first aligned the principal axes of the plates in order to keep the linear frequency dependency of the birefringence. As shown in Figure 2.12(b), the PSP is preserved over a wide range of wavelength. On the other hand, when the fiber is modeled with randomly oriented birefringent plates, as shown in Figure 2.12(c), the output polarization varies as a function of the incident wavelength. This is because the phase retardence is typically a sinusoidal function of the rotation angle and the oscillation period is a nearly linear function of the wavelength in our model. Thus, the randomly distributed rotation angle makes the fiber birefringence nonlinear to the frequency, and therefore the PSP is not preserved.

We evaluate the state fidelity between two pump polarizations for different fiber bending radii as a function of the propagation distance, as shown in Figure 2.12(d). It turns out that the orthogonality of the pumps at PSP is well maintained over the 5 m propagation with the fidelity less than 1 % when the bending radius is greater than 40 cm. With the same fiber model, we compared the result with non-PSPs, and verified the merit of preparing the pumps at PSPs.

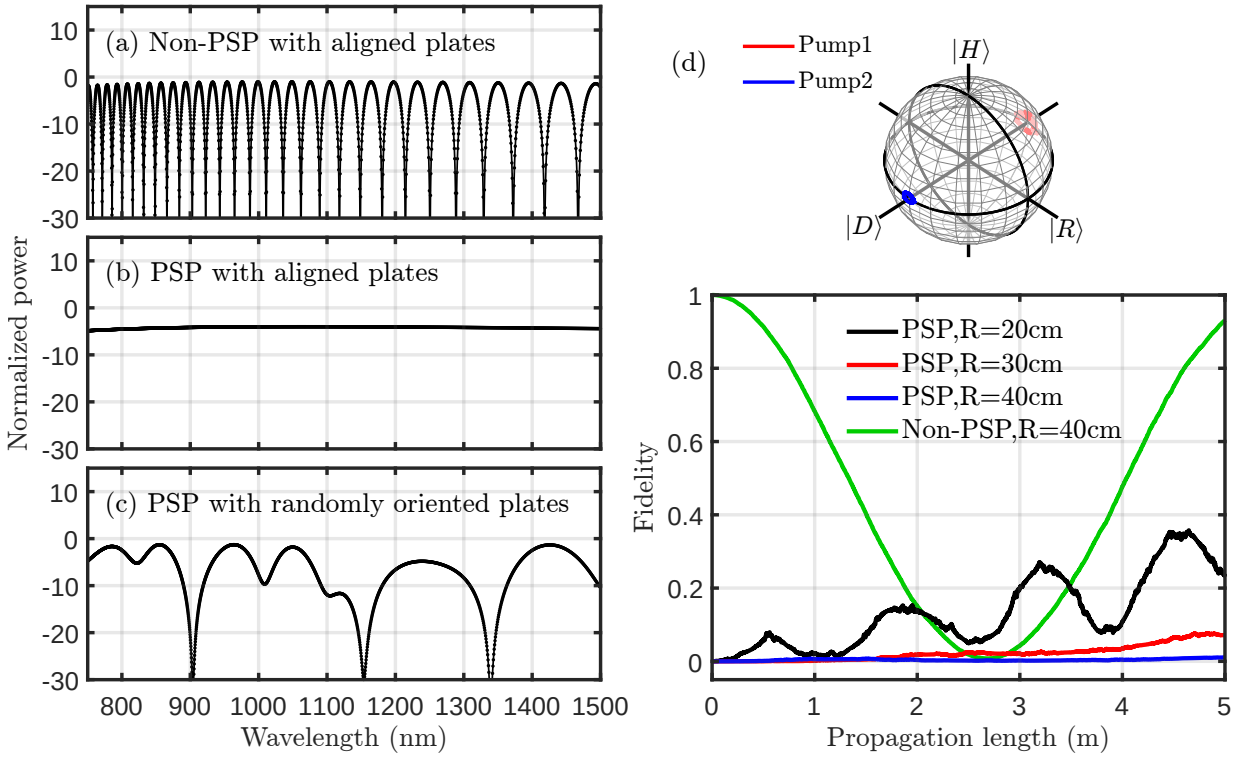

Figure 2.12: Principal states of polarization in the modeled weakly birefringent fiber. (a) Normalized intensity spectra of the coherent and broadband laser light after propagating through the modeled birefringent fiber and then a polarizer. The incident polarization states are not the PSPs and the fiber is modeled with a series of birefringent plates whose principal axes are aligned to each other. (b) The incident states are prepared in PSP. (c) The PSP state propagates through the fiber modeled with randomly oriented birefringent plates. (d) The state fidelity of the output polarization states as a function of the propagation distance. Inset. the evolution of the Stokes vectors of the PSP with the fiber bending radius R =40 cm.

2.3.4 Experimental setup

Figure 2.13 shows our experimental setup. Two pump fields at the wavelength of 785 nm and 1480 nm were generated from continuous wave lasers and coupled into a 5 m–long endlessly single-mode photonic crystal fiber (ESPhCF). We ensured that the fiber was not bent or twisted and lies in room-temperature without any active stabilitzation. The incident polarizations of the two fields were initially prepared at linear and orthogonal

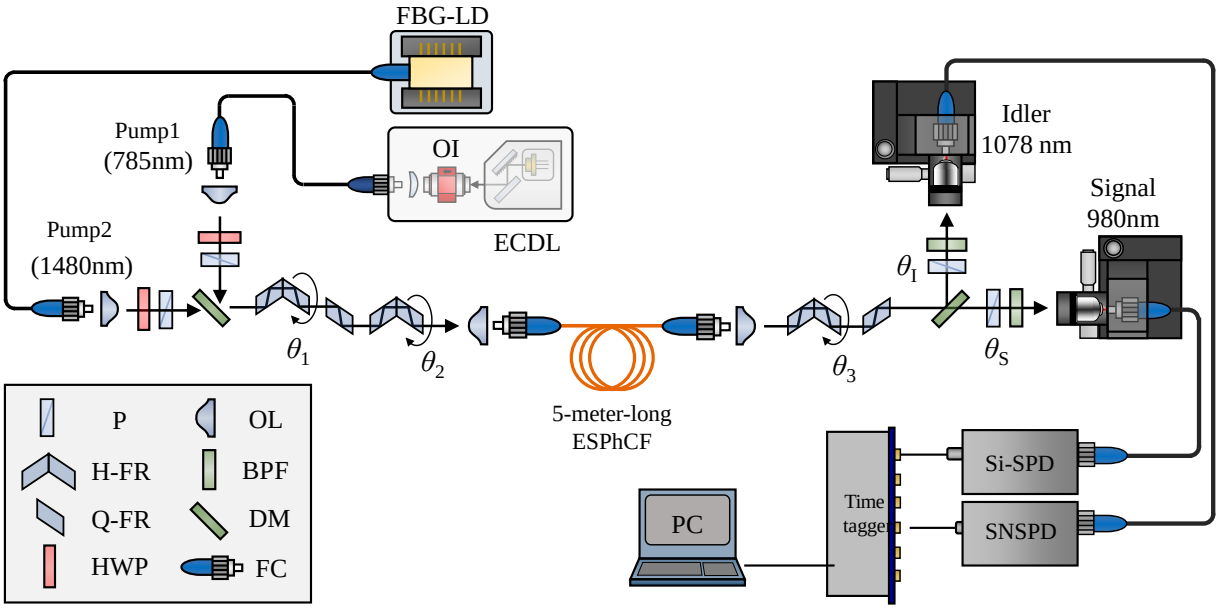

Figure 2.13: A schematic diagram of the experimental setup for direct generation of polarization-entangled photon pairs using an endlessly single-mode photonic crystal fiber; ECDL, external cavity diode laser; DBG-LD, fiber-bragg grating wavelength-stabilized laser diode; OI, optical isolator; Si-APD, silicon-avalanche photodiode; P, polarizer; OL, objective lens; H(Q)-FR, half-(Quarter-)wave fresnel rhomb; DM, dichroic mirror; BPF, bandpass filter; HWP, half-waveplate; FC, fiber connector; ESPhCF, endlessly single-mode photonic crystal fiber.

states, i.e., s- and p-polarizations of the dichroic mirror. They propagated through two half-wave and one quarter-wave Fresnel rhomb retarders (H-FR and Q-FB) altogther. By rotating the two H-FRs (θ_1 and θ_2), we can prepare the arbitrary polarization states while keeping their orthogonality. The generated photon pairs and the two pump fields passed through a H-FR and a Q-FB after exiting the fiber, and the pump polarization states were returned to the linear s- and p-polarization states of the second dichroic mirror. The signal and idler photons are separated and then coupled into single-mode fibers. The pump fields and other stray lights were filtered out by bandpass filters placed at each arm. The signal photons at 980 nm and idler photons at 1078 nm were detected by a Silicon-based single-photon detector (Excelitas, SPCM-AQ4H, Detection Efficiency $\approx 55\,\%$) and superconducting nanowire single-photon detector (Quantum Opus, Opus One, Detection Efficiency $\approx 80\,\%$), respectively.

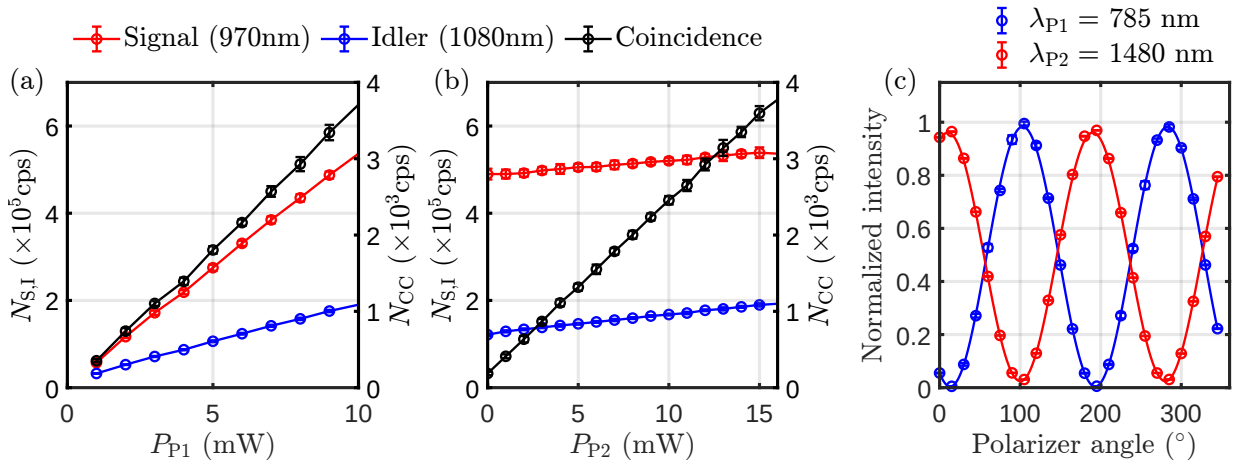

Figure 2.14: Photon-pair generation via dual-pump spontaneous four-wave mixing process. (a) The measured single and coincident counting rate as a function of the pump powers at the wavelength of λ_{P1}=785 nm and (b) λ_{P2}=1480 nm. (c) The variation of the measured optical power of the pump fields as a function of a polarizer's rotation angle. The polarizer was placed before the dichroic mirror and after the two Fresnel's rhombs at the output of the fiber.

2.3.5 Results

Figure 2.14 shows the single and coincident counting rates of the generated photon pairs from the 5 m–long ESPhCF via dual-pump spontanoues four-wave mixing process. We subtracted the dark counting rate of the detectors from the measured single counting rate. We varied one of the two pump powers P_{P1} (λ_{P1}=785 nm) and P_{P2} (λ_{P2}=1480 nm) while the other is fixed to investigate the background noise contributed from each different pump fields. As shown in Figure 2.14(a) and (b), we observed that the pump field at λ_{P1}=785 nm produces a strong background noise which is mainly expected to be the spontanoues Raman-scattered photons.

The output polarization states of the two pump fields were analyzed by the intensity variations of each field as a function of the rotation angle of a single polarizer placed before the dichroic mirror at the output of the fiber (this polarizer is not shown in Figure 2.13). The extinction ratio of the polarizer is greater than one thousand at the both wavelengths of 785 nm and 1480 nm. We adjusted the rotation angles of the three Fresnel's rhombs $\theta_{1,2,3}$ to find a good preservation of the orthogonality of the pump polarizations. The visibilities of the output polarization states at the wavelengths of 785 nm and 1480 nm were measured to be 99.1 % and 95.0 %, respectively.

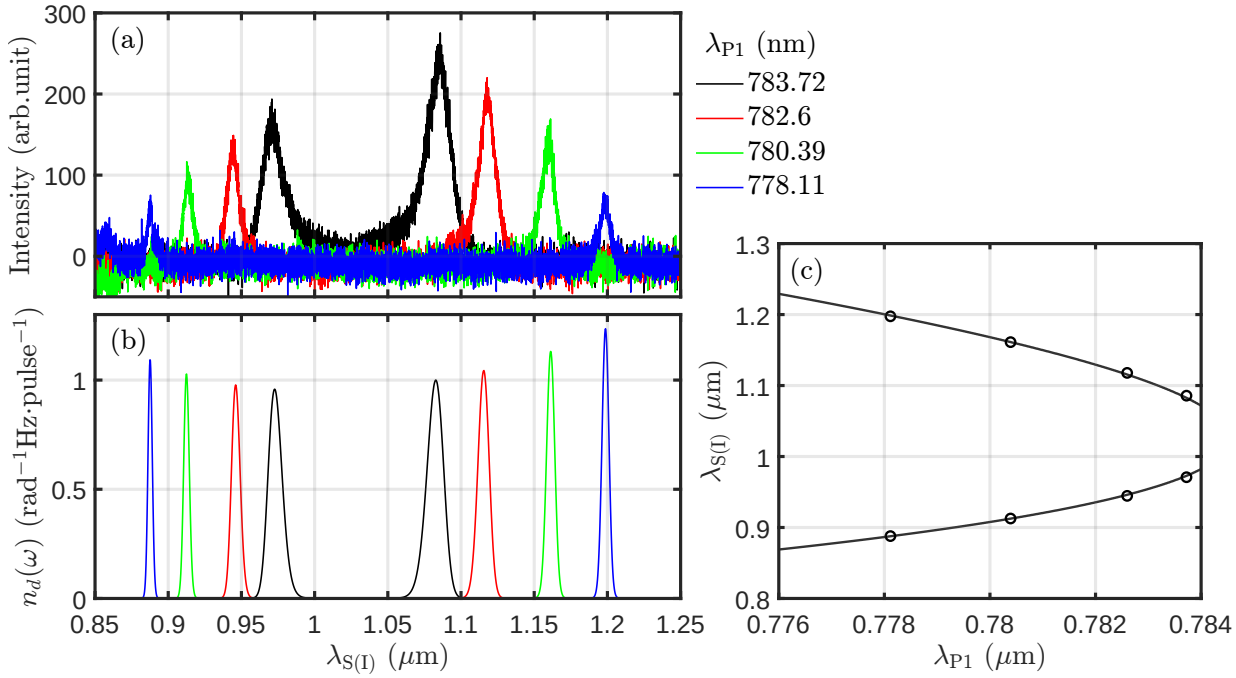

Figure 2.15: Spectra of the generated photon pairs at different pump wavelengths. (a) The measured spectra of the generated photon pairs from a 5 m–long endlessly single-mode photonic crystal fiber. (c) The calculated spectra of the generated photon pairs including the broad linewidths of the pump lasers. (c) The measured (circles) and calculated (black solid lines) central wavelengths of the photon pairs.

Figure 2.15(a) shows the measured spectra of the generated photon pairs at different pump wavelengths after the subtraction of the background. The background spectrum was measured by blocking the pump field at 1480 nm while injecting the pump at 785 nm. We observed that the central wavelengths of the photon pairs varied according to the phase-matching condition. The spectral bandwidth of the generated photons is reduced due to the higher-order dispersions as the central wavelengths are shifted further from the zero dispersion wavelength of 1026 nm. The variation of the peak intensity of each spectrum is mainly attributed to different fiber-coupling efficiencies at the wavelengths of the generated photons. We calculated spectra of the generated fields with the modeled fiber, as discussed in Section 2.3.3. The linewidths of the two pump lasers were included in the calculation based on the measured values with a high-precision optical spectrum analyzer (see Section 4.6.3). As shown in Figure 2.15(b) and (c), the close agreement between the theory and experiment shows the validity of our modeled fiber.

The polarization states of the generated photon pairs will be investigated in the future. We plan to study the polarization correlation in two different polarization states of the pump fields. First, we will measure the photons polarization when both pumps are prepared in the same state of the PSP. We expect to observe that the polarization state of each of the photon pair is identical to the PSP due to the angular momentum conservation. In contrast, when the two pumps are prepared at the two orthogonal PSPs, the polarization state of each photon may appear to be an unpolarized (or mixed) state as generally expected in the entangled state. The polarization correlations will reveal the output polarization state of the paired photons.

2.4 Toward ground-space entanglement distribution

In this section, we provide a conceptual design for a PPS for the QEYSSat mission and the detailed analysis on the attainable pair-generation rate as well as heralding efficiency.

2.4.1 Requirements for entanglement-based QKD in the QEYSSat mission

The PPS must satisfy certain requirements to be operationally useful in the QEYSSat mission. Based on the analysis in the reference [38], we summarize the requirements in the following.

- **Wavelength**
  One of the emitted pair must be in a wavelength range of 780 nm to 795 nm with nominal baseline of 785 nm.
- **Spectral bandwidth**
  Spectral bandwidth of the photons propagating through the ground-to-space link must be less than 1 nm. The photon receiver at the spacecraft contains narrow spectral bandpass filters to block stray light.
- **Pair-emission rate**
  The pair-emission rate must be greater than 100 MHz. Generally, a satellite launched in a higher orbit or close to the horizon requires the PPS to be operated at greater pair-production rate with lower intinsic QBER.

- **Heralding efficiency**
  The probability of heralding the presence of photons arriving at the satellite receiver must be greater than 50 %. The heralding efficiency is defined as the ratio of coincident counting rate between the photon pair (one at the satellite and the other at the ground station) to single counting rate measured at the ground. It includes the detector's efficiency and transmittance of optical components in the ground.

- **Quantum Bit Error Rate (QBER)**
  The quality of the polarization correlation between the emitted photon pair is defined as visibility $V = \left(N_{CC}^{E} - N_{CC}^{U}\right) / \left(N_{CC}^{E} + N_{CC}^{U}\right)$, where N_{CC}^{E} and N_{CC}^{U} are the coincident counting rate measured at expected and unexpected polarization states, respectively. The entangled state must perform the visibility greater than 98 %, which corresponds to the QBER=$(1 - V)/2$ less than 1 %. This includes dark counts and other background noises of the photon detectors.

2.4.2 Design considerations

We have studied two schemes for practical implementations of PPSs. In both demonstrations, we used optical fiber-based nonlinear media to generate photons at well-defined spatial modes without temperature stabilization. However, we noticed that the pair-generation rate of the fiber-based PPSs is too low to be deployed for the QEYSSat mission. Also, spontaneous Raman-scattering process inevitably adds unwanted noise photons which are ultimately translated to the increment of intrinsic QBER. In our demonstration of the BD-Sagnac-EPS in Section 2.2.4, the entanglement visibility was measured to be around 95 %, while the required visibility is above 98 %. Therefore, we decided to utilize periodically poled bulk nonlinear crystals as they have been widely investigated for high-rate photon-pair sources with great signal-to-noise ratio via spontaneous parametric down-conversion (SPDC).

The designed optical configuration for the PPS is depicted in Figure 2.16. We adopt the BD-Sagnac-EPS scheme with further optimizations and the design is conceptually similar to the demonstration in reference [274]. Two identical nonlinear crystals are placed in series with one of them rotated by 90° with respect to the other, producing orthogonally polarized photon pairs that are superposed in the Sagnac loop. One of the key elements in the PPS is an optical nonlinear medium which must be carefully designed in order to generate the photon pairs at the required wavelengths. The designed parameters and experimentally measured values for the nonlinear crystal are summarized in Table 2.2. As a baseline, we choose a bulk periodically poled MgO-doped lithium niobate (PPLN) with

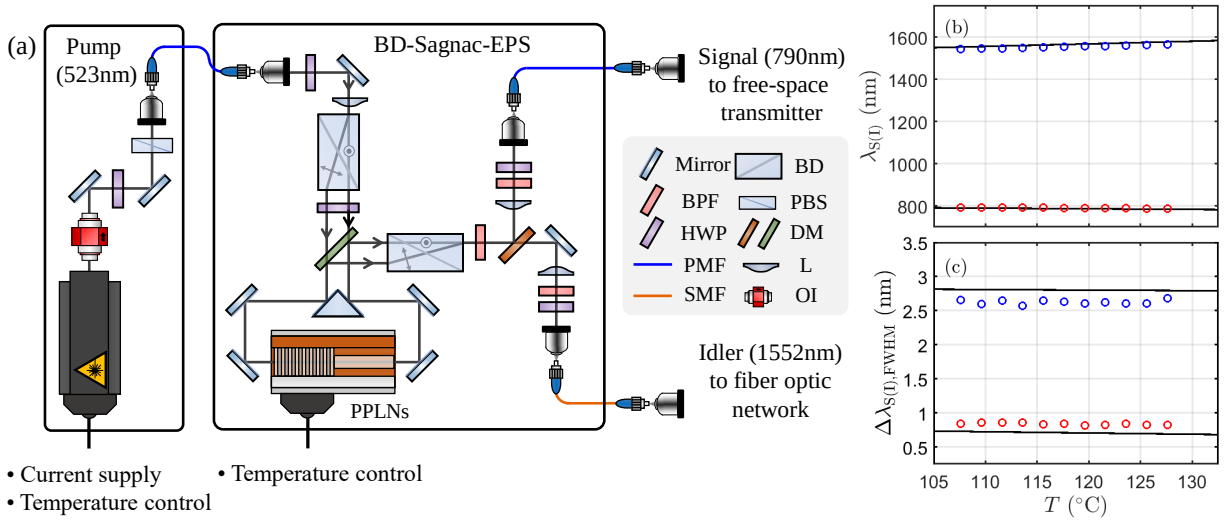

Figure 2.16: Conceptual design of polarization-entangled photon-pair source for the QEYSSat mission. (a) The proposed optical setup for polarization-entangled photon-pair source; BD, beam displacer; BPF, bandpass filter; PBS, polarization beam splitter; HWP, half-wave plate; DM, dicrhoic mirror; L, lens; PMF, polarization-maintaining fiber; SMF, single-mode fiber; OI, optical isolator. (b) Experimental verification of the type-0 quasi-phase matching condition in 10 mm–long PPLN ($\Lambda = 7.10\mu$m). The measured the central wavelengths and (c) spectral bandwidths (FWHM) of the generated photon pairs. The theoretical curves (solid black lines) were obtained from the Sellmeier equation for the material refractive index provided in Appendix A.

the type-0 quasi phase-matching (QPM) condition which exhibits high effective nonlinear coefficient (15.9 pm/V). We engineered the poling period ($\Lambda = 7.10\,\mu$m) of the PPLN crystal such that type-0 QPM (eee) is satisfied to generate the correlated photon pairs at the wavelengths of 790 nm (signal) and 1552 nm (idler) under the continuous-wave pump at 523.6 nm at the temperature of 107 °C. Here, the type-0 QPM (eee) means that the polarizations of three lights (pump, signal, and idler) are aligned to extraordinary axis of the PPLN crystal. The spectral bandwidth of signal and idler photons are 0.73 nm and 2.81 nm, respectively.

The requirement of 50 % (80 % as a goal) heralding efficiency η_{total} includes the transmission of all optical elements η_{optics}, fiber coupling efficiency η_{fc}, and idler detection efficiency η_{det} [38]. With the conservative assumption of the absolute detection efficiency η_{det} =80 % of superconducting nanowire single-photon detectors and the transmission of all optical elements η_d =80 % including filters and polarization-analysis optics, we must achieve the

Table 2.2: Design parameters and measured values for the nonlinear crystal. We mark NA for parameters that are not directly measured in our experiment.

Parameters	Design	Measurement
Material	5 % MgO-doped PPLN	NA
Λ (µm)	7.10	NA
T (°C)	107	107.6
λ_{P} (nm)	523.6	523.64
λ_{S} (nm)	790.8	792.8
λ_{I} (nm)	1552	1542.9
$\Delta\lambda_{\mathrm{S,FWHM}}$ (nm)	0.73	0.84
$\Delta\lambda_{\mathrm{I,FWHM}}$ (nm)	2.81	2.66
L (mm)	10	NA
W_P (µm)	120	118
$W_{S,(I)}$ (µm)	62.5	62 (67)
R_T (Mcps/mW)	2.37	1.80

single-mode fiber coupling efficiency greater than 80 %. This condition is highly dependent on the spatial modes of the photon pairs and pump fields, as well as the optical arrangement.

2.4.3 Theory of collinear spontaneous parametric down-conversion (SPDC)

We provide a brief review on the theoretical formalism of SPDC process [183, 31]. We calculate absolute emission rate of photon pairs based on the Fermi's golden rule for transition probability from vacuum state to single pair-excited state. The transverse modes of the generated photons are decomposed in terms of Laguerre-Gaussian modes, and the single-mode fiber coupling efficiency is determined by the ratio of the lowest mode, i.e., TEM00 Gaussian mode, to the summation over all other higher modes. Here, the coincidence and single rates are calculated without so-called thin-crystal assumption, wherein the beam waists of all fields are constant across the crystal length.

Figure 2.17 depicts SPDC process where a periodically poled nonlinear crystal with the poling period Λ and the length L is driven by a pump field ω_P with a paraxial Gaussian mode and produces photon pairs, i.e., signal ω_S and idler ω_I, via collinear type-0 SPDC process. The central wavelengths $\lambda_{S(I)}$, spectral bandwidths $\Delta\lambda_{S(I)}$, and spatial modes of

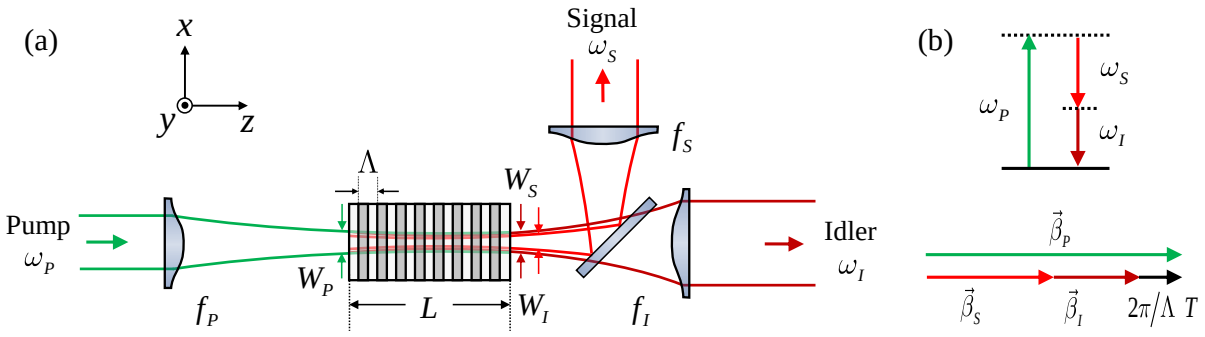

Figure 2.17: A schematic drawing of spontanoues parametric down-conversion process in a periodically poled nonlinear crystal. A pump field at 523.6 nm propagates through a 10 mm-long PPLN crystal (poling period $\Lambda = 7.10\,\mu$m), and generates correlated photon pairs at the wavelengths of 790 nm (signal) and 1552 nm (idler) via type-0 (eee) spontaneous parametric down-conversion (SPDC) process. The generated photon pairs are collected into optical single-mode fibers. The beam waist of the pump, signal, and idler fields at the center of the crystal is denoted as W_P, W_S, and W_I, respectively.

the generated photon pairs are determined by QPM condition. The beam waists of single-mode fiber-collection modes for the pump, signal, and idler fields are denoted as W_P, W_S, and W_I, respectively. As discussed in the previous section, we assume that the medium is lossless and follow the phenomenological approach to describe photon-photon interactions of SPDC process.

We start with writing the quantized electric field operators for signal and idlers

$$\begin{aligned}\hat{\mathbf{E}}_{S(I)} &= \frac{i}{2}\sum_{k_{S(I)}}\sqrt{\frac{2\hbar\omega_{S(I)}}{n_{S(I)}^2\epsilon_0 L}}\mathbf{e}_{S(I)}g_{S(I)}(\mathbf{r})e^{-i\omega_{S(I)}t}\hat{a}_{k_{S(I)}} + \text{h.c.} \\ &\equiv \frac{1}{2}\left[\hat{\mathbf{E}}_{S(I)}^{(+)} + \hat{\mathbf{E}}_{S(I)}^{(-)}\right],\end{aligned} \tag{2.40}$$

where we include the refractive index n to capture the modified field density inside the nonlinear crystal. We treat the pump field classically $\mathbf{E}_P(\mathbf{r},t) = \left[E_P^0\mathbf{e}_P g(\mathbf{r})e^{-i\omega_P t} + c.c.\right]/2$ with the electric field amplitude $E_P^0 = \sqrt{2P/\left(\epsilon_0 n_P c\right)}$ for the input optical power P. Then, the interaction Hamiltonian for SPDC process reads [183]

$$\hat{H}_I = -\frac{2\epsilon_0}{8}\int_{-\infty}^{\infty}\mathrm{d}x\mathrm{d}y\int_{-L/2}^{L/2}\mathrm{d}z\chi^{(2)}(z)\mathbf{E}_P^{(+)}\hat{\mathbf{E}}_S^{(-)}\hat{\mathbf{E}}_I^{(-)} + \text{h.c.}, \tag{2.41}$$

where ϵ_0 and $\chi^{(2)}(z)$ are the vacuum permittivity and the second-order nonlinear susceptibility of the nonlinear crystal, respectively. Here, the factor 2 at numerator originates from the intrinsic permutation symmetry of the second-order nonlinear susceptibility [41]. The periodically poled nonlinear susceptibility function $\chi^{(2)}(z)$ can be expressed by Fourier series

$$\chi^{(2)}(z) = \chi_2 f(z) = \frac{4\chi_2}{\pi} \sum_{m=0}^{M} \frac{(-1)^m}{2m+1} e^{-i(2m+1)Kz}, \tag{2.42}$$

where $K = 2\pi/\Lambda\,(T)$ is the poling spatial frequency. Then, we rewrite the interaction Hamiltonian

$$\hat{H}_I = \frac{d_{\text{eff}} E_P^0 \hbar \sqrt{\omega_S \omega_I}}{n_S n_I L} \sum_{k_S, k_I} \Phi(\Delta k) e^{-i\Delta\omega t} \hat{a}_{k_S}^\dagger \hat{a}_{k_I}^\dagger + h.c. \tag{2.43}$$

with the phase mismatching terms $\Delta\omega = \omega_P - \omega_S - \omega_I$ and $\Delta\beta = \beta_P - \beta_S - \beta_I$, Here, the effective nonlinearity d_{eff} captures the contraction of the nonlinear susceptibility tensor with corresponding polarization vectors ($2d_{\text{eff}} = \mathbf{e}_P \chi^{(2)} : \mathbf{e}_S \mathbf{e}_I$) [41]. The $\Phi(\Delta\beta)$ is the overlap integral of the three transverse mode functions in the crystal

$$\Phi(\Delta k) = \frac{4}{\pi} \sum_{m=0}^{M} \frac{(-1)^m}{2m+1} \int_{-\infty}^{\infty} \mathrm{d}x\mathrm{d}y \int_{-L/2}^{L/2} \mathrm{d}z e^{-i(2m+1)Kz} g_P(\mathbf{r}) g_S^*(\mathbf{r}) g_I^*(\mathbf{r}), \tag{2.44}$$

As is well established, each mode function can be decomposed in terms of Laguerre-Gaussian (LG) modes [2]

$$g_\alpha^{(n,l)}(\mathbf{r};\omega) = \sqrt{\frac{2}{\pi}} \left(\frac{W_\alpha}{q_\alpha}\right)^{l+1} \left(\frac{q_\alpha^*}{q_i}\right)^n L_n^l \left(\frac{2w_\alpha^2 \rho^2}{|q_\alpha|^2}\right) \exp\left(-\frac{\rho^2}{q_\alpha} + ik_\alpha z + il\phi\right), \tag{2.45}$$

with $\rho = \sqrt{x^2+y^2}$, $\phi = \tan^{-1}(x/y)$, and $q_\alpha = w_\alpha^2 + 2iz/\beta_\alpha$.

The pump field is launched from a single-mode fiber and set to be Gaussian mode $g_{\text{P}}^{(0,0)}(\mathbf{r};\omega)$ for the rest of the analysis. For coincident counts, we consider that each of the paired photons is coupled into a single mode fiber which supports the Gaussian mode. Therefore, the pair excitation probability is obtained by evaluating the overlap integral of the three Gaussian transverse modes with $n = l = 0$ for pump, signal, and idler fields.

The single detection probability for signal photons, as an example, is evaluated by the probability of detecting signal photons coupled into a single-mode fiber for all possible modes of the paired idler photons. This is obtained by setting $n = l = 0$ only for the signal mode $g_{\text{S}}^{(0,0)}(\mathbf{r};\omega)$, and summing over the overlap integral with all possible idler modes $g_{\text{I}}^{(n,l)}(\mathbf{r};\omega)$. Since the pump and signal modes are azimuthally symmetric, i.e., Gaussian

mode, the spatial ovelap vanishes unless the idler mode is also azimuthally symmetric ($l = 0$). The spatial mode overlap between the pump $g_{\mathrm{P}}^{(0,0)}$, signal $g_{\mathrm{S}}^{(0,0)}$, and the idler in the nth LG mode $g_{\mathrm{I}}^{(n,0)}$ is expressed as

$$\begin{aligned}\Phi_n(\Delta k) =& \frac{4}{\pi}\frac{1}{(\pi/2)^{3/2}}\sum_{m=0}^{M}\frac{(-1)^m}{2m+1}\int_{-\infty}^{\infty}2\pi\rho d\rho\int_{-L/2}^{L/2}dz\frac{w_P w_S w_I}{q_P q_S^* q_I^*} \\ &\times\left(\frac{q_I}{q_I^*}\right)^n L_n\left(\frac{2w_i^2\rho^2}{|q_i|^2}\right)\exp\left[-\rho^2\left(\frac{1}{q_P}+\frac{1}{q_S^*}+\frac{1}{q_I^*}\right)+i(\Delta k - i(2m+1)K)z\right].\end{aligned} \tag{2.46}$$

The absolute pair-emission rate $N_n^S = \int \mathrm{d}\omega_S R_n(k_S)$ for signal photons at the TEM00 with the paired idler photons at the nth LG mode is evaluated by the integration of transition probability per unit time $R_n(k_S)$ from the initial vacuum state $|i\rangle = |0_{k_S}, 0_{k_I}\rangle$ to the final photon pair state $|f\rangle = \hat{a}_{k_S}^\dagger \hat{a}_{k_I}^\dagger |0_{k_S}, 0_{k_I}\rangle$ over all possible k_S. The transition rate in the modes k_S and k_I is calculated by Fermi's Golden rule in the time-dependent perturbation theory as

$$R_n(k_S) \approx \frac{2\pi}{\hbar}|\langle f|\hat{H}_I|i\rangle|^2\mathcal{D}(\Delta E), \tag{2.47}$$

where the transition probability amplitude $\langle f|\hat{H}_I|i\rangle$ (in the unit of energy) are given as

$$\langle f|\hat{H}_I|i\rangle = \frac{d_{\mathrm{eff}}E_P^0\hbar\sqrt{\omega_S\omega_I}}{n_S n_I L}\Phi_n(\Delta k). \tag{2.48}$$

The density of states $\mathcal{D}(\Delta E)$ per unit energy $\Delta E = \hbar\Delta\omega$ for the idler photons can be calculated as

$$\mathcal{D}(\Delta E) = \frac{\Delta m}{\Delta k_I}\frac{\partial k_I}{\partial(\hbar\Delta\omega)} \approx \frac{L}{2\pi}\frac{n_I}{\hbar c}. \tag{2.49}$$

Here, the $\Delta m/\Delta k_I \approx L/2\pi$ denotes the number of modes per unit of wave vector component k_I in the quasi-continuum approximation for large L. By integrating the transition rate $R_n(k_S)$ over the emission bandwidth, we obtain the emission rate of the signal at the TEM00 and idler at the nth LG mode with the TEM00 pump as

$$N_n^S = \left[\frac{d_{\mathrm{eff}}E_P}{c}\right]^2\frac{\omega_S\omega_I}{2\pi n_S n_I}\int \mathrm{d}\omega_S|\Phi_n(\Delta\vec{k})|^2. \tag{2.50}$$

For a given nonlinear crystal and focal parameters, the coincidence rate $N_{CC} = N_{n=0}^S = N_{n=0}^I$ and single rate $N_{S(I)} = \sum_{n=0}^{\infty} N_n^{S(I)}$ can be calculated to obtain the symmetrized fiber-coupling efficiency $\eta_{\mathrm{fc}} = N_{CC}/\sqrt{N_S N_I}$ and the total pair-generation rate $N_{\mathrm{Pair}} = N_S N_I/N_{CC}$.

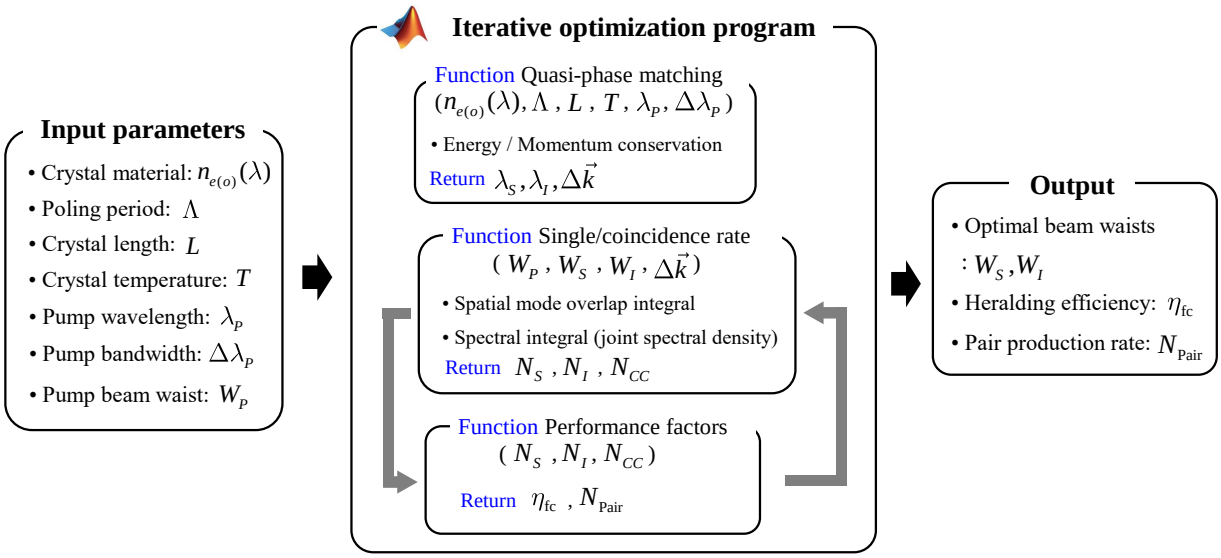

Figure 2.18: Functional block diagram of Matlab program. A user inputs experimental parameters such as the crystal material, poling period, and the crystal length. The Matlab program utilizes a built-in numerical iterative optimization algorithm to search the beam waists of signal and idler photons that maximize the single-mode fiber-coupling efficiency $\eta_{\text{fc}} = N_{CC}/\sqrt{N_S N_I}$ for a given pump beam waist. In the optimization program, single $N_{S,I}$ and coincidence N_{CC} counting rate are calculated. The code for evaluating the counting rates is provided in Appendix C

2.4.4 Numerical optimization for efficiently fiber-coupled photon pairs from SPDC

Based on the forementioned theoretical framework, we numerically search focal conditions for signal and idler photons that maximize the fiber-coupling efficiency η_{fc}, as shown in Figure 2.18. We first calculated the wavelengths of signal and idler photons satisfying the QPM condition, and then all the geometric factors were taken into account for the calculation of the counting rates. Then, we utilized the Matlab built-in iterative optimization algorithm to obtain optimal beam waists of signal and idler photons for the fiber-coupling efficiency for a given pump beam waist.

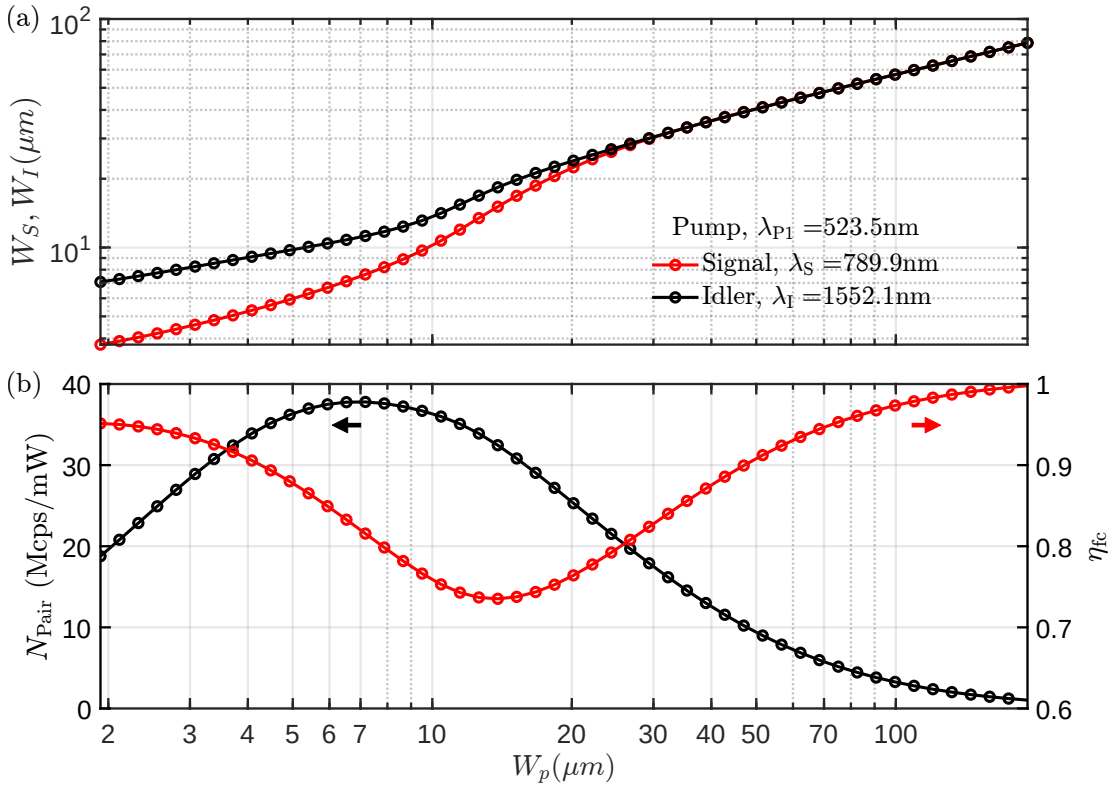

Figure 2.19: Optimal focal parameters for fiber-coupling efficiency of correlated photon pairs generated from SPDC process. (a) Optimal beam waists of signal and idler fields as a function of beam waist of pump light. (b) Photon-pair generation rate (left, black-coloured) and fiber-coupling efficiency (right, red-coloured) at the optimal beam waists.

2.4.5 Results and conclusion

The preliminary simulation results of optimal beam waists of signal and idler photons as a function of input pump beam waist is plotted in Figure 2.19(a). The corresponding fiber-coupling efficiency as well as pair-production rate is shown in Figure 2.19(b). We found that the beam waists of signal and idler fields are almost two times smaller than the incident pump beam waist. The optimal beam waists of photon pairs converge to the same value as the pump waist increases, and they start splitting into different values at the pump waist smaller than 20 µm.

Our simulation shows that the maximum pair-production rate N_{Pair} greater than 30 Mcps/mW can be achieved at tight focal conditions $W_P \approx 7$ µm. More importantly, there exists a

trade-off between the pair-production rate and the fiber-coupling efficiency. The focal condition which yields the coupling efficiency of 95 % or better reduces the pair emission rate to 10 % or less of its maximum value. The 100 Mcps of pair-production rate is achievable with a long pump focal condition. The pump beam waist W_P around 110 µm which yields the fiber-coupling efficiency of 0.96 and the pair production rate of 2.37 Mcps/mW.

In our experimental test, we chose the beam waists of 118 µm, 62 µm, and 67 µm for pump, signal, and idler beams, respectively, according to our simulation result. The pair-production rate was measured to be 1.8 Mcps/mW which agrees well with our simulation result. The small discrepancy may be attributed to manufacturing imperfection of the PPLN crystal; e.g., irregularity of the periodic poling structure and aberrations of pump, idler and signal beams.

2.5 Chapter summary

We discussed two polarization-entangled photon sources for ground-to-satellite free-space quantum channels. First, we designed and analyzed a novel interferometric configuration. By taking advantage of the intrinsic phase stability and the utility in traditional Sagnac-type and Mach-Zehnder-type sources, our beam displacement Sagnac interferometer is a practical and versatile source of entangled photons that can be implemented at various platforms without the requirement of customizing multi-wavelength polarization optics. We presented the detailed analysis for the spatiotemporal walk-off and the temperature-dependent phase shift with commercially available beam displacers. The analysis showed that the designed interferometer is suitable for highly non-degenerate wavelengths and thermally stable. Furthermore, the alignment procedure for our scheme is more straightforward than traditional Sagnac-type sources.

We experimentally tested the functionality of the designed configuration with the pulsed generation of polarization-entangled photon pairs at the wavelengths of 764 nm and 1221 nm from a polarization-maintaining fiber via spontaneous four-wave mixing process. The setup consisted of only commercial off-the-shelf optical items. The strong violation of CHSH-inequality with parameter $S = 2.70 \pm 0.04$ verified the polarization entanglement of the generated photon pairs. The long-term phase stability of the designed interferometer was characterized by performing the polarization correlation measurement over 24 hours, and during that time the visibility remains within a range of 83.9 % to 93.9 % without active phase stabilization. We attribute the observed instability mainly to the external instrumental imperfections, not to the intrinsic property of the designed interferometer or the used components, and this will be further investigated in the future. Nonetheless, the

Allan deviation of less than 8° over the integration time of 1 hour quantitatively showed a good long-term phase stability of the interferometer.

Secondly, we studied a practical scheme of directly producing polarization-entangled photon pairs from a conventional optical fiber via dual-pump spontaneous four-wave mixing. We formulated a vector theory of correlated photon-pair generations and showed that maximally entangled state can be produced from an isotropic optical fiber. Then, we modeled a realistic fiber including weak birefringence by a concatenation of randomly varying and oriented birefringent plates. We investigated the preservation of the orthogonality of two pump polarizations by numerically solving coupled nonlinear Schrödinger equations. It turns out that the principal states of polarizations are preserved for short and weakly birefringent fibers. We also proposed an experimental setup for demonstrations using Fresnel's Rhombs and showed the preservation of pump polarizations. We also presented our preliminary results of photon-pair generation which showed that spontaneous Raman-scattering process is the main source of noise photons.

Finally, we provided a conceptual design of the polarization-entangled photon source for the QEYSSat mission. With the amibition of distributing entangled photons simultanously over fiber-optic networks and ground-to-satellite links, the designed source is capable of producing photon pairs with the spectral linewidths of 0.73 nm and 2.81 nm at the central wavelengths of 790.8 nm and 1552 nm, respectively. Our numerical analysis showed that single-mode fiber-coupling efficiencies of generated photon pairs can be greater than 95 % while the pair-generation rate is estimated to be $N_{\mathrm{Pair}} \sim$2.37 Mcps/mW.

Chapter 3

Characterization infrastructure for optical components in quantum communications with satellites

The content of this chapter is based on the manuscripts that are either preprinted in arXiv or in preparation. Also, some of the experimental results were published in a conference proceeding paper.

1. Youn Seok Lee, Kimia Mohammadi, and Thomas Jennewein. Practical wavefront measurement with scanning pentaprism for optical terminals in free-space quantum communication. *In preparation*

2. Youn Seok Lee, Kimia Mohammadi, Lindsay Babcock, Brendon Higgins, Hugh Podmore, and Thomas Jennewein. Robotized polarization characterization platform for free-space quantum communications. arXiv:2109.01984 (2021) [170]

3. Hugh Podmore, Ian D'Souza, Jeffrey Cain, Thomas Jennewein, Brendon Higgins, Youn Seok Lee, Alex Koujelev, Danya Hudson, Ashley McColgan. QKD Terminal for Canada's Quantum Encryption and Science Satellite (QEYSSat). Proc. SPIE 11851, International Conference on Space Optics — ICSO 2020, 118520H (2021) [237]

Statement of contributions

- **Optical aberration characterization system**
  Prof. Thomas Jennewein and I conceived the idea. I designed, analyzed performance,

and procured components. Kimia Mohammadi and I implemented the experimental apparatus, developed control software, and performed experiments. I analyzed the data and drew conclusions under the supervision of Prof. Thomas Jennewein.

- **Robotized polarization characterization system**
  Prof. Thomas Jennewein and I conceived the idea. I designed, analyzed performance, procured components, and implemented the measurement apparatus and control program. Kimia Mohammadi, Lindsay Babcock, and I implemented the experimental setup for various test optics and performed the measurement. I analyzed the data. Prof. Thomas Jennewein provided a polarization-raytracing code. Dr. Hugh Podmore provided a test optic developed for quantum payload in the QEYSSat mission. Prof. Thomas Jennewein and Dr. Brendon Higgins supervised the project.

3.1 Introduction: optical terminals for the QEYSSat mission

3.1.1 Background

With the recent successful China's Quantum Experiments at Space Scale mission and Micius satellite [310, 249, 311, 312], quantum communications with satellites opened a new platform for long-distance secure key exchange, as well as for fundamental quantum experiments in a relativistic length scale. Several countries around the world are pursuing the quantum links between ground and space in various scenarios [263]. In Canada, the Quantum Encryption and Science Satellite (QEYSSat) mission has been developing a satellite payload and ground stations with the mission objectives of long-distance quantum key distributions (QKD), and of long-distance quantum entanglement tests via the exchange of polarized photons in an uplink configuration [141, 238, 237].

Encoding quantum information in optical polarization is a straightforward and robust approach to free-space quantum communications, but depends critically on preservation of high-purity polarized states of light throughout the optical chain. Degradation of polarization quality necessarily impacts the performance and any protocol, such as QKD, being attempted. In particular, free-space communications with moving platforms such as satellites require specialized photon transceivers to create efficient quantum channels. The transceivers typically consist of a large "front-end" telescope (pointed at the other telescope) supported by small "back-end" optics for multiplexing of quantum light with a strong beacon, fine-pointing actuation, etc. [300, 243, 238, 237]. The preservation of

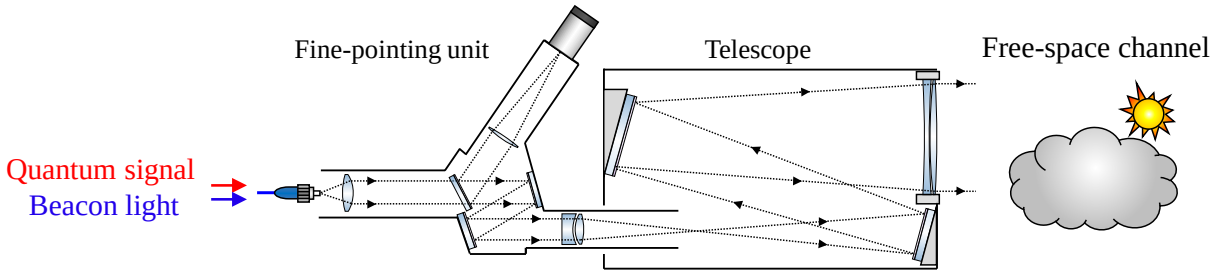

Figure 3.1: A schematic diagram of a examplary free-space optical transmitter.

polarization states throughout such complex optical terminals is challenging because some polarization rotations or depolarizations are fundamentally inevitable and are easily caused by myriad reasons, e.g., stress-induced birefringence, or thermal expansion of birefringent material. Also, optical coatings usually cause phase shifts of polarizations, which could lead depolarizations when the phase shifts are not uniformly applied across the spatial profile of the incident beam. Moreover, the polarization effect depends on the geometry of the optical terminal; mere reflection/refraction changes the polarization state depending on the incident angle. In the QEYSSat mission, the QBER less than 0.5 % must be attained by the entire optical terminal [38], and therefore great care must be taken to design optical terminals to preserve the polarization state and it is essential to ensure polarization is preserved at the major interfaces, and the effect of any individual component on polarization is both well understood and verified.

Optical aberrations of transmitted light also impacts the quality of ground-to-satellite links, and it is challenging to preserve high quality of the transmitted wavefront throughout complex optical terminals. Also, quantum light and beacon laser field are often delivered through a single-mode fiber which must be precisely positioned at the "back-end" of the optical terminal to ensure the collimation of the launched fields. Therefore, characterizing optical aberrations including beam divergence or convergence is also essential during the hardware development for the QEYSSat mission.

In this chapter, we present the development of characterization platforms for both wavefront errors and polarization preservation of the transmitted light for optical elements developed for the QEYSSat mission. We mainly focus on the measurement apparatus and discuss detailed analysis of the system, as well as the validation of methodology.

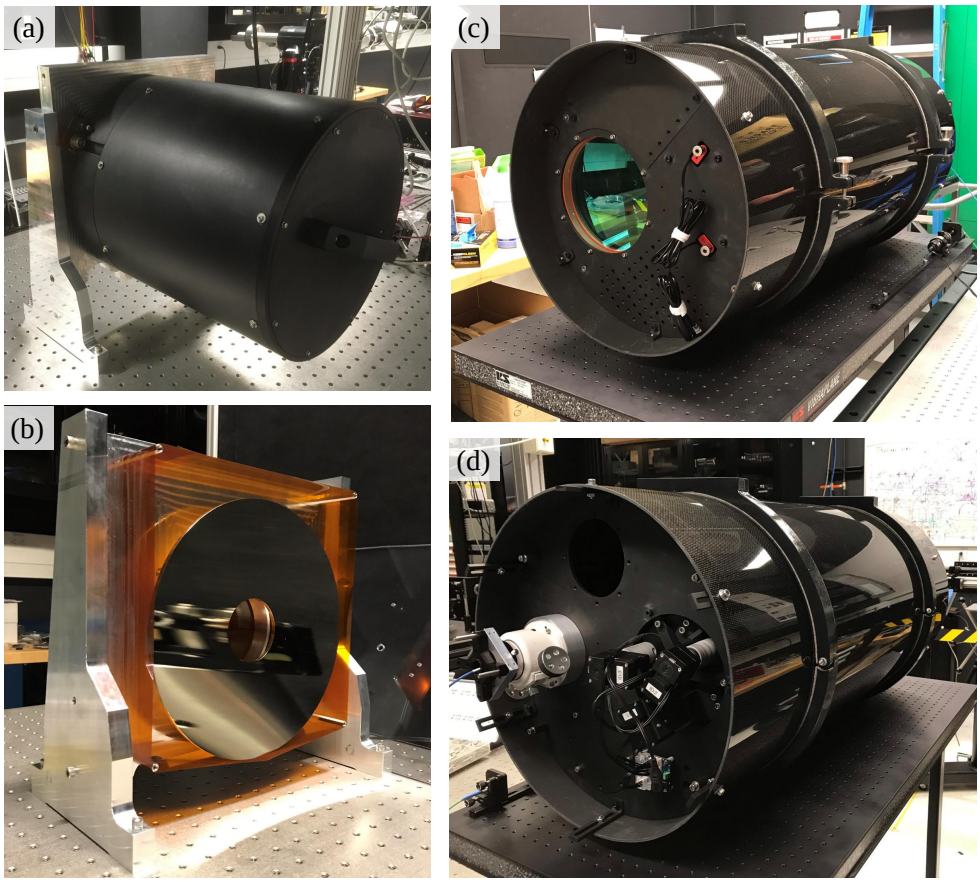

Figure 3.2: Photographs of optical components developed for the QEYSSat mission. (a) A prototype of quantum optical payload telescope and (b) its primary mirror developed by Honeywell Canada Aerospace. (c) The front side and (d) rear side of a quantum optical transmitter telescope developed by the QPL.

3.1.2 Development of free-space optical transceivers

Over the past few years, several optical devices have been designed and implemented for the successful accomplishment of the QEYSSat mission. Table 3.1 lists the selected optical components that are examined in this chapter.

Among various devices, large optical systems, e.g., greater than 10 cm diameter, are required to be designed and tested in the development phase and are critical for successful link. In the QPL, we developed a telescope (IQC-T) as quantum optical transmitter,

Table 3.1: List of devices under test.

Device	Description	Test method	Date
HON-T	Satellite payload prototype telescope [238]	Polarization	February 2020
HON-M	Satellite payload prototype primary mirror [238]	Polarization	March 2020
IQC-L	Custom-designed achromatic doublet	Polarization and wavefront	March 2021
COTS-M	Commercial-off-the-shelf silver-coated mirror (48-118-577, Edmund Optics)	Polarization	March 2021
IQC-T	Quantum transmitter telescope	Polarization and wavefront	March 2021

led by Kimia Mohammadi [212]. With 243.8 cm effective focal length (f/12) and $\pm 0.1^\circ$ field of view (FoV), the IQC-T is optimized at 780 nm, 980 nm, and 1550 nm for transmission throughput greater than 95 % and wavefront error less than 0.25λ Peak-to-Valley (PV) value. It consists of two protected silver-coated mirrors (COTS-M), and a 20.3 cm–diameter achromatic doublet (IQC-L) that are precisely aligned in a pre-defined location by the optomechanical mounts. The size of the achromatic doublet lens and the design specifications were determined by quantum link-budget analysis [212], including the impact of optical aberrations under atmospheric turbulence. The kinematic mirror mounts are all motorized by electromechanical actuators for the precise alignment with consistent repeatibility.

On the receiver side, a 26 cm catadioptric telescope (HON-T) was developed by Honeywell Canada Aerospace under contract to the Canadian Space Agency [238]. The telescope is a classic on-axis Cassegrain design consisting of a spherical primary mirror (HON-M), hyperbolic secondary mirror supported by a three-legged spider, and a field-widening aspheric singlet lens to extend the telescope FoV up to $\pm 0.3^\circ$. The optical surfaces of the primary and secondary were fabricated in aluminum by single-point diamond turning, and the mirror reflectivity was enhanced via protected silver coating. Direct assembly of the telescope was achieved through precision machining of the telescope spider and field lens mount, which provided controlled air-gaps and correct tip/tilt between the primary and secondary mirrors.

3.2 Characterization of optical aberrations with scanning pentaprism

3.2.1 Motivation

One of the most popular devices to measure wavefronts is the Shack-Hartmann sensor (SHS) [236]. It pixelizes the transverse profile of incident light and measures wavefront slopes of individual sections with an array of lenses. One major drawback of existing devices is their limited entrance pupil size which is typically 1 cm^2, making it difficult to be directly used for large optics such as telescopes. There have been different approaches to characterize aberrations of individual optical components. For example, the thickness variation of transmissive optics was tested using calibrated lenses and curved mirrors to effectively reduce the pupil size of the test optic [220, 92]. Also, the aberration characterizations of telescopes have been performed where the SHS is attached to the eyepiece of the telescope and star light is used as a point source [241, 79]. The surface roughness of reflective optics or wafers has been measured by laterally scanning a SHS across the test optic and stitching the measured wavefronts [247, 154]. The forementioned methods require an additional calibration of the measurement apparatus and/or post-processing of the measured data. Also, the required optics are often customized and thus expensive. Furthermore, the dynamic range of wavefront measurements is limited by the sensor area $\sim$1 cm^2. More importantly, all the schemes require special customization for testing a single optical element at a time—characterizing aberrations throughout a complete optical assembly would be much preferable in free-space optical communications.

We developed a practical and mobile wavefront measurement platform for large optics of up to 30 cm diameter, as well as optical terminals developed for quantum communications with satellites. We used a pentaprism which scans across the aperture of a test optic to sample the transmitted light for the measurement of local wavefront slopes. The pentaprism is the only moving part during the measurement and the 90° deflection angle is insensitive to the rotation of the pentaprism to first order, thereby providing a precise way of characterizing optical aberrations of the transmitted light. This technique has been used for the collimation test of telescopes [305] and the precise topographic measurement for both curved [275, 10] and flat large mirrors [309, 245], as well as wafers [96]. We conduct a proof-of-principle experiment for a transverse linear measurement of the transmitted wavefront for our 20.3 cm achromatic doublet developed for a quantum optical transmitter in the QEYSSat mission (IQC-L).

3.2.2 History of the system development

The initial idea of using a pentaprism for collimation tests was provided by our industry collaborator INO before I joined the QPL group in May 2018, and Prof. Thomas Jennewein conceived the first test configuration. A preliminary test was carried out under the supervision of Dr. Jean-Philippe Bourgoin in June 2018. Lindsey Babcock and I developed the first automated version of the measurement system in May 2019, which was used as a subsystem of a polarization characterization platform to verify the beam collimation. In April 2020, I conceived the idea of using a corner cube to shorten the length of the test setup, allowing for the whole scanning system to be safely rotated by a motorized rotational stage for scanning in different directions. I carried out the design analysis and implemented a subpixel centroid algorithm. In March 2021, after procuring all necessary components, Kimia Mohammadi and I built the final version of the measurement apparatus and performed aberration characterizations on IQC-L and IQC-T. The test was completed in April 2021.

3.2.3 System design and methodology

Conceptual design and experimental setup

Figure 3.3(a) shows our experimental setup for measuring the transmitted wavefront on a device under test (DUT) of the IQC-L. A continuous-wave laser operating at the wavelength of λ=785 nm is coupled to a single-mode fiber which is mounted on a motorized translation stage. The DUT is installed on a rotation stage (RVS80CC, Newport), which allows us to tilt the lens around the vertical y-axis with the accuracy better than 0.01°. We determine the focal position of the lens by back-propagating a collimated visible laser to the lens. This allows precisely positioning the fiber in the xy-plane and a rough estimation of the focal plane in the z-direction due to the long Rayleigh length. The fiber produces diverging light propagating through the DUT and the transmitted light is then roughly collimated.

The measurement apparatus consists of a pentaprism (CCM1-PS932, Thorlabs) and a pinhole that are mounted on a motorized linear stage (FSL40, FUYU) actuated by a stepper motor over the travel range of 40 cm. The guiding rail is straight with deviation no more than 0.085 mm. The linear stage moves the pentaprism across the aperture of the DUT and samples the light through the pinhole with a diameter of 4 mm. At each position of the pentaprism, the sampled light with the angle of incidence θ is deflected by 90°. Then, an imaging lens (f_2 =500 mm) converts the angle θ to the position of the focused spot $\Delta = f_2 \tan(\theta)$. In our setup, the pentaprism is the only moving part during

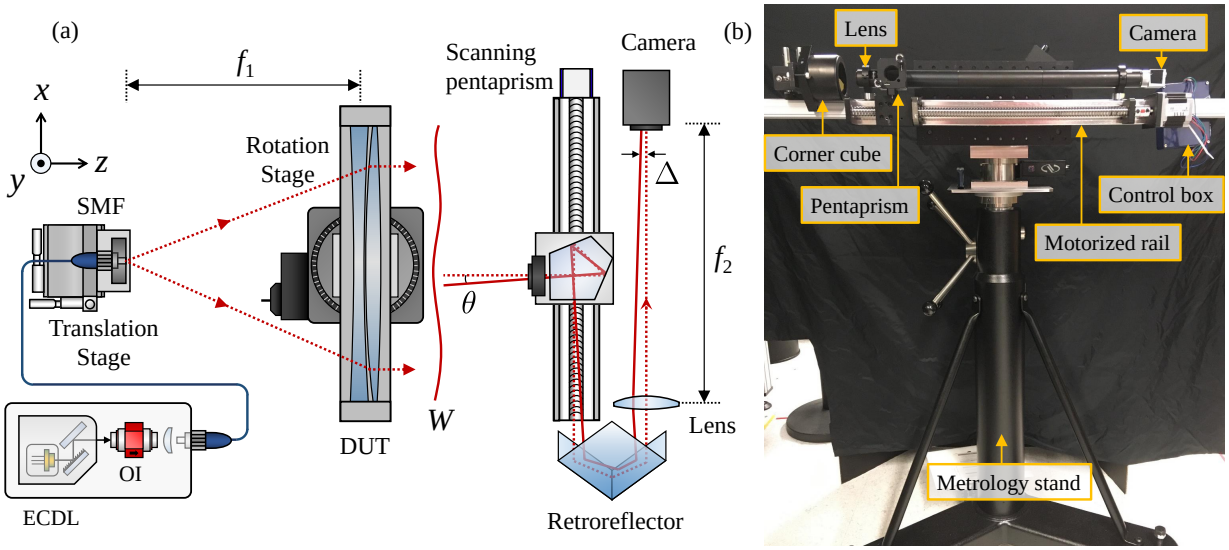

Figure 3.3: Experimental setup for optical aberration characterizations. (a) A schematic diagram of the experimental setup; ECDL, external cavity diode laser; SMF, single-mode fiber; OI, optical isolator; DUT, device under test. A scanning pentaprism deflects the incident light by 90° and a convex lens converts the incident angle to the position of centroid spot on the camera. A motorized linear stage moves the pentaprism across the diameter of the incident light. (b) A photograph of the measurement system with scanning pentaprism.

the measurement. The beauty of using the pentaprism is that the centroid in the xz-plane is not sensitive to three pentaprism's rotation angles to the first order. Also, note that the spot position is insensitive to translational shift of the incident light to the first order. Therefore, the designed scheme is capable of detecting the variation of the incident angle caused only by the thickness irregularity of the test optic. The CMOS camera (acA1920-40um, Basler) records the variation Δ with subpixel centroid algorithms [7]. Under the paraxial approximation for the imaging lens, the relationships between the local wavefront slope S, the transmitted wavefront $W(x, y)$, the variation of the centroid Δ, and the incident angle θ may be written as

$$S = \frac{\partial W(x, y)}{\partial x} = \tan(\theta) = \frac{\Delta}{f_2}. \tag{3.1}$$

In our proof-of-principle demonstration, we perform a transverse linear measurement of the transmitted wavefront. A simple numerical integration of the measured slopes over the

scanning range yields the reconstruction of the transmitted wavefront: $S_i = (W_{i+1} - W_i)/h$, where h is the distance between the adjacent pentaprism positions. The numerical relation between the measured slope values S_i and the reconstructed wavefront W_i can be expressed by a N by $N+1$ sparse matrix $\mathbf{A}$ as

$$\vec{S} = \mathbf{A}\vec{W}, \tag{3.2}$$

where N is the number of the pentaprism positions during the scanning. To solve this linear equation, we first multiply the transpose of the matrix $\mathbf{A}$ to both sides of the equation: $\mathbf{A}^{\mathrm{T}}\vec{S} = \mathbf{A}^{\mathrm{T}}\mathbf{A}\vec{W}$. Since the matrix $\mathbf{A}^{\mathrm{T}}\mathbf{A}$ is singular, we impose an additional condition of the zero-mean value of the wavefront $\vec{W}$ across the test optic, as discussed in [272]. We add an additional row of ones to the matrix $\mathbf{A}$ to construct the $N+1$ by $N+1$ extended matrix $\mathbf{A}_e$. Then, the solution of the transmitted wavefront $\vec{W}$ can be obtained by multiplying the inverse matrix of $\mathbf{A}_e^{\mathrm{T}}\mathbf{A}_e$ as

$$\vec{W} = (\mathbf{A}_e^{\mathrm{T}}\mathbf{A}_e)^{-1}\mathbf{A}^{\mathrm{T}}\vec{S}. \tag{3.3}$$

The uncertainty of the wavefront measurement δW was simply estimated from the standard deviation of the wavefront-slope measurements multiplied by the distance between two adjacent pentaprism position: $\delta W = \delta S \times h$. This is valid because the measured slope values already include the errors of positioning the pentaprism.

Our measurement setup is built on a 34 mm×34 mm×1000 mm aluminum extrusion rail (XT34-1000, Thorlabs), as shown in Figure 2.5(b). To reduce the total length of the apparatus while keeping a long focal length of the imaging lens, we used a corner cube reflector to fold the sampled light. The scanning pentaprism system is mounted on a 2-axis rotational stage for alignment of the system as well as for scanning in different directions across the test optic. The whole assembly is mounted on a portable and height-adjustable heavy duty metrology stand (233 Series, BRUNSON), thereby constructing a mobile wavefront sensor for large optics.

Design analysis

According to our design specifications, the optical path difference of our DUT is estimated to be 0.066λ of Peak-to-Valley (PV) value which is mainly caused by spherical aberration. However, the manufacturing process of the lens causes additional aberrations from the surface irregularity of about PV $W_{\mathrm{PV}} = 0.17\lambda$. Our goal is the resolution of the divergence-angle measurement to be 2.5 µrad which yields the wavefront-measurement precision of 5 nm for a 2 mm step size of scanning pentaprism. Under the paraxial approximation

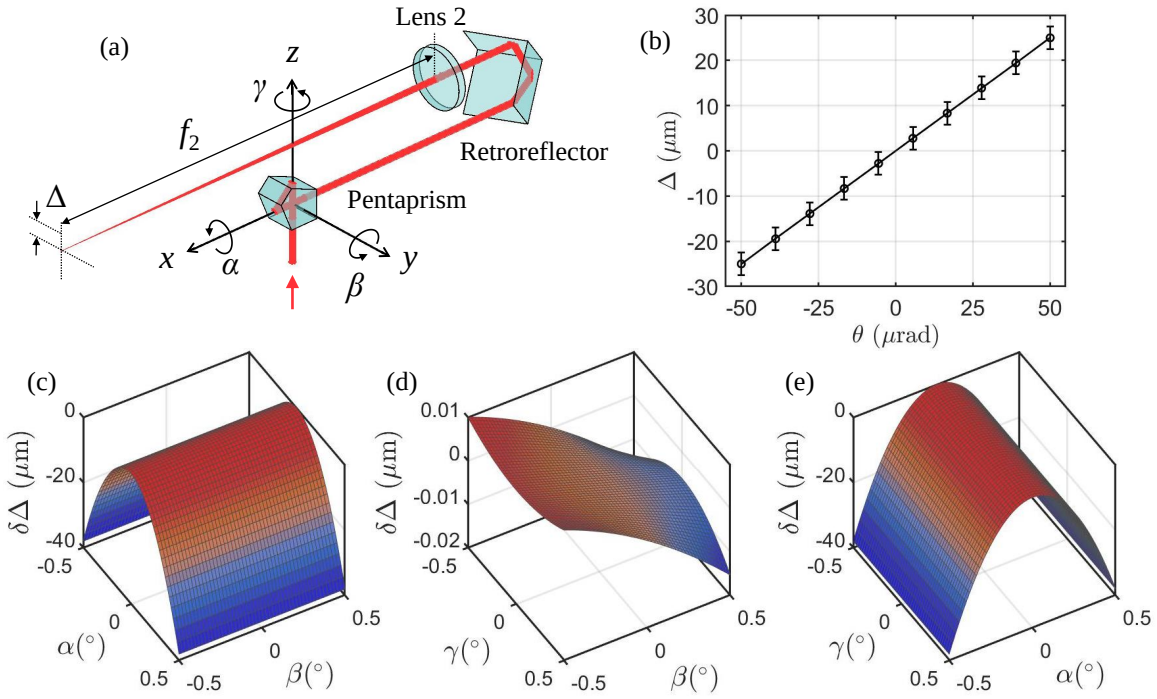

Figure 3.4: 3D raytracing analysis of the wavefront measurement apparatus. (a) Optical configuration of our wavefront measurement apparatus. (b) Monte-Carlo estimation of the precision of the centroid position measurement with randomly distributed rotation angle of the pentaprism. (c)–(e) The centroid variation $\delta\Delta$ as a function of the rotation angles of the pentaprism.

of the imaging lens (f_2 =500 mm), the 4 mm aperture size of the iris yields a spot size of 240 µm which covers more than 40 pixels of our imaging sensor. With a conservative assumption of the centroid estimation precision being 1/10 of the pixel size of 5.86 µm [7], the measurement precision of the divergence angle θ is estimated to be approximately 1 µrad in the absence of any systematic errors. Also, our imaging sensor size (11.3 mm × 7.1 mm) gives the dynamic range of our wavefront sensor of the PV value of greater than 50λ.

To estimate the measurement precision of centroid positions after accounting higher order effects, we investigated the variation of centroid positions $\delta\Delta$ as a function of the rotation angles of the pentaprism via three-dimensional raytracing, as shown in Figure 3.4. In our model, the rotations were performed in the order z-, y- and x-axis (labeled γ, β,

α, respectively) and we assume the perfect pentaprism: no tilt-angle between adjacent surfaces. The Figure 3.4(c)–(e) shows the variation of the spot position $\delta\Delta$ for normal incident light $\theta = 0°$ under pentaprism rotation from $-0.5°$ to $0.5°$. Rotation around the x-axis (α rotation) showed the most significant impact on the slope measurement, with quadratic response. Meanwhile, the centroid measurement was relatively insensitive to the β and γ rotations. The α rotations (around the x-axis) during the measurement can be suppressed by monitoring the retro-reflected light with auto-correlators and feedback, as demonstrated in other deflectometries [309, 245]. It is worth noting that, although the variation is on the order of tens of nanometers, the centroid depends on the β rotation (around the y-axis), which is attributed to the spherical aberration of the imaging lens.

We performed a Monte-Carlo analysis to determine the precision of the slope measurement. We varied the incident angle θ from $-50\,\mu\text{rad}$ to $50\,\mu\text{rad}$ with $11.1\,\mu\text{rad}$ increments and sampled ten thousands randomly distributed pentaprism-rotation angles in a range from $-0.25\,\text{rad}$ to $0.25\,\text{rad}$ at each incident angle. The mean value and the standard deviation of the centroids Δ were calculated as a function of the angles of incidence, as shown in Figure 3.4(b). The centroid position uncertainty characterized by the averaged standard deviations was estimated to be $2.5\,\mu\text{m}$, which is translated to the divergence-angle uncertainty of $5\,\mu\text{rad}$.

3.2.4 Results

To experimentally obtain the wavefront-measurement precision including all systematic errors, we performed the characterization with sufficient redundency. The $20\,\text{cm}$ measurement range of the scanning pentaprism is discretized with step size of $2\,\text{mm}$. At each position, the camera adjusts its exposure time to keep a good signal-to-noise ratio (SNR>10) while ensuring no saturated pixels. Then, we captured twenty frames of images and calculated the centroid positions in the x-direction for all images. The full scan of the pentaprism was repeated five times, and therefore at each pentaprism position we collected one hundred centroid values. Total runtime of our experiment is about 30 minutes.

Wavefront slope measurement

We measured the centroid positions at various positions of the launch fiber to characterize and calibrate our measurement apparatus. Two parameters must be experimentally obtained: the focal lengths of the DUT (f_1) and the imaging lens (f_2). First, we adjusted the fiber position in the z-direction to find the minimal divergence angle, as shown in

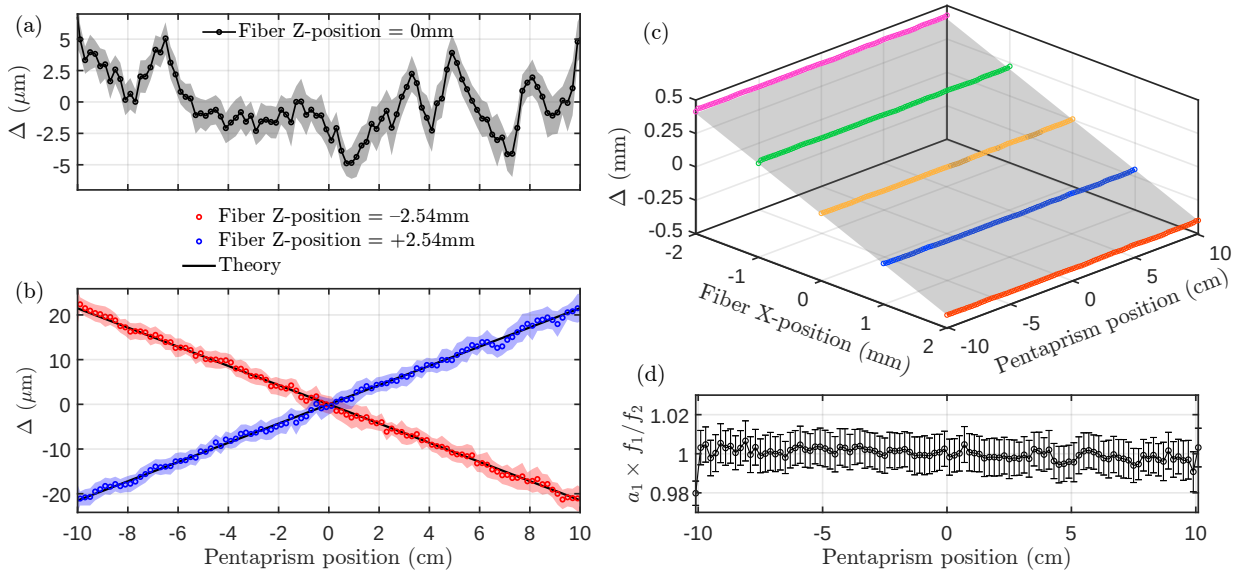

Figure 3.5: Wavefront slope measurements and system calibration. (a) The measured centroid position Δ values as a function of the pentaprism position for collimated light and (b) for de-focused light. Black solid lines represent the theoretical prediction calculated from a three-dimensional raytracing. (c) Characterization of the centroid position measurement with the scanning pentaprism. At each pentaprism position, the centroid position is measured for five different positions of the optical fiber in the x-direction. The dependency of the measured five centroid position values to the corresponding fiber positions is linearly fit to obtain the focal ratio of the DUT to the imaging lens (f_1/f_2). (d) The slope coefficient a_1 of the linear function $y = a_1 x + a_b$ multiplied by f_2/f_1 is plotted as a function of the pentaprism position.

Figure 3.5(a). We observed that the variation of centroid values was kept within a PV value of Δ_{PV} =9.53 µm. The focal length of the DUT f_1 =(243 ± 1) mm was measured with a laser-distance measurer, which showed good agreement with the design parameter. The centroid variation Δ is mainly attributed to the thickness variation of the DUT. The averaged standard deviation of the centroid measurements was found to be 0.24 µm which is twenty times smaller than a pixel size of the camera being used. Note that the presented results were averaged over five times of a full scan of the measurement. This excellent repeatibility shows a great stability of our measurement apparatus.

To find the focal length of the imaging lens, we shifted the launch fiber in the z-direction by ±2.54 mm and obtained the difference of centroid variations by subtracting the

measured values at the original fiber position, as shown in Figure 3.5(b). This removes the wavefront error caused by the DUT's surface irregularity, and leaves contributions mainly from the beam divergence or convergence owing to the de-focused fiber position. Thus, the obtained results can be accurately predicted by modeling the experiment via three-dimensional raytracing. We used the measured focal length of the test optic and compared the experimental results with the predicted values (black solid lines) to determine the focal length of the imaging lens f_2 =(500 ± 1) mm. We characterized a closeness between the theory and experiment by a statistical parameter $R^2 = 1 - \sum_{i=1}^{n}(y_i - f(x_i))^2 / \sum_{i=1}^{n}(y_i - \bar{y})^2$ with $\bar{y}$ denoting the mean value of y_i. Here, y_i and $f(x_i)$ are the measured and theoretically prediected values, respectively. The R^2–values for both -2.54 mm and $+2.54$ mm fiber shifts were calculated to be 99.8 %. This excellent quantitative agreement validates our measurement apparatus as a collimation test system. With the obtained focal lengths, the Δ_{PV} =9.53 µm is translated to the maximum divergence angle of θ_{PV} =19.1 µrad.

We further characterized the uniformity of our measurement precision over the range of scanning pentaprism. We recorded the centroid positions for five different fiber positions in the x-direction at each pentaprism position, as shown in Figure 3.5(c). The ratio of the centroid shift measured at the camera to the distance of the fiber translation is given by the focal ratio of the DUT and the imaging lens: f_2/f_1. We performed the least-squares regression with the linear function $y = a_1 x + a_2$ to the measured spot positions and fiber positions at every pentaprism position. The obtained slope value $a_1 \pm \delta a_1$ at each pentaprism position measures the focal ratio f_2/f_1, where the uncertainty of the regression δa_1 is given by the diagonal elements of a covarience matrix. Then, we verified the focal length of the imaging lens $f_2 = \bar{a}_1/f_1$ =500 mm with $\bar{a}_1$ denoting the averaged slope value over the scanning range. In our approach, the precision of estimating the fiber positions from the measured centroid positions at the camera is given by the uncertainty of imaging the fiber position $\delta\bar{a}_1 \times f_1/f_2$. The averaged uncertainty was obtained to be $\delta\bar{a}_1 \times f_1/f_2 = 0.009$, meaning that the centroid values can be determined with the uncertainty better than 1 % over the entire scanning range. Note that $a_1 \times f_2/f_1 = -1$ (inversed image). The uniformity of the estimation over the scanning range is quantified by the variation of the obtained mean value $a_1 \times f_2/f_1 = -1 \pm 0.003$, as shown in Figure 3.5(d).

Wavefront reconstruction

We reconstruct the transmitted wavefront from the measured centroid positions shown in Figure 3.5(a). The wavefront is normalized by the wavelength of λ=785 nm, as shown in Figure 3.6(a). The averaged uncertainty over the 20 cm travel range of the pentaprism is estimated to be δW =0.007λ. This exceptional precision is comparable with the performance

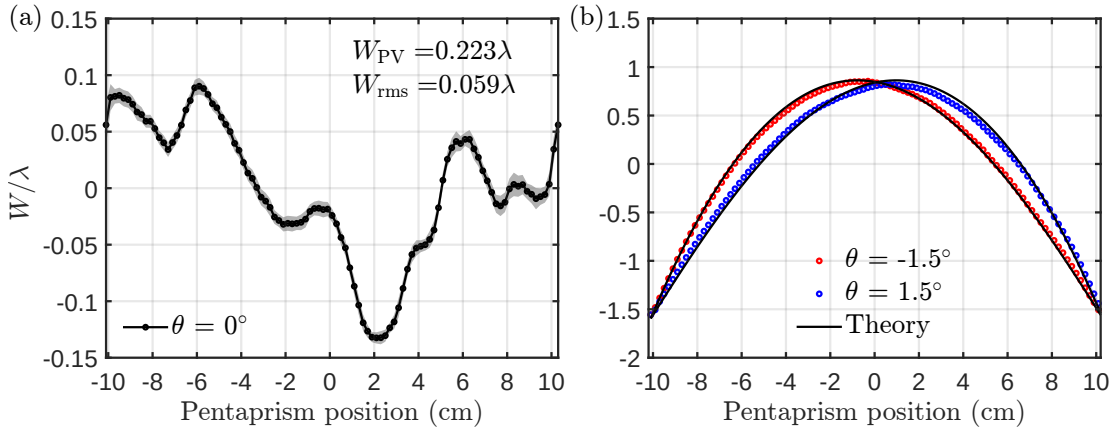

Figure 3.6: Reconstructed wavefront of the transmitted light from (a) the aligned lens and (b) tilted lens. Black solid lines represent the theoretical prediction calculated from a three-dimensional raytracing.

of shearing interferometers [173, 304]. Most previous reports on the wavefront measurement for large optics with SHSs exhibited the precision of order of 0.02λ to 0.1λ [220, 92, 154]. This outperformed precision of our scheme is attributed to excellent stability of our scanning pentaprism system and the long focal length of the imaging lens.

We characterized aberrations for a tilted DUT and compared the result with theoretical prediction. The test optic was rotated by $\pm 1.5^\circ$ around the vertical y-axis. The measured wavefront at each tilt angle was subtracted from the wavefront measured at the normal angle, as shown in Figure 3.6(b), which removes the thickness variation of the DUT from manufacturing imperfections. We calculated the transmitted wavefront from our raytracing model (black solid lines in Figure 3.6(b)). The R^2 parameters were calculated to be 99.9 % and 99.6 % for the -1.5° and $+1.5^\circ$ tilt angles, respectively. The quantitative agreement between theory and experimental results further validates our wavefront measurement system with the scanning pentaprism.

3.3 Robotized polarization characterization platform

3.3.1 Motivation

Characterization of the polarization effect of an optical element is performed by injecting known polarization states and measuring the outcomes. The polarization testbed must be

capable of precise generation and accurate measurement of polarization states. Especially for devices in free-space quantum communications, the task must be performed for the optical elements of small to large sizes which constitute the quantum optical terminals. Moreover, the polarization state analysis must be attained at the range of orientations and positions over which the terminal's components will operate. This is challenging with commercially available polarimeters because they are typically optimized for a small field of view (FoV) with a limited beam aperture, necessitating significant modification of the testbed for each test optic. As a consequence, most prior works limited their focus, such as on telescopes [306] or for an entire assembly in an end-to-end manner [115, 307].

The characterization of instrumental polarization has a long history and it has been developed in many different research areas. As for relatively small optics, the test can be performed in the lab relatively easily. Since the size is well standardized, once the system is built and validated, one can perform the test for various optics without major modifications of the setup. Also, the angle-dependent polarization test can be achieved by an ellipsometry-like method [254, 111]. However, most of the previously reported methods are specialized in non-divergent elements. On the other hand, large telescopes or mirrors often require a specialized test platform. One of the widely used methods for polarization tests on a large telescope, which has been developed in solar observatories, is to build a similar-sized calibration unit in front of the aperture which consists of arrays of rectangular foils that transmit linearly polarized light. By aligning the polarization axes of the individual foils parallel to each other and using sunlight as an incident light passing through the calibration unit, the polarization test is performed on the collected light at the input of the telescope [11, 157, 27, 135]. This approach is a relatively quick and simple test, but it does not provide information on the polarization properties at individual sections of the telescope aperture. Also, the test had to incorporate large calibrated optical units and be performed in an outdoor environment. Futhermore, the approach is designated only for telescopes—the test setup is not adaptive to other large optical elements such as lenses and curved mirrors.

In mobile applications, such as satellite-assisted quantum communications, the telescopes are usually the reflector-type due to the weight limit of the satellite, and the relatively small aperture size of the telescope (12 cm to 25 cm) compared to astronomical telescopes [38]. The polarization quality of the telescope is optimized for a specific wavelength, and it is often in a near-infrared range from 780 nm to 1550 nm. Due to this restriction, the telescope will be custom-designed and expensive. Therefore, an indoor test is highly preferable to keep the payload components intact and to maintain controllable conditions. Moreover, it is desired to obtain a full map of the instrumental polarization across the aperture, which helps to diagnose issues that may be localized, e.g. pressure

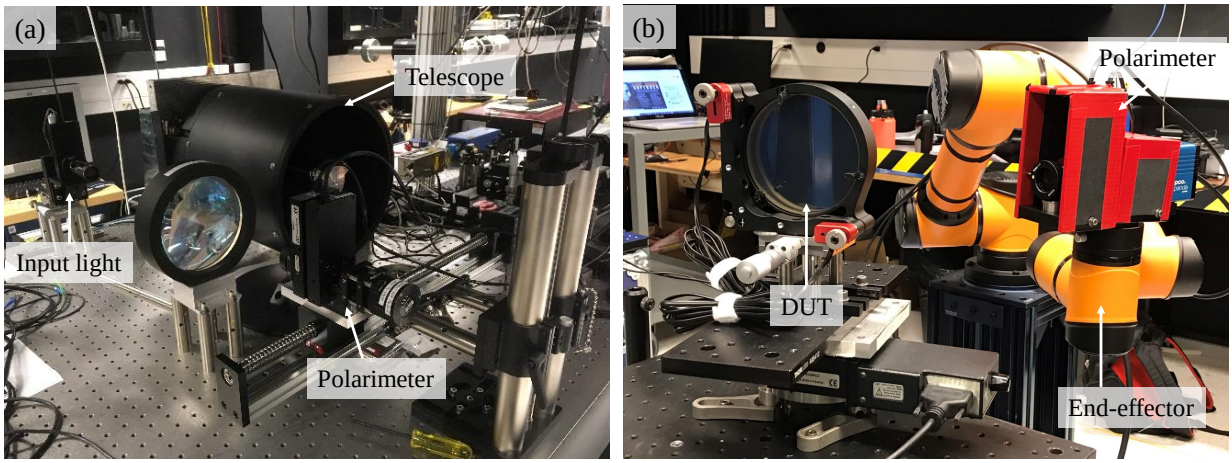

Figure 3.7: Photographs of the polarization characterization system developed at the QPL in (a) October 2018 and (b) March 2021.

points on the optics and obstructions due to structural elements.

3.3.2 History of the system development

An initial version of a polarimeter was mounted on the optical bench by Sebastian Slaman [268], but could only accommodate limited angular motion. We have developed the widely movable polarization setup since August 2018 with a scanning range of over 80 cm, and angular range of around 180°. Our initial version of the measurement apparatus for telescopes utilized one motorized linear rail for horizontal scanning with manual adjustment of the height of the scanning system, as shown in Figure 3.7(a) (scanning ranges were 30 cm and 25 cm in horizontal and vertical directions, respectively). This laterally scanning polarimeter was used for the first characterization of the initial version of the HON-T in September 2018. To upgrade the system with full range of motion in all axis over a larger range of motion, we procured a six-axis robotic manipulator in April 2019 to replace the linear rails. Lindsay Babcock and I implemented the polarization characterization system in May 2019, and validate the system by performing tests on various optical systems including a COTS telescope, a glass plate, and pentaprism from June to August 2019. With the improved polarimeter and analysis program, the polarization characterization for HON-M and HON-T has been performed until March 2020. I designed a new imaging polarimeter and upgraded the control software with graphical user-interface (GUI) in January 2021. The upgraded polarization testbed supported the hardware development

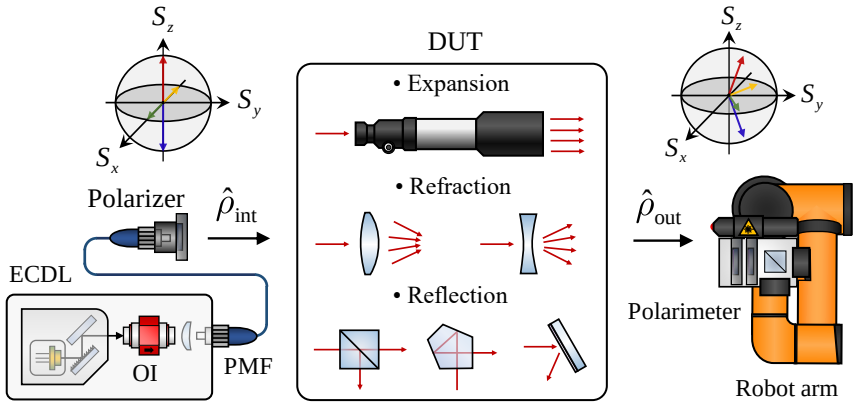

Figure 3.8: A conceptual design of the robotized polarization characterization platform. Four different linearly polarized states are injected into the device under test (DUT) and a sample of the transmitted or reflected light is examined. The output beam size and direction varies depending on the type of test optics.

for quantum optical ground stations at the QPL by tests on IQC-L, COTS-M, and IQC-T.

3.3.3 Conceptual design of polarization characterization system

Figure 3.8 illustrates the concept of our polarization characterization platform. We inject several well-defined polarization states into a device under test (DUT) and perform polarization state tomography on the output states to see how they change. To match our intended application, we consider four incident polarization states: $|H\rangle$ (horizontal), $|V\rangle$ (vertical), $|D\rangle$ (diagonal, 45°), and $|A\rangle$ (antidiagonal, −45°). This is sufficient to determine performance of the system in the context of BB84-style QKD protocol[1]. In our system, the light source is an external cavity diode laser (DLpro, Toptica photonics) operating in continuous-wave mode at 785 nm wavelength, which produces a stable intensity over a long period of time for the polarization test. The input polarization state is initially determined by an optical isolator and delivered through a polarization-maintaining fiber. Upon exiting the fiber, the laser light passes through a linear-film polarizer (LPVIS100, Thorlabs) mounted on a motorized rotation stage (PR50PP, Newport). This rotation stage rotates the fiber and the polarizer altogether to define the four input polarization state with the accuracy of ±0.025°. Once the light has been sent through the test optic, it reaches a po-

[1]To perform full process tomography, such as to establish Mueller matrices, one could straightforwardly incorporate additional circularly polarized incident states.

larimeter which is attached to a six-joint robotic manipulator (AUBO-i5, AUBO Robotics). The robot manipulator precisely moves the polarimeter to measure the output polarization state at the desired positions and angles. The polarimeter projects the output state onto six polarization-basis states ($|H\rangle$, $|V\rangle$, $|D\rangle$, $|A\rangle$, $|R\rangle$ right-circular, and $|L\rangle$ left-circular), and thus sufficient measurements for complete polarization state tomography are performed.

Here, we summarize the main advantages of our test system. First, our test setup is applicable for a wide range of sample sizes and ranges of motion without major modifications. Also, from measurement to data analysis, the whole procedure is automated and therefore many different types of samples can be tested with consistently high precision. Secondly, the capability of an angle-dependent polarization measurement enables the test for small optics for reflection-induced polarization rotation as a function of incident angle. Moreover, the input polarization states can be directly characterized, and therefore the precision of the polarization test is limited by the extinction ratio of measurement polarizers. A typical extinction ratio for polarized beam splitter (PBS) cube is 1000:1, which yields an accuracy of 0.1% QBER. One option to improve the extinction ratio is to use linear-film polarizers whose typical extinction ratio is 10000:1, or other types of polarizing elements such as a Glan-Taylor prism (extinction on order 100000:1). In this case, the main limiting factor becomes the SNR of the detector.

3.3.4 Detailed design for subsystems

Six-axis collaborative robot arm

Our robotic manipulator is driven by six geared servo-motors with absolute encoders at all joints. This robot has a reach of 0.924 m, which can easily scan over the entire trajectory around the optics being tested. The robot has a payload capacity of 5 kg and itself weighs 24 kg. According to the manufacturer's specifications, the robot has position repeatability of 0.02 mm and position accuracy of 2 mm. The average orientation repeatability and accuracy are 0.004° and 0.5°, respectively. A pre-programmed teaching pendant supports manual control by the user-friendly interface in a touch screen tablet, while Python and C++ SDK provided by the manufacturer allows us to remotely control the robot arm. Both methods can independently control the orientation and position of the robot's end effector.

The robotic manipulator has two pre-set coordinate systems: base coordinates and sensor coordinates, and the option to set a user-defined coordinate system, as shown in Figure 3.9. The base and sensor coordinates are referenced to the absolute position $\{x, y, z\}$

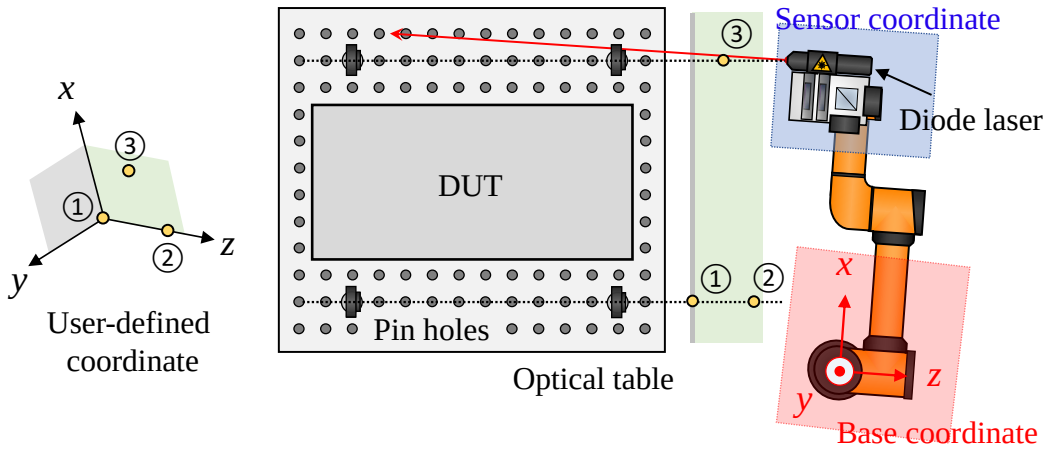

Figure 3.9: Three coordinate systems of the six-axis robot arm: base, sensor, and user-defined coordinates and an example method of the coordinate alignment. Three points, one at the origin, another on the z-axis, and the other on the xz-plane, define a user-coordinate system. The number labels indicate positions used for relative calibaration of the coordinate systems.

and the orientation $\{\alpha, \beta, \gamma\}$ of the end effector, respectively. These six parameters and the six joint angles can be transformed to each other via forward and inverse kinematics. For testing purposes, it is convenient to define the robot's trajectory in a coordinate system whose one axis is parallel to the light propagation direction, which was chosen to be the z-axis. The accurate alignment of this coordinate system is essential to ensure the polarimeter follows the desired path of scanning across the test optic. Following is an example of our procedure we developed to determine the user-defined coordinate system.

Three orthogonal axes are required to create a user-defined coordinate system. These axes can be determined using three points in various combinations. Here, we describe one example method to determine the coordinate system; inputting one point at the origin ①, another point along the z-axis ②, and the other at anywhere on the xz-plane ③. We set up two sets of two pinholes at the same height on the optical table that the test optic was mounted and aligned to. The four pinholes define two parallel lines which are parallel to the surface of the optical table. A diode laser is attached on the end effector of the robot arm, and the laser light is manually aligned through the two in-line pinholes using the robot teaching pendant. This point was then recorded and set as the origin point. The laser was then moved further away from the table and carefully re-aligned through the same two pinholes to define the point along the z-axis. Finally, the laser was aligned to the

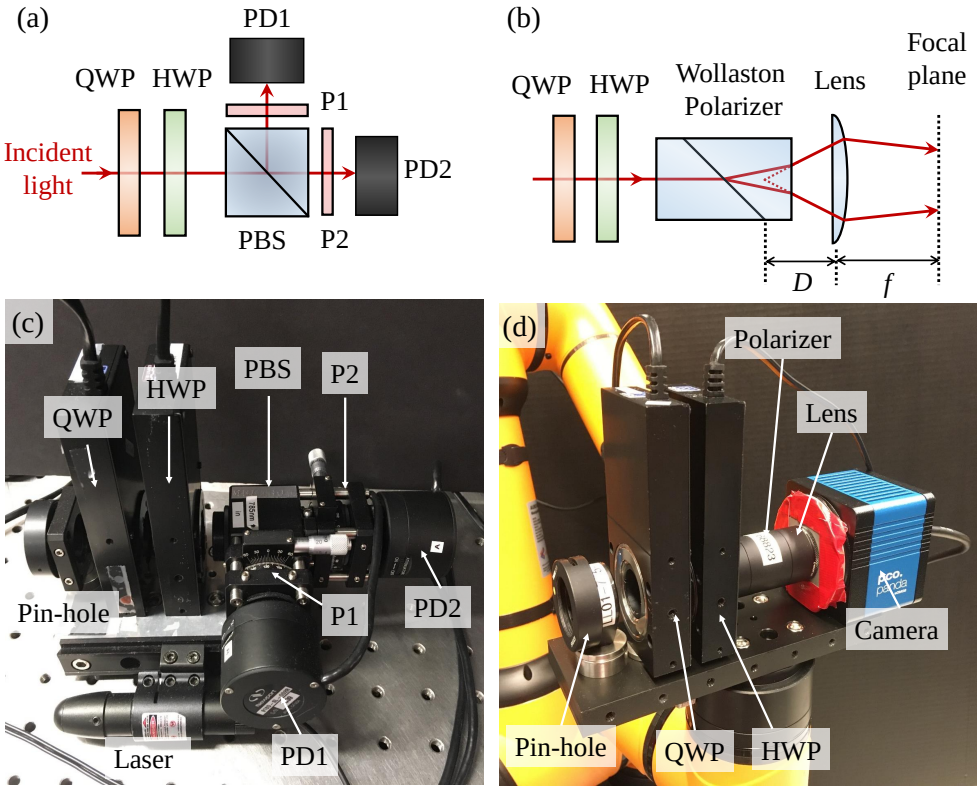

Figure 3.10: Two polarimeters used for polarization characterizations: a conventional division-of-amplitude polarimeter (DOAP) and high-precision imaging polarimeter (HPIP). The schematic diagram of (a) DOAP-v2 and (b) HPIP; QWP, quarter-wave plate; HWP, half-wave plate; P, polarizer; PD, photodiode. Photos of the (c) DOAP-v2 and (d) HPIP.

second set of pinholes, and the position was recorded as a point on the xz-plane. In this way, the orientation of the end effector is aligned such that the polarimeter is faced towards the incident beam, and thus the angles α and β are automatically calibrated. The angle γ is defined by the incident horizontal polarization axis, and the pre-calibrated polarimeter is oriented such that the power measured at the vertical polarization state is minimized.

Polarimeters

We developed two different types of polarimeters that are illustrated in Figure 3.10. Both include an iris, quarter-wave plate (QWP) and half-wave plate (HWP). The plates rotate the projection state to six tomographically complete polarization states ($|H\rangle$, $|V\rangle$, $|D\rangle$,

$|A\rangle$, $|R\rangle$, and $|L\rangle$). The projected states are converted to the intensity distributions at the output port of either the PBS or Wollaston polarizer (68-823, Edmund Optics). The main difference between the two polarimeters is the optical power measurement device. One utilizes two identical optical power meters at the output ports of the PBS, which we call a division-of-amplitude polarimeter (DOAP), and the other uses a CMOS camera (pco.panda.4.2, PCO) with an imaging lens (f =30 mm, 49-115, Edmund Optics) at the output of the Wollaston prism, which we call a high-precision imaging polarimeter (HPIP). From the measured results, we found that the reflection port of the PBS exhibits worse polarization extinction ratio (100:1) than the transmitted port (1000:1). Then, we added two film polarizers (colorPol® VISIR CW02, CODIXX) at the two output ports of the PBS in order to improve the polarization-extinction ratio to $>$ 10000:1 for more thorough characterizations of the prototype payload telescope HON-T and its primary mirror HON-M. It is worth noting that we did not include the polarizers in the DOAP at the initial stage of validating the system with tests on a COTS pentaprism and glass plate. Throughout this chapter, we label the DOAP without and with the film polarizer DOAP-v1 and DOAP-v2, respectively.

Our HPIP is capable of measuring the incident polarization states and the angle of incidence (AOI) altogether. Figure 3.11(a) shows the detailed schematic diagram of our HPIP. A convex lens is placed after the Wollaston polarizer such that the far-field image of the intensity distribution is mapped on the focal plane where an imaging sensor of the CMOS camera is placed to read out the image $N(x, y)$. In this way, the variation of the AOI appears as the translation of the intensity distribution by $\Delta x_{e(o)}$ and $\Delta y_{e(o)}$ which can be precisely measured by sub-pixel centroid algorithms [7].

We consider the variation of the AOI that mainly comes from the imperfect orientation of the robotic end effector which is defined by three rotation angles (α,β,γ) around the three orthogonal axes (x,y,z), respectively, as shown in Figure 3.11(a). The angular deviation under consideration is on the order of 0.5° and aberrations of the imaging lens are neglected. As the split angle between the ordinary and extraordinary light exiting the polarizer depends on its tilt angle [264], we calculate the central point of the two centroids $\Delta x = (\Delta x_e + \Delta x_o)/2$ and $\Delta y = (\Delta y_e + \Delta y_o)/2$ to cancel such effect. Thus, under the paraxial approximation for the lens, the centroid shifts Δx and Δy are related to the AOI by the formula

$$\begin{aligned} \Delta x &= f \tan\beta, \\ \Delta y &= f \tan\alpha. \end{aligned} \tag{3.4}$$

Note that the γ–rotation (around the z-axis) is not directly detected by measuring the shift of the intensity distribution as it rather appears as the variation of the intensity because

the polarizer and the camera are rotated altogether.

Design analysis of the high-precision imaging polarimeter

In the following, we focus on the detailed analysis of the HPIP design as the DOAP has been commonly used and studied in other literature [12]. Although the usage of the camera provides accurate estimation of the AOI, one major drawback of such an imaging polarimeter is the limited dynamic range of optical power measurements with the camera. The issue becomes significant especially when the polarization measurement basis is aligned to the incident polarization axis. For example, our camera exhibits dynamic range of 21,500:1, an order of magnitude smaller than the extinction ratio of the Wollaston polarizer (200,000:1). The signal-to-noise ratio (SNR) of the captured images directly impacts the precision of measuring polarization states. For a given camera with its quantum efficiency η and the exposure time ΔT, the SNR is given by

$$\mathrm{SNR} = \frac{P\eta\Delta T}{\sqrt{N_{\text{shot}}^2 + I_{\text{dark}}\Delta T + N_{\text{read-out}}^2}}, \tag{3.5}$$

where P is the optical power of the incident light, $N_{\text{shot}} = \sqrt{P\eta\Delta T}$ is the shot noise, I_{dark} is the dark current, and $N_{\text{read-out}}$ is the read-out noise. To keep acceptable SNR over a wide range of incident optical power, we capture two images for a given waveplate setting. The camera adjusts the exposure time $\Delta T_{e(o)}$ to improve the SNR for the power measurement of extraordinary (ordinary) light at a time. For sufficient optical incident power and long exposure time, the SNR is mainly determined by shot noise. The optical powers $P_{e(o)}^{(i)}$ at the i-th waveplate setting are obtained by the averaged pixel values over a region around the intensity distribution of extraordinary (ordinary) light per unit exposure time of the camera $\Delta T_{e(o)}$ as

$$P_{e(o)} = \frac{1}{\Delta T_{e(o)}}\left[\sum_{i,j=1}^{n}\frac{N(x_i, y_i)}{n} - \sum_{i,j=1}^{m}\frac{N(x_i, y_i)}{m}\right]. \tag{3.6}$$

Here, we subtracted background noises with the averaged pixel values over the outside of the region to calculate the net power values. n and m are the number of pixels including incident power values and background noises, respectively. Then, we determine the measured polarization states by evaluating for each Stokes vector $\vec{S} = [S_0, S_1, S_2, S_3]^\top$, where S_0 is the total power of the incident light, S_1 denotes the bias for $|H\rangle$ and $|V\rangle$, S_2 for $|D\rangle$ and $|A\rangle$, and S_3 for $|R\rangle$ and $|L\rangle$.

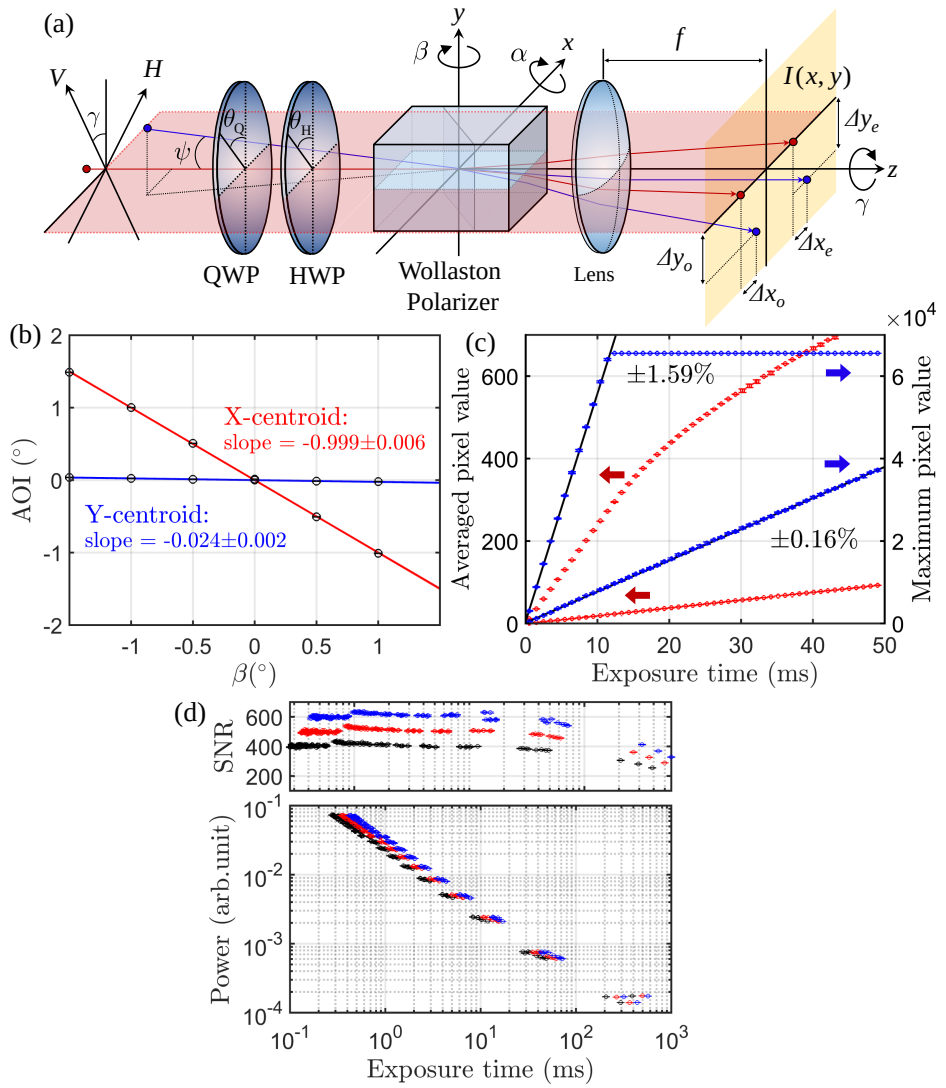

Figure 3.11: Design analysis of a high-precision imaging polarimeter (HPIP). (a) A schematic diagram for the optical configuration of the polarimeter; HWP, half-wave plate; QWP, quarter-wave plate. Experimental characterization in terms of (b) the angle of incidence via the centroid position measurements, (c) the linearity of the camera exposure time, and (d) the dynamic range of the optical power measurement.

We characterized our polarimeter in terms of the accuracy of the centroid and power measurement as well as the dynamic range. First, we mounted the polarimeter on the

robotic manipulator, injected laser light in a fixed propagation direction, and measured the centroids Δx and Δy as a function of the rotation β which are then converted to the AOI via Equation 3.4. The slope is estimated to be nearly unity in x–axis via least-square fitting with 0.6 % standard error of the regression, indicating accurate AOI measurement, as shown in Figure 3.11(c). Secondly, with a constant incident optical power, we recorded the maximum pixel values as a function of the camera exposure time to ensure linearity of the exposure time control, as shown in Figure 3.11(d). The slope is estimated by the same fitting method, and the relative uncertainty of the power measurement is estimated to be around 1 %. Finally, the dynamic range is characterized by varying the incident power. We varied the incident optical power while allowing automated control of the camera exposure time to maintain a constant SNR over the range of incident power, as shown in Figure 3.11(e). The optical power was measured over a range of three orders of magnitude while maintaining SNR greater than 200 by adjusting the exposure time between 0.2 ms and 500 ms. With our camera capable of exposure times of 0.01 ms to 5000 ms, we expect that a dynamic range of $100,000:1$ can be readily achieved.

3.3.5 Polarimeter model, error analysis, and calibration

We model our HPIP with Mueller matrices and analyze polarization measurement errors caused by the imperfect robotic movement as well as manufacturing imperfections of optical components being used. We assume that the error of translating the polarimeter impacts negligibly on the polarization measurement, while the imperfect orientation of the polarimeter is modeled by the the tilted waveplates and the polarization axis misalignment.

Polarimeter model

Our HPIP is modeled by the Mueller matrices of the polarizer $\mathbf{M}_{\mathrm{P}}$ and waveplates $\mathbf{M}_{\mathrm{WP}}$ as

$$\mathbf{M}(\theta_P, \theta_H, \theta_Q; \phi_H, \phi_Q) = \mathbf{M}_{\mathrm{P}}(\theta_P)\mathbf{M}_{\mathrm{WP}}(\theta_H; \phi_H)\mathbf{M}_{\mathrm{WP}}(\theta_Q; \phi_Q). \tag{3.7}$$

The polarizer and waveplates are parametrized by the azimuthal rotation angle θ and phase retardance ϕ:

$$\mathbf{M}_{\mathrm{H(Q)}}(\theta;\phi) = \begin{bmatrix} 1 & 0 & 0 & 0 \\ 0 & C^2 + S^2\cos\phi & CS(1-\cos\phi) & -S\sin\phi \\ 0 & CS(1-\cos\phi) & C^2\cos\phi + S^2 & C\sin\phi \\ 0 & S\sin\phi & -C\sin\phi & \cos\phi \end{bmatrix}, \\ \mathbf{M}_{\mathrm{P}}(\theta) = \frac{1}{2}\begin{bmatrix} 1 & C & S & 0 \\ C & C^2 & CS & 0 \\ S & CS & S^2 & 0 \\ 0 & 0 & 0 & 0 \end{bmatrix}. \tag{3.8}$$

Here, C and S are $\cos(2\theta)$ and $\sin(2\theta)$, respectively. With $\mathbf{M}_{\mathrm{P}}$ we assume the Wollaston polarizer differs negligibly from perfectly polarizing. Ideally, the phase retardances of the HWP and QWP are $\phi_H = \pi$ and $\phi_Q = \pi/2$, respectively. We model the polarization extinction between extraordinary and ordinary paths of the Wollaston polarizer by the rotation of the polarizer $\theta_P \in \{0°, 90°\}$. Also, for complete tomography, the rotation angle of the waveplates are in corresponding pairs of $\theta_{H,Q} \in \{(0°, 0°), (22.5°, 45°), (0°, 45°)\}$. The optical power for each combination of the rotation angles can be calculated by multiplying the first row of the Mueller matrix $\vec{M} = [M_{00}, M_{01}, M_{02}, M_{03}]^\top$ to the incident Stokes parameter $\vec{S}_{\mathrm{in}}$. As we have three rotation angle settings of the waveplates and two ports of the polarizer, the six power measurements can be described by the 6×4 matrix $\mathbf{A} = [\vec{M}^{(H)}, \vec{M}^{(V)}, \vec{M}^{(D)}, \vec{M}^{(A)}, \vec{M}^{(R)}, \vec{M}^{(L)}]^\top$ called an *instrument matrix*. Here, the superscript (i) represents each configuration of the polarimeter settings for the power measurements in the horizontal, vertical, diagonal, anti-diagonal, right-circular, and left-circular polarization-basis states. Then, the six power values $\vec{P} = [P_e^{(H)}, P_o^{(V)}, P_e^{(D)}, P_o^{(A)}, P_e^{(R)}, P_o^{(L)}]^\top$ for the input polarization state can be written as

$$\vec{P} = \mathbf{A} \cdot \vec{S}_{\mathrm{in}} + P_d, \tag{3.9}$$

where we added a constant value P_d for randomly fluctuating power noises from the camera including the dark current, shot noise, and stray light. Then, the Stokes vector $\vec{S}_{\mathrm{meas}} = \mathbf{W} \cdot \vec{P}$ is obtained from the measured power vector $\vec{P}$ multiplied by the pseudoinverse of the instrument matrix called a *data reduction matrix* $\mathbf{W} = (\mathbf{A}^\top \cdot \mathbf{A})^{-1} \cdot \mathbf{A}^\top$. The obtained Stokes vector is used to reconstruct the density matrix $\hat{\rho}_{\mathrm{out}}$ of the measured polarization state:

$$\hat{\rho}_{\mathrm{out}} = \frac{1}{2}\left[\hat{\mathbb{1}} + \frac{S_1}{S_0}\hat{\sigma_z} + \frac{S_2}{S_0}\hat{\sigma_x} + \frac{S_3}{S_0}\hat{\sigma_y}\right], \tag{3.10}$$

where $\hat{\mathbb{1}}$ is the 2×2 identity matrix.

We characterize the quality of the output polarization states with the quantum state fidelity $\mathcal{F}$, purity $\mathcal{P}$, and QBER. The fidelity is a measure of the similarity between the measured state $\hat{\rho}_{\text{out}}$ and the incident state $\hat{\sigma} = |H\rangle\langle H|$ (and similarly for V, D, and A states) which is generally defined as

$$\mathcal{F} = \text{Tr}(\hat{\rho}_{\text{out}}\hat{\sigma}) + 2\sqrt{\det(\hat{\rho}_{\text{out}})\det(\hat{\sigma})}. \tag{3.11}$$

Assuming that our incident states $\hat{\sigma}$ are prepared at pure states, which gives $\det(\hat{\sigma}) = 0$, the fidelity can be simplified as $\mathcal{F} = \text{Tr}(\hat{\rho}_{\text{out}}\hat{\sigma})$. The purity, defined as $\mathcal{P} = \text{Tr}(\hat{\rho}^2_{\text{out}})$, describes the degree of polarization, where $\mathcal{P} = 1$ means a pure state and $\mathcal{P} = 1/2$ indicates a fully mixed state, i.e., unpolarized light. Finally, the QBER is obtained directly from the measured power values $P^{(i)}_{e(o)}$ at the i-th waveplate setting. For example, the QBER for the horizontal state of the incident light is calculated as $\text{QBER} = P^{(V)}_e/(P^{(H)}_e + P^{(V)}_o)$.

The three quality parameters, i.e., fidelity $\mathcal{F}$, purity $\mathcal{P}$, and QBER, are related to each other. For a single qubit of polarized light, the $\text{QBER} = 1-\mathcal{F}$ indicates the deviation of the measured state from the incident state. However, the purity depends on the type of noise or instrumental polarizations. For example, if the initial state is prepared in $\hat{\rho}_{\text{in}} = |H\rangle\langle H|$ and then experiences depolarization due to a symmetric noise, then the output state can be modeled as $\hat{\rho}_{\text{out}} = p|H\rangle\langle H| + (1-p)(|V\rangle\langle V| + |H\rangle\langle V| + |V\rangle\langle H|)$. In this case, the fidelity $\mathcal{F} = \text{Tr}(\hat{\rho}_{\text{in}}\hat{\rho}_{\text{out}}) = p$ is related to the degree of polarization while the purity $\mathcal{P} = p^2$ represents only the loss of coherence between the basis states $|H\rangle$ and $|V\rangle$.

Polarization measurement errors due to tilted polarimeters

Based on the above model, we study how orientation of the robot's end effector (α, β, γ) changes the reconstructed density matrix $\hat{\rho}_{\text{out}}$. First, it is obvious that the γ rotation causes misalignment of the incident polarization state with respect to the principal axes of the waveplates and the polarizer, as depicted in Figure 3.11(a). This can be modelled by equally adding the robot's rotation angle γ to the azimuthal angles as the waveplates and polarizer rotate altogether: $\theta_{P(Q,H)} \to \theta_{P(Q,H)} + \gamma$. The α and β rotations are related to the tilt angle of the waveplates $\psi = \cos^{-1}\big(\cos(\alpha)\cos(\beta)\big)$. The phase retardance of the waveplates for a given tilt angle ψ and azimuthal rotation angle θ is expressed in a closed form [111]

$$\phi(\theta,\psi) = \frac{2\pi}{\lambda}d\left(\sqrt{n_e^2 - \frac{n_e^2\cos^2(\theta) + n_o^2\sin^2(\theta)}{n_o^2}\sin^2(\psi)} - \sqrt{n_o^2 - \sin^2(\psi)}\right), \tag{3.12}$$

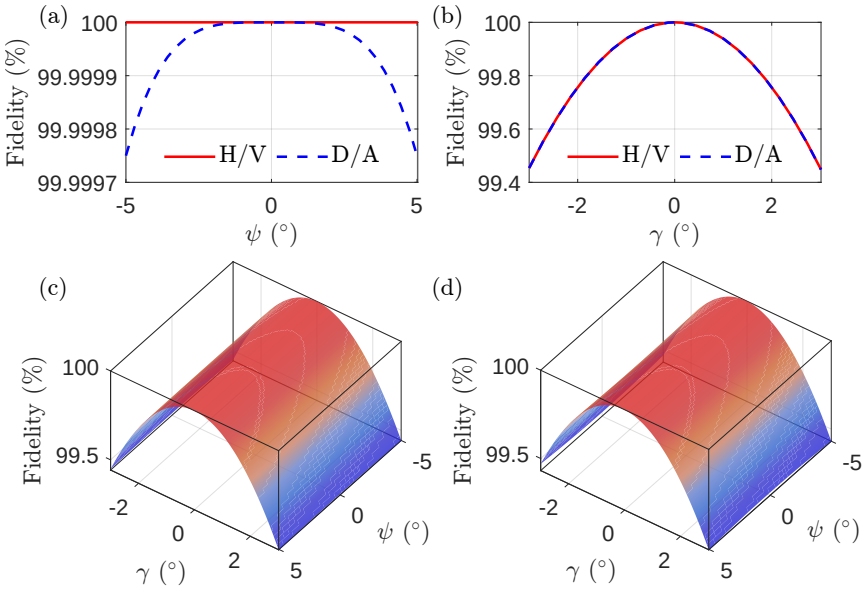

Figure 3.12: Quantum state fidelity for polarization states characterized by tilted polarimeters. The fidelity is calculated by our theoretical model for four linearly polarized states (horizontal H, vertical V, diagonal D, and anti-diagonal A) as a function of (a) the tilt angle ψ and (b) the rotation angle γ. (c)–(d) three-dimensional plot for the calculated fidelity.

where λ is the wavelength of the incident light, d is the thickness of the waveplate, and n_o and n_e are the ordinary and extraordinary refractive indices, respectively. Here we considered a single-crystal waveplate for simplicity.

We evaluated the quantum state fidelity of the reconstructed density matrix in Equation 3.10 for the four linear input polarizations as a function of the rotation angle γ and the tilt angle ψ, as shown in Figure 3.12. In our calculation, we modelled the ideal MgF_2 single-crystal zeroth-order QWP and HWP operating at a wavelength of 785 nm: $d_H = 33.6\,\mu m$, $d_Q = 16.8\,\mu m$, $n_e = 1.3869$, and $n_o = 1.3752$. We found that the fidelity is degraded mainly due to the γ rotation and it scales quadratically, whereas the effect for the ψ rotation is relatively negligible.

Polarimeter calibration

We calibrate our polarimeter by a conventional method [37] to obtain the instrument matrix including the manufacturing imperfections of the HWP and QWP as well as any

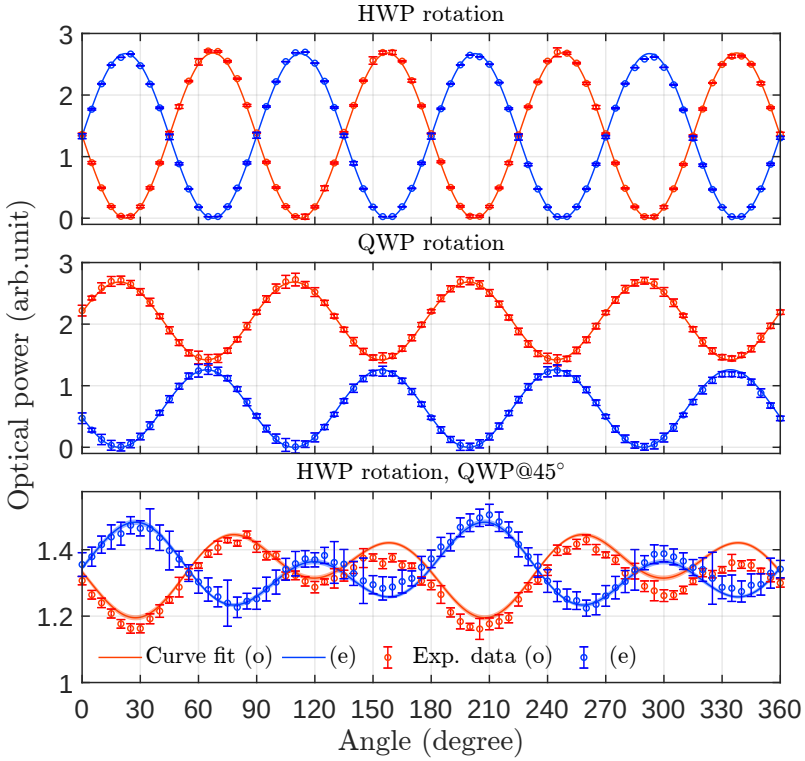

Figure 3.13: Experimental results of calibrating the high-precision imaging polarimeter. Optical powers are measured under the rotation of half- and quarter-wave plates. The incident light is horizontally polarized. The circles show the mean values of twenty power measurements of the ordinary and extraordinary light. The solid curves are fits to the model in Equation 3.9, and the shaded regions represent the 95 % confidence interval for the fitting curve. Top: the half-waveplate (HWP) is rotated without the presence of QWP. Middle: the QWP is rotated while the HWP is aligned to the horizontal polarization axis. Bottom: the HWP is rotated while the QWP is oriented at 45° with respect to the incident polarization direction.

other systematic error such as the waveplate misalignment. We injected a horizontally polarized input state, and recorded the optical powers of the ordinary and extraordinary rays of the polarizer as a function of the rotation angle of the waveplates in three different configurations, as shown in Figure 3.13. First, we rotated the HWP without the QWP to find the angle for the principal axis of the HWP (top). Then, we rotated the QWP while the axis of the HWP has aligned to the incident horizontal polarization (middle). Finally, we rotated the HWP through 360° while the optic axis of the QWP was rotated

by 45° with respect to the incident polarization direction (bottom). Data were collected at 5° increments. For each waveplate setting, we captured twenty frames of images to calculate the mean values and standard deviations of the optical power for the ordinary and extraordinary rays of the Wollaston polarizer. Also, we maintained SNR greater than two hundred via auto-exposure time control. Thus, we obtained 438 power values with different waveplate settings.

To determine the phase retardance $\phi_{H,Q}$ and misalignment $\theta_{H0,Q0}$ of the waveplates, we used a least-squares fit of the 438 measured power values to our polarimeter model in Equation 3.9 with fitting parameters $\{\phi_H, \phi_Q, \delta\theta, \theta_{H0}, \theta_{Q0}, P_d, P_e, P_o\}$, as shown in Figure 3.13. Here, θ_{H0} and θ_{Q0} are the azimuthal angles of the HWP and QWP where their optic axes are aligned to the horizontal polarization. $\delta\theta$ is the azimuthal rotation error between the HWP and QWP due to potential offsets of the two rotation stages. We noticed that the power-measurement efficiencies were slighly different at the two orthogonal basis states; $P_{e(o)}$ quantifies these differential incident optical powers. The fit parameters are $\{\phi_H = 3.1872\text{rad}, \phi_Q = 1.6292\text{rad}, \delta\theta = -0.0137\text{rad}, P_d = 4.6423 \times 10^{-6}, P_{0,T} = 2.6829, P_{0,R} = 2.6741\}$. The 95 % confidence intervals for ϕ_H, ϕ_Q, and $\delta\theta$ are less than 1.0×10^{-4} rad. The corrected instrument matrix is

$$\mathbf{A}_\mathrm{C} = \begin{bmatrix} 0.5000 & 0.5000(0) & 0.0000(1) & 0.0000(3) \\ 0.5000 & -0.5000(0) & 0.0000(1) & 0.0000(3) \\ 0.5000 & -0.0032(1) & 0.5006(0) & -0.0124(3) \\ 0.5000 & -0.0032(1) & -0.5006(0) & 0.0124(3) \\ 0.5000 & 0.0296(0) & 0.0129(3) & -0.4990(0) \\ 0.5000 & -0.0296(0) & -0.0129(3) & 0.4990(0) \end{bmatrix}. \tag{3.13}$$

Note that the absence of the uncertainty in the first column in Equation 3.13 is attributed to exact number of the element in the first column and first row of the Mueller matrix of our polarimeter in Equation 3.7. The zero in parentheses means that the statistical uncertainty is smaller than the smallest digit of the mean value shown in Equation 3.13. The standard deviation of the instrument matrix is based on the uncertainty (i.e., 95 % confidence intervals) of the least-squares fit to the mean value of the twenty separate power measurements. This means, the standard deviations of the measured powers presented as error bars in Figure 3.13 are not taken into account for estimating the fit parameters. To test repeatability, we performed the calibration process five times after repositioning the robot arms from different initial poses: the relative variation of the extracted phase-retardance was measured to be less than 0.2 %.

We performed Monte-Carlo analysis to estimate the total polarization measurement uncertainty including both phase-retardance error of the waveplates and motion-induced

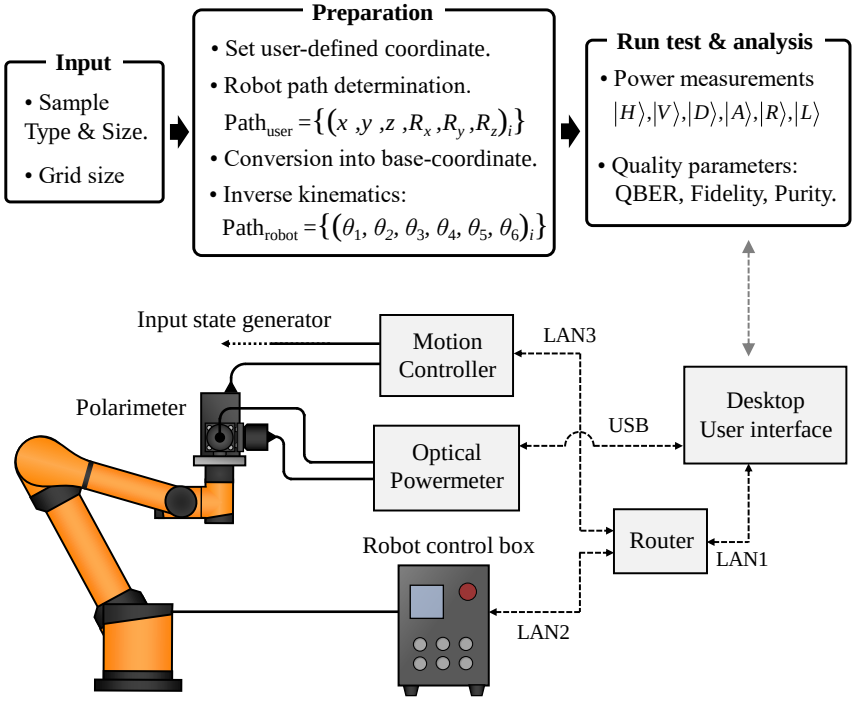

Figure 3.14: Polarization-test procedure and the control system. A polarimeter attached on a six-axis collaborative robot arm follows the output lights and analyzes the output polarization state. The polarization test processes are fully automated by the custom-built control software.

polarization error, incorporating the measured values of ϕ_H and ϕ_Q. We adjusted the thickness of the waveplates to match the phase retardance to the experimentally obtained values ($\phi_H = 3.1872$rad and $\phi_Q = 1.6292$rad). We sampled one hundred thousand uniformly distributed random values for the robot arm's orientation error from $\alpha, \beta, \gamma \in$ (-1°,+1°) and obtained root-mean-square quantum state fidelity deviation and QBER of 0.01 % and 0.05 %, respectively.

3.3.6 Control software

A general procedure of the polarization test and the interfaces of the characterization setup are depicted in Figure 3.14. For each sample, a user must input parameters such as sample size, grid size, and directory to save the data. From the sample size and grid size values, an optimal path is calculated and an array of positions is generated in a user-defined

coordinate system, which is then transformed into the base coordinates. The positions and orientations in the base and sensor coordinates are converted to a series of joint angles via an inverse kinematics solver and fed into the robot arm controller.

First generation

The first generation of the control program was scripted in a high-level, widely known programming language such as Matlab. It was used to operate the system with the DOAPs. As shown in Figure 3.15, for each input polarization, the robot will scan through each position, taking 5–10 power measurements at each of the six different polarization measurement settings. After this entire process has been completed, polarization state tomography is applied to the results from power measurements at every grid position. The outcome of this analysis will present the measured polarization states with fidelity, purity, and QBER. All rotational stages for the input polarizer, the wave plates, as well as small optics stage, are controlled by a single motion controller (XPS-Q8, Newport). We developed software tool kits in Python for the communication to three different devices: the motion controller, six-axis robot manipulator, and optical power meter (2936-R, Newport). Then, the Matlab script calls the Python class to control the device and performs post-processing, e.g., polarization state reconstruction and error analysis, on the measured results.

Second generation

Our second generation of the program was motivated to include two features. First, it allows real-time monitoring of the position and orientation of the robot arm by GUI programmed in C++ with Qt designer. The procedures for defining a user-defined coordinate system and calibrating the HPIP become much simpler thanks to the convenient interface of reading and writing the robot's coordinate and the angle of the rotation stages. Secondly, real-time control of the scientific CMOS camera significantly reduces the measurement time. The program monitors the total intensity being detected by the camera, and performs the polarization measurements only when the intensity is greater than a preset threshold value. If it is below the threshold, the robot moves to the next position. Also, the auto-exposure time control ensures maintaining good signal-to-noise ratio during the measurement. Finally, the captured images are post-processed during the test to output and store only the mean values and the standard deviations for the measured powers and centroids, which requires less storage of intermediate data.

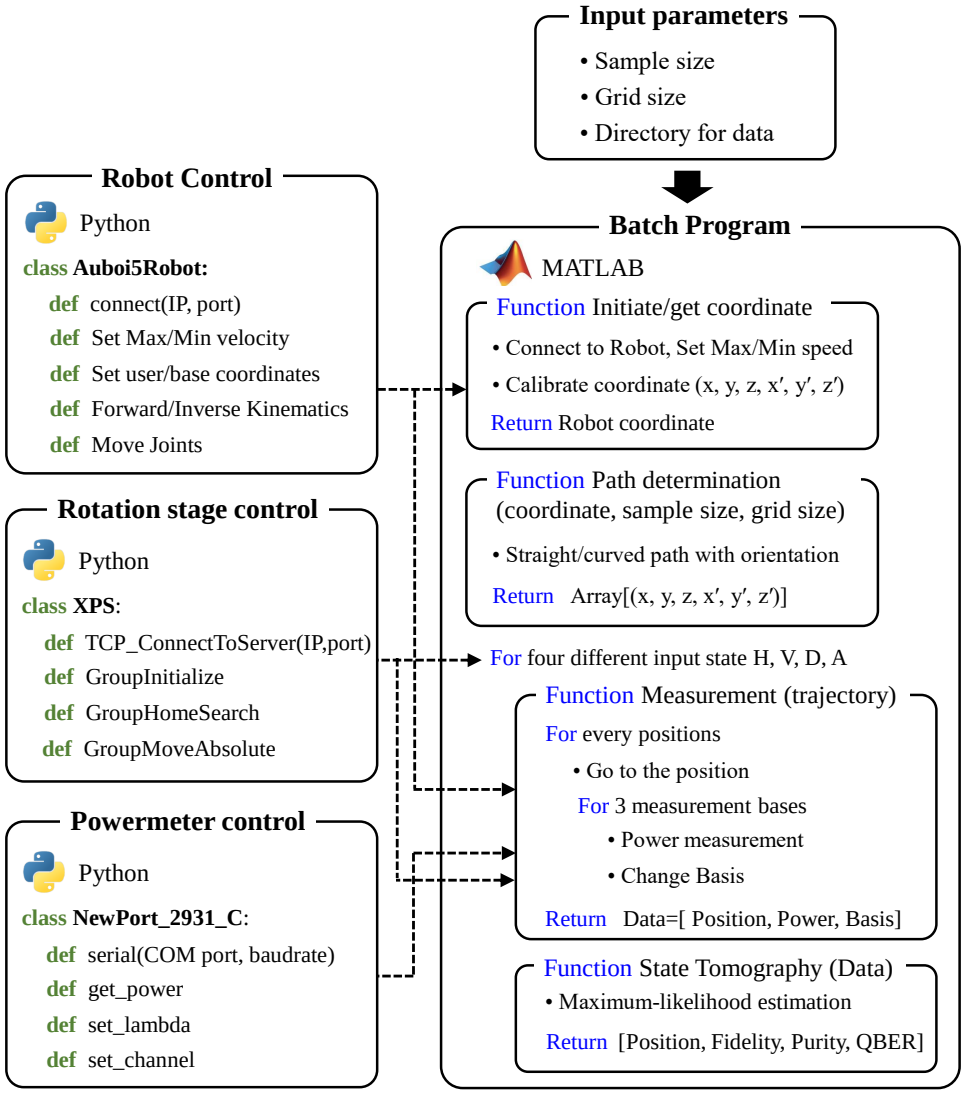

Figure 3.15: Functional block diagram of the control program for polarization tests. The main program is scripted in Matlab, which calls functions from Python class for the control of robot arm, rotational stage, and optical power meter. The Matlab script automates the entire system including taking measurements and analyzing data.

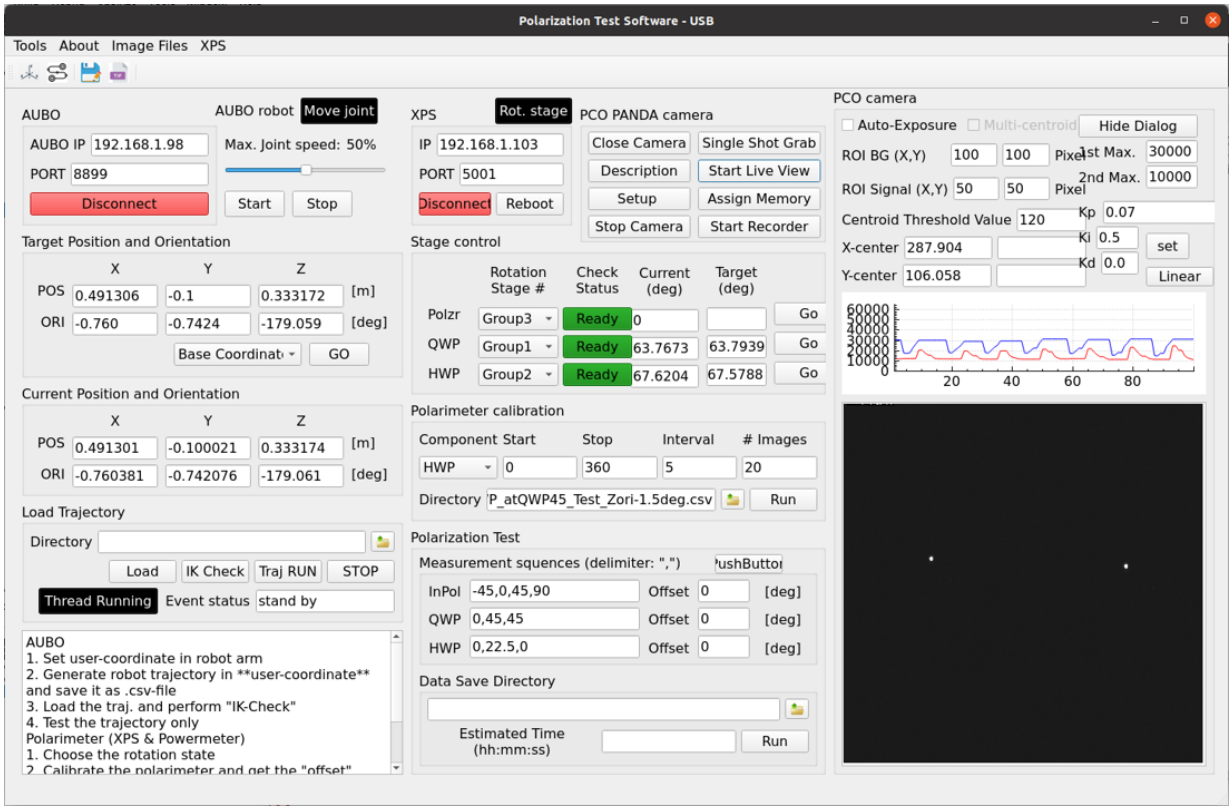

Figure 3.16: A screenshot of the upgraded control software for the polarization characterization system using HPIP.

3.3.7 Experimental setup

Figure 3.17 shows our optical configuration to perform the polarization tests on four different optics: small reflective optics, large lens, telescopes, and concave mirrors. First, as for small reflective optics, we characterized the polarization maintenance as a function of the incident angle by rotating the test optic in evenly sized increments with a fixed incident beam direction. The robot arm moves the polarimeter to track the reflected light from the test optics in an arced path, and polarization measurements are performed at each incident angle, as shown in Figure 3.17(a). We ensure that the light path and the rotational axis coincide such that the arced path is simply defined by the radius from the center of the test optic to the center of the end effector. The radius is then measured by a laser-distance measurer. Given a set of incidence angles and the radius, the program could simply determine the robot arm path by converting from polar coordinates to Cartesian

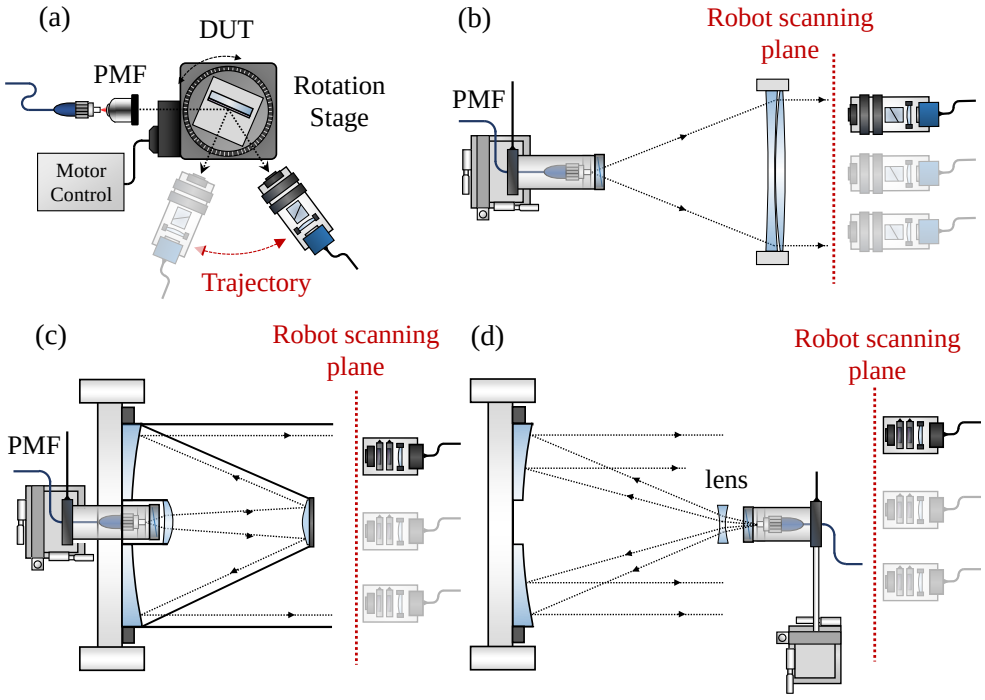

Figure 3.17: A schematic diagram of the experiment setup. (a) Angle-dependent polarization charaterization on the reflective optics; PMF, polarization-maintaining fiber. Polarization tests for (b) a large lens (20.3 cm diameter) with the fixed angle of incidence, (c) afocal Schmidt-Cassegrain telescope (26 cm diameter), and (d) its primary mirror.

coordinates. The quality parameters, e.g., state fidelity, purity, and QBER, are derived from the measured data, and polarization maintenance is examined at various incident angles.

As for the large test optics, we placed a polarization-maintaining fiber at the focal position of the test optics, producing diverging light with well-defined polarization states. Characterization of the input polarization states of the diverging light can be achieved by a similar method to the angle-dependent polarization test as in the test for small optics; the polarization measurements are taken in an arced path around a stationary diverging beam. The test optics produces a large collimated light, the cross section of which is discretized with an evenly-spaced 15×15 section grid for the polarization measurements. The robot arm scans the polarimeter through all 225 positions at a given input polarization in the transverse direction (as in a raster scan) to perform the tomographic measurement across the entire output beam, as shown in Figure 3.17(b)–(d). The whole 2-dimensional scan is

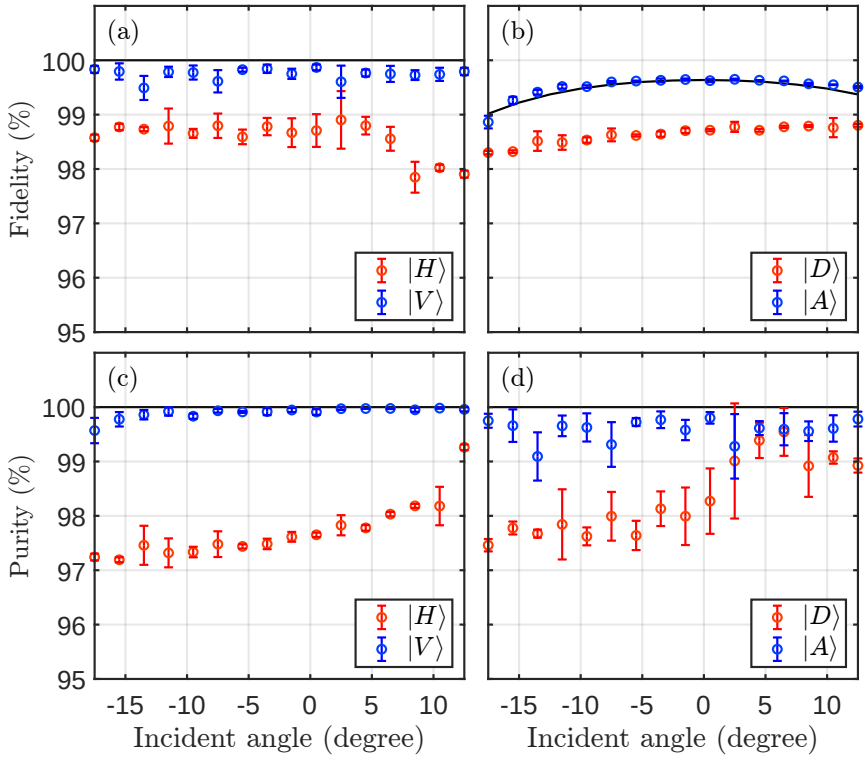

Figure 3.18: Polarization characterization for the test optic of an 2.54 cm pentaprism. (a)–(b) The fidelity and (c)–(d) purity are measured for incident horizontal $|H\rangle$, vertical $|V\rangle$ states, diagonal $|D\rangle$, and anti-diagonal $|A\rangle$ states. Black solid lines are the theoretical curve obtained from the 3D polarization ray tracing.

repeated for four different input polarization states. Since all power measurements at six orthogonal polarization bases are performed at a position, and then the robot arm moves the polarimeter to the next position, the ensemble average of the quality parameters, e.g., fidelity and purity, over the measured area represent the performance lower bound of the test device and the standard deviation includes the position and orientation error of the robot arm. The scanned area also includes the corners and the secondary mirror of the telescope where no light is expected. These sections are not included in the analysis. As for the test for the primary mirror of the telescope, we disassembled the secondary mirror and the spider, and located the fiber launcher at the focal plane of the primary mirror. Our wavefront characterization system is utilized to ensure the collimation of the output beam.

Table 3.2: Characterization of incident polarization states for the test on pentaprism and glass plate with DOAP-v1. Such unphysical values are the result of experimental imperfection and statistical fluctuations (further described later in the text)

Input state	Fidelity (%)	Purity (%)	QBER (%)
$\|H\rangle$	99.20 ± 0.01	99.21 ± 0.16	0.80 ± 0.01
$\|V\rangle$	99.86 ± 0.01	100.88 ± 0.15	0.14 ± 0.01
$\|D\rangle$	99.10 ± 0.01	98.42 ± 0.16	0.81 ± 0.01
$\|A\rangle$	99.89 ± 0.01	99.98 ± 0.11	0.12 ± 0.01

3.3.8 Test results with division-of-amplitude polarimeters

Pentaprism and glass plate

We performed angle-dependent polarization tests on a pentaprism and a glass plate. The pentaprism provides the simplest test procedure because the output light is always deflected 90° to the incident light, which means that the position and orientation of the robot arm are fixed during the test. This test is expected to show the stability of the polarization characterization system with the static pose of the robot arm, as well as the quality of the coordinate alignment procedure. On the other hand, the polarization states of the reflected light from a glass plate can be analytically calculated by the Fresnel equations. Our custom-built three-dimensional polarization raytracing program [315] was used to estimate the state fidelity and purity after the reflection from the pentaprism and glass plate as a function of incidence angle.

We first characterized the four incident polarization states $|H\rangle, |V\rangle, |D\rangle, |A\rangle$ by using a collimated laser light at 785 nm wavelength with $1/e^2$ beam diameter of 1.2 mm. The results are summarized in Table 3.2. In this test, we used DOAP-v1, and the polarization extinction ratio is about 1000:1 which is the main limiting factor for the measurement precision. More importantly, the extinction ratio of the reflection port is an order of magnitude worse than the transmission port, which is clearly observed by the measured QBERs for $|V\rangle$ and $|A\rangle$ being slightly better than $|H\rangle$ and $|D\rangle$.

Figure 3.18 shows the fidelity and purity of the polarization states measured for the reflected light from the pentaprism (CCM1-PS932, Thorlabs). For each rotation angle of the pentaprism and the polarization measurement basis setting, we repeated the power measurements five times. The mean and standard deviations were used for state tomography to examine the polarization maintanence. The test pentaprism is made of N-BK7 with aluminum coated on the two reflection surfaces. From the refractive index of the aluminum

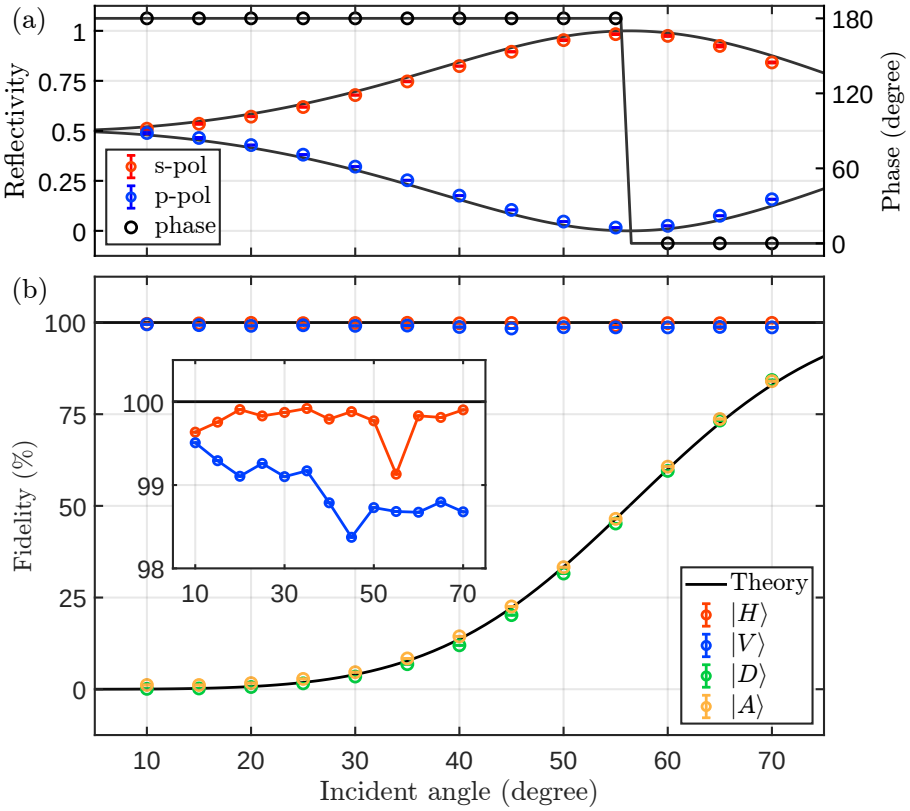

Figure 3.19: Polarization-test results on a glass plate. (a) Polarization-dependent reflectivity of s- and p-polarizations. (b) Quantum state fidelity for the four incident states. For the theoretical curve presented in black lines, we assumed the refractive index of the glass plate to be 1.5.

coating [205], we calculate the output polarization state by using our polarization raytracing program. In Figure 3.18, black lines indicate the theoretical values of the fidelity and purity as a function of the incident angle. An excellent agreement with experimental results is observed particularly for the $|V\rangle$ and $|A\rangle$ state, and the discrepancies for the other polarization states are mainly attributed to the poor extinction ratio of the reflection port of PBS.

Figure 3.19(a) shows the experimentally measured reflectivity and the theoretical curve for s- and p-polarizations of a 25.4 mm×76.2 mm×1.02 mm microscope glass plate. We aligned the $|H\rangle$ and $|V\rangle$ states to be the p- and s-polarizations, respectively, and measured the optical powers of the reflected light with the six polarization measurement settings.

The angle-dependent reflective coefficients at the interface between two different optical media, i.e., air and glass, for s- and p-polarizations are given by the Fresnel equations

$$\begin{aligned} r_p &= \frac{n_1 cos\theta_1 - n_2 cos\theta_2}{n_1 cos\theta_1 + n_2 cos\theta_2}, \\ r_s &= \frac{n_1 cos\theta_2 - n_2 cos\theta_1}{n_1 cos\theta_2 + n_2 cos\theta_1}, \end{aligned} \tag{3.14}$$

where θ_1 and θ_2 are the angle of incidence and refraction, respectively. n_1 and n_2 are the refractive indices of the two materials. The measured optical power $P_{H,V}$ for $|H\rangle$ and $|V\rangle$ states are normalized by the total power $P_V + P_H$, and the relative phase shift between the $|H\rangle$ and $|V\rangle$ states was obtained from the reconstructed output polarization states via polarization state tomography. The theoretical curves of the normalized reflectivity for the s- and p-polarization and the phase shift were calculated from the absolute square of the reflective coefficients, i.e., $|r_{s,p}|^2/(|r_s|^2 + |r_p|^2)$, and the Brewster's angle, respectively. At Brewster's angle, the sign of the reflective coefficient for p-polarization is flipped; the relative phase value is changed from 180° to 0°.

Figure 3.19(b) shows that the measured fidelity for the four incident polarization states are in good agreement with theoretical curves. We observed that the $|H\rangle$ and $|V\rangle$ states are well preserved as they are aligned to p- and s-polarizations. And, as shown in Figure 3.19(a), the reflectivities of the two states converges to 50 % as the incident angle becomes close to zero and there is a relative π–phase shift upon reflection. This indicates that the incident $|D\rangle$ and $|A\rangle$ states are expected to become their orthogonal states after reflection at normal incident angle. Indeed, the state fidelity for $|D\rangle$ and $|A\rangle$ was measured to be close to zero at small incident angle. The 50 % fidelity at around the 56° incident angle is attributed to the perfect transmission and reflection for p- and s-polarizations at the Brewster's angle, which also appears as a slight fidelity drop for the $|H\rangle$ state (see the inset of Figure 3.19(a)). Reproducing the analytic curve for the case of air-glass interface with the experimental results validates our methodology of the angle-dependent polarization characterization.

Quantum satellite payload telescope (HON-T) and its primary mirror (HON-M)

We now turn our attention to the polarization characterizations of the prototype telescope HON-T and its primary mirror HON-M developed for the QEYSSat quantum payload. Here, we use the DOAP-v2: the division-of-amplitude polarimeter with two thin film polarizers inserted at both outputs of the PBS.

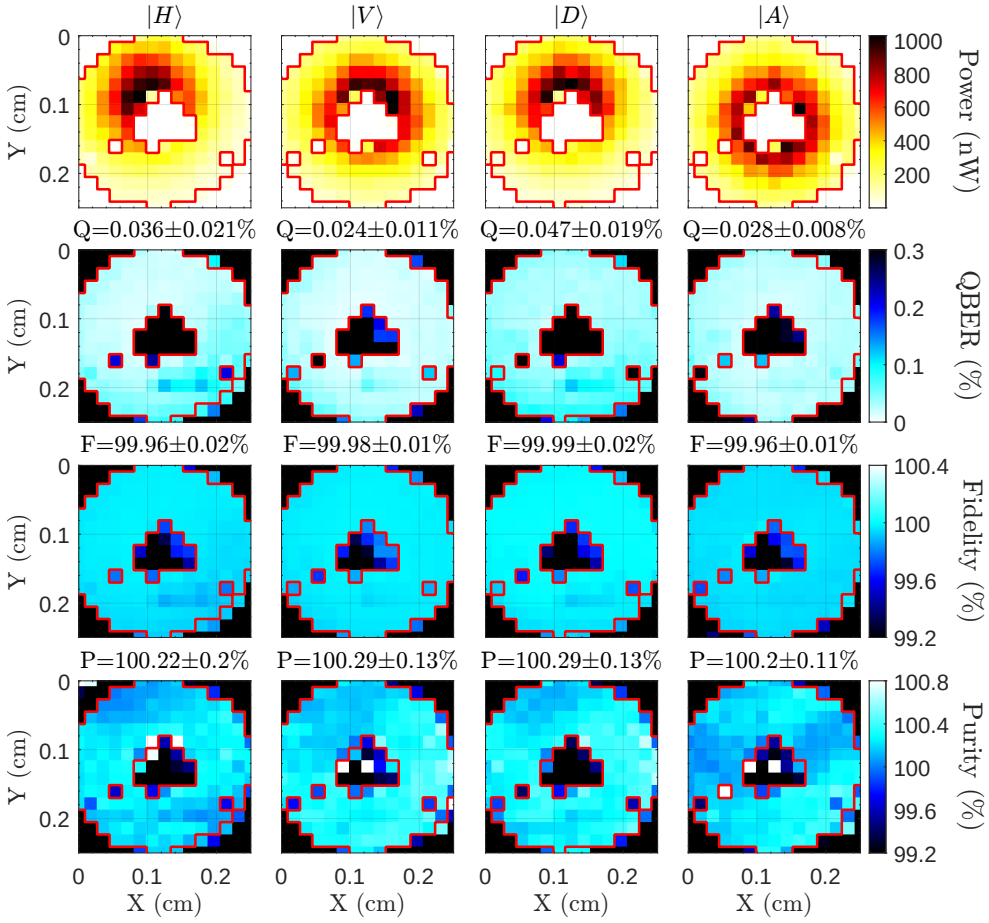

Figure 3.20: Polarization-test results for a prototype satellite payload telescope (HON-T). The color maps show the measured optical power, the quantum bit error rate (QBER), the quantum state fidelity, and the purity for four input polarization states: $|H\rangle, |V\rangle, |D\rangle, |A\rangle$. The areas enclosed with solid red lines indicate the sections where the measured optical power is greater than 50 nW. We calculate the ensemble averaged values of the fidelity, purity, and QBER within these areas.

Figure 3.20 shows the polarization test results for the HON-T via color maps of the power, QBER, fidelity, and purity for each input polarization state. The region marked with red lines indicates the area in which the quality parameters are averaged. The outcome of this test shows great polarization maintenance as the ensemble averaged fidelities for all four input states are above 99.9 %. The promising result of QBER less than 0.05 % indicates that our prototype telescope is suitable to be deployed for the free-space QKD

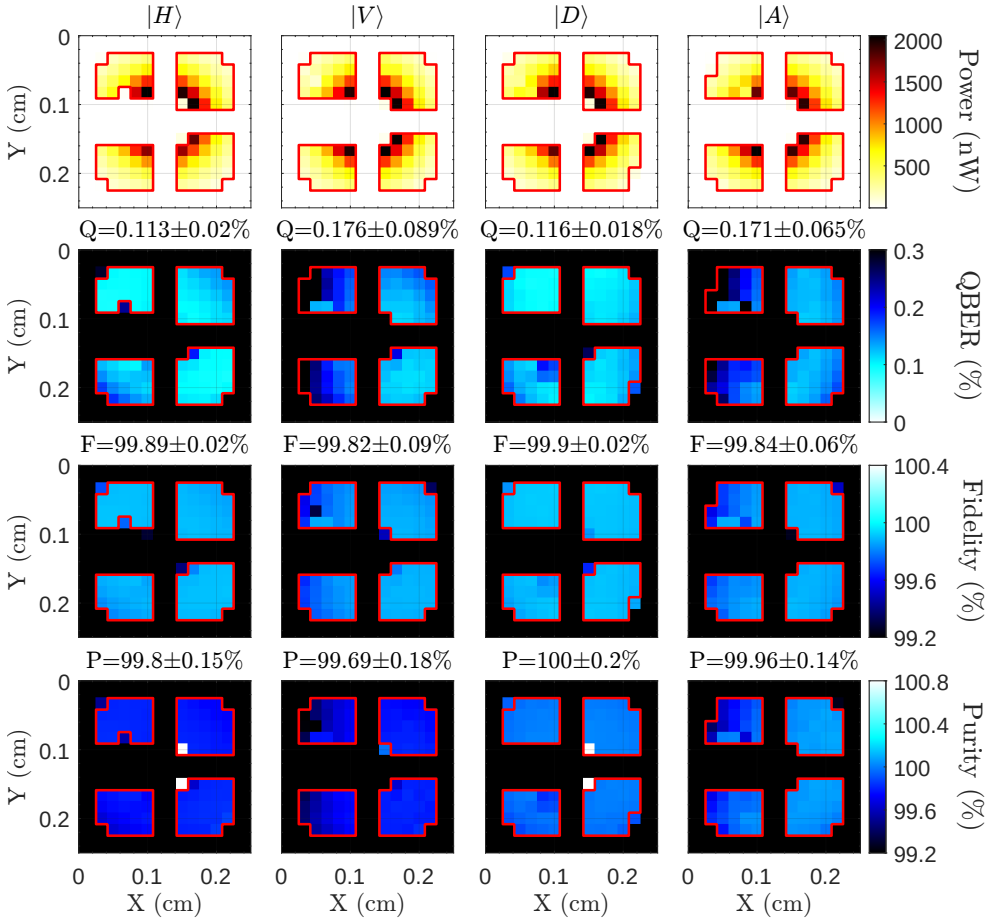

Figure 3.21: Polarization-test results for the primary mirror (HON-M). The color maps of the optical power, the quantum bit error rate (QBER), the quantum state fidelity, and the purity. The sections in which the measured power above the threshold power of 100 nW are considered for the calculation of the ensemble averaged values of the quality parameters.

experiment. The standard deviations for the fidelity and QBER are less than 0.03 %, which demonstrates good precision of our polarimetry using the robot arm.

Figure 3.21 shows the test results for the HON-M. We perform the test only for the selected four sections of the mirror in order to reduce the time for the polarition test. The average fidelity and purity are measured to be 99.86±0.03% and 99.86±0.09%, respectively, and the average QBER is measured to be 0.14±0.03%. The observed polarization maintenance for the primary mirror is slightly worse than the whole telescope assembly.

This may be mainly attributed to the background noise that can be easily captured within the FoV of the concave mirror. Since our blackout enclosure has an aperture wider than the telescope diameter, we noticed that there was significant stray light coming from our control computer which was located behind the robot arm.

3.3.9 Test results with high-precision imaging polarimeter

Commercial off-the-shelf silver-coated mirror (COTS-M)

We measured the polarization states of the reflected light from a 10 cm–diameter protected silver-coated mirror (COTS-M) as a function of the reflection angle. Collimated light with 4 mm $1/e^2$ beam diameter was sent to the center of the mirror. The horizontal and vertical states of the input polarizations were aligned to p- and s-polarizations of the mirror, respectively. We rotated the mirror to vary the reflection angle from 5° to 52.5°, and the robot arm follows the reflected beam in an arced path. The trajectory was defined by the measured radius from the center of the mirror to the center of the end effector with a laser-distance measurer. At each angle, twenty frames were captured to calculate the mean and standard deviation of the measured powers and centroids while maintaining SNR above one hundred. The full scan of the polarization test was repeated four times for statistical certainty.

Figure 3.22(a) shows the variation of the AOI to the polarimeter during the test. AOI variation was maintained within ±0.2°, indicating good coordinate alignment and excellent repeatability. As shown in Figure 3.22(b), the averaged purity and fidelity for horizontal and vertical input polarization states are maintained above 99 % over the entire reflection angle range, indicating good alignment of horizontal and vertical polarization states to the s- and p-polarizations of the mirror.

The polarization-dependent reflectivity of the protected silver mirror can be accurately calculated by multilayer coating calculations [303]. It is expected that the comparison between experimental data and theoretical prediction validates our methodology, i.e., the usage of robot arm to move the polarimeter for angle-dependent polarization characterization. We modeled the protected silver film with a 92 nm–thick SiO_2 layer coated on top of a 1 µm-thick silver layer. The transmissive and reflective coefficients of the s- and p-polarizations were calculated by a conventional optical admittance method [75]. The coefficients were then used to obtain the polarization states of reflected light. In Figure 3.22(b), black lines indicate theoretical values of fidelity and purity as a function of reflection angle. We characterize a closeness between theory and experiment by the standard error of regression SER = $\sqrt{\sum_{i=1}^{n}(y_i - f(x_i)^2/(n-k)}$ with k denoting the number

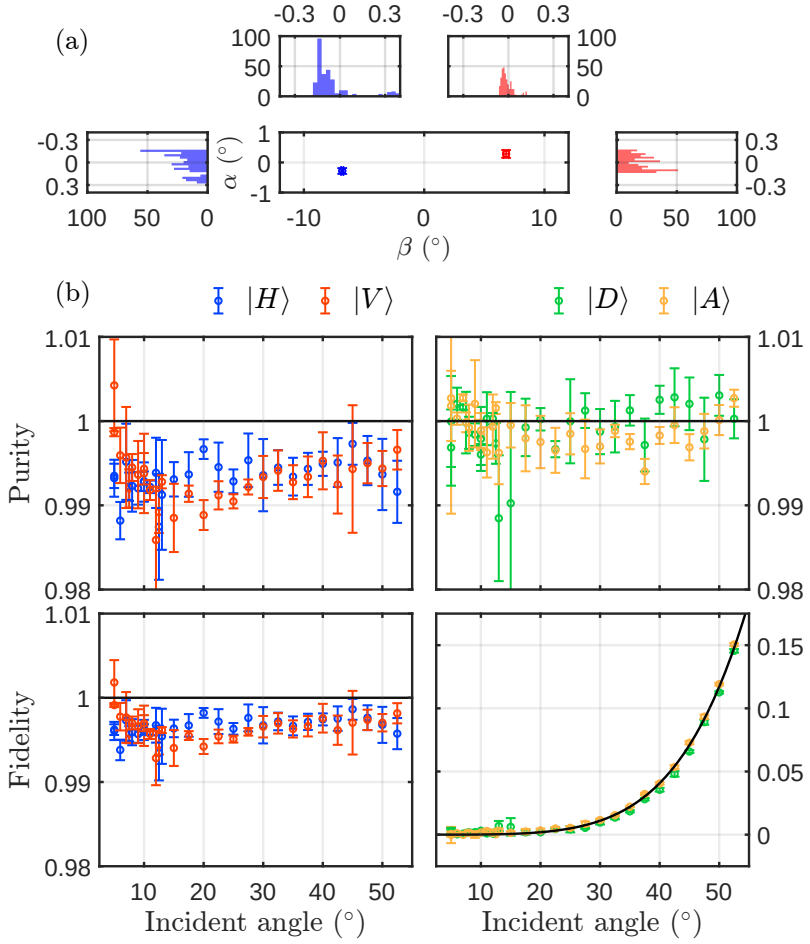

Figure 3.22: Experimental results from the angle-dependent polarization characterization on the protected silver-coated mirror (COTS-M). (a) The variation of the measured AOI. (b) The fidelity and purity of the measured polarization states for incident horizontal $|H\rangle$, vertical $|V\rangle$ states, diagonal $|D\rangle$, and anti-diagonal $|A\rangle$ states. Circles show the measured data and solid black lines indicate theoretical predictions based on multilayer thin-film coating calculations.

of free parameters for the theoretical model. In our case, we consider the thickness of SiO_2 and silver layer as free parameters, and thus $k = 2$. Here, y_i and $f(x_i)$ are the measured and theoretically prediected values, respectively. We calculated SER of fidelity being better than 0.4 % for all four input polarization states, showing the excellent agreement between theory and experiment.

Table 3.3: Median values of the fidelity, purity, and QBER for the transmitted polarization states from the 20.3 cm custom-designed len. Lower and upper quartiles are listed in parantheses.

Input state	Fidelity (%)	Purity (%)	QBER (%)
$\|H\rangle$	99.60	99.59	0.40
	(99.01,99.73)	(99.53,99.70)	(0.27,0.99)
$\|V\rangle$	99.68	99.79	0.32
	(99.03,99.84)	(99.44,100.00)	(0.16,0.97)
$\|D\rangle$	99.55	99.50	0.35
	(98.99,99.70)	(99.38,99.56)	(0.19,0.97)
$\|A\rangle$	99.52	99.42	0.42
	(98.97,99.68)	(99.27,99.51)	(0.28,1.01)

In our experiment, the density matrices of measured polarization states are reconstructed by calculating the Stokes vector that is normalized by the total intensity averaged over three different polarization measurement bases. As we used collimated light with beam diameter of 4 mm and set the pin-hole size to be 2 mm, any positional instability while rotating the waveplates causes total intensity variation. This effect may yield unphysical quantum states whose purity is greater than unity, as seen in Figure 3.22(b). This issue can be resolved by either larger pinhole size or other alternative tomographic reconstructions such as the maximum likelihood estimation.

Quantum optical transmitter component (IQC-L)

We characterize the polarization maintenance of our IQC-L developed for the quantum optical ground station. We applied the same method as in the test for the telescope and primary mirror. We placed an optical fiber at the focal position of the IQC-L which produces diverging light with well-defined polarization states. The lens outputs large collimated light with fixed direction and position. We added a 20 cm–diameter mask in front of the lens to block stray light because the numerical aperture of the fiber used in the experiment was larger than the lens. We ensured that the transmitted light was collimated with divergence angle less than ± 10 µrad measured by our aberration characterization system.

Figure 3.23(a) shows the variation of measured AOI during the polarization test. It was observed that the AOI to the polarimeter was maintained within $\pm 0.5°$. The measured purity and fidelity are presented in the color maps shown in Figure 3.23(b). We discarded values where the incident light is too weak to be detected with the exposure time greater

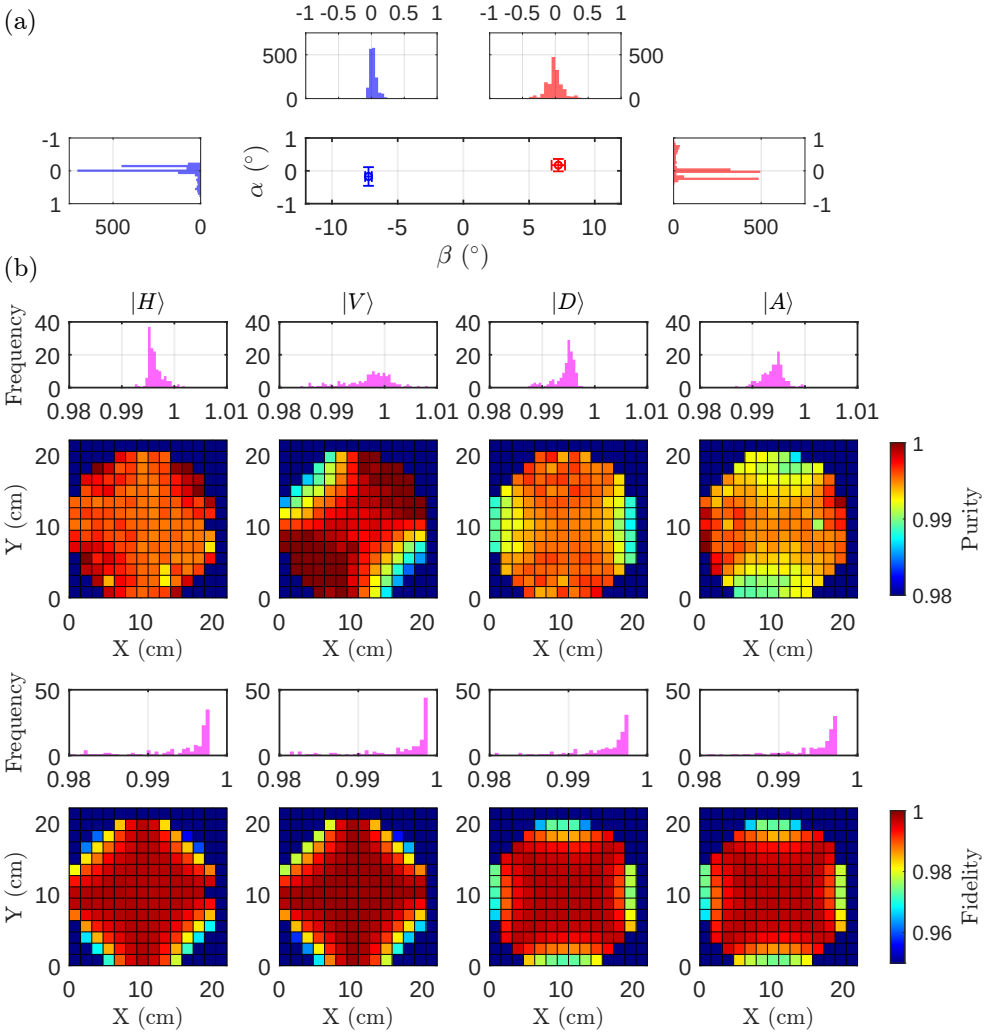

Figure 3.23: Polarization-test results for a 20.3 cm custom-designed achromatic doublet (IQC-L). (a) The variation of the measured AOI. (b) The color maps of fidelity and purity of the measured states for incident horizontal $|H\rangle$, vertical $|V\rangle$, diagonal $|D\rangle$, and anti-diagonal $|A\rangle$ states.

than 100 ms. Histograms of remaining values indicate the uniformity of transmitted polarization states across the aperture. QBERs for the four incident polarization states were directly calculated from the raw power measurements. The median and quartiles of the three quality parameters, i.e., fidelity, purity, and QBER, are listed in Table 3.3. The outcome of this test shows great polarization maintenance as the typical fidelities for all

four input states are greater than 99.5 %. The promising result of the QBER less than 1 % indicates that the lens is suitable for the free-space QKD experiment.

It is worth noting that the high-fidelity region shows a "cross-mark" feature on the color maps. This feature seemingly depends on the input polarization states; plus–sign in horizontal and vertical state and X–shape in the diagonal and anti-diagonal input states. In our setup, the input polarization states are defined by the rotation of the polarizer and the fiber together, and the high fidelity region is correlated to this rotation angle, indicating that the high- and low-fidelity region may not be attributed to the quality of the test optic, but rather by the uniformity of the input polarization state across the lens aperture. The reason for the imperfect state preparation with the polarized diverging beam will be further investigated. The full characterization for the instrumental polarization of the lens can be performed by directly characterizing the input states with the same polarimeter and comparing the results as in Mueller-matrix polarimetries [20].

3.4 Chapter summary

The first part of this chapter presents the development of a practical characterization system for optical aberrations of free-space quantum communication optics. The direct measurement of local wavefront slopes across output aperture of the test optic identifies the collimation of the transmitted light. We performed a proof-of-principle experiment for a linear measurement of the transmitted wavefront and analyzed the measurement apparatus using a three-dimensional raytracing method. The test optic was chosen to be 20.3 cm diameter achromatic doublet developed for the QEYSSat mission. With sufficiently redundant measurements and statistical analysis, it was shown that our wavefront-measurement system exhibits the precision better than 0.01λ. We compared the measured wavefronts with the theoretical predictions and excellent agreement between the two results validates our methodology.

Our transverse linear measurement apparatus can be implemented at reasonable costs. The simple optical configuration requires minimal efforts for alignment, yet the system performs excellent stability and precision to characterize aberrations of large collimators. The wavelength range of our measurement setup is limited by the spectral sensitivity of the camera which can be switched without major modifications. We believe our practical test platform for characterizing aberrations is a useful tool for both scientific and industrial applications in diverse fields including optical satellite communications and astronomical observatories.

The second part of this chapter describes our robotized polarization characterization platform for optical devices in free-space quantum communications. Our system can easily be adjusted for performing polarization tests on diverse reflective or refractive optical systems with a wide range of aperture sizes (up to 30 cm), and either curved or flat surfaces at consistently high precision. We developed two different polarimeters: the DOAP and HPIP. The DOAP-v2 performs better than the HPIP in terms of the measurement precision. It was capable of measuring QBER less than 0.04 %. On the other hand, the HPIP is capable of monitoring the variation of incident angle, and thus the misalignment due to the robot's motion can be detected. This could even be used for implementing a feedback mechanism to correct the polarimeter's position and orientation in the future. The precision of the HPIP was mainly limited by the dynamic range and signal-to-noise ratio of the power measurement.

The measurement apparatus can be readily set up in outdoor and used for deployed systems. The characterization process is fully automated once the robot's coordinate system is calibrated. We presented our theoretical analysis of the polarization measurement error caused by the tilt and rotation of the polarimeter, and showed that the misalignment of the polarization axis due to the azimuthal rotation is a dominant measurement error. This rotation error could be detected and compensated by injecting more incident states to fully characterize the change of the polarizations, as in conventional Mueller-matrix polarimetries. It is also worth noting that the input polarization states can be directly characterized in our system, and therefore the precision of the polarization characterization of the test optic is limited by the measurement device.

We performed polarization tests on various optical elements including a pentaprism, microscope glass plate, protected silver-coated mirror, telescopes, large concave mirror and lens. The angle-dependent polarization characterization for the small reflective optical elements validated our test system with excellent agreement between the test results and theoretical predictions. The polarization characterization on the prototype optical components for the QEYSSat mission provided a lower bound of the performance of the test optics, which includes imperfection of the input state preparation. In our setup, the standard deviation from the ensemble-averaged value for the test optics takes into account various systematic errors, e.g., the robotic motion, waveplate rotation, beam collimation, optical power readout, etc.

Our polarization characterization clearly demonstrates the viability of using an industrial robotic manipulator to study large optical components and systems. Our theoretical model and experimental demonstration showed that the motional precision achieved is sufficient to draw robust conclusions from the optical measurements. Although not presented here, the telescope assembly IQC-T exhibited transmitted wavefront error less than 0.04λ

RMS-value, and polarization-preservation with the state fidelity greater than 99.5 % [212]. We believe that our robotized polarization characterization platform could therefore also support the development of free-space optical components or terminals for a broad range of applications including laser communications, lidars, and astronomical observatories.

Chapter 4

Quantum frequency transducer for single-photon quantum communications with satellites

In this chapter, we present the development of quantum frequency transducers (QFTs) using two different optical media: a silicon nitride ring resonator and a photonic crystal fiber. We describe designing and analyzing ring resonators via numerical simulations of optical nonlinear phenomena which provide thorough assessment to device performance. We perform a theoretical analysis and experimental demonstration of the frequency translation using a photonic crystal fiber and discuss our preliminary results as well as future works.

Statement of contributions

- **Quantum frequency translation using a silicon nitride ring resonator**
  The presented research was in collaboration with Dr. Robin Williams's group at National Research Council Canada (NRC). The project was conceived by Prof. Thomas Jennewein. I carried out numerical simulations for designing and analyzing ring resonators. Dr. Robin Williams provided information about silicon nitride materials and specifications of quantum dot single-photon sources developed at NRC.

- **Quantum frequency translation using a photonic crystal fiber**
  Prof. Thomas Jennewein and I conceived the idea of using a photonic crystal fiber. I

carried out the analysis for the performance assessment, procured prerequisites, and conducted the experiment.

4.1 Introduction

4.1.1 Quantum frequency transducers

QFT is a quantum photonic device which translates the frequency of an electromagnetic field to the desired frequency while preserving other quantum information. The idea was first proposed by Prem Kumar in 1990 [162] and demonstrated by the same group two years later [126]. They used sum-frequency generation process in a $\chi^{(2)}$ medium and showed the preservation of nonclassical intensity correlation of squeezed light. Over the past decades, there has been growing interest in the development of highly efficient, low-noise, and scalable QFTs for various applications.

The first QFT-assisted quantum device was frequency up-conversion single-photon detectors for photons at telecom wavelengths as quantum key distribution (QKD) became more advanced and even commercialized in fiber-optic networks [291, 231, 232, 195, 178]. Later on, QFTs were used to interface optical fiber channels with different quantum light sources such as single-photon sources [232, 139, 265, 219] and paired photon sources [136, 138, 202]. Recent technological advances made it possible to transfer photonic quantum information to matter qubits for storage and processing [201, 137, 202, 296, 267, 69, 314]. Furthermore, it has also been shown that a QFT can be used for photonic quantum information processing in frequency domain [159, 64, 150]. Other interesting applications are the generation of quantum states of light [25, 24] and the enhancement of measurement precisions [319].

QFTs are typically made of optical nonlinear media where frequency translation process is driven by one or two strong pump fields. Unlike parametric amplification processes such as photon-pair generations where the pump fields amplifies photonic excitations, here in QFTs the pump fields mediate energy exchange between input signal and output target frequency modes. Indeed, the frequency translation process is mathematically expressed as a beam-splitter operation, i.e., coherent mode conversion. Therefore, in principle, noise-free frequency translation with unity efficiency can be achieved.

Two of the most popular schemes have been sum-frequency generation and four-wave mixing Bragg-scattering (FWM-BS) processes [204] using $\chi^{(2)}$ (second-order) and $\chi^{(3)}$

(third-order) optical nonlinear media, respectively. With the mature technologies of ferroelectric domain engineering in $\chi^{(2)}$ media such as periodically-poled lithium niobate (PPLN), the former method has been utilized more commonly than the latter and its typical conversion efficiency ranges from 50 % to 90 %. One problem is that the pump wavelength rapidly increases as the signal and target wavelengths get closer to each other. For example, the wavelength conversion from the input signal at 985 nm to target wavelengths at 785 nm via sum-frequency generation requires the pump field at the wavelength of 3866 nm. To address this issue, FWM-BS has become a popular method lately. In FWM-BS, the energy exchange between input and target photons is obtained by coherent (Bragg) scattering from the frequency beat between two pump fields, which provides flexibility of choosing the target wavelength. Recently, 97 % intraband frequency-translation efficiency was achieved via FWM-BS process using a 100 m–long dispersion shifted fiber [150].

A common challenge in QFTs is to strongly drive only the desired frequency-translation process while suppressing other unwanted nonlinear processes. For a given medium with its nonlinearity γ and length L, the unity conversion efficiency requires $\gamma PL \sim \pi$ with P denoting incident pump power. This means, one needs either a strong pump field or long interaction length. For example, a 500 m–long highly nonlinear optical fiber ($\gamma \sim$10 $\mathrm{W^{-1}\,km^{-1}}$) typically requires single pump power of around 100 mW. The requirement of the strong pump power could be relieved by either recycling the field inside an optical cavity [253] or reducing the mode area via waveguide structures [231, 5, 230, 195, 178]. As will be discussed later, both the cavity-assisted enhancement of optical nonlinearity and the tight localization of the guided fields can be achieved by integrated optical circuits such as ring resonators and photonic crystal waveguides [127, 293]. However, this strongly driven nonliear medium easily involves other unwanted processes, e.g., spontaneous Raman-scattering, which usually adds noise photons or decrease the conversion efficiency.

There has been significant progress in the development of QFTs with the great ambition of establishing a global quantum internet. Recently, Lu *et al.* proposed a scheme of using third-order sum-frequency generation for low-noise frequency up-conversion process, which allows using a single pump field at the long wavelength, thereby suppressing spontaneous Raman-scattered photons [191]. According to their analysis, 80 % conversion efficiency can be achieved with 50 mW pump light using a high-Q ring cavity. Another notable interesting approach for QFTs is a rapid adiabatic passage scheme for broadband frequency conversions [21, 74]. Also, there has been gradual progress to extend a frqeuency-translation range from optical domain to microwaves, which is mainly motivated by the networks of superconducting quantum processors with quantum optical channels [166].

4.1.2 Motivations

The development of QFTs presented in this chapter is mainly motivated by QKD over a ground-to-satellite quantum link using quantum dot single-photon sources (QD-SPSs).

Single-photon quantum key distribution

As discussed in Section 1.2.1, the complete operation of QKD requires a sequence of executions of the invoked protocol such as an authentication, photon transmission, and post processing. One of the most practical protocols is the decoy-state BB84 which allows using attenuated lasers with as high asymptotic key rate as the case of using single photons. However, for a ground-to-satellite quantum link, since the high photon loss and limited contact time reduce the size of sifted key, statistical fluctuations play a significant role in the parameter estimation during the post processing. To ensure unconditional security, one must take the maximum bound of the fluctuation to completely eliminate possible leakage of information to eavesdroppers, which reduces the length of the attenable final key. This reduction, so-called finite-size effect, turns out to be considerable in the case of using coherent pulse sources as each pulses includes substantial amount of multi-photons [49].

It has been conceived that single-photon sources could outperform weak coherent pulse sources under this condition thanks to their low multi-photon components. Single-photon QKD has been experimentally demonstrated in both optical fiber and free-space channels [9, 278, 118]. However, due to technological limitations such as low photon-extraction efficiency and residual multiphotons ("high" $g^{(2)}(0)$), the benefit of using single-photon sources in QKD had yet to be clearly demonstrated or actively investigated. The development of QD-SPS has been advanced to yield the generation rate higher than 100 MHz with the extraction efficiency higher than 80 % [299, 287, 71]. Recently, the QPL and our collaborators at NRC conducted an indoor experiment for proof-of-principle demonstrations using single photons generated by a semiconductor quantum dot (QD) embedded in a photonic nanowire. The experiment and theoretical analysis showed the enhancement of secure key rate by almost an order of magnitude [55]. Here, we aim to use the QD-SPS for our QEYSSat mission by translating the wavelength of emitted photons at 985 nm to around 785 nm.

Integrated silicon photonic circuits with single-photon sources

One of the exciting technological advances in QD-SPS is the capability of deterministic growth of quantum dots and its integration with a silicon photonic platform [316, 73, 71,

225]. It opens new synergistic opportunities for integrated quantum photonic devices using mature technologies in silicon photonics. Recently, our collaborators at NRC demonstrated a pick-and-place method for InAsP quantum dots using a nanomanipulator installed in a scanning electron microscope [211]. The pre-selected single quantum dots can be picked by a tungsten tip and placed on silicon nitride waveguides. QFTs based on a silicon nitride ring resonator can be integrated with QD-SPSs, thereby constructing on-chip wavelength-tunable single-photon sources.

Chip-scale optical elements have already been widely deployed in classical fiber-optic communications, such as phase- and amplitude-modulators and wavelength-multiplexers. Likewise, integrated quantum photonics will form the backbone of future quantum networks [301]. Nanophotonic devices provide features that cannot easily be attained in bulk optics, such as high optical nonlinearity and long interaction time. Also, their efficient integration with matter qubits, e.g., color centers in diamonds [298], could play a major role as on-chip information processors or quantum memories. At the time of writing this thesis, one of the notable major and national developments in this area is Quantum Foundry funded NSF's Quantum Leap Challenge Institutes program. Also, UK-Canada and Europe QLSI (Quantum Large Scale Integration with Silicon) projects invest to the development for the integrated quantum photonic devices. Researchers recently printed a roadmap which envisions large-scale integration of versatile and reconfigurable quantum photonic integrated circuits to be implemented in the next decade [217].

4.2 Theory of four-wave mixing Bragg-scattering in waveguides and ring resonators

In this section, we provide a theory of FWM-BS in waveguides and ring resonators. Figure 4.1(a) depicts the system of our interest where the frequency of incident photons ω_{S} (signal) is translated to the target frequency ω_{T} (target) after interactions with pump fields (pump1 and pump2) mediated by a $\chi^{(3)}$ medium. For high efficiency, the four fields must satisfy a phase-matching condition

$$\begin{aligned} \omega_{P1} - \omega_{P2} &= \omega_T - \omega_S, \\ \beta\left(\omega_{P1}\right) - \beta\left(\omega_{P2}\right) &= \beta\left(\omega_T\right) - \beta\left(\omega_S\right), \end{aligned} \tag{4.1}$$

where β is a propagation constant of the medium.

Optical waveguides or fibers support guided modes with a continuous frequency range, and the phase mismatching is characterized by propagation constants of the four fields

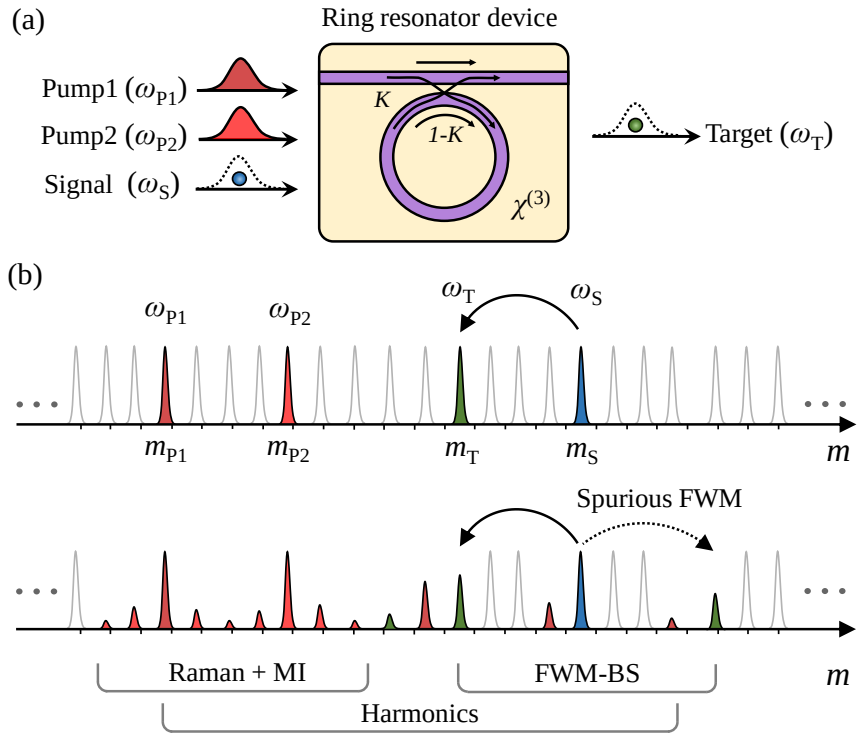

Figure 4.1: A schematic diagram of quantum frequency translation using a ring resonator. (a) Two classical pump fields (ω_{P1} and ω_{P2}) are injected to a ring resonator together with a quantum signal field (ω_S) whose wavelength is translated to the target wavelength (ω_T). (b) The frequency-translation process is based on four-wave mixing Bragg-scattering (FWM-BS). The interaction between the two pump fields mediates the coherent mode translation from the signal to the target. Ideally, the ring resonator is populated by the four fields interacting to each other via FWM-BS process (top). However, in practice, there are unwanted nonlinear processes such as spontaneous Raman-scattering, modulation instability (MI), and higher-order harmonics of the pump fields (bottom).

$\Delta\beta = \beta(\omega_{P1}) - \beta(\omega_{P2}) + \beta(\omega_S) - \beta(\omega_T)$. On the other hand, in ring resonators, as shown in Figure 4.1(b), the periodic coupling of a ring cavity (radius R) to a waveguide alters the dispersion with resonant peaks provided by $2\pi R n_{\text{eff}}(\lambda) = m\lambda$ where m and n_{eff} are integer mode numbers and an effective refractive index, respectively. Therefore, the phase-matching condition for the four resonant modes $m_{P1,P2,S,T}$ of the intracavity fields

can be rewritten as

$$\begin{aligned} \hat{\omega}_{P1} - \hat{\omega}_{P2} &= \hat{\omega}_T - \hat{\omega}_S, \\ m_{P1} - m_{P2} &= m_T - m_S, \end{aligned} \tag{4.2}$$

where $\hat{\omega}_m$ is the resonant frequency of the m-th modes. This means that the momentum conservation (the second equation in Equation 4.2) is always satisfied for carefully counted longitudinal modes. However, due to higher-order dispersions, the four modes may not satisfy the energy conservation (the first equation in Equation 4.2) with the frequency mismatching $\Delta\hat{\omega} = \hat{\omega}_{P1} - \hat{\omega}_{P2} + \hat{\omega}_T - \hat{\omega}_S$.

The unity conversion efficiency from $\hat{\omega}_\mathrm{S}$ to $\hat{\omega}_\mathrm{T}$ can be achieved when there are only four fields circulating inside the cavity with the phase-matching condition satisfied in Equation 4.2. However, in reality, there are always other nonlinear processes. For example, as depicted in Figure 4.1(b), two strong pump fields typically produce their harmonics as well as spontaneous Raman-scattered fields. Each pump field also seeds parametric amplification process, i.e., modulation instability (MI). All these additional fields introduce noises and hinder the preservation of quantum information. Furthermore, for given signal and pump fields, there are two modes satisfying the momentum conservation: $m_T^{(+)} = m_{P2} - m_{P1} + m_S$ and $m_T^{(-)} = m_{P1} - m_{P2} - m_S$. Since the energy of the signal field is then distributed to two modes via FWM-BS process (for example, the target mode $m_T^{(+)}$ and the conjugated mode $m_T^{(-)}$), this spurious FWM process reduces the conversion efficiency from the signal mode to the desired target mode. We will discuss methods to suppress such unwanted processes later in Section 4.3.1. The following is the analysis for the time evolution of FWM-BS process to estimate frequency-translation efficiency. We first discuss the process in waveguides and then move to ring resonators.

4.2.1 Generalized nonlinear Schrödinger equation

The time evolution of optical fields including thrid-order nonlinear interactions in a waveguide is described by a generalized nonlinear Schrödinger equation (GNLSE)

$$\frac{\partial A(z,t)}{\partial z} = -\frac{\alpha_0}{2}A + \sum_{n=2}^{\infty} i^{n+1}\frac{\beta_n}{n!}\frac{\partial^n A}{\partial t^n} + i\gamma\left(1 + \frac{i}{\omega_0}\frac{\partial}{\partial t}\right)\left(A(z,t)\int_{-\infty}^{t} R(t-t')|A(z,t')|^2 \mathrm{d}t'\right) \tag{4.3}$$

with $\beta_n = \partial^n\beta/\partial\omega^n$. Here, α_0 and γ denote the propagation loss and optical nonlinearity of the waveguide, respectively. The detailed derivation is provided in graduate-level nonlinear optics textbooks [6], and here we only note several points for interpretation purposes.

First, the Equation 4.3 essentially describes the time evolution of temporal envelope of the launched field at a fixed polarization (For the evolution of vector fields, see coupled nonlinear Schrödinger equation in Section 2.3.3). The first term and second term on the right side describes the variation of the temporal modes after their infinitesimal propagation due to the linear and nonlinear interactions, respectively, that are governed by the medium dispersion $\beta(\omega)$ and the optical nonlinearity γ, respectively. The underlying assumption is that the electric field $E(x, y, z, t)$ propagates along z with a fixed transverse mode. Optical nonlinear effects are not strong enough to modify the waveguide dispersion which determines the spatial profiles of guided modes. In other words, the electric field can be expressed as a simple product of three complex functions $E(x, y, z, t) = F(x, y)A(z, t)e^{i(\beta_0 z - \omega_0 t)}$: a transverse mode profile $F(x, y)$, slowly varying longitudinal temporal field $A(z, t)$, and a fast carrier with the carrier frequency $\omega_0 = 2\pi f_0$. This separation of variable splits the Maxwell's wave equation into two partial differential equations (PDEs); one is the eigenvalue equation for the transverse mode $F(x, y)$ and the other describes the time evolution of for the temporal envelop $A(z, t)$. The GNLSE is derived from the latter one normalized by the effective mode area defined as

$$A_{\text{eff}} = \frac{(\int\int \epsilon_r(x,y)|F(x,y)|^2 dxdy)^2}{\int\int_{\text{core}} \epsilon_r^2(x,y)|F(x,y)|^4 dxdy}, \tag{4.4}$$

where ϵ_r is the relative permittivity. Also, it is worth noting that we have adopted a reference frame moving at the group velocity at the carrier frequency, so that the phase accumulation is accounted only for higher-order dispersions: $\sum_{n=2}^{\infty} i^{n+1} \frac{\beta_n}{n!} \frac{\partial^n}{\partial t^n}$. This is not necessary, and we can also take the frame rotating at the carrier frequency, which then includes the first-order dispersion: $\sum_{n=1}^{\infty} i^{n+1} \frac{\beta_n}{n!} \frac{\partial^n}{\partial t^n}$.

The nonlinear coefficient $\gamma = n_2\omega_0/(cA_{\text{eff}})$ is in the unit of $\text{W}^{-1}\text{m}^{-1}$ and the amplitude A is assumed to be normalized such that $|A|^2$ represents the optical power. Here, n_2 is the Kerr nonlinear refractive index ($n_2 \approx 2.5 \times 10^{-19}\text{m}^2\text{W}^{-1}$ for Si_3N_4). In the time-domain description, the nonlinear coefficient γ depends only on the central frequency of an incident optical pulse and is considered as a constant parameter. The frequency dependence of nonlinearity is described by the time-derivative term in Equation 4.3 which also ensures the energy conservation [199]. Later, in the modified GNLSE which turns into coupled mode equations for describing ring resonators, the γ will be a frequency-dependent parameter with a slightly different definition of the effective mode area.

The temporal shape is affected by a Raman response function $R(t-t')$ only for a short pulse propagation. In quasi-continuous wave operations, only Raman gain, i.e., imaginary part of the response function, plays a major role and produces uncorrelated photons over

a wide wavelength range near the pump frequency. This originates from incoherent scattering of incident pump photons with medium optical phonons. The scattered photons particularly from the ground-state phonons are inevitably produced at longer wavelengths, i.e., Stokes photons, which cannot be removed even with cryogenic coolings of the medium.

To study the dynamics of FWM-BS, we make several assumptions to simplify the Equation 4.3. First, we assume that the waveguide is lossless ($\alpha_0 = 0$) and supports a single transverse mode, e.g., single-mode fibers. Secondly, the medium dispersion is approximated by the Taylor-expansion near the zero-dispersion wavelength $\beta_2(\omega_{\mathrm{ZDW}}) = 0$ and it is truncated at the second-order, which makes the linear interaction term vanish in Equation 4.3. Third, we consider the frequency translation driven by monochromatic CW lasers, which makes the Raman response function $R(t-t')$ set to be a δ-function. Finally, we consider the interaction length or time is not too long for the pump fields to be depleted and their temporal modes are assumed to be preserved. Then, we express the field $A(z,t)$ as the sum of four fields $A(z,t) = \sum_{i=\mathrm{P1,P2,S,T}} A_i(z,t)e^{i(\beta(\omega_i)z-\Delta\omega_i t)}$ with $\Delta\omega_i = \omega_i - \omega_{\mathrm{ZDW}}$. Then, we obtain four coupled mode equations which read

$$\begin{aligned}
\frac{dA_{\mathrm{P1}}}{dz} &= i\gamma\left(|A_{\mathrm{P1}}|^2 + 2|A_{\mathrm{P2}}|^2\right)A_{\mathrm{P1}},\\
\frac{dA_{\mathrm{P2}}}{dz} &= i\gamma\left(2|A_{\mathrm{P1}}|^2 + |A_{\mathrm{P2}}|^2\right)A_{\mathrm{P2}},\\
\frac{dA_{\mathrm{S}}}{dz} &= i\gamma\left(2|A_{\mathrm{P1}}|^2 + 2|A_{\mathrm{P2}}|^2\right)A_{\mathrm{S}} + i\gamma A_{\mathrm{P1}}A_{\mathrm{P2}}^{*}A_{\mathrm{T}}e^{i\Delta\beta z},\\
\frac{dA_{\mathrm{T}}}{dz} &= i\gamma\left(2|A_{\mathrm{P1}}|^2 + 2|A_{\mathrm{P2}}|^2\right)A_{\mathrm{T}} + i\gamma A_{\mathrm{P1}}^{*}A_{\mathrm{P2}}A_{\mathrm{S}}e^{i\Delta\beta z},
\end{aligned} \tag{4.5}$$

where $\Delta\beta = \beta(\omega_{P1}) - \beta(\omega_{P2}) + \beta(\omega_S) - \beta(\omega_T)$ is the phase-mismatching term. The Equation 4.5 can be analytically solved and the energy exchange between the signal and target mode is described by a sinusoidal function. The frequency-translation efficiency η is given as

$$\eta = \frac{r^2}{k_{\mathrm{BS}}^2}\sin^2(k_{\mathrm{BS}}L). \tag{4.6}$$

The full derivation is provided in the reference [88]. The maximum conversion efficiency is obtained when $k_{\mathrm{BS}}L = \sqrt{\Delta\beta^2 + 4\gamma^2P^2}L = \pi/2$. We consider $\Delta\beta \approx 0$, i.e., the phase-matching condition, and the typical optical nonlinearity γ =10 $\mathrm{W^{-1}\,km^{-1}}$ of photonic crystal fibers. For the pump power of around 0.5 W, the fiber length required for $k_{\mathrm{BS}}L = \pi/2$ is about 160 m.

4.2.2 Lugiato-Lefever equation

We turn our attention to FWM-BS inside a ring cavity. The dynamics for the intracavity fields can be described by the GNLSE, but now with a boundary condition imposed by a cavity-waveguide coupling. For a guided field $A_{\text{in(out)}}$ in a waveguide and its power transfer rate K to a ring cavity, the intracavity field $A^{(n+1)}(0,t)$ at the beginning of $(n+1)$th roundtrip is related to the field $A^{(n)}(L,t)$ at the end of n-th roundtrip by so-called Ikeda map as

$$\begin{bmatrix} A^{(n+1)}(0,t) \\ A^{(\text{out})} \end{bmatrix} = \begin{bmatrix} \sqrt{1-K} & i\sqrt{K} \\ i\sqrt{K} & \sqrt{(1-K)} \end{bmatrix} \begin{bmatrix} A^{(n)}(L,t)e^{-i\delta_0} \\ A^{(\text{in})} \end{bmatrix}, \tag{4.7}$$

where L is the the roundtrip length of the ring cavity and δ_0 is the linear phase accumulated over one roundtrip.

We assume that the variation of the intracavity fields over a single roundtrip is very small and the single roundtrip length or time can be treated as an infinitesimal step in the time scale of optical nonlinear interactions such as frequency-translation process. Then, the Ikeda map for the intracavity field can be rewritten as

$$A^{(n+1)}(0,t) = \left(1 - \frac{K}{2} - i\delta_0\right)\left(A^{(n)}(0,t) + \frac{\partial A(z,t)}{\partial z}L\right) + i\sqrt{K}A_{\text{in}}, \tag{4.8}$$

where we used the approximation of $e^{-i\delta_0}\sqrt{1-K} \approx (1-i\delta_0)\,(1-K/2) \approx (1-K/2-i\delta_0)$. This mean-field picture is valid in high-Q ring resonators where the time scale of amplitude evolution is much slower than a single roundtrip time $t_R = n_g L/c$ with n_g denoting the group velocity of the ring cavity. We use the GNLSE to describe the evolution of the intracavity fields. By keeping only first-order terms, we obtain

$$A^{(n+1)} - A^{(n)} = \left(-\frac{\alpha_0 L}{2} - \frac{K}{2} - i\delta_0 - i\sum_{n=2}^{\infty}\frac{\beta_n}{n!}\left(i\frac{\partial}{\partial t}\right)^n + i\gamma L|A|^2\right)A^{(n)} + i\sqrt{K}A_{\text{in}}. \tag{4.9}$$

Finally, we formulate a PDE describing the externally driven nonlinear dynamics of the intracavity fields in a slow time scale of the roundtrip time t_R, also known as Lugiato-Lefever equation (LLE) [193]

$$t_R\frac{\partial}{\partial t}A(t,\tau) = \left[-\alpha - i\delta_0 - i\sum_{n=2}^{\infty}\frac{\beta_n}{n!}\left(i\frac{\partial}{\partial t}\right)^n + i\gamma L|A|^2\right]A(t,\tau) + i\sqrt{K}A_{\text{in}} \tag{4.10}$$

with $\alpha = (\alpha_0 L + K)/2$. The LLE has been extensively used to study optical nonlinear phenomena in ring cavities particularly with a single pump field, including optical frequency

comb generation [223, 65] and soliton crystal formation [66]. It can be efficiently evaluated by split-step Fourier methods [214] or Newton-Rhapson methods [65], and the results have been shown to agree well with experiments [213].

The LLE is essentially identical to the coupled (longitudinal) mode equations, which is clearly apparent in the frequency domain. Following discussions in reference [175], we consider the intracavity field $A(t,\tau) = \sum_m A_m(t)\exp(-i\omega_m\tau)$ as a collection of plane waves oscillating at the evenly spaced frequencies $\{\omega_m\}$. In the derviation of LLE, we chose an infinitesimal time step to be a single roundtrip t_R, and the frequency grid is spanned with the spacing of the free-spectral range at the central frequency ω_0. Unlike waveguides or optical fibers, the boundary condition of the ring cavity discretizes the supported longitudinal modes with resonant frequencies $\{\hat{\omega}_m\}$, which does not generally coincide with the equally spaced frequency grid $\{\omega_m\}$; the spacings in the resonant modes vary according to the dispersion. The Fourier transformation of the Equation 4.10 yield a coupled mode equation

$$t_R\frac{\mathrm{d}A_m}{\mathrm{d}t} = -\left(\alpha_m + i\delta_m\right)A_m + i\gamma_m L\mathcal{F}\{|A(t,\tau)|^2A(t,\tau)\}_m + i\sqrt{K_m}A_{\mathrm{in},m}, \tag{4.11}$$

where the detunings $\delta_m = (\hat{\omega}_m - \omega_m)$ are determined by the dispersion of the ring cavity which is characterized by the resonant frequencies $\hat{\omega}_m = \hat{\omega}_0 + \sum_{n\geq 1} L\beta_n\left(\hat{\omega}_m - \omega_m\right)^n/(n!t_R)$. Note that we now evaluate the optical nonlinearity $\gamma_m = n_2\omega_m/\left(cA_{\mathrm{eff}}(\omega_m)\right)$ and the coupling rate K_m at each frequency mode. The definition of the effective mode area is derived from the variational principle, as presented in the supplementary material of reference [175],

$$A_{\mathrm{eff}}(\omega_m) = \left(\frac{n_0(\omega_m)}{n_g(\omega_m)}\right)^2\frac{\left(\iint \epsilon_r(x,y,\omega_m)|F(x,y,\omega_m)|^2\mathrm{d}x\mathrm{d}y\right)^2}{\iint_{\mathrm{core}}\epsilon_r^2(x,y,\omega_m)|F(x,y,\omega_m)|^4\mathrm{d}x\mathrm{d}y}, \tag{4.12}$$

where n_0 and n_g are the refractive index and group index of the ring cavity, respectively. The conversion efficiency η is defined as the ratio of a photon flux at the waveguide output to the incident photon flux at the waveguide input

$$\eta = \frac{A_{\mathrm{eff}}(\omega_{\mathrm{T}})}{A_{\mathrm{eff}}(\omega_{\mathrm{S}})}\frac{\Phi(\omega_{\mathrm{T}})}{\Phi(\omega_{\mathrm{S}})} \text{ with } \Phi(\omega) = \frac{|A(\omega)|^2}{\hbar\omega}. \tag{4.13}$$

The description of the nonlinear dynamics among all resonant modes in ring cavities, including spurious FWM and MI, requires the numerical evalutation of the GNLSE with the boundary condition in Equation 4.7, which is further discussed later in Section 4.3.2. For now, we only consider the four modes, i.e., two pumps, signal and target fields, and restrict

their nonlinear interactions to the FWM-BS as in the discussion with waveguides 4.2.1. Assuming the undepleted CW pump fields, the Equation 4.11 is expressed as

$$\begin{aligned}
t_R\frac{dA_{\mathrm{P1}}}{dt} &= -\left(\alpha_{\mathrm{P1}}+i\Delta\phi_{\mathrm{P1}}\right)A_{\mathrm{P1}}+i\sqrt{K_{\mathrm{P1}}P_{\mathrm{P1}}},\\
t_R\frac{dA_{\mathrm{P2}}}{dt} &= -\left(\alpha_{\mathrm{P2}}+i\Delta\phi_{\mathrm{P2}}\right)A_{\mathrm{P2}}+i\sqrt{K_{\mathrm{P2}}P_{\mathrm{P2}}},\\
t_R\frac{dA_{\mathrm{S}}}{dt} &= -\left(\alpha_{\mathrm{S}}+i\Delta\phi_{\mathrm{S}}\right)A_{\mathrm{S}}+2i\gamma_{\mathrm{S}}LA_{\mathrm{P1}}^{*}A_{\mathrm{P2}}A_{\mathrm{T}}+i\sqrt{K_{\mathrm{S}}P_{\mathrm{S}}},\\
t_R\frac{dA_{\mathrm{T}}}{dt} &= -\left(\alpha_{\mathrm{T}}+i\Delta\phi_{\mathrm{T}}\right)A_{\mathrm{T}}+2i\gamma_{\mathrm{T}}LA_{\mathrm{P1}}A_{\mathrm{P2}}^{*}A_{\mathrm{S}}+i\sqrt{K_{\mathrm{T}}P_{\mathrm{T}}},
\end{aligned} \tag{4.14}$$

where the detunings $\Delta\phi_{\mathrm{P1(P2)}}=\left(\hat{\omega}_{\mathrm{P1(P2)}}-\omega_{\mathrm{P1(P2)}}\right)t_R-\gamma_{\mathrm{P1(P2)}}L\left(|A_{\mathrm{P1(P2)}}|^2+2|A_{\mathrm{P2(P1)}}|^2\right)$ and $\Delta\phi_{\mathrm{S(T)}}=\left(\hat{\omega}_{\mathrm{S(T)}}-\omega_{\mathrm{S(T)}}\right)t_R-2\gamma_{\mathrm{S(T)}}L\left(|A_{\mathrm{P1}}|^2+|A_{\mathrm{P2}}|^2\right)$ include the ring cavity dispersion as well as the self- and cross-phase modulations.

The steady state solution can be obtained by denoting $dA/dt=0$. First, the solution for the pump fields are $A_{\mathrm{P1(P2)}}=i\sqrt{K_{\mathrm{P1(P2)}}P_{\mathrm{P1(P2)}}}/\left(\alpha_{\mathrm{P1(P2)}}+i\Delta\phi_{\mathrm{P1(P2)}}\right)$. Then, we solve the coupled equations of the third and fourth line in Equation 4.14, which describe the energy exchange between the signal and target modes, by rewriting them in a matrix form as

$$\begin{bmatrix}A_{\mathrm{S}}\\A_{\mathrm{T}}\end{bmatrix}=\begin{bmatrix}-i\left(\alpha_{\mathrm{S}}+i\Delta\phi_{\mathrm{S}}\right) & -2\gamma_{\mathrm{S}}LA_{\mathrm{P1}}^{*}A_{\mathrm{P2}}\\ -2\gamma_{\mathrm{T}}LA_{\mathrm{P1}}A_{\mathrm{P2}}^{*} & -i\left(\alpha_{\mathrm{T}}+i\Delta\phi_{\mathrm{T}}\right)\end{bmatrix}^{-1}\begin{bmatrix}\sqrt{K_{\mathrm{S}}}A_{\mathrm{S,in}}\\ \sqrt{K_{\mathrm{T}}}A_{\mathrm{T,in}}\end{bmatrix}. \tag{4.15}$$

The solution of the steady state intracavity fields is given by

$$\begin{aligned}
A_{\mathrm{S}} &= \frac{i\left(\alpha_{\mathrm{T}}+i\Delta\phi_{\mathrm{T}}\right)\sqrt{K_{\mathrm{S}}}A_{\mathrm{S,in}}-2\gamma_{\mathrm{S}}LE_{\mathrm{P1}}^{*}A_{\mathrm{P2}}\sqrt{K_{\mathrm{T}}}A_{\mathrm{T,in}}}{\left(\alpha_{\mathrm{S}}+i\Delta\phi_{\mathrm{S}}\right)\left(\alpha_{\mathrm{T}}+i\Delta\phi_{\mathrm{T}}\right)+\left(4\gamma_{\mathrm{T}}\gamma_{\mathrm{S}}L^2|A_{\mathrm{P1}}|^2|A_{\mathrm{P2}}|^2\right)},\\
A_{\mathrm{T}} &= \frac{-2\gamma_{\mathrm{S}}LE_{\mathrm{P1}}^{*}E_{\mathrm{P2}}\sqrt{K_{\mathrm{S}}}A_{\mathrm{S,in}}+i\left(\alpha_{\mathrm{S}}+i\Delta\phi_{\mathrm{S}}\right)\sqrt{K_{\mathrm{T}}}A_{\mathrm{T,in}}}{\left(\alpha_{\mathrm{S}}+i\Delta\phi_{\mathrm{S}}\right)\left(\alpha_{\mathrm{T}}+i\Delta\phi_{\mathrm{T}}\right)+\left(4\gamma_{\mathrm{T}}\gamma_{\mathrm{S}}L^2|A_{\mathrm{P1}}|^2|A_{\mathrm{P2}}|^2\right)},
\end{aligned} \tag{4.16}$$

which are then coupled to the waveguide field as $A_{\mathrm{S(T),WG}}=A_{\mathrm{S(T),in}}+i\sqrt{K_{\mathrm{S(T)}}}A_{\mathrm{S(T)}}$ to evaluate the output waveguide fields:

$$\begin{aligned}
A_{\mathrm{S,WG}} &= A_{\mathrm{S,in}}-\frac{\left(\alpha_{\mathrm{T}}+i\Delta\phi_{\mathrm{T}}\right)K_{\mathrm{S}}A_{\mathrm{S,in}}}{\left(\alpha_{\mathrm{S}}+i\Delta\phi_{\mathrm{S}}\right)\left(\alpha_{\mathrm{T}}+i\Delta\phi_{\mathrm{T}}\right)+\left(4\gamma_{\mathrm{T}}\gamma_{\mathrm{S}}L^2|A_{\mathrm{P1}}|^2|A_{\mathrm{P2}}|^2\right)},\\
A_{\mathrm{T,WG}} &= \frac{-2i\gamma_{\mathrm{S}}LA_{\mathrm{P1}}^{*}A_{\mathrm{P2}}\sqrt{K_{\mathrm{T}}K_{\mathrm{S}}}A_{\mathrm{S,in}}}{\left(\alpha_{\mathrm{S}}+i\Delta\phi_{\mathrm{S}}\right)\left(\alpha_{\mathrm{T}}+i\Delta\phi_{\mathrm{T}}\right)+\left(4\gamma_{\mathrm{T}}\gamma_{\mathrm{S}}L^2|A_{\mathrm{P1}}|^2|A_{\mathrm{P2}}|^2\right)}.
\end{aligned} \tag{4.17}$$

The frequency-translation efficiency η is then calculated to be

$$\eta=\frac{A_{\mathrm{eff}}(\omega_{\mathrm{T}})}{A_{\mathrm{eff}}(\omega_{\mathrm{S}})}\frac{\omega_S}{\omega_T}\frac{4\gamma_{\mathrm{S}}^2L^2|A_{\mathrm{P1}}|^2|A_{\mathrm{P2}}|^2K_{\mathrm{T}}K_{\mathrm{S}}}{\left|\left(\alpha_{\mathrm{S}}+i\Delta\phi_{\mathrm{S}}\right)\left(\alpha_{\mathrm{T}}+i\Delta\phi_{\mathrm{T}}\right)+4\gamma_{\mathrm{T}}\gamma_{\mathrm{S}}L^2|A_{\mathrm{P1}}|^2|A_{\mathrm{P2}}|^2\right|^2}. \tag{4.18}$$

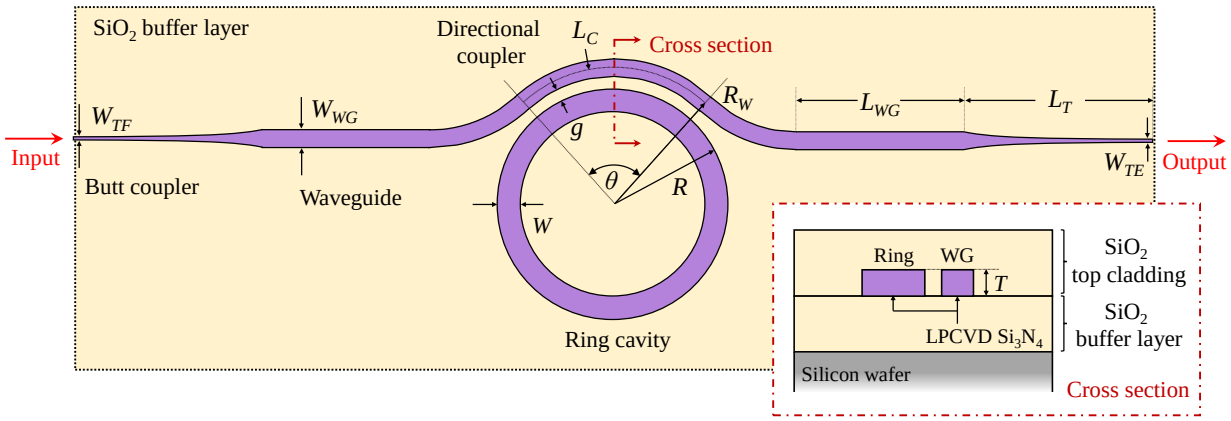

Figure 4.2: Structure of a quantum frequency transducer using a silicon nitride ring resonator. For detailed description of each parameter, see Table 4.1.

Obviously, the conversion efficiency is unity when the propagation loss is negligible $\alpha \approx 0$ and the two fields are both resonant $\Delta\phi_{\mathrm{S}} = \Delta\phi_{\mathrm{S}} = 0$. This is because we assumed that there exist only four modes inside the cavity that are interacting to each other via FWM-BS process.

4.3 Design considerations

The development of nanophotonic quantum devices generally requires a thorough design process from a conceptual level to the precise estimation of the performance. It involves a sophisticated modeling of the device and assessment to the functionality with accurate computations based on the theory of electromagnetism. It is important to clearly define the design specifications, validate the numerical tools being used, and eventually verify the design with experiment. In this section, we discuss a set of requirements for the QFT to be used for QD-SPS and provide our detailed designing process. As optical ring resonators are extensively described in literatures [258, 3], we adopt formula for basic properties, e.g., free-spectral range and linewidth, in the following discussions.

Figure 4.2 sketches the structure of our ring resonator. The device is made of stochiometric Si_3N_4 deposited on a 5 µm–thick SiO_2 layer. The fabricated Si_3N_4 layer is protected by a SiO_2 top cladding which also provides the symmetric distribution of the dielectric constant. To ease fabrication process, we restrict the height to be constant across the entire structure, as shown in the inset of Figure 4.2. In terms of functionalities, the device mainly

Table 4.1: Design parameters for the quantum frequency transducer. Sellmeier equations for the refractive indices of Si_3N_4 and SiO_2 are provided in Appendix A.

Parameter	definition	designed value
T	Thickness	800 nm
R	Radius of ring resonator	50 µm
W	Width of ring resonator	1360 nm
g	Gap for directional coupler	300 nm
$L_C = R_W\theta$	Coupling length	10 µm
W_{WG}	Width of waveguide	660 nm
W_{TF}	Tapering width for the input	120 nm
W_{TE}	Tapering width for the output	100 nm
L_T	Tapering length	≥100 µm

consists of three parts: ring cavity, directional coupler, and Butt coupler. The input and output light are considered to be coupled with single-mode fibers at both ends of the QFT. The field propagations are supported by the low-loss Si_3N_4 waveguide which is coupled with a ring cavity where the FWM-BS process generates the frequency-translated light. The geometry of each part is uniquely determined by a set of parameters summarized in Table 4.1.

4.3.1 Requirements

Target wavelength and acceptance bandwidth

First and foremost, the QFT shall translate the wavelength from 985 nm to 785 nm. The signal wavelength may be changed depending on QD-SPSs to be used, but the target wavelength is restricted to be within the QEYSSat quantum channel wavelength range from 780 nm to 795 nm. During the design phase, the dependence of geometric parameters to the wavelengths for the frequency-translation process must be characterized such that the device operating at the desired input wavelength can readily be designed at will.

The frequency-translation process must cover the entire spectral bandwidth of the incident field. Typical linewidth of the emitted photons from a cryogenic-cooled QD-SPS is a few gigahertz. The linewidth of the corresponding resonant mode must be greater than the bandwidth of the photons. This sets the maximum loaded Q-factor of the designed ring resonator. For example, the FWHM linewidth λ_{FHWM} =1 GHz of the resonent mode

at 985 nm gives the Q-factor $\mathcal{Q} \approx 3 \times 10^5$, and the higher $\mathcal{Q}$ comes with the narrower linewidth.

Low-noise process with high efficiency

As discussed in the previous section, the frequency-translation process inevitably involves other optical nonlinear processes which could potentially limit the conversion efficiency. We mainly consider four competing third-order nonlinear processes inside the ring cavity: FWM-BS, spurious FWM, MI, and sponteneous Raman-scattering. The dispersion must be tailored such that the four fields satisfy the phase-matching condition only for FWM-BS process. Also, it is highly preferable to place pump wavelengths longer than the signal and target fields to avoid spontaneous-Raman scattered photons. As a goal, the intrinsic conversion efficiency is greater than 90 % at the pump power of several milliwatts.

We focus on the phase-matching condition for FWM-BS process. The resonant frequency $\hat{\omega}_m$ can be Taylor-expanded with respect to the resonant mode index m closest to the zero-dispersion wavelength m_0

$$\hat{\omega}_m = \hat{\omega}_{m_0} + \hat{\omega}^{(1)}_{m_0}(m-m_0) + \frac{\hat{\omega}^{(2)}_{m_0}}{2!}(m-m_0)^2 + \frac{\hat{\omega}^{(3)}_{m_0}}{3!}(m-m_0)^3 + \frac{\hat{\omega}^{(4)}_{m_0}}{4!}(m-m_0)^4 + \cdots \quad (4.19)$$

with $\hat{\omega}^{(n)}_{m_0} = \mathrm{d}^n\hat{\omega}/\mathrm{d}m^n$. Here, the derivative of the discrete frequency modes is calculated by the finite-difference method, e.g., $\mathrm{d}\hat{\omega}/\mathrm{d}m = \hat{\omega}_m - \hat{\omega}_{m-1}$. Figure 4.3 shows the decomposition of the ring-cavity dispersion $\hat{\omega}_m$ up to the fifth order with the mode $m_0 = 577$ at the zero-dispersion wavelength for an examplary structure (the parameters listed in Table 4.1). Then, the frequency-mismatching term for FWM-BS process $\Delta\hat{\omega}_{\mathrm{BS}} = \hat{\omega}_{\mathrm{P1}} - \hat{\omega}_{\mathrm{P2}} + \hat{\omega}_{\mathrm{T}} - \hat{\omega}_{\mathrm{S}}$ can be rewritten as

$$\begin{aligned}\Delta\hat{\omega}_{\mathrm{BS}} = {} & \hat{\omega}^{(1)}_{m_0}(m_{\mathrm{P1}} - m_{\mathrm{P2}} + m_{\mathrm{T}} - m_{\mathrm{S}}) \\ & + \hat{\omega}^{(3)}_{m_0}/6\big[(m_{\mathrm{P1}}-m_0)^3 - (m_{\mathrm{P2}}-m_0)^3 + (m_{\mathrm{T}}-m_0)^3 - (m_{\mathrm{S}}-m_0)^3\big] \\ & + \hat{\omega}^{(4)}_{m_0}/24\big[(m_{\mathrm{P1}}-m_0)^4 - (m_{\mathrm{P2}}-m_0)^4 + (m_{\mathrm{T}}-m_0)^4 - (m_{\mathrm{S}}-m_0)^4\big] + \cdots .\end{aligned} \quad (4.20)$$

The first and second terms of Equation 4.20 vanish by the momentum conservation. In fact, all odd-order terms are cancelled due to the symmetric position of the four resonant modes. Thus, the conversion efficiency is mainly limited by the fourth-order term.

One obvious method to suppress the higher-order dispersion is to bring the four resonant modes close to the zero-dispersion wavelength. However, as discussed in reference [172], the spurious FWM process and MI can be suppressed by placing the pumps far away

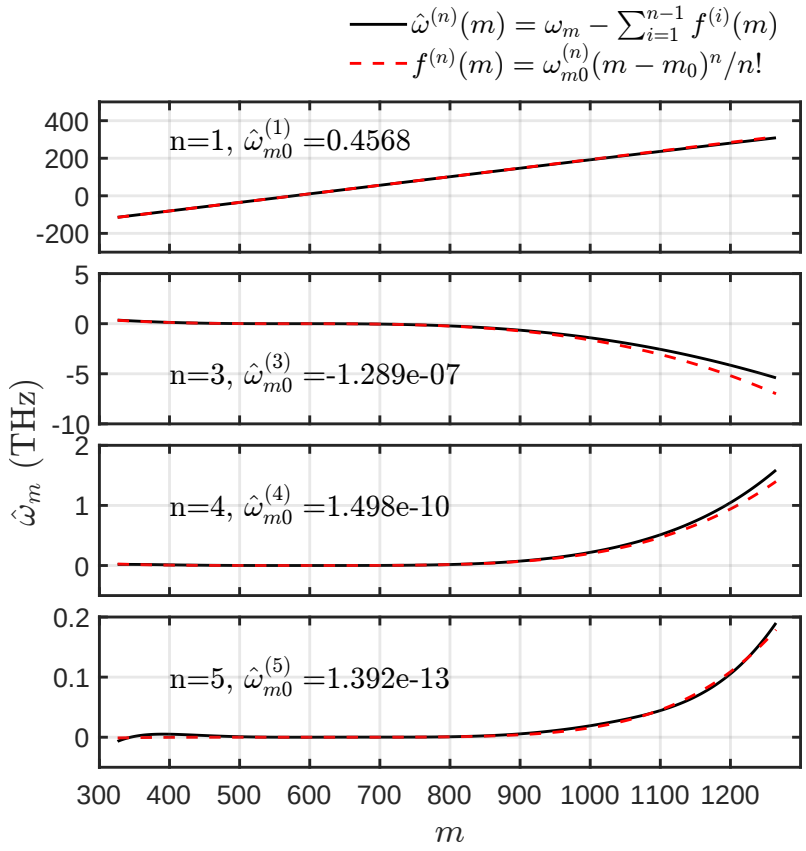

Figure 4.3: Taylor expansion of the resonant frequency $\hat{\omega}_m$ up to the fifth order for an examplary ring cavity with respect to the resonant mode index m. The detailed explanation is provided in the main text.

from the zero-dispersion wavelength, which introduces higher order dispersion to reduce the bandwidth of the two processes. For example, the third-order dispersion breaks the symmetry between the desired FWM-BS and the spurious FWM $\hat{\omega}_T^{(-)} = \hat{\omega}_{P1} - \hat{\omega}_{P2} - \hat{\omega}_S$, and creates the energy discrepancy between them. This trade-off must be taken care to maximize the conversion efficiency by the simulations of the designed device.

One may concern that it would be notoriously difficult to fabricate the structure whose four selected resonant modes are precisely aligned to satisfy the phase-matching condition, e.g., $\Delta\hat{\omega}_{\mathrm{BS}} < \delta\hat{\omega}_{\mathrm{FWHM}}$. However, it turns out that the detuned pump fields with stronger optical power can mediate the energy exchange by virtually populating photons in the resonant modes. This picture is clear when we interpret it from the perspective of an

atomic system which exhibits many energy levels as an analogue of the resonant modes of the ring cavity. The atomic population transfer from one level to another can be seen as the frequency translation from one resonant mode to another. Indeed, the mathematical description of the FWM-BS is closely related to the population exchange of coherently driven two-level atomic system [293]. Also, demonstrations of the FWM-assisted frequency conversion with cold atoms have been performed with detuned pump fields [246].

After accounting all the forementioned aspects, we chose the pump wavelengths to be around λ_{P1} ∼1064 nm to 1100 nm and $\lambda_{\mathrm{P2}} \sim 1470$ nm to 1550 nm by placing the zero-dispersion wavelength at around $\lambda_{\mathrm{ZDW}} \sim 1030$ nm to 1050 nm. This provides additional benefits of using commercially available narrow-linewidth lasers for pump fields. Another advantage of the selected wavelengths is that the QFT could readily be adapted for frequency translation from the QD wavelength at $\lambda_{\mathrm{S}} \sim 985$ nm to telecom wavelength by operating one of the pump at $\lambda_{\mathrm{T}} \sim 785$ nm with minor modifications in the design.

Overcoupling regime: waveguide-cavity coupling rate greater than cavity dissipation rate

One of the most critical requirements is to keep the ring resonator in the overcoupling regime at the wavelengths of all four fields. This means that the field injection rate $K(\omega_m)$ from the waveguide to the ring cavity must be greater than the dissipation rate α_0 of the intracavity fields in order to keep the fields coherently accumulated and amplified inside the cavity. In other words, the coupling-Q factor $\mathcal{Q}_c$ must be smaller than the intrinsic Q-factor $\mathcal{Q}_i$ of the ring resonator.

In general, the coupling rate between the cavity and the waveguide is proportional to the amount of the mode overlap between the two guided fields. The amount of the overlap can be adjusted by the structural parameters, e.g., g and W_{WG}. However, since the field confinement is dependent on the wavelength: shorter wavelength comes with better confinement, the coupling rate is dramatically decreased at short wavelengths, which creates a large difference of the coupling Q-factor $\mathcal{Q}_c(\omega_m) = \hat{\omega}_m/\kappa_m^2$ between 1470 nm and 785 nm with $K_m = |\kappa_m|^2$. To overcome this problem, we use a pulley coupler and engineer the coupling length L_c to control the flow of the fields between the ring cavity and the waveguide [124].

For high-Q ring resonators, we assume that the coupling between the two guided modes do not change their own transverse mode profiles. We treat the ring-cavity modes as perturbations to the waveguide modes. To the first order, the coupling coefficient between

the ring cavity and the curved waveguide over the pulley region is given by

$$\kappa_{\text{pulley}} = \int_{-\theta_0}^{\theta_0} \left[\frac{i\omega_m}{4} \int_0^{W_{WG}} \int_0^{T} (\epsilon(r,z) - \epsilon_0) \mathbf{E}_{\text{R}} \cdot \mathbf{E}_{\text{WG}} r \mathrm{d}r \mathrm{d}z \right] e^{i(\beta_{\text{WG}} R_W - m)\theta} \mathrm{d}\theta, \tag{4.21}$$

where $\mathbf{E}_{\text{WG}}$ is the unperturbed electric field vector in the curved waveguide normalized to unit power and $\mathbf{E}_{\text{R}}$ is the uncoupled resonator mode field normalized to unit energy.

The pulley coupler includes the point-contact coupling at the two ends of the pulley region, and the total directional coupling coefficient $\kappa_m = \kappa_{\text{pulley}} + \kappa_{\text{point}}$ is given by the sum of the two coefficients for the pulley and point-contact couplers. The point-contact coupling coefficient κ_{point} can be calculated by integrating the inner product of the two normalized electric vectors between the ring cavity and the straight waveguide over the interaction region. The full derivation of the coupling coefficient is provided in reference [271], and the formalism of coupled mode theory is provided in the textbooks [200, 270]. As seen in Equation 4.21, one can selectively lower the coupling-Q factor [124] at the desired wavelengths by engineering the propagation constant of the waveguide with the width W_{WG} and radius R_W as well as the coupling length $L_C = R_W\theta$.

Availability of Si_3N_4 film

Silicon nitride has been chosen to be a good material for integrated quantum photonic devices because of its good optical transparency from visible to infrared wavelength (400 nm to 2350 nm), high intrinsic tensile stress, substantial Kerr nonlinearity with negligible two-photon absorptions, as well as the wafer-scale fabrication process [218]. Nowadays the propagation loss of less than 1 dB m^{-1} can be readily achieved, opening a new nanophotonic platform for cavity-assisted nonlinear photonics such as photon-pair generation, optical frequency comb, and frequency conversion. A comprehensive review on the state-of-art Si_3N_4 photonics is provided in reference [34].

Two notable technological breakthroughs in the field has put the Si_3N_4 as the next generation of nanophotonic platform. First, for quantum applications where optical nonlinearity plays a major role, it is often required that the Si_3N_4 film is thicker than 500 nm to properly tune the spectral location of the zero-dispersion wavelength. However, due to the high film stress of Si_3N_4, the film gets severely cracked when the thickness is greater than 400 nm during the deposition process. This had been one of the major challenges that limits the device yield. Recently, this issue has been addressed by multiple groups (see section 2 in reference [34]). One of the notable solution is the two-step deposition process where the wafer is 45°–rotated after the first round of deposition, distributing uniaxial

strain to avoid film cracks [83, 82]. In this method, the Si_3N_4 film can be deposited with the thickness greater than 800 nm. The second breakthough is a significant reduction of the propagation loss in Si_3N_4 waveguides via thermal annealing after the fabrication process. The insight was that the propagation loss is mainly limited by the surface roughness, not the material's intrincic absorption properties. The annealing process reduces the surface roughness, which brought the Q-factor greater than 170 million [143].

We consider that our QFT is fabricated on 800 nm–thick Si_3N_4 film (MPW-IR series, LIGENTEC) and assume 0.05 dB cm^{-1} propagation loss. Also, it is important to experimentally characterize the material's refractive index by spectroscopic ellipsometer and other methods. We designed the QFT with the measured refractive indices provided by the company. However, the results presented in this chapter is produced with the modeled materials by Sellmeier equations provided in Appendix A.

High single-mode fiber-coupling efficiency

We aim to have the QFT efficiently coupled to single-mode fibers at both ends for three input fields and one output field. The device throughput is as important as the frequency-translation efficiency to improve the length of the secure key in satellite-assisted QKD. The three input fields at the wavelength of 985 nm, 1065 nm, and 1469 nm are anticipated to be delivered through an ultra-high numerical aperture fiber (UHNA3, Nufern), whereas the output field at 785 nm is coupled to a conventional single-mode fiber (780-HP, Nufern). The coupling coefficient η_B is related to the mode overlap factor between the waveguide mode $\{\mathbf{E}_{WG}, \mathbf{H}_{WG}\}$ and the optical fiber $\{\mathbf{E}_F, \mathbf{H}_F\}$ as

$$\eta_B(\omega) = \frac{\iint \vec{z} \cdot (\mathbf{E}^*_{WG} \times \mathbf{H}_F + \mathbf{E}_F \times \mathbf{H}^*_{WG})\, dxdy}{\iint \vec{z} \cdot (\mathbf{E}^*_{WG} \times \mathbf{H}_{WG} + \mathbf{E}_{WG} \times \mathbf{H}^*_{WG})\, dxdy}. \tag{4.22}$$

The electromagnetic fields in conventional single-mode fibers are weakly guided and their typical mode areas are around 5 µm^2 to 10 µm^2, whereas silicon photonic device performs much tighter confinement of the guided mode 0.3 µm^2 to 0.5 µm^2 due to the large refractive index difference. This big discrepancy of the mode areas yields a poor coupling efficiency between the two modes. One common solution is to transform the mode profile via adiabatic tapering of the waveguide. By changing the shape of the waveguide slow enough that the guided modes remain in the same fundamental eigenstates, one can manipulate the spatial mode without causing significant losses [190]. When the waveguide's cross-section becomes small enough, the guided mode reaches so-called "squeezed out regime" or "sub-wavelength regime" where most of the field is guided through the

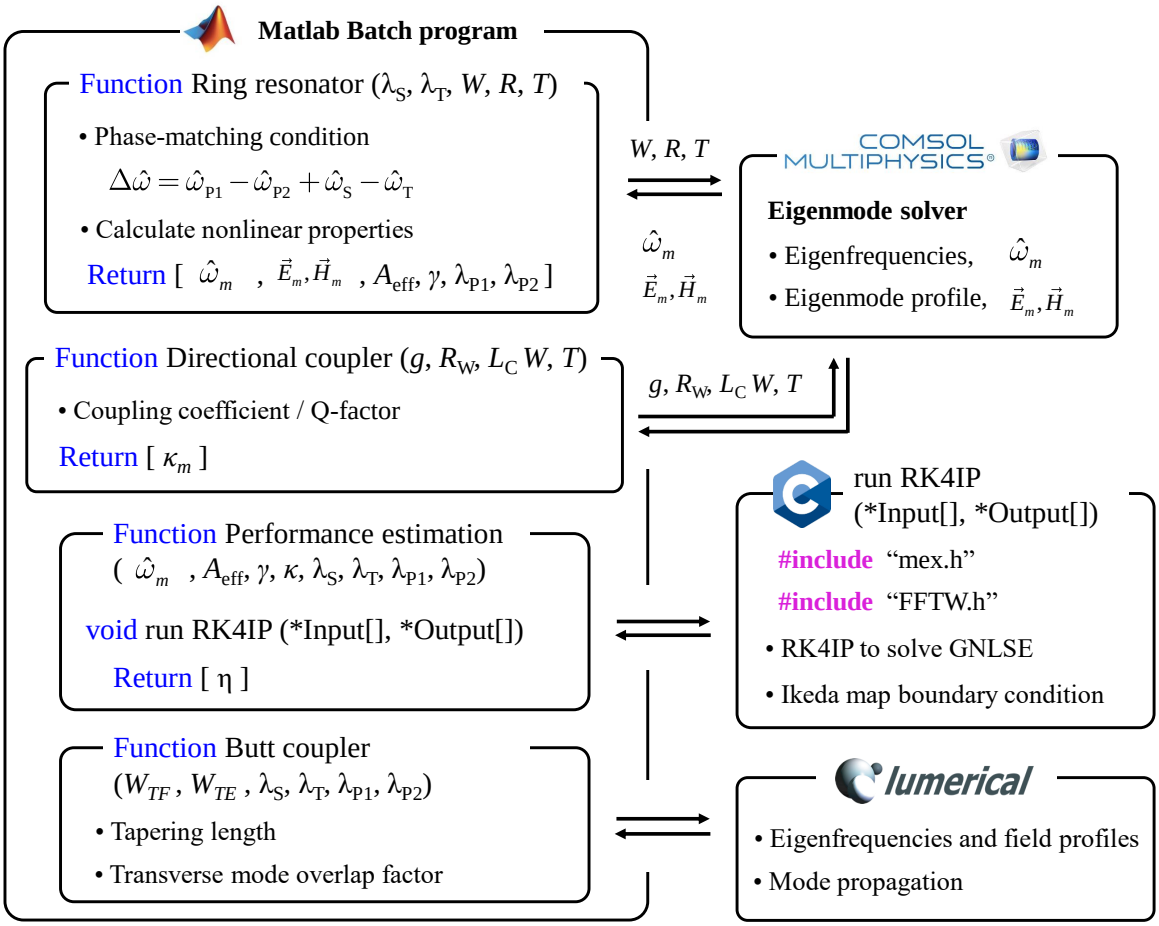

Figure 4.4: A functional block diagram of the design process. The structural parameters for a ring cavity is determined before the design of a directional coupler. Butt couplers is designed separately.

cladding [26]. It has been demonstrated that a simple lateral tapering yields greater than 90 % of coupling efficiency [320]. We adopt this technique in our QFT design.

It is worth noting that many designs of adiabatic tapers have been proposed with different shapes of tapering [93], such as linear, exponential, parabolic, and etc. In this study, we used a linear waveguide taper for simplicity.

4.3.2 Design methods

Our design process is essentially the iterative optimization of the geometric parameters of the QFT based on the numerical evaluation of the device performance. Generally, the time evolution of the electromagnetic field in the ring resonator including the couplers is fully described by three-dimensional (3D) Maxwell's wave equations including the Kerr nonlinearity with source fields. Although the direct evaluation of the 3D Maxwell's equation is possible using finite-difference time-domain (FDTD) method, it is computatonally very expensive to keep the spatial resolution at tens of nanometers for the ring cavity whose radius is tens of micrometers. Especially for high-Q cavities, numerically solving the Maxwell's equation in time domain is not preferred because one must wait a long time until the intracavity field decays to precisely estimate the quality factor.

In our scheme, following the theory presented in Section 4.2, we separate the 3D Maxwell's equation into two: the eigenvalue equation for the transverse modes and the PDE for the time evolution of the longitudinal modes, provided by the separation of variables $E(x, y, z) = F(x, y)A(z)e^{i\beta z+\omega t}$ with the forementioned assumptions. We first obtain the eigenmodes of the individual subsystems by solving the former equation using finite-element eigenmode solver. Then, we evaluate the optical properties of the QFT such as the dispersion $\hat{\omega}_m$, optical nonlinearity γ_m, and waveguide-ring coupling rate κ_m. Those parameters are eventually fed into our custom-built coupled mode equation solver to estimate the frequency-translation efficiency and bandwidth.

A functional block diagram of our design workflow is illustrated in Figure 4.4. We developed a design software package which consists of multiple commerical softwares of finite-element and finite-difference eigenmode solver that are interfaced with Matlab. The QFT performance is estimated by a numerical propagator of the GNLSE with the Ikeda map (GNLSE-IM) via an algorithm named Runge-Kutta fourth-order in interaction picture (RK4IP). This is written in C and integrated with Matlab's MEX function.

For given geometric parameters and material's refractive indices, we first run the finite-element method (FEM) eigenmode solver (COMSOL multiphysics) to obtain a set of eigenfrequencies $\{\hat{\omega}_m\}$ and corresponding transverse mode profiles $\{\vec{E}_m, \vec{H}_m\}$ of the resonant modes over the range of wavelength of interest. We then calculate phase-matched pump wavelengths λ_{P1} and λ_{P2}, effective mode area A_{eff}, as well as nonlinear coefficients γ_m. For pre-determined geometric parameters of the ring cavity, we run another FEM simulations to obtain the eigenmodes for the directional coupler. At this time, we run the simulation twice for one coupler: one is for the curved waveguide and the other is for the straight waveguide. We then evaluate the coupling coefficients for point-contact κ_{point} and pulley-coupled waveguides κ_{pulley}, which are summed together to determine the total coupling

coefficient κ for the directional coupler. The obtained parameters $\hat{\omega}_m$,$\lambda_{\mathrm{S,T,P1,P2}}$, γ_m, κ_m are finally substituted to the GNLSE-IM which fully models the third-order nonlinear processes with all resonant modes and evaluate the conversion efficiency. We design the Butt couplers separately by using a finite-difference eigenmode propagator (Lumerical MODE) after the design for the ring cavity and waveguide is finalized. The following are the details of individual numerical computations.

Finite element method for electromagnetic eigenmode solver: COMSOL multiphysics

FEM is a numerical technique to obtain an approximated solution for a PDE that describes the time evolution of complex physical systems. Unlike finite difference methods (FDMs) which directly solve the differential form of PDEs by approximating the differential operations with Taylor expansion, the FEM finds an approximated solution for an integral form of a PDE by using weighted residual methods. It is based on a sound mathematical background, and its flexible meshing capability enables an efficient and accurate computations for complex physical structures. There are already commercial packages of FEM solvers e.g., COMSOL multiphysics, FreeFEM, Elmer FEM, and one can easily run the simulation without facing mathematical details.

The COMSOL multiphysics provides methods to solve the Maxwell's wave equation with user-defined boundary conditions for the desired geometry of dielectric constants. The eigenmodes are obtained by solving the Maxwell's equation in the frequency domain. As the geometry of the straight waveguide and the electric field profiles are defined by the 2D cross section, the solution can be efficiently obtained with requiring expensive computational resources. Similarly, for pulley waveguides, since the curvature is fixed, the geometry can also be defined in 2D by the axial symmetry and the method is also provided by COMSOL multiphysics. However, the solution for the resonant modes in the ring cavity requires an additional boundary condition which is not included in the built-in Maxwell equation solver. This forces us to rewrite the Maxwell's equation in the weak form including the boundary conditions for ring resonators. The solution can be obtained using the COMSOL's eigenmode solver. We adopted the mathematical formulation developed by Mark Oxborrow [227] and Cheema *et al.* [58] for the accurate modeling of our ring cavity.

For any numerical simulations, it is important to validate the method by comparing the solutions with well known cases or analytic solutions before applying for complex systems. We testify the COMSOL eigenmode solvers in two steps. First, we compare the results for a simple 2D slab waveguide, as shown in Figure 4.5, where the TE eigenmode profiles E_y

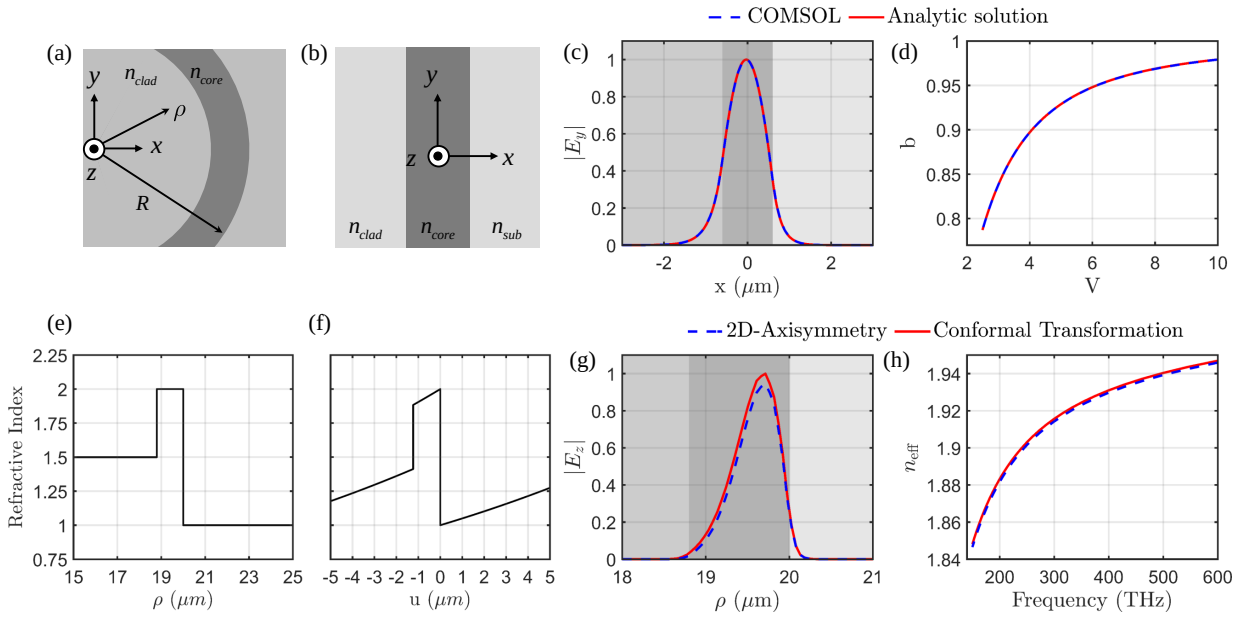

Figure 4.5: Validation of COMSOL eigenmode solver. The definition of the coordinate system for two dimensional (a) curved waveguide and (b) straight waveguide. (c)–(d) The comparison of the numercally computed results with analytical solutions. (e)–(f) Refractive index of an example of the curved waveguide and its corresponding conformal transformation to the straight waveguide. (g)–(h) The comparison of the results for the two cases.

and eigenfrequencies can be analytically calculated as

$$E_y = \begin{cases} B_\pm \exp\left[-q\left(|x| - d\right)\right], & \text{if } |x| > d, \\ A\cos\left(px - m\pi/2\right), & \text{if } |x| \le d, \end{cases}$$
$$2V\sqrt{1-b} = m\pi + \tan^{-1}\sqrt{\frac{b}{1-b}} + \tan^{-1}\sqrt{\frac{b+\delta}{1-b}}, \tag{4.23}$$

with $p^2 = n^2k_0^2 - \beta^2$, $q^2 = \beta^2 - n^2k_0^2$, $B_\pm = A\cos\left(pd \mp m\pi/2\right)$, the normalized parameters $V = k_0 d\sqrt{n_{\text{core}}^2 - n_{\text{sub}}^2}$, $b = \left(\bar{n}^2 - n_{\text{sub}}^2\right)/\left(n_{\text{core}}^2 - n_{\text{sub}}^2\right)$, $\delta = \left(n_{\text{sub}}^2 - n_{\text{clad}}^2\right)/\left(n_{\text{core}}^2 - n_{\text{sub}}^2\right)$. The excellent agreement between the numerical results from the COMSOL and analytic solutions verifies that our numerical tool for straight waveguides is ready for further usage.

Curved waveguides with the curvature R in cylindrical coordinate can be mapped onto leaky straight waveguides via the conformal transfomration $u = -R\log\left(\rho/R\right)$ with the

refractive index $\tilde{n}(u) = n(Re^{u/R})e^{u/R}$ [117], as shown in Figure 4.5(e)–(f). Given that our straight waveguide solutions are verified with the analytical solution, we test our solutions for curved waveguides in COMSOL axisymmetric domain by the comparison with the results calculated for the corresponding leaky straight waveguide, as shown in Figure 4.5(g)–(h).

Fourth-order Runge-Kutta in interaction picture for nonlinear Schrödinger equation with Ikeda map

In the LLE formalism discussed in Section 4.2.2, where the equal frequency spacing is determined by the free-spectral range at a central frequency ω_0, it is not trivial to systematically accommodate multiple on-resonant pump fields. On the other hand, the GNLSE-IM does not have any restrictions in the setting of frequency grids. To accomodate multiple pump fields, we numerically evaluate the field variation over one roundtrip according to the Equation 4.3 and then apply the coupling with the waveguide according to Equation 4.7. We repeat the calculations over many roundtrips until the fields reaches the steady states. The GNLSE can be efficiently solved by RK4IP method described in reference [130, 23]. The frequency grids are defined with spacings that are fine enough to resolve the spectral shape of individual resonant peaks. As we will show later, this setup helps understanding nonlinear resonant peak shifts as well as mode splittings at the high pump powers.

This method is, however, at the expense of higher computation cost compared to the LLE formalism. This is mainly because the propagation step size cannot be larger than the cavity length and the fine frequency grid requires the massive size of array to compute. For example, a typical Q-factor of 2×10^5 with no loss exhibits the spectral FWHM of a few GHz. In order to resolve the resonant feature with 10 frequency bins we need to have 2^{22} frequency bins to cover the wide spectral range of 0.3 µm-1.8 µm. Also, higher Q-factor comes with a larger number of frequency bins and more roundtrips of electric field propagation.

The RK4IP method involves computing Fast-Fourier Transformation (FFT) and inverse-FFT four times for a single roundtrip of ring cavity (see Appendix B for the source code). To accelerate the computation speed, we implement the RK4IP algorithm in two different approaches; one is to make use of GPU-accelerated FFTs and the other is to write it in C with the *FFTW* library. For the former method, the Matlab script is written such that the frequency array is directly stored in and processed by the GPU. The array of the steady-state fields is called back to the RAM. In this method, we were able to speed up a single run of the simulation by a factor of 10 compared with using only Matlab built-in FFT executed by the CPU. On the other hand, the *FFTW* library provides high-speed FFTs

on the very large array. Our C script can be directly called by Matlab's MEX-function. Although a single simulation time is two times slower than pure Matlab GPU-accelerated simulation, the main advantage of this method is to massively parallelize a batch of simulations. For example, if we want to calculate the conversion efficiency as a function of the incident pump powers or the propagation losses, then the simulations for individual power values or losses can be assigned to different cores and run simultaneously.

Finite-difference eigenmode solver: Lumerical MODE

For the tapered waveguide with Butt couplers, the assumption of the constant transverse modes over the field propagation breaks down. The tightly localized mode in the waveguide is gradually transformed to the field distributed over the cladding. Thus, the forementioned separation of the electric field variable and the method of calculating the transverse and longitudinal modes separately are no longer valid.

We use a different numerical technique to obtain the efficiency of the power transfer from the waveguide to the optical fiber. The strategy is first to discretize the waveguide with multiple cells along the propagation direction and obtain the supported eigenmode in each cell by solving the Maxwell's equation in frequency domain via a finite-difference eigenmode (FDE) solver. Then, boundary condtions at each cell interface are applied to formulate scattering matrices. The amount of the power transfer from one cell to the next can be efficiently calculated from coupling coefficients from one mode to the other. Lumerical MODE provides accurate methods for the FDE solver and the bi-directional mode propagation via their US patented Continuously Varying Cross-sectional Subcell (CVCS) method. The beauty of using this method is that, once the modes are calculated for all the cells, the propagation length can be modified without having to recalculate the modes. Also, the computational time scales well with propagation distance, and therefore it is very useful for optimizing tapered waveguides or mode convertors.

4.4 Detailed design analysis

In this section, we discuss the detailed analysis for the designed QFT and estimate the conversion efficiency. The structural parameters are listed in Table 4.1. Based on the numerical simulations for the ring cavity and pulley waveguide, we calculate the optical characteristics of the device such as phase-matched pump wavelengths, optical nonlinearity, and coupling Q-factor, as summarized in Table 4.2. The following are the detailed assessment to each subsystem.

Table 4.2: Optical properties of the designed QFT from 985 nm ($m_S = 607$) to 785 nm ($m_S = 777$). The structural parameters are summarized in Table 4.1. The zero-dispersion wavelength λ_{ZDW} and optical nonlinear coefficient γ as well as the effective mode area A_{eff} were obtained by the simulation with COMSOL multiphysics. The wavelengths of the pump fields λ_{P1} and λ_{P2} satisfy the phase-matching condition. The coupling Q-factor $\mathcal{Q}_c = \hat{\omega}_m/\kappa_m^2$ was calculated using Equation 4.21.

Derived parameters		Description
λ_{ZDW}	1028.83 nm ($m = 579$)	Zero-dispersion wavelength
λ_{P1}	1064.64 nm ($m = 557$)	Pump1 wavelength
λ_{P2}	1469.47 nm ($m = 387$)	Pump2 wavelength
A_{eff} (S, T, $P1$, $P2$)	0.653, 0.589, 0.676, 0.798 (μm^2)	Effective mode area
γ (S, T, $P1$, $P2$)	2.44, 3.40, 2.18, 1.34 ($W^{-1}m^{-1}$)	Nonlinear coefficient
$\mathcal{Q}_c$ (S, T, $P1$, $P2$)	3.13, 9.26, 4.01, 1.66 ($\times 10^5$)	Coupling-Q factor of ring cavity

4.4.1 Ring cavity and phase-matching condition

The key aspect in the design of the ring cavity is to engineer the dispersion for the efficient frequency translation from $\lambda_{\mathrm{S}} = 985$nm to $\lambda_{\mathrm{T}} = 785$nm with one pump at around $\lambda_{\mathrm{P1}} = 1064$nm and the other at the telecom S-band. The 2D FEM eigenmode solver outputs a collection of eigenfrequencies $\{\hat{\omega}_m\}$ with the azimuthal mode number m and the corresponding eigenmode profiles of the resonant TE modes, as shown in Figure 4.6. Our approach to find the phase-matched pump wavelengths is following. First, we find the resonant modes closest to the signal $m_{\mathrm{S}} = 607$ (985 nm) and target wavelength $m_{\mathrm{T}} = 777$ (785 nm), and record the mode number difference $\Delta m = m_{\mathrm{S}} - m_{\mathrm{T}} = 170$. Then, we search two pump modes that are separated by the same mode number Δm, ensuring the momentum conservation, and minimize the phase-mismatching function $\Delta\hat{\omega}_m = \hat{\omega}_{m_{\mathrm{S}}} - \hat{\omega}_{m_{\mathrm{T}}} + \hat{\omega}_m - \hat{\omega}_{m+\Delta m}$. We obtained the two pump modes $\lambda_{\mathrm{P1}} = 1064.64$nm ($m_{\mathrm{P1}} = 557$) and $\lambda_{\mathrm{P2}} = 1469.47$nm ($m_{\mathrm{P2}} = 387$) with $\Delta\hat{\omega}_{m=557} = -1.26$GHz.

We evaluated the effective mode area from the obtained field profiles using Equation 4.12 and obtained the optical nonlinearity of the ring cavity, as shown in Figure 4.6(c). The wavelength dependency of the effective mode area originates from mainly two factors: first, the wavelength-dependent refractive indices of the Si_3N_4 and SiO_2 materials and second, the relative size of the optical potential well, i.e., the geometric distribution of the dielectric materials, to the wavelength of the guided field. The averaged value over the four fields is estimated to be $A_{\mathrm{eff}} \approx 0.68\,\mu\mathrm{m}^2$ which corresponds to the optical nonlinearity $\gamma \approx 2.34\,\mathrm{W}^{-1}\,\mathrm{m}^{-1}$.

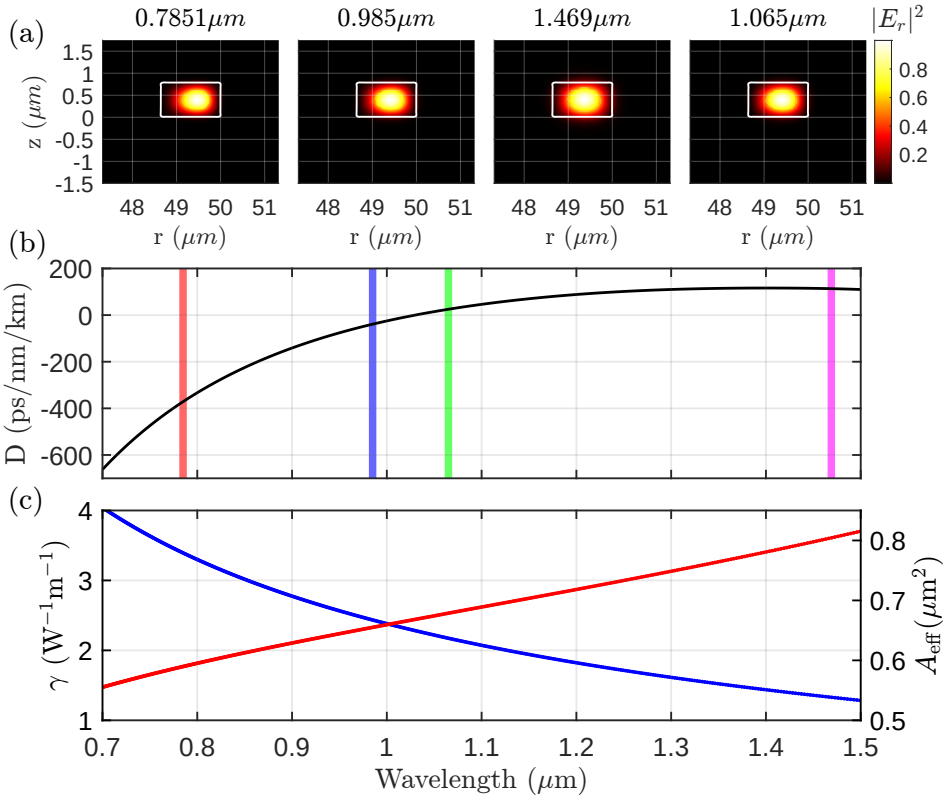

Figure 4.6: Optical properties of the designed ring cavity. (a) The color maps of the intensity profiles of the four resonant modes. (b) The group velocity dispersion D. (c) The optical nonlinearity γ and effective mode area A_{eff} as a function of the wavelength.

We investigate the dependency of the phase-matched pump wavelengths to the structural variation of the ring cavity, i.e., width, thickness, and radius. This is because the designed structure will never be exactly same as the real device, and the absolute value of the phase-mismatching doesn't have much meaning. Rather, it is more useful to study the tendancy or sensitivity of the phase-matched wavelengths to the structure parameters. Figure 4.7 shows the variation of the optimal pump wavelengths as a function of the different geometric parameters. The least-squares method with a linear function is applied to quantify the sensitivity. It is observed that the phase-matching condition exhibits the highest sensitivity to the ring width $\sim$0.5 nm nm^{-1} and the least dependency on the ring radius $\sim$3 nm µm^{-1}.

Note that the sign of the sensitivity to the ring width appears to be opposite to the other

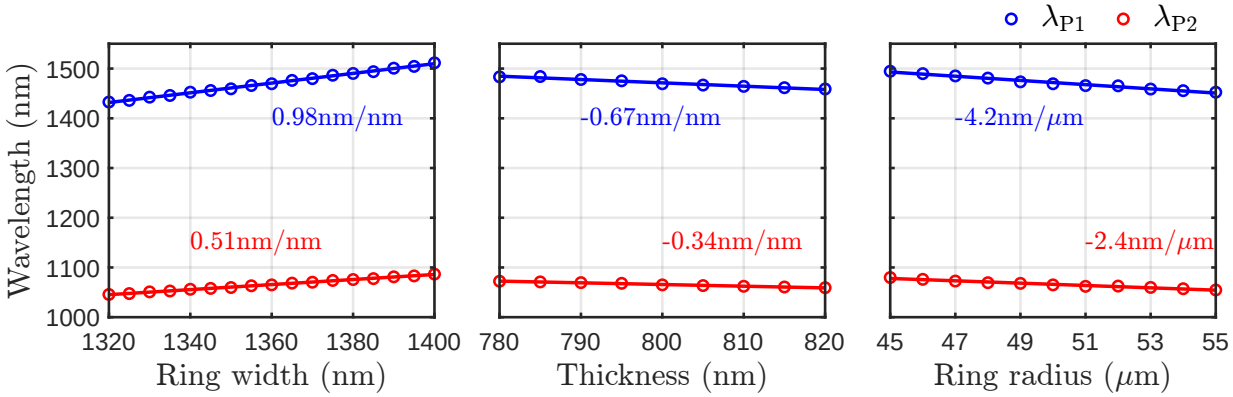

Figure 4.7: Phase-matched pump wavelengths as a function of structural parameters of the ring cavity: (a) width, (b) thickness, and (c) radius. When one parameter varies, the other two parameters are fixed at the value listed in Table 4.1.

two parameters. This feature could be utilized to compensate the wavelength variation due to the imperfact fabrication process. One of the standard methods to measure the thickness in the fabrication process is to use an ellipsometry after the film deposition and then double-check it with a stylus profilometer after patterning the structure. A typical precision of this measurement for a 1 µm–thick sample is 5 nm to 10 nm. The thickness variation may be compensated by adjusting the width of the ring cavity, and eventually the phase-matching condition can be optimized by tuning the radius during the experiment. One example to adjust the ring cavity size is to apply voltages across the piezoelectric materials placed at the center of the ring, as demonstrated in the reference [145].

4.4.2 Pulley coupler and overcoupling regime

The pulley coupler is designed to maintain the ring cavity operating in the overcoupling regime. We assume that the propagation loss in the Si_3N_4 waveguide is $0.05\,\mathrm{dB\,cm^{-1}}$, and its corresponding intrinsic Q-factor is around one million which sets the maximum value of our coupling Q-factor. We obtained the eigenmodes for both the straight waveguide and the curved waveguide, and calculated the coupling coefficient κ_m including the point-contact and pulley regions, as shown in Figure 4.8(b). The coupling Q-factor for the point-contact coupler (black solid line) dramatically decreases as the wavelength increases. It varies from $\mathcal{Q}_c \sim 10^8$ at $\lambda \sim$650 nm to $\mathcal{Q}_c \sim 10^5$ at $\lambda \sim$1500 nm. On the other hand, the coupling-Q factor for the designed pulley waveguide lies well below a million at all four wavelengths.

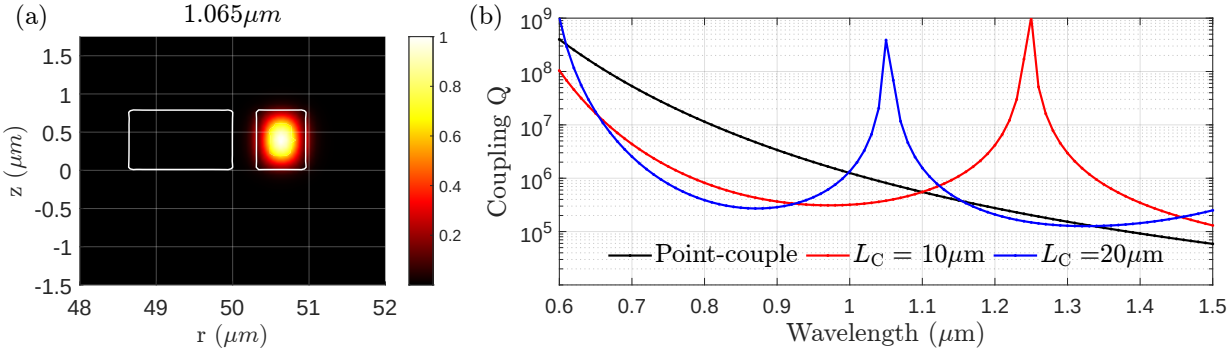

Figure 4.8: Simulation results of the designed pulley coupler. (a) The color map of the normalized intensity profile of a pump mode at the wavelength of 1065 nm. The white squares represent the refractive index distribution of the cross section of the ring cavity (left) and the pulley coupler (right). (b) The coupling-Q factor as a function of wavelength.

The coupling Q-factor shows a peak in a certain wavelength, which originates from the phase-matching between the two guided modes in the curved waveguide and the ring cavity. The two coupled modes exchange the electromagnetic energy during the propagation, and the exchange rate is determined by their phase difference. For a fixed coupling length L_C, the coupling of the two modes destructively interfere at a certain wavelength, and therefore effectively increases the reflectivity of the ring cavity. The peak position can be located at the desired wavelength by adjusting the coupling length, as shown in Figure 4.8(b).

4.4.3 Frequency-translation efficiency

We evaluated the frequency-translation efficiency by solving the GNLSE-IM via the RK4IP method. We detuned one of the pump fields $\omega_{\mathrm{P1}} = \hat{\omega}_{\mathrm{P1}} + \Delta\hat{\omega}$ by the frequency mismatch $\Delta\hat{\omega}$ =−1.26 GHz while keeping the other pump on resonant. Figure 4.9(a) shows the spectrum of the steady-state intracavity fields at the incident pump powers $P_{\mathrm{P1}} = P_{\mathrm{P2}}$ =20 mW. The present target field with the high magnitude compared with other spurious field, e.g., conjugated fields, indicates the dominant FWM-BS process in the ring cavity, which justifies the isolation of only four modes for the analytical discussions in Section 4.2.2. This is further verified by the comparison of the numerically obtained conversion efficiency with the analytical solution in Equation 4.18, as shown in Figure 4.9(b)-(d). Note that the solutions for the pump fields in Equation 4.14 are obtained including the self- and cross-phase modulations, and the steady-state pump fields are substituted into the Equation 4.18.

We first evaluated the efficiency η at the output of the waveguide as a function of the

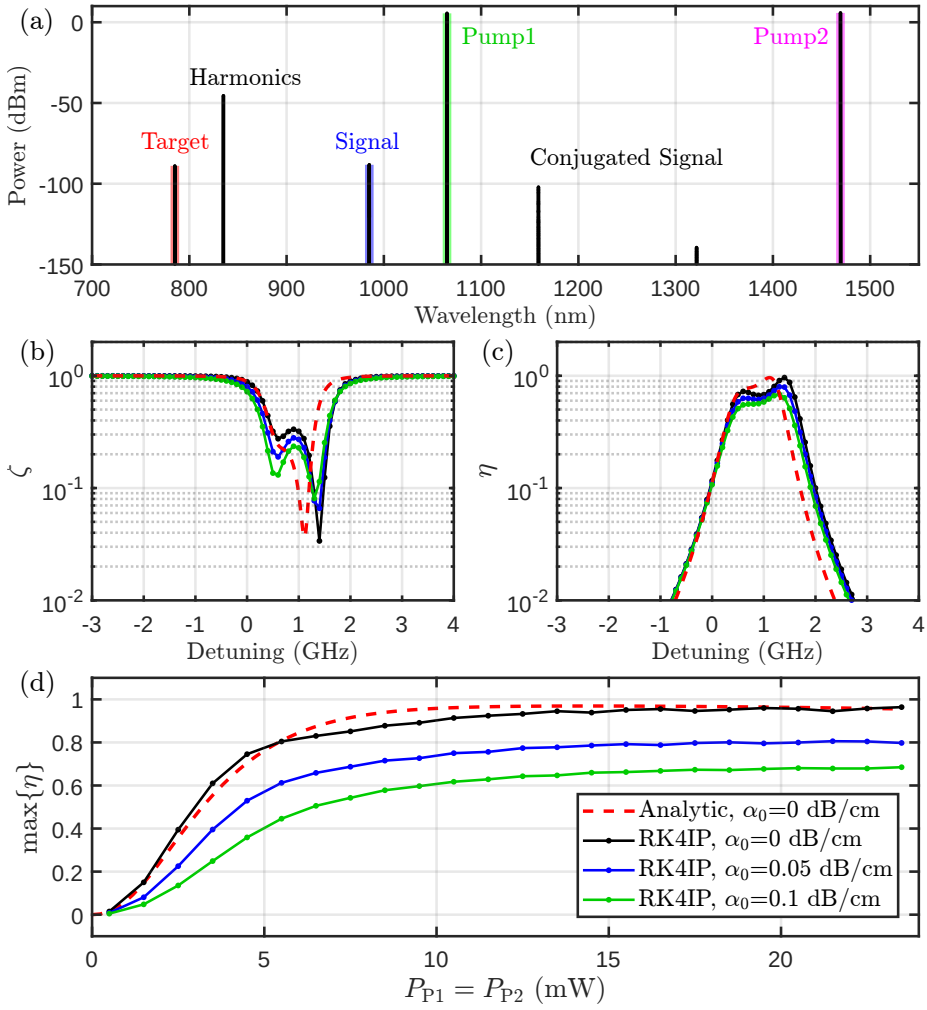

Figure 4.9: Numerical evaluation of quantum frequency-translation efficiency in the designed ring resonator. (a) The spectrum of steady state intracavity fields at the incident pump powers $P_{\mathrm{P1}} = P_{\mathrm{P2}}$ =20 mW. (b) Signal depletion rate ζ at λ_{S} =985 nm and (c) frequency-translation efficiency η at λ_{T} =785 nm as a function of the signal detuning. (d) The maximum frequency-translation efficiency at the detuned frequency as a function of the incident pump power $P_{\mathrm{P1}} = P_{\mathrm{P2}}$.

signal detuning, as shown in Figure 4.9(b) and (c). We observed that the strong intracavity pump fields shift the resonant frequencies of the signal and target modes via the cross-phase modulation. The different shifting rate between the four resonant frequencies limits the

conversion efficiency as clearly seen in the analytical solutions. Also, the resonant mode is split into two peaks as the pumps drive stronger, indicating the strong coupling between the signal and target modes. In this region, the conversion process becomes too fast for the on-resonant signal field to be coherently accumulated inside the ring cavity, and the optimial conversion process occurs at the detuned frequency. This phenomenon can also be interpreted in the dressed picture of two-level atomic system, as discussed in reference [293].

Figure 4.9(d) plots the maximum conversion efficiency $\max\{\eta\}$ as a function of the incident pump field. This includes the efficiencies for the detuned signal fields. The maximum possible conversion efficiency $\max\{\eta\}$ =95 % can be achieved at the single pump power $P_{\mathrm{P1}} = P_{\mathrm{P2}}$ =15 mW for the lossless medium $\alpha_0 = 0$. With moderate propagation loss α_0 =0.05 dB cm^{-1}, the 80 % is attainable with the similar pump power. We emphasize that this high efficiency was obtained after taking into account all possible the nonlinear interactions among all resonent modes. Remarkably, the excellent agreement of our numerical result with the analytical solution further supports that the unwanted processes are well suppressed in our system and the efficiency is mainly limited by the propagation loss of the ring cavity.

4.4.4 Interface to standard optical fibers: Butt coupler

Finally, we discuss the last piece of our QFT design: Butt couplers and the tapered waveguides. As shown in Figure 4.10, we evaluated the single-mode fiber (780-HP, Nufern) coupling efficiency η_{B} for various waveguide structures. The waveguide thickness was fixed to 800 nm due to the availability of the Si_3N_4–deposited wafers and the width was determined by the pulley waveguide.

We first varied the width of the Butt coupler W_{TF} and calculated the Butt coupling coefficient η_{B} from the eigenmode profiles for the waveguide and the fiber using the Lumerical MODE. The highest attainable coupling efficiency for 785 nm and 985 nm were found to be over 95 % at the waveguide width of 100 nm and 120 nm, respectively. The nominal coupling efficiency for the pump fields is estimated to be around 80 % to 90 %.

We next study the efficiency of the optical power transfer from the waveguide to Butt coupler through the linearly tapered waveguide. With the tapered region divided into thirty cells, we computed the eigenmodes for the individual cross sections of the cells, as shown in Figure 4.10(a). The eigenmodes are propagated bi-directionally using the CVCS method in the Lumerical MODE. We found that the transfer efficiency doesn't change once the length is greater than 100 µm.

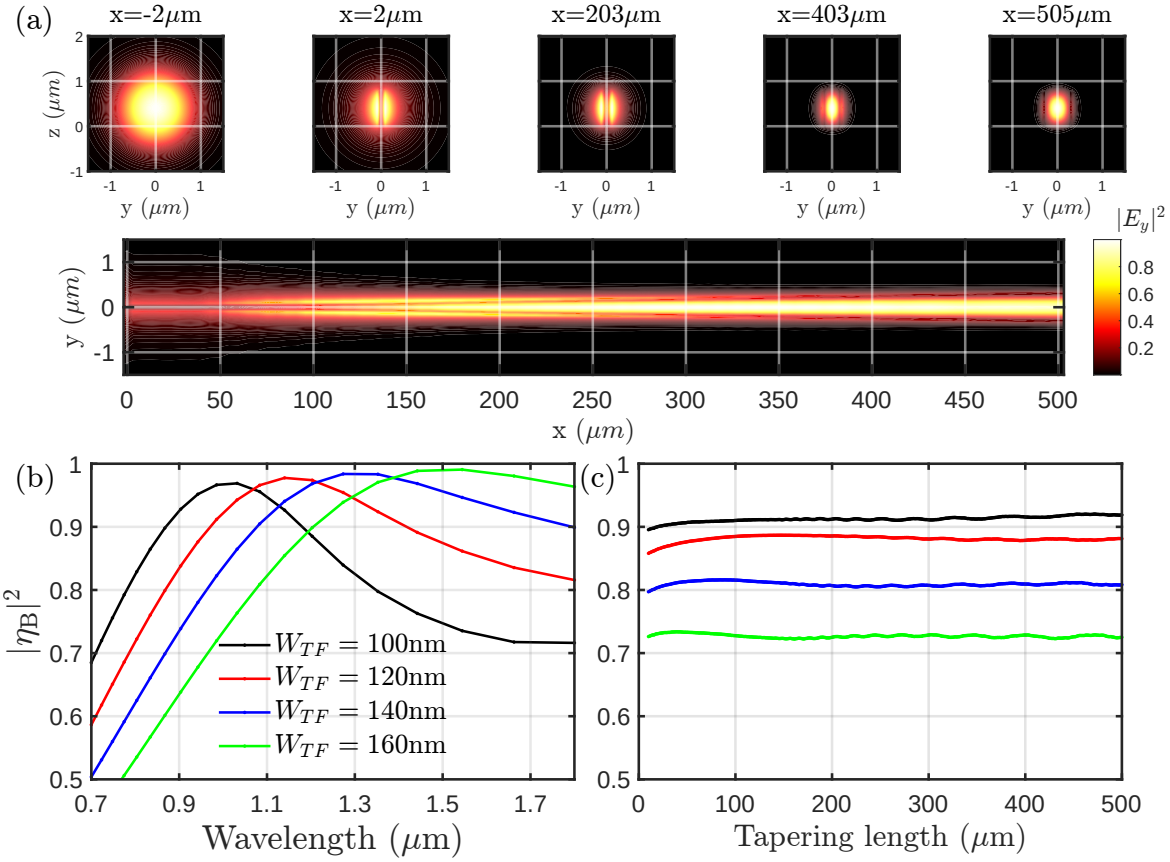

Figure 4.10: Simulation results of the designed Butt coupler. (a) The color maps of the intensity profiles of the guided mode in the tapered waveguide. (b) The estimated coupling efficiency to a single-mode fiber (780-HP, Nufern) as a function of the wavelength. (c) The coupling efficiency as a function of the tapering length at 985 nm.

4.5 Progress in experimental demonstrations

4.5.1 Timeline

The realization of the designed QFT requires the multiple iterations of the fabrication and characterization process. We planned to fabricate the device in the nanofabrication facility at the NRC, and then characterize it in the QPL. Our first goal was to validate our design method by experimentally testing basic properties of the ring resonator, e.g., free-spectral ranges and Q-factors, with simplified sample devices. During the test, we expected to

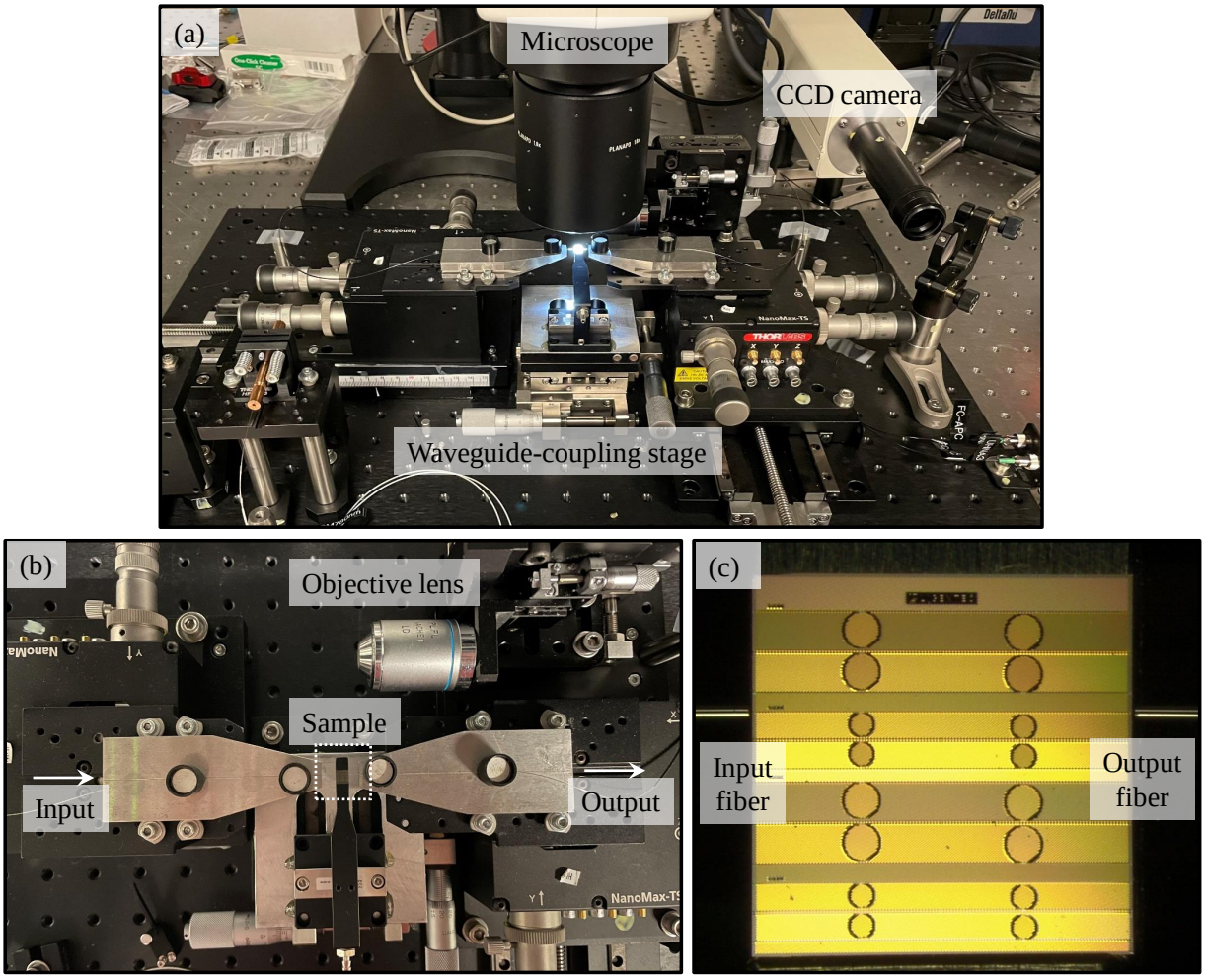

Figure 4.11: Photographs of the experimental setup for the characterization of ring resonators. (a)–(b) The waveguide-coupling setup developed in October 2020. (c) A test sample of ring resonators fabricated by the company LIGENTEC.

obtain the precise model for the refractive indices of the materials, which will then be used for the final design for the frequency translation.

The development of the design method started in August 2018 and it was completed in January 2020. The implementation of the characterization platform in the QPL required procuring equipment such as lasers, microscopes, and fiber-coupling stage. I visited the NRC for a week to learn the laboratory setup and characterization procedures for the

nanophotonic device in March 2019. We prepared the required hardware and the initial characterization system in February 2020. My second visit to the NRC to fabricate the test sample was planned in the late March 2020. However, the experimental activities were hampered by the COVID-19 which stopped all visitor's access to the NRC laboratory. As an alternative, we procured two test samples from a company named LIGENTEC in October 2020. Also, our NRC collaborator provided us with two samples whose structural parameters are closer to one of our designed QFT.

4.5.2 Experimental setup

Figure 4.11 shows our experimental setup for the characterization of ring resonators. Incident fields at 785 nm and 1480 nm were generated by two external cavity diode lasers and then delivered through an ultra-high numerical aperture fiber (UHNA3, Nufern). The output fields from the ring resonators were coupled to a single-mode fiber for the examination of transmission as a function of the detuning frequency of the incident field. The two fibers were mounted on three-axis translation stages (MAX313D, Thorlabs) for the precise position control. The sample device which possesses multiple ring resonators with different design parameters was placed on an optical waveguide sample holder (F273-5, MiSUMi) which can be manually translated in a plane parallel to the optical table.

The injection to and collection from the waveguide of the ring resonator were achieved by the following procedure. First, we translated the input fiber close to the sample and precisely adjusted the position of the fiber tip near the waveguide. The process was monitored through a stereo microscope (M125C, Leica) whose magnification can be tuned from 12.8 to 160. To ensure that the incident field is coupled to the waveguide (not guided through the slab), we image the output field profile by using a high-NA objective lens and a CCD camera. Then, the coupling of the incident field is further optimized by maximizing the power of the output field. Finally, we switch the objective lens with the optical fiber to couple the output field.

4.6 Alternative approach using photonic crystal fibers

In this section, we present our study of an alternative approach for the frequency translation from 985 nm to 785 nm using a polarization-maintaining endlessly single-mode photonic crystal fiber (PM-ESPhCF). The idea of placing the pump wavelengths far enough from the zero-dispersion wavelength for the suppression of the unwanted nonlinear processes

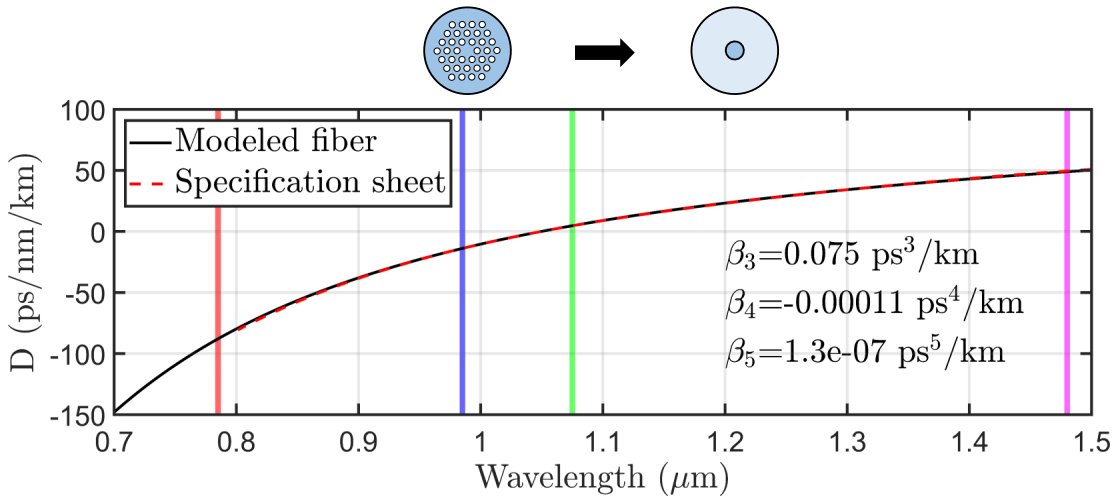

Figure 4.12: Group-velocity dispersion for the endlessly single-mode photonic crystal fiber which is modeled as a cylindrical single-mode fiber with large core-to-clad refractive index difference. The $\beta_n = \partial^n\beta/\partial\omega^n$ is the coefficient of the Taylor expansion of the dispersion with respect to the zero-dispersion wavelength.

can also be applied same for the fiber system [172]. We procured the 100 m–long PM-ESPhCF (ESM-5-125-PM, Photonics Bretagne) whose dispersion with the zero-dispersion wavelength at 1050 nm is similar to the designed ring resoantor.

4.6.1 Theoretical modeling for frequency translations in optical fibers

Our PM-ESPhCF can be effectively modeled by a cylindrical single-mode fiber with the large core-to-clad refractive index $\Delta n = 0.12$ and the 5 µm core diameter. In this way, the eigenmodes and eigenfrequencies (and propagation constants) can be analytically calculated [6]. Figure 4.12 shows the comparison between the group velocity dispersions calculated with the modeled fiber and the specification of the PM-ESPhCF provided by the manufacturer. The close agreement between the two dispersions indicates the validity of the approximation. The propagation constant $\beta(\omega)$ is Taylor-expanded with respect to the zero-dispersion wavelength ω_0 as

$$\beta(\omega) = \omega - \omega_0 + \beta_1(\omega - \omega_0) + \frac{\beta_2}{2!}(\omega - \omega_0)^2 + \cdots \tag{4.24}$$

with $\beta_n = \partial^n\beta/\partial\omega^n|_{\omega_0}$. Our fiber exhibits a high $\beta_3 \approx 0.075\text{ps}^3/\text{km}$, indicating a good suppression of spurious FWM process and the MI. The electric field profiles of the eigenmodes are used to calculate the optical nonlinearity $\gamma \sim 10\,\text{W}^{-1}\,\text{km}^{-1}$.

The phase-matched pump wavelengths are λ_{P1} =1075 nm and λ_{P2} =1480 nm with the zero-dispersion wavelength around λ_{ZDW} =1050 nm. In the optical fiber-based QFT, it is important to ensure the availability of the pump lasers which provide high pump power and the narrow spectral linewidth. A few watts of pump powers at λ_{P1} =1075 nm and λ_{P2} =1480 nm can be readily obtained by Ytterbium-doped fiber amplifiers and Raman amplifiers, respectively. One could also implement an optical parametric oscillator to obtain the two pump fields.

It is worth noting that there are a few practical disadvantages in our configuration. First, optical elements must operate in a broad wavelength range, i.e., 785 nm to 1500 nm. In particular, the objective lens for the fiber coupling must be achromatic over the wavelength range from 985 nm to 1480 nm. One way to address this issue is to fiber-couple the pump and signal fields into three different fibers and combine them with fiber-based wavelength multiplexers whose output port may be spliced with the PM-ESPhCF. The second issue is the very narrow phase-matching bandwidth at 785 nm and 1480 nm which is attributed to the long fiber length and the higher-order dispersions. This means that one must prepare the incident fields whose the linewidth is narrower than the phase-matching bandwidth for the efficient frequency translation.

We numerically solved the GNSLE via RK4IP algorithm for the modeled PM-ESPhCF with the length of 100 m. We included the propagation loss α =20 dB km^{-1} based on the specification sheet. The frequency translation efficiency $\eta = |A(\omega_T)|^2/|A(\omega_S)|^2$ is calculated as a function of the incident pump powers $P_1 = P_2$, as shown in Figure 4.13(b). The conversion efficiency can also be obtained by the analytical solution in Equation 4.6 with the assumption that the nonlinear process occurs only among the four fields, i.e., two pumps, signal and target, and the pump fields are undepleted (black line in Figure 4.13(a)). Our simulation predicted that the maximum conversion efficiency 63 % can be achieved at the incident pump power $P_{\text{P1}} = P_{\text{P2}} \sim 750$ mW, which is mainly limited by the propagation loss. The excellent agreement between the numerical and analytical results indicates that the spurious FWM and the MI are negligble, and the contribution from the fourth-order dispersion does not significantly reduce the conversion efficiency.

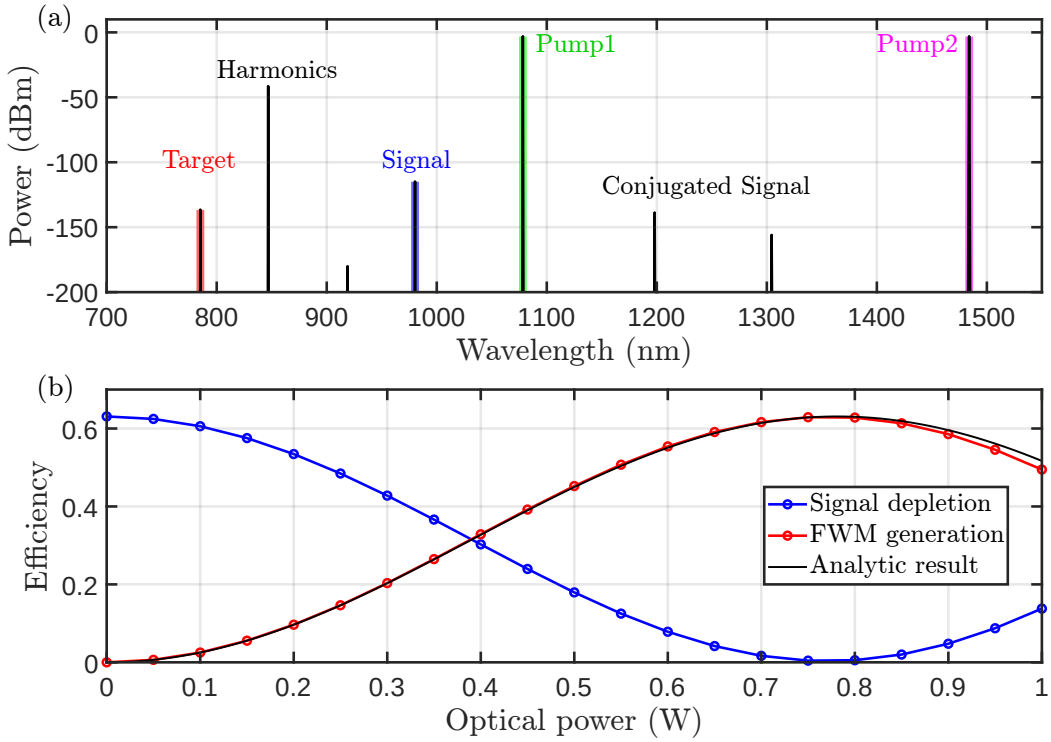

Figure 4.13: Numerical simulation of the four-wave mixing Bragg-scattering process for the modeled 100 m–long PM-ESPhCF. (a) The spectrum of the electric fields evaluated at the output of the fiber with incident pump powers $P_{\mathrm{P1}} = P_{\mathrm{P2}} = 0.75$W. (b) The frequency-translation efficiency as a function of incident pump powers. A close agreement with the analytical expression in Equation 4.6 indicates that the spurious FWM process is negligible.

4.6.2 Experimental setup

Figure 4.14 illustrates our experimental setup. Due to the availability of lasers in our lab, we rearranged the signal, target, and pump wavelengths and demonstrated the frequency translation from λ_{S} =785 nm to λ_T ∼1075 nm. The two pump fields are produced from a picosecond mode-locked pulse laser (Tsunami, Spectra-Physics) at λ_{P1} =985 nm and a fiber-Bragg grating laser diode (FBG-LD, QFBGLD-1480-500, Qphotonics) at λ_{P2} =1480 nm. The signal field is generated from an external cavity diode laser (ECDL) at wavelength of λ_{S} =785 nm. The 100 m–long PM-ESPhCF is coiled with the radius greater than 20 cm.

All three laser fields, i.e., two pumps and signal, are combined into a single spatial

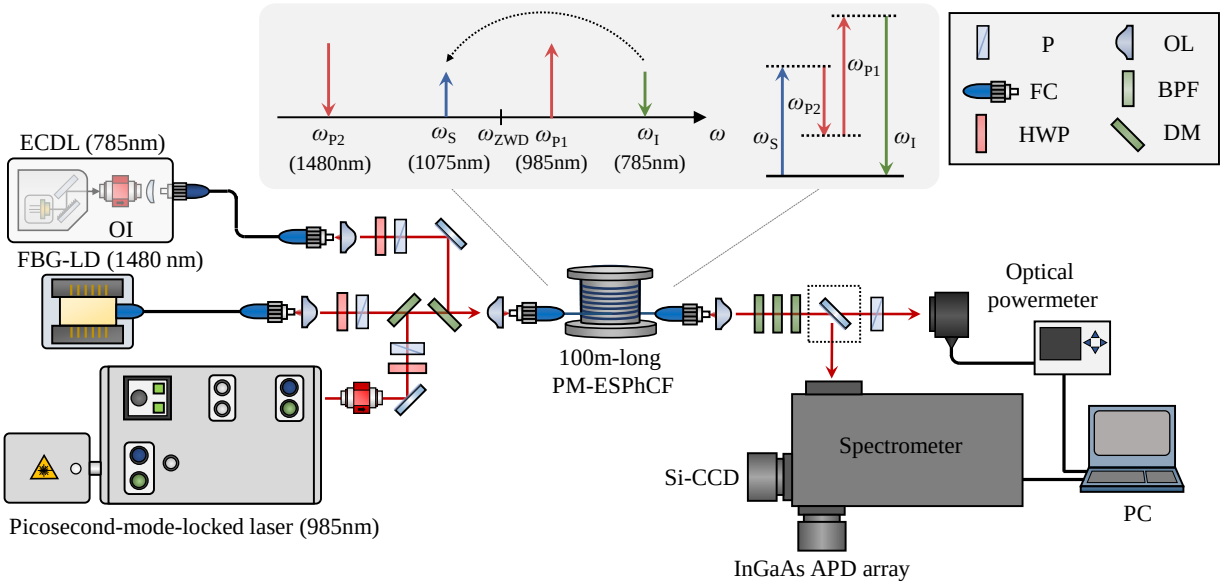

Figure 4.14: A schematic drawing of the experimental setup for optical frequency translation from 985 nm to 785 nm; ECDL, external cavity diode laser; DBG-LD, fiber-bragg grating wavelength-stabilized laser diode; OI, optical isolator; Si-CCD, silicon-based charge coupled device; APD, avalanche photodiode; P, polarizer; OL, objective lens; DM, dichroic mirror; BPF, bandpass filter; FC, fiber connector; PM-ESPhCF, polarization-maintaining endlessly single-mode photonic crystal fiber.

mode by dichroic mirrors and coupled into the 100 m–long PM-ESPhCF through a high-NA objective lens (C110TMD, Thorlabs). Due to the chromatic dispersion of the objective lens and the uncoated lens surfaces, the achieved fiber coupling efficiencies were 10 %,40 %, and 20 % at the wavelengths of λ_S =785 nm, λ_{P1} =985 nm, and λ_{P2} =1480 nm, respectively. The spectral properties of generated FWM field and the conversion efficiency are characterized by a high-precision optical spectrometer and an optical powermeter, respectively.

4.6.3 Results

Phase-matching condition and bandwidth

We generated the FWM field at the wavelength of around λ_T ∼1100 nm for the input signal at λ_S =786.4 nm with the pumps operating at λ_{P1} =965 nm and λ_{P2} ∼1480 nm, as shown in Figure 4.15. The spectral linewidth (FWHM) of the generated FWM field is

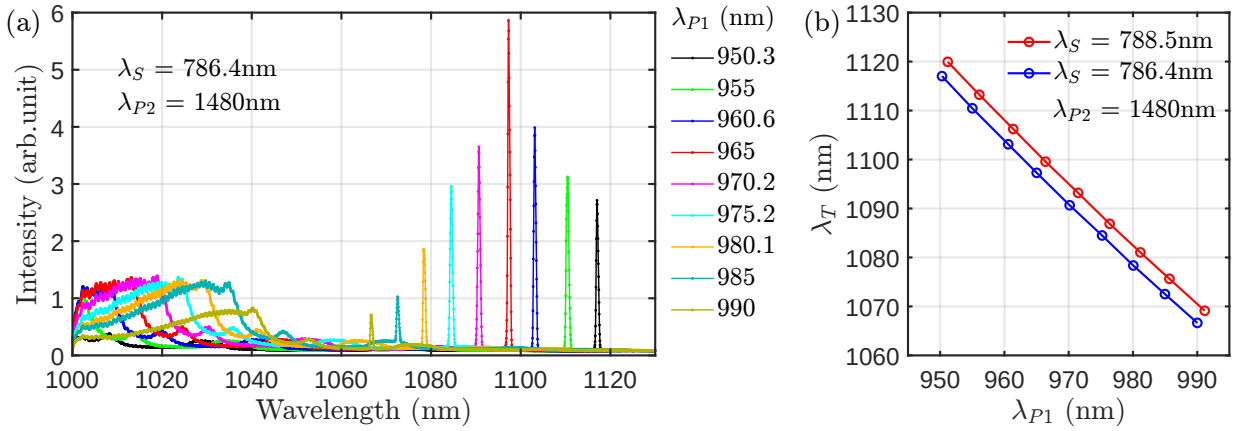

Figure 4.15: Measured spectra of the frequency-translated field. (a) The measured spectra of the FWM field at different pump wavelength λ_{P1}. (b) The wavelength of the generated FWM light λ_T as a function of the central wavelength of an incident pump field λ_{P1}.

measured to be (0.5 ± 0.1) nm, which is mainly limited by the spectral resolution of the measurement apparatus. We varied the wavelength of one of the pumps from λ_{P1} =950 nm to 990 nm with the other fixed at λ_{P1}=1480 nm. The central wavelength of the FWM light was translated according to the phase-matching condition. Although the output power of the generated FWM field varies, this shows the wavelength tunability for our frequency transducer. Also, note that the presence of the strong spontaneous Raman-scattered light, as shown in Figure 4.15(a), limits the minimum input power of the incident signal field, which is a main bottleneck in the current setup to be used for the frequency translation with quantum light.

There are commercially available lasers producing the power over 2 W with the wavelength tunability from 1060 nm to 1080 nm. For example, FLT photonics has developed a ASE-free tunable fiber laser which can be a potential replacement for our mode-locked pulsed laser, which makes it possible to perform the frequency translation for QD-SPS at wavelength from 970 nm to 990 nm to the 785 nm QEYSSat quantum channel wavelength. A strong suppression of the Raman noise from anti-Stokes photons is also expected after the replacement which may make the system suitable for quantum light with the increased signal-to-noise ratio.

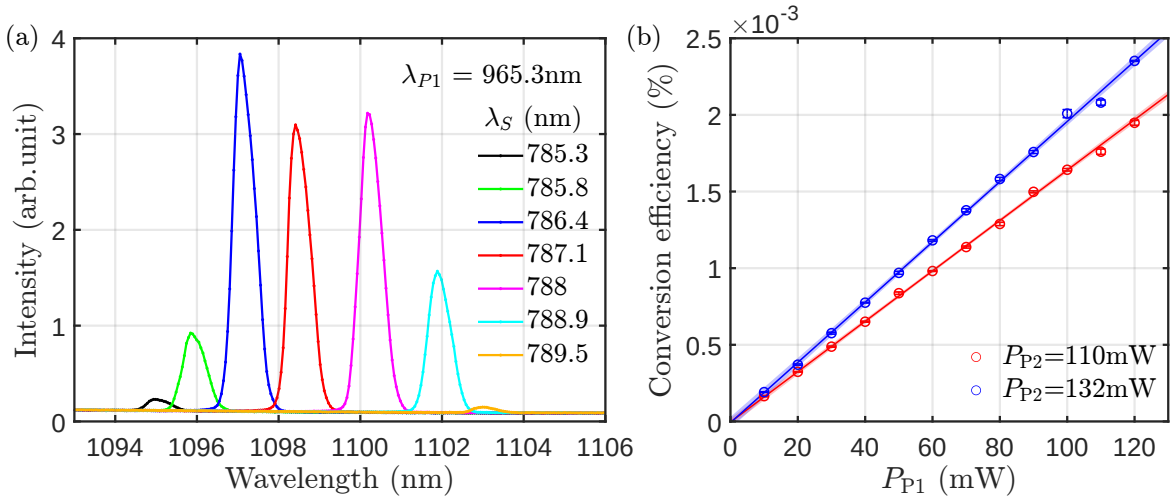

Figure 4.16: Measured spectral bandwidth and efficiency of the optical frequency translation. (a) The measured FWM spectra at different incident signal wavelength λ_S. (b) The frequency-translation efficiency as a function of the incident pump power.

Frequency-translation bandwidth and efficiency

We characterized the frequency-translation acceptance bandwidth by tuning the input signal wavelength while the two pump wavelengths are fixed. Assuming that all the laser linewidths are very small (delta-function spectra), the phase-matching bandwidth at 785 nm, 965 nm, and 1480 nm for the 100m-long fiber were calculated to be 0.002 nm, 0.03 nm, and 0.0015 nm, respectively. This means that, if we sweep the wavelength of the signal laser light and fix the wavelength of the pump lasers, the FWM light must be generated with the acceptance bandwidth of 0.002 nm. However, we found that the intensity of the FWM light was maintained over 50 % over the 3 nm tuning range of the signal field, as shown in Figure 4.16(a), which is three orders of magnitude greater than the theoretical estimation. This is mainly attributed to the broad linewidth of the pump lasers being used. The spectral linewidth (FWHM) of the mode-locked laser at 985 nm and the FBG-LD at 1480 nm were measured to be 0.06 nm and 0.71 nm, respectively, as shown in Figure 4.17. We confirmed that the acceptance bandwidth was reduced to less then 1 nm after replacing the FBG-LD with an external cavity diode laser (OSICS ECL-1480, Yenista) operating at 1480 nm.

As shown in Figure 4.16(b), the frequency-translation efficiency, which is defined as the ratio of the average power of the FWM field to the incident signal field, was measured as a

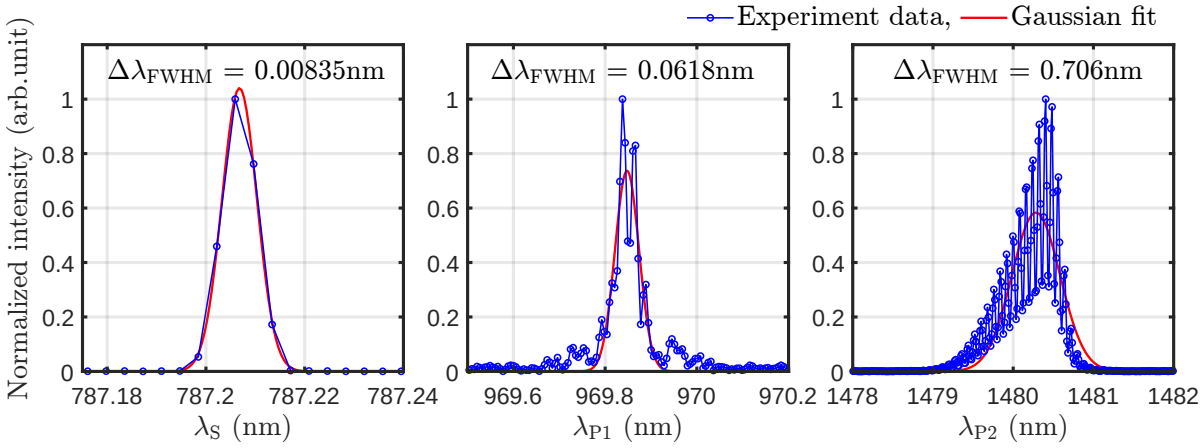

Figure 4.17: Measured spectral linewidths of three lasers for signal and two pump fields.

function of the incident pump power. The 1.7×10^{-5} conversion efficiency was obtained at the average pump power of $P_{\mathrm{P1}} = P_{\mathrm{P2}} = 110\,\mathrm{mW}$. This includes the system efficiency such as the transmissions of the filters and dichroic mirrors. The obtained efficiency is three orders of magnitude smaller than the theoretical expectation, which is mainly attributed to the broad linewidth of the FBG-LD being used: three orders of magnitude broader than the phase-matching bandwidth.

4.7 Chapter summary and outlook

4.7.1 Summary

We studied two different approaches for frequency translations. First, we designed and analyzed a Si_3N_4 ring resonator for the frequency translation from 985 nm to 785 nm via four-wave mixing Bragg-scattering (FWM-BS) process. The device is fully characterized by numerical simulations, and the linear and nonlinear dynamics of intracavity fields are accurately modeled by coupled mode equations under the approximation of weak coupling between the ring cavity and waveguide. A finite element eigenmode solver was utilized to precisely evaluate the optical properties of the designed ring resonator, e.g., nonlinear interaction strength and cavity-assisted field enhancement. Then, the Kerr nonlinear dynamics among the entire resonant modes was computed to estimate the frequency-translation efficiency. The frequency transducer is designed to interface with standard single-mode fibers via transverse mode engineering with the tapered waveguide and Butt couplers.

The frequency-translation process in our designed QFT is driven by two pump lasers operating at the 1065 nm and 1469 nm wavelengths. By engineering the dispersion of the ring cavity, we ensured that the phase-matching condition is satisfied for FWM-BS process while suppressing the modulation-instability process and spurious FWM process. The pulley coupler was designed to operate the ring cavity in the overcoupling regime at the wavelengths of the four fields. The designed QFT performs the maximum conversion efficiency of 80 % achieved at 20 mW pump powers after accounting the 0.05 dB cm^{-1} propagation loss. The numerical estimation showed a good agreement with analytical solutions for the coupled mode equations with only four isolated modes, which verifies the excellent suppression of the spurious FWM process.

Secondly, we utilized a 100 m–long photonic crystal fiber exhibiting high optical nonlinearity. We theoretically modeled and experimentally demonstrated the frequency translations from 785 nm to 1076 nm by using a commerical photonic crystal fiber pumped by two lasers operating at 985 nm and 1480 nm. Our theoretical analysis predicted a high conversion effieciency, which however experimantally was not achieved primarly due to the lack of high-quality pump lasers. We characterized the spectral properties of the generated FWM field and the efficiency of the frequency translation. With the verified phase-matching conditions under different pump wavelengths, we anticipate that our frequency transducer is capable of translating the wavelength for quantum-dot-based single-photon sources operating at around 970 nm to 990 nm to our QEYSSat quantum wavelength range 780 nm to 795 nm.

4.7.2 Future work

Experimental demonstration of the frequency translation using a ring resonator

Our design method for ring resonators will be verified by experimentally testing sample devices in the future. Two important parameters must be measured and compared with the simulations: the free-spectral ranges and Q-factors at the wavelengths of the four fields (signal, target, and two pumps). The free-spectral ranges will provide the dispersion of the ring cavity which determines the phase-matching condition. The coupling Q-factor can be estimated by the measured (loaded) Q-factor with the pre-characterized propagation loss. The characterization requires the precise measurement of the intensity variation of the output field as a function of the incident field detuning in the range of 10 GHz with the tuning step size of less than 1 GHz. This can be achieved by using electro-optic modulators to tune the sideband frequency of the input field whose fundamental frequency is stabilized to a certain atomic transition.

The demonstration of the frequency translation will be performed in the future. The conversion efficiency and signal-to-noise ratio will be investigated for the feasibility of using quantum-dot single-photon sources. One experiment we can conceive is to prepare two identical frequency transducers which can translate the wavelength from 790 nm to 985 nm at the pump wavelengths of 1106 nm and 1550 nm. One of them can be directly used to translate the wavelength from 1550 nm to 985 nm with the pumps operating at the other two wavelengths. Then, we could use our polarization-entangled photon source, which is presented in Section 2.4, and the wavelengths of the emitted photon pairs are translated to 985 nm by the two frequency transducers. The indistinguishability between the two frequency-translated photons can be examined, e.g., Hong-Ou-Mandel interference, which can helps characterizing the functionality of the frequency transducers.

Polarization-modulated frequency translation using a photonic crystal fiber

One of the technical challenges in using QD-SPSs for free-space quantum communications is to modulate the polarization states of the generated single photons. Most of the QD-SPSs produce one particular polarization state of the emitted photons, and one has to insert polarization-modulation components before sending the photons through an optical transmitter. High-speed polarization-modulators, such as phase-modulators, come with insertion loss of typically 3 dB. Also, most of the high-speed modulators are developed at the telecom wavelengths. The photon loss is critical because single photons cannot be amplified unlike weak coherent pulse sources.

One of the future works using the fiber-based frequency transducer is the polarization-modulation of the frequency-translated field by altering the polarization states of the pump field. This is inspired by the polarization-insensitive frequency tranlsation which has been implemented with both classical and quantum fields [279, 116]. The replacement of the varying polarization states of the incident signal photons with one of the pump fields is expected to have the same effect on the output polarization of the frequency-translated field due to the symmetric arrangement of the four waves. However, as discussed in Section 2.3.3, two non-orthogonal pump polarizations cause nonlinear polarization rotations via self- and cross-phase modulation for all pumps, signal and target states.

We propose that our beam-displacment Sagnac interferometer can be used for the polarization-modulated frequency translation, as depicted in Figure 4.18. In this case, unlike the demonstration in Section 2.2.3, only one beam displacer is required because the polarization state of the FWM field is parallel to the pumps as in type-0 photon-pair generation process. The two frequency translation processes at orthogonal polarizations, i.e., horizontal $|H\rangle$ and vertical $|V\rangle$, are superposed inside the Sagnac loop. In the proposed

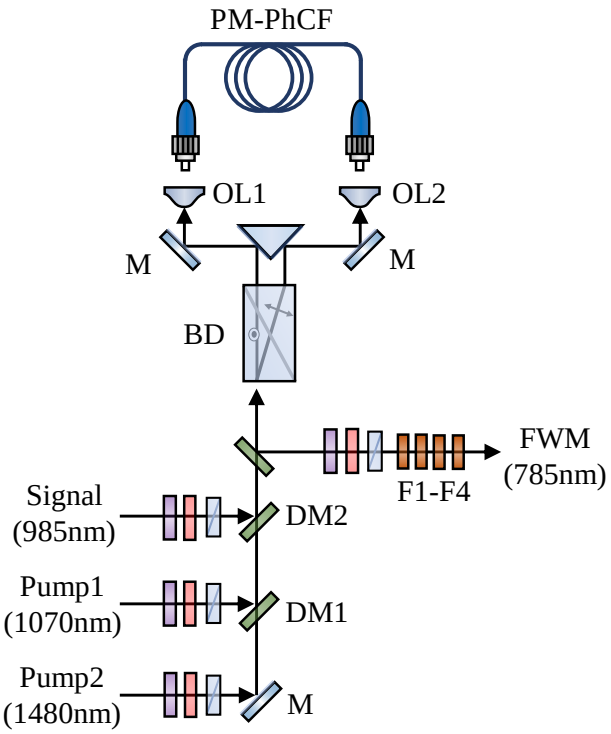

Figure 4.18: Proposed experimental scheme for polarization-modulated frequency translation. See Figure 4.14 for the optics labels and acronym.

scheme, the polarization states of the input signal photons and one of the two pumps are initially prepared at diagonal state $|D\rangle = 1/\sqrt{2}\,(|H\rangle + |V\rangle)$. Then, we modulate the polarization states of the other pump to one of the four polarization states of diagonal, antidiagonal $|A\rangle = 1/\sqrt{2}\,(|H\rangle - |V\rangle)$, right-circular $|A\rangle = 1/\sqrt{2}\,(|H\rangle + i|V\rangle)$, and left-circular $|L\rangle = 1/\sqrt{2}\,(|H\rangle - i|V\rangle)$. We expect the output FWM states will vary according to the pump state due to the angular momentum conservation.

Chapter 5

Hybrid nanophotonic platform with neutral atoms for universal quantum matter

In Chapter 4, quantum frequency transducers using ring resonators provided the means of interfacing quantum light sources at different wavelengths with ground-to-satellite quantum links. The underlying physics was a coherent mode conversion of electromagnetic quanta (e.g., from signal frequency mode to target mode) provided by the optical nonlinearity of the classical dielectrics. However, this nonlinear optical process is only strong when the photon-number states are linearized. That is, the total energy of the photonic system is linearly proportional to the number of photonic excitations, which is mainly due to the absence of quantum dielectrics, e.g., single quantum emitters. The underlying Hamiltonian is a beam-splitter type and does not generate non-classical states on its own. As a result, there is no photon-photon interaction; the quantum state of one photon depends on the other, e.g., controlled single-qubit gates. Note that this is distinguished from parametric amplification processes (discussed in Chapter 2) which indeed generate non-classical states, i.e., squeezed states.

In this chapter, we introduce quantum dielectrics (neutral atoms) into nanophotonic devices, forming a hybrid nanophotonic platform with strong light-matter interactions. From the work of cavity quantum electrodynamics (QED), there is a plethora of research where individual quantum systems are exploited as the resource for generating interesting quantum states in the regime of strong coupling domain. In this domain, strong interactions between photons are possible and allow the functionalization of otherwise passive dielectrics

(e.g., an optical cavity). The scope of this chapter is to explore quantum many-body physics with an array of atoms whose photon-exchange interactions are engineered by the tailored electromagnetic vacuum of dielectrics. That is, whereas the earlier chapters may concentrate on the quantum channels and interfaces, what we try to address in this chapter is a pathway to create the quantum nodes through light-matter interactions. The main contents of this chapter was preprinted in arXiv:

Y. Dong, J. Taylor, Y. S. Lee, H. R. Kong, and K. S. Choi. Waveguide QED toolboxes for universal quantum matter. arXiv:1712.02020v4 (2021) [76]

I am allowed by the policies of arXiv and by permision from my co-authors to republish part of the work here.

Statement of contributions

The research presented in this chapter was conducted in the UQML group from January 2017 to April 2018 under the supervision of Prof. Kyung Soo Choi.

- **Development of the theoretical framework for universal quantum matter using waveguide QED system**
  Dr. Ying Dong and Prof. Kyung Soo Choi conceived the idea of the proposed waveguide QED system and carried out the theoretical analysis. Jacob Taylor carried out the tensor-network numerical simulation. Hyeran Kong performed Schrieffer-Wolf analysis of the SU(N) models and field theories. I designed photonic crystal waveguides and performed the computations of electromagnetic Green function, which supported the feasibility of realizing the proposed scheme. Prof. Kyung Soo Choi provided an initial version of Matlab code to calculate the Green function using FDTD solvers. I wrote the Scheme codes to calculate photonic band structures and Casimir-Polder potentials. Prof. Kyung Soo Choi and I procured and assembled the UQML-Andromeda cluster server.

- **A cluster UHV system and other experimental activities**
  Prof. Kyung Soo Choi and I conceived the overall architecture of the ultra-high vacuum (UHV) system and planned the experimental setup. I designed, procured, cleaned, and air-baked the components for the cluster UHV system under the supervision of Prof. Kyung Soo Choi. Hyeran Kong provided the procedure and equipment for cleaning and air-baking UHV components. I designed the sample transporter with the docking stage for the loadlock system. I implemented and tested the presented electronics based on the circuit diagram provided by Prof. Kyung Soo Choi, Dr. Chang Liu, and Hyeran Kong.

5.1 Introduction

Fundamental light-matter interaction is one of the most impactful subjects to our life and there is a long history of its understanding and manipulation. With the birth of cavity QED [297] and technolgoical advances in quantum optics, the atom strongly coupled with a single-mode electromagnetic field has now become a toolbox to store and process the quantum information of the individual photonic quanta [156]. The manipulation of the internal states of atoms and the coherent information exchange between photons and atoms can be precisely controlled with very high success probability (>99 %) [35, 248]. Many different physical platforms have emerged to emulate such a perfectly controllable atomic system with the ambition to coherently link them by quantum channels to form universal quantum computers or simulators, e.g., circuit QED, quantum dots, NV center [114, 125].

With the network of atomic systems, one of the exciting frontiers in quantum information science is the realization of complex many-body systems [156]. The idea is to explore condensed matter physics by naturally mapping a complex many-body Hamiltonian to physical quantum spin networks and investigating its time evolution followed by a set of measurements. This bottom-up approach allows us to understand exotic quantum matter from the perspective of quantum information science, e.g., long-range entanglements in topological quantum phases of matter [59]. Researchers have realized such quantum many-body systems using a quantum network of atoms in lattices [109], Rydberg atoms [43], and quantum degenerate gases inside single- or multi-mode optical cavities [210].

Hybrid nanophotonic system with cold atoms has merged as the paradigmatic platform for engineering long-range spin models with unprecedented complexities [56]. With recent developments in atom-photon interfaces with photonic crystals [148, 163, 147, 132, 282, 283, 101, 100, 121], there has been significant interest towards assembling quantum many-body systems by garnering the control over individual quantum systems [184, 13, 33]. The coherently driven atoms under the tailored electromagnetic vacuum by the presence of exotic dielectrics exhibit a unique feature of engineering their mechanical interactions, as discussed in the following sections.

In this chapter, we present the theoretical and experimental effort toward the realization of a fully programmable quantum spin network in a waveguide QED system with neutral atoms and photonic crystals. In Section 5.2, we describe our proposed waveguide QED system which allows designing the interactions between atoms with any combination of SU(2)-spin operators. In Section 5.3, we provide a quantum optics theory used to design and analyze a conceivable experimental platform with nanophotonic structures. In Section 5.4, we focus on the detailed design considerations for a photonic crystal waveguide and present our custom-built computational resource. In Section 5.5, we present the

detailed analysis on the designed nanophotonic structure to show the feasibility of realizing our proposed scheme. We evaluate coherent spin-spin interaction rate between atoms and correlated spontaneous decay rates. Also, the accurate calculation of Casimir-Polder force and Stark shifts shows the formation of a stable trapping potential for a string of Cesium atoms near the designed structure with appropriate illumiation of laser fields. In Section 5.6, we summarize our experimental progress with our custom-built cluster UHV system.

5.2 Motivation

5.2.1 Background: photon-mediated atom-atom interactions in waveguides

Our goal is to develop a network of atoms with the connectivity provided by atom-light interactions in a waveguide QED system. On the one hand, the internal spin states of atoms must be interfaced with a photonic channel such that the information of the matter qubits must be efficiently read out without dissipating into environments. On the other hand, the type and strength of the interactions between the atoms, i.e., the connectivity of the network, must be engineered to simulate other quantum systems.

To contrast the unique feature of waveguide QED systems with photonic crystals, we first consider one of the simplest waveguide QED systems: an array of two-level atoms trapped near a cylindrical waveguide, as depicted in Figure 5.1(a). We consider the waveguide with the core diameter smaller than the wavelength λ of the guided field, e.g., nanofiber, where the majority of the field propagates through the cladding, e.g., air, and therefore there is substantial overlap between the photon's transverse mode and optical scattering cross-section. The optical properties of the guided field is determined by the dispersion relation of the waveguide, as shown in the inset of the Figure 5.1(a). In this setup, we characterize coupling strength between the atoms and the guided photons by spontaneous decay rate of the atoms into the guided mode (GM) Γ_{1D} given as

$$\Gamma_{1D} = \frac{1}{2}\frac{c}{v_g}\sigma_0 A_{\text{eff}}(\vec{r}_A)\Gamma_0. \tag{5.1}$$

Here, Γ_0 is the free-space decay rate in the absence of the dielectric and v_g is the group velocity of the guided field oscillating at the transition frequency of the atoms with c denoting the vacuum speed of light [57]. σ_0 and A_{eff} are the optical cross-section and the

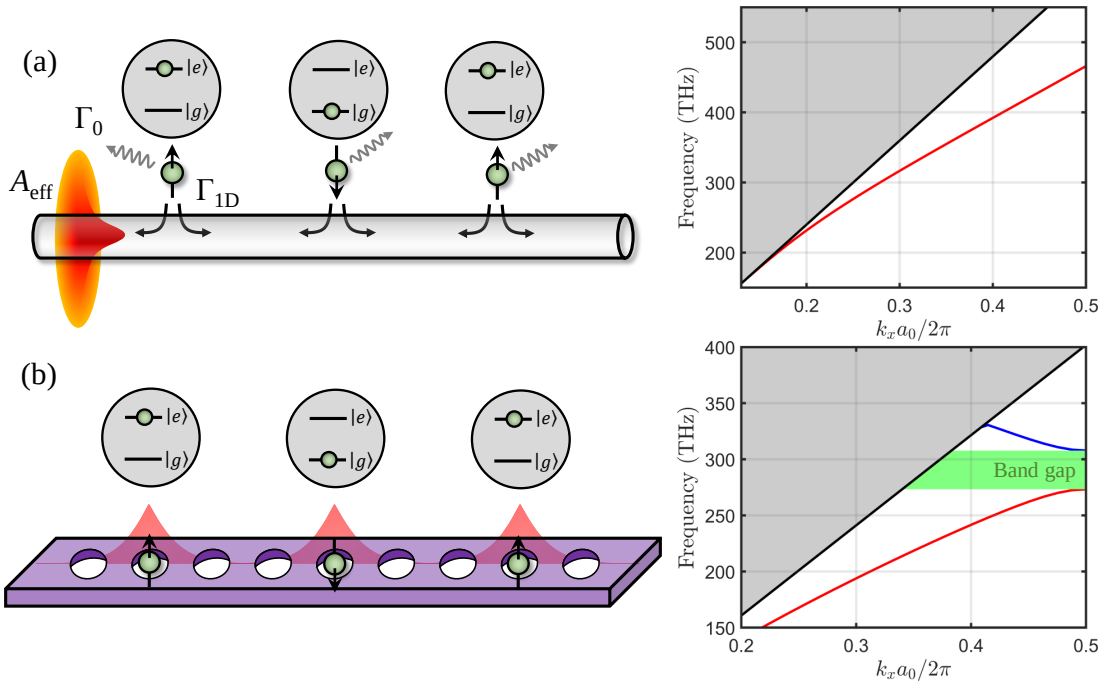

Figure 5.1: Examplary waveguide QED systems with neutral atoms. (a) An array of two-level atoms interacting with each other through photons guided through a tapered nanofiber and (b) a photonic crystal waveguide. The interactions between the atoms are governed by dispersion relations of the nanofiber and waveguide (right).

effective mode area of the guided mode, respectively. We desire the strong atom-photon coupling, i.e., $\Gamma_{1D}/\Gamma_0 \gg 1$, for the efficient interface between the atoms and photons. As clearly shown in Equation 5.1, the strong atom-photon coupling can be obtained by a slow group velocity $v_g \ll c$ and a small effective mode area $A_{\text{eff}} \ll \lambda$.

In the context of realizing quantum many-body physics, much of interesting dynamics take place with the off-resonent atom-light interaction. When the optical frequency of the guided field is detuned from the transition frequency of the atoms, a photon emitted from one atom virtually populates the GM and reabsorbed by another atom, thereby effectively mediating spin-exchange interactions between the atoms. Therefore, the atom-light coupling rate is directly related to the photon-mediated spin-exchange rate. The coherent spin-spin interaction rate is desired to be greater than any other dissipation rate in order to investigate the spin dynamics of the atoms. Also, the capability of engineering individual interactions between atoms is crucial for mapping high-dimensional and complex

Hamiltonians onto 1D or 2D lattice atoms. However, systems with monolithic waveguides only provides all-to-all connections with the fixed interaction strength among trapped atoms.

Photonic crystal waveguides (PhCWs) provide both the strong atom-light coupling and the tunability of photon-mediated spin-spin interactions. As shown in Figure 5.1(b), the periodic and highly contrast distribution of dielectrics exhibits an exotic dispersion relation, i.e., photonic bands, with the tightly confined GM [146]. In particular, the presence of a photonic band gap (PBG) provides a unique feature of atom-light interactions. For example, when the atomic transition frequency is resonant with the guided mode at the band edge, the high effective mass of the guided field significantly reduces the group velocity and this slow-light effect dramatically enhances the atom-photon coupling rate. The strong atom-light interaction assisted by the PhCW acting like an optical cavity stimulates collective dissipations of the atoms into the GM (e.g., superradience [100]) while suppressing dissipations into other environmental modes. The enhanced spontaneous decay rate into a single photonic mode (i.e., Purcell-effect) has been actively exploited in quantum-dot applications [186].

With the atomic transition frequency resides within PBG (i.e., detuned from the band edge), the underlying lattice of atoms cannot dissipate propagating waves into the GMs of the photonic structure. However, in a strong coupling regime, where the atom-light coupling rate is much greater than any other dissipation rates, the mere presence of the atoms at sites seeds dynamic defect modes which support stable atom-field bound states in the form of exponentially decaying evanescent waves [148, 163, 78, 262, 50], as depicted in Figure 5.1(b). The large effective mass provided by the flat band edge leads to a short localization length for correlations in "many-body" photon Hamiltonian, which tranlsate to tightly localized atom-photon bound states in the bandgap [148]. From the perspective of quantum optics, the localization is related to the presence of squeezed states in the vicinity of the atom, which becomes classical radiation as they exit the dielectric media [99]. This tightly localized fields mediate short-range spin-exchange interaction between the adjacent atoms [113, 104]. The complex spin-exchange strength can be engineered for atoms coupled to 1D photonic crystals with auxiliary Raman sidebands and digital time-steps [184], which has been utilized for a wide range of translationally-invariant pairwise models for quantum magnetism [131].

The effective spin-exchange interaction between the atoms through the localized photons results from the modified electromagnetic vacuum of the dielectric, consisting of both the passive photonic structure and the active emitters. Such a quantum dielectric is inherently renormalized by the strong coherent and dissipative radiative forces between the atoms, i.e., photonic Lamb shifts. In other words, the spin-exchange interaction can be

viewed as a van der Waals-type interaction which originates from a vacuum (in our case, virtually populated photon in the GM)-driven dipole-dipole interaction. Such a nanoscopic quantum force modifies the mechanical vacuum of the atomic motion. Then, Bogoliubov phonons can be distributed across the atomic sample as a collective bath that in turn couples to the spin system.

5.2.2 Waveguide QED system for universal quantum matter

We will specifically harness the coherent coupling between atomic motion and internal states in a 1D PhCW for the realization of an analogue universal quantum simulator. Our approach is based upon the unique capability of a PhCW to induce strong photon-mediated forces between proximal neutral atoms and to create many-body atomic states of internal spin and external motion. In particular, we utilize the coupling of spin matter to atomic motion generated by *spin-independent* forces of the synthetic vacuum of the PhCWs to mediate the underlying long-range spin-spin interactions. In our approach, translationally-variant binary interaction $\hat{H}_{i,j} \approx \sum_{\alpha,\beta} J_{\alpha,\beta}^{(i,j)} \hat{\sigma}_{\alpha}^{(i)} \hat{\sigma}_{\beta}^{(j)}$ between spins i,j is arbitrarily designed for any combination of SU(2)-spin operators $\hat{\sigma}_{\alpha}^{(i)}$, $\hat{\sigma}_{\alpha}^{(j)}$ with α,$\beta \in \{x, y, z\}$. More generally, our spin network allows complex Hamiltonian graphs with connectivity that can no longer be represented by spatial lattices and dimensions, thereby realizing a universal 2-local Hamiltonian in an analog quantum system.

Universal quantum matter

In 1996, Seth Lloyd showed that quantum computers can be programmed to simulate other quantum systems [184]. Universal quantum simulators, which means the quantum computer capable of simulating any other quantum systems, can be obtained by applying a series of gate operations in the pre-defined orders with digitized time steps. The idea is supported by that any Hamiltonian with local interactions can be represented by the summation of a set of the Hamitonians whose time evolutions are accurately controlled. Nowadays, this quantum computer running numerical simulations for other quantum systems is referred to as "digital quantum simulators". This approach requires an error correction with large number of physical qubits as generally needed for running quantum algorithms in quantum computers.

Alternatively, our approach is to prepare a physical system whose time evolution naturally emulates other quantum systems, also known as "analogue quantum simulators" [47]. In 2018, Cubitt *et al.* proved that the arbitrary SU(2) binary Hamiltonian, which can be

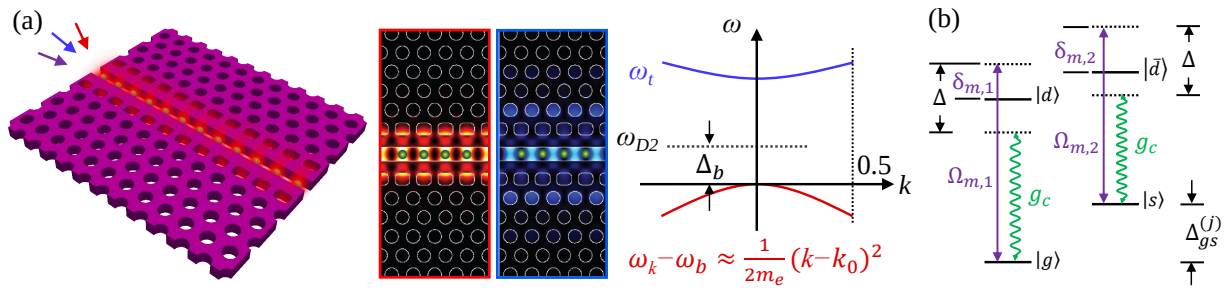

Figure 5.2: Proposed many-body waveguide QED system. (a) An examplary waveguide QED spin network. A slotted squircle photonic crystal waveguide enables a versatile platform for highly tunable defect guided modes. Green spheres represent the trapped atoms whose resonant frequency for electronic excitation is detuned by Δ_b with respect to the frequency of the guided mode ω_b. (b) Two laser fields $\Omega_{m,1}$, $\Omega_{m,2}$ with detunings $\delta_{m,1}$, $\delta_{m,2}$ create strong photonic Lamb shifts between two atoms localized within a photonic bandgap. The bandgap is detuned by Δ with respect to the laser frequencies.

realized in our proposed waveguide QED system, belongs to one of the universal Hamiltonian families which can replicate all other quantum many-body Hamiltonians [70]. This means that an arbitrary Hamiltonian can be efficiently mapped on a lattice or an array of atoms by engineering the interaction properties between any two atoms. Also, the simulation can be performed at any desired accuracy without requiring the quantum error corrections. More importantly, one can create the case that the interesting model does not really exist in the digital quantum simulators, whereas an analogue quantum simulator has all the physical properties of the target system in addition to the time-evolved states. In fact, there are instances of complex models where we anticipate from computational complexities that even a universal quantum computer would not be able to obtain the ground state efficiently.

Our proposed waveguide QED system can be viewed as a prerequisite to synthesize universal quantum matter. The reason why I call "matter" instead of simulators is that the proposed scheme can go beyond simulating other quantum systems and one can even create new quantum states of matter which physically exists (e.g., ultracold atomic cloud levitated inside a vacuum chamber). To be specific, our universal quantum matter is realized in the form of the internal spin states and external motions of atoms as well as light that are all intertwined truly by the electromagnetic vacuum of the dielectric.

Physical platform

As shown in Figure 5.3, our basic building block is a system of neutral atoms strongly coupled to a GM of the 1D PhCW represented by the red line of Figure 5.3(a). The dispersion relation of the GM in PhCW near the band edge $k = k_0$ (corresponding to frequency ω_b) can be approximated by $\omega_k - \omega_b \approx -\frac{1}{2m_e}(k-k_0)^2$ with effective mass $1/m_e = -(\partial^2\omega_k/\partial k^2)$ for the first brillouin zone. The band edge at frequency ω_b is red-detuned by $\Delta_b = \omega - \omega_b > 0$, so that the atomic transition frequency ω_{D2} lies within the band gap. Here, the atom-photon coupling constant is given by $g \approx d\sqrt{\omega_b/4\pi\epsilon_0 A_{\text{eff}}}$ near ω_b where A_{eff} is the effective mode area. We envision that each atom is tightly localized with trap frequency w_t and lattice constant a_0 by a nanoscopic optical potential with a trapping field that populates a higher-order GM (blue line).

Spin-independent dipole-dipole interaction

In our scheme, the atoms exhibit two excited states labelled $|d\rangle$ and $|\bar{d}\rangle$ and two hyperfine ground states $|g\rangle$ and $|s\rangle$, as shown in Figure 5.3(b). A pair of coherent fields $\Omega_{m,1}, \Omega_{m,2}$ are applied to couple the ground states $|g\rangle$ and $|s\rangle$ to the excited states $|d\rangle$ and $|\bar{d}\rangle$, respectively. As discussed previously, the driven atom cannot dissipate into the GM inside the band gap, but form the atom-field bound states in the form of evanescent waves. In the off-resonant regime $f = \Omega_{m,1}/\delta_{m,1} = \Omega_{m,2}/\delta_{m,2} \ll 1$, the virtually populated photon in the GM mediates the atom-atom interactions without alternating their internal spin states. For example, for given two proximal atoms located at the sites i and j that are prepared in four different initial states, the interaction between the atomic spin states and photons in the GM can be expressed as

$$\begin{aligned}
&|g\rangle_i|g\rangle_j|0\rangle \xrightarrow{\Omega_1} |e\rangle_i|g\rangle_j|0\rangle \xrightarrow{g_c} |g\rangle_i|g\rangle_j|1\rangle \xrightarrow{g_c} |g\rangle_i|e\rangle_j|0\rangle \xrightarrow{\Omega_1} |g\rangle_i|g\rangle_j|0\rangle,\\
&|g\rangle_i|s\rangle_j|0\rangle \xrightarrow{\Omega_1} |e\rangle_i|s\rangle_j|0\rangle \xrightarrow{g_c} |g\rangle_i|s\rangle_j|1\rangle \xrightarrow{g_c} |g\rangle_i|d\rangle_j|0\rangle \xrightarrow{\Omega_2} |g\rangle_i|s\rangle_j|0\rangle,\\
&|s\rangle_i|g\rangle_j|0\rangle \xrightarrow{\Omega_2} |d\rangle_i|g\rangle_j|0\rangle \xrightarrow{g_c} |s\rangle_i|g\rangle_j|1\rangle \xrightarrow{g_c} |s\rangle_i|e\rangle_j|0\rangle \xrightarrow{\Omega_1} |s\rangle_i|g\rangle_j|0\rangle,\\
&|s\rangle_i|s\rangle_j|0\rangle \xrightarrow{\Omega_2} |d\rangle_i|s\rangle_j|0\rangle \xrightarrow{g_c} |s\rangle_i|s\rangle_j|1\rangle \xrightarrow{g_c} |s\rangle_i|d\rangle_j|0\rangle \xrightarrow{\Omega_2} |s\rangle_i|s\rangle_j|0\rangle.
\end{aligned} \tag{5.2}$$

As clearly shown in the expression, this photon-mediated spin-exchnage interaction is independent of the atomic internal spin states. In the limit of $fg \ll \Delta$ (i.e., atomic transition frequency residing deep inside the band gap), the quantum dipole-dipole interaction driven by the virtually populated waveguide vacuum may be treated as the mechanical interaction which originates from photonic Lamb shifts $\Delta_{\text{Lamb}}^{(i,j)} = \frac{g_c^2|u_{k_0}|}{\Delta} e^{-|i-j|a_0/L_c}$ with the effective interaction strength $g_c = g\sqrt{2\pi/L_c}$ and the effective interaction range $L_c = \sqrt{1/m_e\Delta}$. Here,

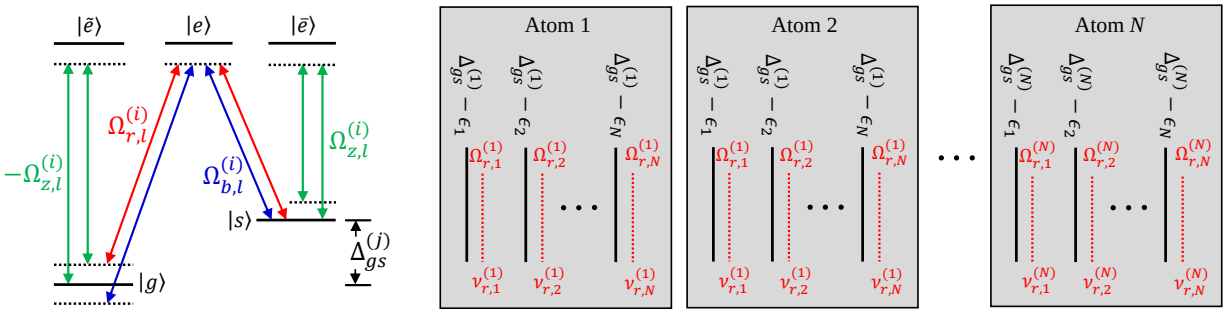

Figure 5.3: Fully programmable spin-spin interactions for any combination of SU(2) spin operators via Raman-sideband engineered spin-motion couplings. (a) Energy level diagram. (b) Raman-sideband engineering. Programmable Raman fields $\Omega_{\alpha,l}^{(j)}$ selectively couples internal spin states $|g\rangle$, $|s\rangle$ of atom j to photonic band $l \in \{1, \cdots, N\}$ with two-photon detuning $\nu_l^{(j)}$. To do so, we need to make sure that each single sideband with frequency $\nu_l^{(j)}$ (red dash line) is nearly resonant to $\Delta_{gs}^{(j)} - \epsilon_l$ (black solid line). For simplicity, we only depict the red sidebands coupling.

Δ denotes the pumping laser detuning from the band edge. If the atomic wavefunction is tightly localized enough such that $x_0 \ll L_c \approx a_0$ with $x_0 = \sqrt{\hbar/2mw_t}$ denoting the zero point fluctuation, this mechanical interaction between the nearest-neighbour atoms yields a collective phononic excitation, as in trapped ions.

Remarkably, unlike trapped ions, the collective phonon spectrum ϵ_l (i.e., the eigenfrequencies of the collective motional states) exhibits high anharmonicity which originates from the exponential function of the mechanical interaction. Also, the phononic Hamiltonian becomes an emergent property of the system, which can then be designed through the electromagnetic vacuum. This would be the qualitative difference, where we can have coherent phononic bath, but also a dissipative one. Moreover, current systems of trapped ions have scalability issues due to the phonon mode spreading. This is because of the 1/r like potential of the phononic interaction which flattens the phonon bands, and reduce the addressable phonon modes. In our case, the interaction is more generally expontential and short-ranged, where the phonon modes do not diminish in the energy difference. Furthermore, this interaction potential may be engineered as well.

Arbitrary spin-spin interaction through collective motions of atoms

We now introduce the Raman-sideband engineering for the phonon-mediated spin-spin interaction. Let us take the red-detuning coupling shown in Figure 5.3(c) as an example. To gain independent control over the interaction coefficients between any atom pair, we need to distinguish the coupling of an individual atom i to a particular Bogoliubov mode l. To do so, we first introduce a site-dependent ground-state energy shift $\hat{H}_A = \sum_i \Delta_{gs}^{(i)} \hat{\sigma}_z^{(i)}$ with $\Delta_{gs}^{(i)} = \Delta_{gs}^{(i)} + g_F m_F B(x_i)$ in the form of a linear Zeeman gradient $B(x_i)$. We require that the ground-state shift $\delta\Delta_{gs}$ between neighboring sites is larger than the width of the phonon spectrum $|\epsilon_N - \epsilon_1|$. This gaurantees that the frequency difference $\Delta_{gs}^{(i)} - \epsilon_l$ is different for all pairs of (i, l), as shown in Figure 5.3(d).

Then, we apply a spatially global Raman field $\Omega_{+,l}^{(i)}$ with N^2 sidebands, i.e., N atoms $\times$ N photon modes, to the atom chain through the GM. Each single sideband with frequency $\nu_{+,l}^{(i)}$ is nearly resonant to $\Delta_{gs}^{(i)} - \epsilon_l$ with detuning $\Delta_l^{(i)}$, thus effectively coupling the spin operator $\hat{\sigma}_+^{(i)}$ to the phononic mode $\hat{b}_l$ only. That is, our Raman fields populate a single guided mode with N^2 sideband modes, which could be generated by a single phase-amplitude modulator. Similar arguments may also be applied to the blue-detuning coupling and Z–coupling. For sufficiently cooled atoms, in the Lamb-Dicke regime, the phonon fields can be adiabatically elliminated, and we obtain the phonon-mediated fully programmable 2-body Hamiltonian

$$\hat{H}_{\text{2-body}} \approx \sum_{i,j,\alpha,\beta} J_{\alpha,\beta}^{(i,j)} \hat{\sigma}_\alpha^{(i)} \hat{\sigma}_\beta^{(j)} + \sum_{i,\gamma} h_\gamma^{(i)} \hat{\sigma}_\gamma^{(i)} \tag{5.3}$$

for any combination of $\alpha, \beta, \gamma \in \{x, y, z\}$ and between any two spins at sites i, j. The spin-exchange rate $J_{\alpha,\beta}^{(i,j)}$ and the bias field $h_\gamma^{(i)}$ can be arbitrarily designed by tuning complex amplitudes of the Raman fields $\Omega_{\alpha,l}^{(i)}$ with $\alpha \in \{+, -, z\}$. The full derivation of the Equation 5.3 with clear mathematical connection between the interaction coefficients $J_{\alpha,\beta}^{(i,j)}$, $h_\gamma^{(i)}$ and the Raman fields are provided in reference [76]. Here, we emphasize that, for any set $\{J_{\alpha,\beta}^{(i,j)}, h_\gamma^{(i)}\}$, at least one solution $\{\Omega_{\alpha,l}^{(i)}, \Delta_l^{(i)}\}$ can be obtained to the target model within certain physical constraints, e.g., laser power.

Many-body QED and simulatable quantum systems

In a larger perspective of many-body QED developed at the UQML group, our waveguide QED system as subcategory employs a photonic crystal which allows photonic clouds with

non-trivial properties, such as chiral and symmetry-protected topology, to dress the atom. The engineering of the photonic bands open the possibility of introducing novel forms of interactions to the atoms, which otherwise are not available in its native form.

The proposed scheme allows engineering the dynamical gauge structure in a completely analog fashion. Our spin-assembly approach provides the toolboxes for universal open quantum many-body systems with complexities far beyond of regular spin lattices heretofore explored. This thesis provides only a summary of our proposed scheme. For more detailed derivation and application to the complex spin network, see the reference [76]. The followings are simulatable quantum systems that were not covered in this section.

- Chiral spin liquids in Kagome lattice
- Interacting SU(n) lattice models
- Detecting the scrambling of quantum gravity with out-of-time-order correlators (OTOC) on the Sachdev-Ye model
- Wess-Zumino-Witten (WZW) conformal field theories (CFTs) for atom strings in photonic crystals, and operator product algebra of the field theory

5.3 Green function formalism for open quantum system with dielectrics

Two key requirements to realize our proposed scheme are the high localization of the atom-field bound state whose effective interaction length is about one lattice constant $L_c \approx a_0$ and the stable trapping potential formed at the anti-nodes of the guided mode function with the sufficient cooling to reach the Lamb-Dicke regime. Also, the dissipation rate of the spin network must be much smaller than the coherent interaction rate. To design a nanophotonic structure satisfying the above requirements, it is necessary to understand how it impacts the internal spin states of atoms as well as their external motions. In this section, we present the quantum optics theory that has recently been developed to describe atom-light interactions in the presence of an arbitrary dielectric by using electromagnetic Green functions. There are a number of great articles and theses [122, 15, 67] which provide a full derviation as well as concise review on this formalsim. Here, we only provide the summary of the main results and their physical interpretations without derivations.

5.3.1 Brief review of the quantization of electromagnetic fields with dielectrics

The attempt to include the dielectrics in the quantization scheme began in 1948 [140], but the full canonical quantization of electromagnetic field with dielectrics which satisfies the causality (e.g., Kramers-Kronig relation) was completed in 1992 by Bruno Huttner and Stephen M. Barnett [134]. The strategy was to explicitly introduce the dielectrics that is microscopically modeled as a collection of bosonic polarization fields, as first introduced by Fano [87], in order to construct the conserved Hamiltonian. The diagonalization of the total Hamiltonian yields a collection of polariton-like bosonic operators $\hat{\mathbf{f}}(\mathbf{r}', \omega)$, i.e., a combination of electromagnetic vacuum and material polarizations, which satisfies the commutation relations

$$\begin{aligned} &[\hat{f}_k(\mathbf{r}, \omega), \hat{f}^\dagger_{k'}(\mathbf{r}', \omega')] = \delta_{k,k'}\delta(\omega - \omega')\delta(\mathbf{r} - \mathbf{r}'), \\ &[\hat{f}_k(\mathbf{r}, \omega), \hat{f}_{k'}(\mathbf{r}', \omega')] = 0. \end{aligned} \tag{5.4}$$

This fundamental electromagnetic excitations are associated with the polarization noise operator $\hat{\mathbf{P}}_{\mathrm{N}}(\mathbf{r}, \omega)$ which describes the polarization fluctuations necessarily tied with the coupling to the lossy reservoir, as expressed in

$$\hat{\mathbf{P}}_{\mathrm{N}}(\mathbf{r}, \omega) = i\sqrt{\frac{\hbar\epsilon_0}{\pi}\,\mathrm{Im}\,\epsilon(\mathbf{r}, \omega)}\hat{\mathbf{f}}(\mathbf{r}, \omega), \tag{5.5}$$

where ϵ_0 and μ_0 are vacuum permittivity and permeability, respectively. Here, the dielectric constant $\epsilon(\mathbf{r}, \omega)$ naturally satisfies the Kramers-Kronig relations.

This quantization approach was extended to inhomogeneous dielectrics by Gruner and Welsch [110] in 1996, which is also known as macroscopic QED. They followed the reverse process of Huttner and Barnett on the basis of Green function expansion. They showed a clear connection between the diagonalized Hamiltonian and macroscopic Maxwell's equations including the Langevin-noise source term [80] as an open system. The electric field operator is given by

$$\begin{aligned} \hat{\mathbf{E}}(\mathbf{r}, \omega) &= i\mu_0\omega^2\sqrt{\frac{\hbar\epsilon_0}{\pi}}\int \mathrm{d}\mathbf{r}'\sqrt{\mathrm{Im}\{\epsilon(\mathbf{r}', \omega)\}}\mathbf{G}(\mathbf{r}, \mathbf{r}'; \omega)\cdot\hat{\mathbf{f}}(\mathbf{r}', \omega) + h.c. \\ &\equiv \hat{\mathbf{E}}^+(\mathbf{r}, \omega) + \hat{\mathbf{E}}^-(\mathbf{r}, \omega), \end{aligned} \tag{5.6}$$

where $\mathbf{G}(\mathbf{r}, \mathbf{r}'; \omega)$ is the dyadic Green fucntion satisfying the classical Maxwell's equation

$$\left[\nabla\times\nabla\times - \frac{\omega^2}{c^2}\epsilon(\mathbf{r}, \omega)\right]\mathbf{G}(\mathbf{r}, \mathbf{r}'; \omega) = \mathbf{I}\delta^{(3)}(\mathbf{r} - \mathbf{r}'), \tag{5.7}$$

where $\mathbf{I}$ is the unity tensor. The Green function satisfies the identity

$$\frac{\omega^2}{c^2}\int \mathrm{d}^3\mathbf{s}\,\mathrm{Im}\{\epsilon(\mathbf{r}',\omega)\}\mathbf{G}_{ik}(\mathbf{r},\mathbf{s};\omega)\mathbf{G}^*_{ik}(\mathbf{r}',\mathbf{s};\omega) = \mathrm{Im}\,\mathbf{G}^*_{ij}(\mathbf{r},\mathbf{r}';\omega), \tag{5.8}$$

which naturally imposes the fluctuation-dissipation theorem. Besides the beauty of incorporating the causality of electromagnetism, the practical advantage of this formalism is that all the information about the dielectric is included in the classical Green function which can be accurately calculated with finite-difference time-domain (FDTD) methods. The physical interpretation of the above expression is that the presence of the dielectric material modifies the electric field even without any sources due to the fluctuation of the material polarization driven by surrounding electromagnetic vacuum.

5.3.2 Atom-light interactions in dielectrics

Now we turn our attention to the interaction between the modified electric field $\hat{\mathbf{E}}(\mathbf{r},t)$ and N two-level atoms, as shown in Figure 5.4. For the atoms being considered as quantum dielectric objects with the internal electronic energy states of $|g\rangle$ and $|e\rangle$ that are separated by an energy $\hbar\omega_A$, the atom-light interaction may be treated to be a collection of quantum dipoles $\hat{\mathbf{d}}$ driven by the electric field, and therefore the interaction Hamiltonian is given as $\hat{H}_{\mathrm{int}} = -\hat{\mathbf{E}}(\mathbf{r},t)\cdot\hat{\mathbf{d}}(t)$. The total Hamiltonian is expressed as

$$\hat{H} = \int \mathrm{d}^3\mathbf{r}\int_0^\infty \mathrm{d}\omega\hbar\omega\hat{\mathbf{f}}^\dagger(\mathbf{r},\omega)\hat{\mathbf{f}}(\mathbf{r},\omega) + \sum_{j=1}^{N}\frac{\hbar\omega_A}{2}\hat{\sigma}_j^z - \sum_{j=1}^{N}\hat{\mathbf{E}}(\mathbf{r}_j,t)\cdot\left(\mathbf{d}_j\hat{\sigma}_j + \mathbf{d}_j^*\hat{\sigma}_j^\dagger\right), \tag{5.9}$$

where the dipole matrix elements are $\mathbf{d} = \langle g|\hat{\mathbf{d}}|e\rangle$ and $\mathbf{d}^* = \langle g|\hat{\mathbf{d}}|e\rangle$, and the Pauli spin operators are the annihilation operator $\hat{\sigma} = |g\rangle\langle e|$ and creation operator $\hat{\sigma}^\dagger = |e\rangle\langle g|$.

Our goal is to study the time evolution of the state of the N atoms represented by the density matrix $\hat{\rho}(t)$ whose equation of motion is referred to as a master equation. The full derivation is lengthy and it is provided in the reference [122] with the detailed explanations step by step. A short recap of the procedure is following. First, we solve the Heisenberg equation for the field operator under the Markov approximation. After some algebra using Green function identity in Equation 5.8 and the Kramers-Kronig relation, we obtain the electric field operator

$$\hat{\mathbf{E}}^+(\mathbf{r},t) = \hat{\mathbf{E}}^+_{\mathrm{free}}(\mathbf{r},t) + \mu_0\omega_A^2\sum_{j=1}^{N}\mathbf{G}(\mathbf{r},\mathbf{r}_j;\omega_A)\cdot\mathbf{d}_j\hat{\sigma}_j(t). \tag{5.10}$$

As clearly shown in Equation 5.10, the modified electromagnetic vacuum is given by the free-space vacuum $\hat{\mathbf{E}}^{+}_{\text{free}}(\mathbf{r},t)$ plus the field generated by the vacuum-driven atomic quantum dipoles propagating through the modified vacuum by the dielectrics which is represented by the Green function. Next, we calculate the Heisenberg equation for an arbitrary atomic operator. After substituting the electric field operator in Equation 5.10 to the Heisenberg equation and converting it from Heisenberg picture to the Schrodinger picture, we obtain the master equation for the atomic state $\hat{\rho}(t)$. One may include a driving field at frequency ω_L with the detuning $\Delta_A = \omega_L - \omega_A$ from the atomic resonance frequency. Following the same procedure in the interaction picture, the driven-dissipative evolution of the reduced density matrix of an atomic system under the Markov approximation is obtained with master equation

$$\dot{\hat{\rho}} = \frac{i}{\hbar}\left[\hat{H}_0, \hat{\rho}\right] + \mathcal{L}[\hat{\rho}], \tag{5.11}$$

where the conservation part is

$$\hat{H}_0 = \sum_{j=1}^{N} \frac{\hbar\Delta_A}{2}\hat{\sigma}_j^z + \sum_{j,k=1}^{N} J_{jk}\hat{\sigma}_j^{\dagger}\hat{\sigma}_k \tag{5.12}$$

and the dissipative Lindblad is

$$\mathcal{L}[\hat{\rho}] = -\frac{1}{2}\sum_{j,k=1}^{N}\Gamma_{jk}\left(\hat{\sigma}_j^{\dagger}\hat{\sigma}_k\rho - 2\hat{\sigma}_k\rho\hat{\sigma}_j^{\dagger} + \rho\hat{\sigma}_j^{\dagger}\hat{\sigma}_k\right). \tag{5.13}$$

The spin-exchange rates J_{ij} and the collective dissipation rate Γ_{ij} are expressed in terms of the Green function as

$$\begin{aligned}\Gamma_{ij} &= \frac{2\mu_0\omega_A^2}{\hbar}\,\text{Im}\left[\mathbf{d_i}^{*}\mathbf{G}\left(\mathbf{r}_i,\mathbf{r}_j;\omega_L\right)\mathbf{d_i}\right],\\ J_{ij} &= \frac{\mu_0\omega_A^2}{\hbar}\,\text{Re}\left[\mathbf{d_i}^{*}\mathbf{G}\left(\mathbf{r}_i,\mathbf{r}_j;\omega_L\right)\mathbf{d_i}\right].\end{aligned} \tag{5.14}$$

Notice that all geometric properties of the material is included in the Green function which can be calculated classically.

5.3.3 Exact Green function via FDTD method

An electromagnetic Green function for a given dielectric structure $\epsilon(\mathbf{r},\omega)$ can be obtained by FDTD methods. We first define a computation space with the dielectric structure

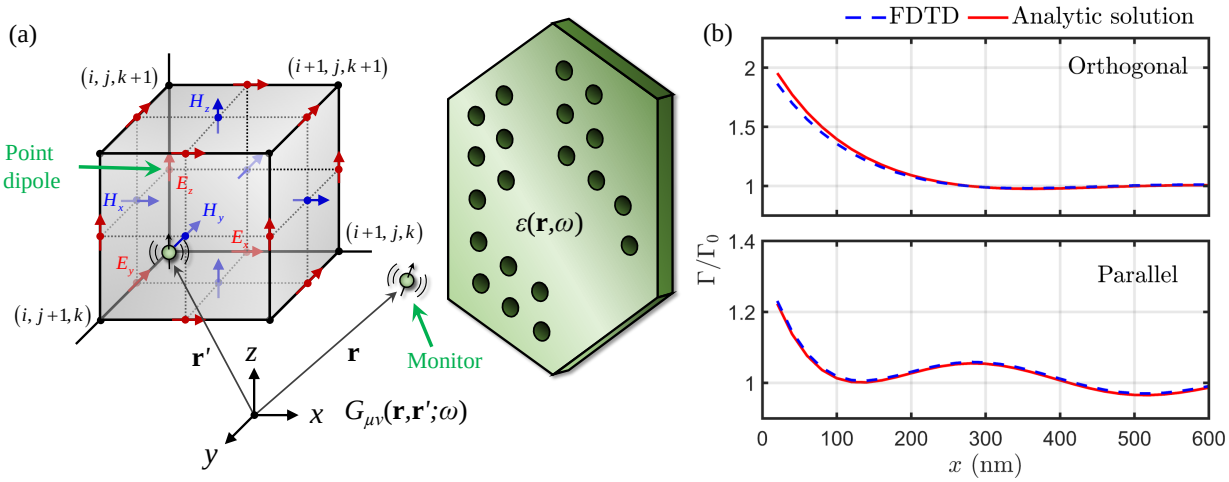

Figure 5.4: FDTD simulation for a dyadic Green function $G_{\mu\nu}(\mathbf{r}, \mathbf{r}'; \omega)$ and its validation by comparison with analytical solutions. (a) A schematic diagram of the FDTD simulation with Yee cells for a dielectric material $\epsilon(\mathbf{r}, \omega)$. (b) The spontaneous decay rates Γ normalized by the free-space decay rate Γ_0 for the D_2–transition of a Cesium atom near an infinite glass plate with refractive index $n = 1.45$. The decay rate was calculated as a function the distance x between the atom and glass plate. The numerical evalulation using local Green functions via Lumerical FDTD Solutions (blue dashed line) is compared with the analytical solutions [168] (red solid line) for the atom polarized in normal and parallel direction to the plate.

discretized by Yee cells at the desired resolution, as shown in Figure 5.4(a). We then place a point dipole source oscillating in μ–direction at location $\mathbf{r}'$ (i.e., $\mathbf{P}(\mathbf{r}; \omega) = \mathbf{P}(\omega) \cdot \hat{e}_\mu \delta(\mathbf{r} - \mathbf{r}')$) and a "monitor" at $\mathbf{r}$ where the electric field $\mathbf{E}(\mathbf{r}; \omega)$ is evaluated by propagating the source field via Maxwell's equation

$$\nabla \times \nabla \times \mathbf{E}(\mathbf{r}; \omega) - \frac{\omega^2}{c^2} \epsilon(\mathbf{r}, \omega) \mathbf{E}(\mathbf{r}; \omega) = \mu_0 \omega^2 \mathbf{P}(\omega) \cdot \hat{e}_\mu \delta(\mathbf{r} - \mathbf{r}'). \tag{5.15}$$

Comparing it with the definition of the Green function in Equation 5.7, we obtain the the Green function related to the calculated electric field by the expression

$$G_{\mu\nu}(\mathbf{r}, \mathbf{r}'; \omega) = \frac{E_\nu(\mathbf{r}, \omega)}{\mu_0 \omega^2 P_\mu(\mathbf{r}'; \omega)} = \frac{\mathcal{FT}\left[E_\nu(\mathbf{r}; t)\right]}{\mu_0 \omega^2 \mathcal{FT}\left[P_\mu(\mathbf{r}'; t)\right]}, \tag{5.16}$$

where $\mathcal{FT}[\,]$ represents a Fourier transform.

It is obvious that the local Green function $G_{\mu\nu}(\mathbf{r}, \mathbf{r}; \omega)$ diverges as it requires a field evaluated at the location of a point source $\mathbf{r}'$. To obtain physically meaningful results, the Green function must be analytically integrated over a small volume around the source (i.e., regularized Green function). The FDTD naturally handles such regularization process by averging the electric field over a unit Yee cell [295], which typically provides an accurate nonlocal Green function $G_{\mu\nu}(\mathbf{r}, \mathbf{r}'; \omega)$. To ensure this numerical averaging process for local Green function to be the same as the analytical integration, one must pay a particular attention to the placement of a dipole source. As illustrated in Figure 5.4(a), the source location must be shifted by a half unit cell in its oscillating direction. The shifted position is where the electric field is calculated during the FDTD simulation (e.g., E_z–position for the source $\mathbf{P}(\omega) \cdot \hat{e}_z \delta(\mathbf{r} - \mathbf{r}')$) whereby we ensure that only a single dipole point is excited instead of creating possibly eight effective dipoles at the corners.

To testify our method, we calculated the spontaneous decay rate Γ for the D_2–transition of a Cesium atom near a infinitely large dielectric plate with the refractive index $n = 1.45$. The local Green function $G_{\mu\nu}(\mathbf{r}, \mathbf{r}; \omega)$ was calculated via Lumerical FDTD Solutions at a position of the atom, and the Equation 5.14 relate the Green function to the atomic decay rate. It can also be obtained from analytical solutions from the reference [168], and therefore the comparison between the two results validates our numerical method. Figure 5.4(b) shows the spontaneous decay rate normalized by free-space decay rate Γ_0. The decay rate was evaluated for the Cesium atom polarized in the normal (top) and parallel (bottom) directions to the plate. We observed excellent agreement between the numerical results and analytical solutions across the distance from 20 nm to 600 nm for both cases.

5.3.4 Casimir-Polder force

We present the quantum theory for the numerical time-domian simulation of dispersive electromagnetic forces due to the presence of dielectrics–also known as Casimir-Polder forces. The microscopic origin of this force is the modified vacuum-induced energy shift of an atomic ground state. The amount of the energy shift can be calculated by the purterbation theory, as shown by G. S. Agrawal in 1975 [4]. Recently, with the development of the canonical quantization scheme with dielectrics, Buhmann *et al.* showed the derviation of more general electromagnetic forces to both macro- and mirco-objects starting from the Lorentz force formula [45, 46].

With the interaction Hamiltonian $\hat{H}_{\text{int}} = -\hat{\mathbf{E}}(\mathbf{r}, t) \cdot \hat{\mathbf{d}}(t)$ under the dipole approximation, the ground-state energy shift for a single atom in second-order perturbation theory [4, 46]

is given by

$$\Delta E = -\sum_{k,\zeta} \int d^3\mathbf{r}\mathcal{P} \int_0^\infty d\omega \frac{\left|\langle g|\hat{\mathbf{d}}|e\rangle \cdot \langle 0|\hat{\mathbf{E}}|1_\lambda(\mathbf{r},\omega)\rangle\right|^2}{\hbar(\omega_{k0}+\omega_{\mathbf{k}})}, \tag{5.17}$$

where k and ζ are the indices for the wave vector and the polarization of the electric field, respectively. Here, the state $|1_{\mathbf{k},\zeta}(\mathbf{r},\omega)\rangle = \hat{\mathbf{f}}_\lambda^\dagger|0\rangle$ represents a single excitation of the polariton-like bosonic field in the k mode and the ζ polarization. We substitute the Equation 5.6 to Equation 5.17 and use the identity 5.8 to yield

$$\Delta E = -\frac{\mu_0}{\pi}\sum_k \mathcal{P}\int_0^\infty \frac{d\omega}{\omega_{k0}+\omega}\omega^2 \mathbf{d}_{0k}\cdot \mathrm{Im}\,\mathbf{G}(\mathbf{r}_A,\mathbf{r}_A;\omega)\cdot\mathbf{d}_{k0} \tag{5.18}$$

with $\mathbf{d}_{k0} = \langle k|\hat{\mathbf{d}}|0\rangle$. The position-dependent ground state energy shift is obtained by the local scattering Green function $\mathbf{G}_s = \mathbf{G} - \mathbf{G}_0$ with respect to the vacuum $\mathbf{G}_0$ as

$$U_{\mathrm{CP}}(\mathbf{r}_a) = -\frac{\hbar\mu_0}{2\pi}\,\mathrm{Im}\left[\int_0^\infty d\omega\omega^2\,\mathrm{Tr}\left[\boldsymbol{\alpha}(\omega)\cdot\mathbf{G}_s(\mathbf{r}_A,\mathbf{r}_A;\omega)\right]\right], \tag{5.19}$$

where the dynamic polarizability tensor of the atomic ground state $\boldsymbol{\alpha}(\omega)$ is defined as

$$\boldsymbol{\alpha}(\omega) = \lim_{\epsilon\to 0}\frac{2}{\hbar}\sum_k \frac{\omega_{k0}\mathbf{d}_{0k}\mathbf{d}_{k0}}{\omega_{k0}^2-\omega^2-i\omega\epsilon} \tag{5.20}$$

The contour integral in Equation 5.20 can be numerically evaluated in time domain, which was originally developed for macroscopic objects in reference [252]. The strategy is to deform the contour integration into the upper imaginary plane, in particular, along the complex frequency contour of the form $\omega = \xi\sqrt{1+i\sigma/\xi}$, parametrized by a real number $\xi \geq 0$ and a constant $\sigma > 0$. Here, we apply this technique to the Casimir-Polder potential for a single atom, and derive the same result presented in reference [132].

We first rewrite the Equation 5.20 as

$$U_{\mathrm{CP}}(\mathbf{r}_a) = -\frac{\hbar\mu_0}{2\pi}\,\mathrm{Im}\left[\int_0^\infty d\xi\frac{d\omega}{d\xi}\omega^2(\xi)\,\mathrm{Tr}\left[\boldsymbol{\alpha}^{(0)}(\omega(\xi))\cdot\mathbf{G}^{(1)}(\mathbf{r}_A,\mathbf{r}_A;\omega(\xi))\right]\right]. \tag{5.21}$$

To rewrite it in the time domain, we use the convolution theory to express

$$\int_0^\infty d\xi x_{ji}(\xi)G_{ij}(\xi) = \int_0^\infty dt x_{ji}(-t)G_{ij}(t), \tag{5.22}$$

where $x_{ji}(\xi) = \frac{d\omega}{d\xi}\omega^2(\xi)\alpha_{ji}(\omega(\xi))$ is the Fourier transform of $\tilde{x}_{ji}(t) = \int_0^\infty d\xi x_{ji}(\xi)e^{-i\xi t}$ and $G_{ij}(t) = \int_{-\infty}^{\infty} d\xi G_{ij}(\xi)e^{-i\xi t}$. Here, we take one element of the inner product between the polarizability tensor and the Green tensor since the Fourier transformation is linear. While $\tilde{x}_{ji}(t)$ could be evaluated relatively easily, calculating $G_{ij}(t)$ could be tricky because it is not the Fourier conjugate of $G_{ij}(\omega)$.

Following the discussion in reference [252], we setup the Maxwell's equation to calculate $G_{ij}(t)$ using the FDTD solver [226] with the modified material property. For a given dielectric function $\epsilon'(\mathbf{r}, \xi)$ and a dipole current source $\mathcal{J}(\mathbf{r}, \xi) = \hat{e}_\mu \delta^{(3)}(\mathbf{r} - \mathbf{r}')$, the FDTD solver evalulates the electric field $\mathbf{E}(\mathbf{r}, t)$ whose Fourier transform $\mathbf{E}(\mathbf{r}, \xi) = \frac{1}{2\pi}\int dt \mathbf{E}(\mathbf{r}, t)e^{i\xi t}$ satisfies the frequency-domain Maxwell's equation

$$\left[\nabla \times \nabla \times -\xi^2 \mu_o \epsilon'(\mathbf{r}, \xi)\right] \mathbf{E}(\mathbf{r}, \xi) = i\mu_0 \xi \mathcal{J}(\mathbf{r}, \xi). \tag{5.23}$$

Comparing the Equation 5.23 with the definition of the Green tensor in Equation 5.7, we can assign the following dielectric function to the FDTD solver

$$\epsilon' = \frac{\omega^2}{\xi^2}\epsilon = \left(1 + i\frac{\sigma}{\xi}\right)\epsilon(\mathbf{r}, \omega(\xi)), \tag{5.24}$$

Then, the resulting electric field $\mathbf{E}$ will have the following correspondence to our target Green function

$$i\xi E_{ij} = G_{ij}(\xi), \tag{5.25}$$

Using the dielectric function in Equation 5.24, we can calculate the Equation 5.22 through the field solution $\mathbf{E}(\mathbf{r}, t)$

$$\int_0^\infty d\xi x_{ji}(\xi) G_{ij}(\xi) = \int_0^\infty g_{ji}(-t)\mathrm{E}_{ij}(\mathbf{r}, t), \tag{5.26}$$

with

$$\begin{aligned} g_{ji}(t) &= \int_0^\infty d\xi g_{ji}(\xi)e^{-i\xi t}, \\ g_{ji}(\xi) &= i\frac{\omega^2}{\xi}\frac{d\omega}{d\xi} = -i\xi\sqrt{\left(1 + i\frac{\sigma}{\xi}\right)}\left(1 + i\frac{\sigma}{2\xi}\right)\alpha_{ij}(\omega(\xi)). \end{aligned} \tag{5.27}$$

5.4 Designing photonic crystal waveguides for many-body waveguide QED

In this section, we present numerical simulation tools to design a PhCW structure. We consider a spin network of Cesium atoms localized along a Si_3N_4 PhCW with highly tunable

GMs in terms of TE photonic band gap, effective photon mass m_e, and mode area A_{eff} near the band edge $k_x = k_0$. Figure 5.5(a) shows a general layout of the structure of our slotted squircle photonic crystal waveguide (SqPhCW).

5.4.1 Design considerations

The full realization of our waveguide QED system requires the capability to maintain favorable figure of merit $\mathcal{F} = \Delta_{\text{Lamb}}/\Gamma_{\text{tot}}$ with short-ranged mechanical interactions between the trapped atoms, where the localization length $L_c = \sqrt{1/2m_e\Delta_e}$ is comparable to the lattice constant a_0. Here, $\Delta_e \simeq 2\Delta_b$ denotes the detuning of atomic transition to the effective cavity mode [78], and Δ_b is the detuning of the atomic transition frequency to the band edge. In the following, we listed a set of requirements as a guidance of the designing process.

1. **Wide angular field of view for optical access**
   The very first requirement is the optical access to a nanostructure not only for the pump fields and Raman-sideband lasers into the GMs but also for complex laser cooling and trapping sequences. This requirement restricts the dimensions of photonic crystal structures to 1D and 2D slabs. Because of the lack of full 3D PBGs, the total decay rate $\Gamma_{\text{total}} = \Gamma_{\text{1D}} + \Gamma'$ consists of both the waveguide decay Γ_{1D} and the homogeneous decay Γ'. While Γ_{1D} is significantly suppressed for large Δ_e, majority of slow-light PhCWs do not have the adequate band structure with $\mathcal{F} \gg 1$ for small L_c.

2. **Precise matching of the waveguide properties to atomic spectral lines**
   Our proposed scheme requires the strong coupling between atoms and photons in waveguide modes while keeping the tight and stable potential formed around individual Cesium atoms. The precise tailoring of photonic dispersion is extremely crucial to match optical properties of the designed waveguide to atomic spectral lines. We consider the Cesium D_2–transition λ_{D2} =852 nm.

3. **Sufficient localization of atom-induced cavity**
   Extremely flat band structure of the GM is required to have the localization length $L_c = \sqrt{1/2m_e\Delta_e}$ to be comparable with the lattice constant a_0. While it is not necessary to have nearest-neighbor interactions, the atomic collective motion can experience band-flattening effect due to the long-range tunnelling, hence reducing the local addressability of the spin-motion coupling.

4. **Stable trapping of atoms in the presence of substantial Casimir-Polder forces**
   To form an atomic chain, a stable potential energy must be prepared at each site. Since they are in the vicinity of the highly refractive dielectric structure, atoms are expected to experience a substantial Casimir-Polder forces. The designed structure must incorporate the proper laser cooling and trapping process to form a stable potential. We utilize the far-off-resonant trap (FORT) with the blue-detuned trapping field at one of the magic wavelengths λ_{trap} =793.5 nm for the Cesium D_2–transition.

5. **The device must be readily manufacturable.**
   The standard electron-beam lithography technology can fabricate nanophotonic devices with the accuracy of a few nanometers, which may shift the frequency of photonic band edge far off from the atomic transition. Also, the fabricated device with large optical access is suspended in air and hence extremely fragile. Therefore, the fabrication tolerance must be included during the analysis for the designed structure and the proper fixture to support the suspended waveguide must be designed.

5.4.2 Design methods

We designed a variation of a slotted PhCW that utilizes PBG of the 2D slab as the guiding mechanism, as illustrated in Figure 5.5(a) with the design parameters summarized in Table 5.1. The dispersion is tailored by a line defect introduced to a triangular TE-PBG slab, where a significant portion of the energy of the GM is localized within the air slot. We introduce anomalous squircles in the vicinity of the air slots to alter their band curvatures. The rationale of our dispersion engineering is that the combination of the lattice constant a_0, the hole radius r, and the air slot width w_s can tune the locations of the band edge frequencies with respect to the band gap of the slab, while the additional squircle geometries defined by the asymmetry a, b cause differential energy shifts between the z-even bands of opposite x-symmetry. By placing the bands deep into the PBG of the surrounding slab, we suppress the k-space interval $[k_c, k_l]$ where the in-plane field profile of the guided mode is localized by index-guiding near the light cone. The proximal squircle geometry then flattens the GM across the band-gap guided k–space fraction $[k_l, k_0]$. In addition, the out-of-plane emission Γ_h is affected by the distance of the squircles to the slot.

Figure 5.5(b) depicts a functional block diagram of our design workflow. Since there are multiple requirements that must be simultanously satisfied and the structure parameters

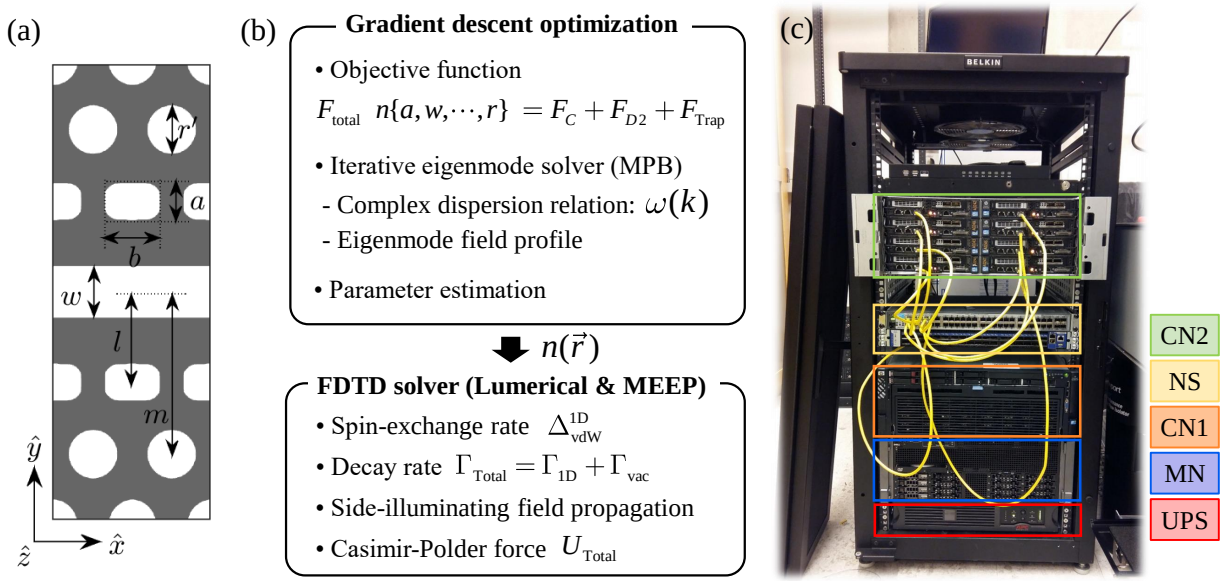

Figure 5.5: The design process for photonic crystal waveguides and UQML-Andromeda cluster server. (a) The definition of structural parameters for a slotted squircle photonic crystal waveguide. (b) The workflow of the numerical simulations. (c) A photograph of our UQML-Andromeda cluster server in November 2017.

are coupled to each other, it is not practical to twick the parameters individually to search an optimal structure. We applied a gradient descent algorithm for the SqPhCW geometry $n(\vec{r})$ (design variables) to minimize the objective function $F_{\text{total}}(n(\vec{r}))$ with intermittent thermal excitations to avoid local extrema, as with simulated annealing. The objective function is expressed as

$$\begin{aligned} F_{\text{total}}(n(\vec{r})) &= F_c + F_{D2} + F_t, \\ F_c &\propto |m_e|^{-2}, \\ F_{D2} &= |\omega_b - \omega_{D2} + \Delta_b|^2, \\ F_t &= |\omega_b - \omega_t|^2, \end{aligned} \tag{5.28}$$

where F_c is the contribution from the band curvature and $F_{D2}(F_t)$ is the frequency deviations of $|F = 4\rangle \rightarrow |F' = 5\rangle$ transition frequency $\omega_{D2} = 2\pi\nu_{D2}$ (blue-detuned magic-wavelength frequency $\omega_t = 2\pi\nu_t$) for atomic Cesium from band edges ω_b of the respective modes. During the optimization sequence, the complex band diagram is computed by open-source software package named MIT photonic bands (MPB) [149] to estimate the effective mass m_e and the localization length L_c. After convergence, we switch over to a

Table 5.1: Final design variables for the SqPhCW with slab index n=2. The uncertainty ± 1 nm is added for the normal distributions of the disordered SqPhCW structure in Figure 5.5.

Lattice constant a_0	(366 ± 1) nm	Slot width w	(266 ± 1) nm
Slab thickness t	(200 ± 1) nm	Squircle radius r_s	(99 ± 1) nm
Secondary radius r'	(105 ± 1) nm	Hole radius r	(109 ± 1) nm
First line shift l	(413 ± 1) nm	Secondary line shift m	(729 ± 1) nm
Squircle height a	(79 ± 1) nm	Squircle width b	(124 ± 1) nm

finite structure with device length L_d and apply a combination of filter-diagonalized FDTD and FDFD methods with the Yee lattice modified to directly optimize the dyadic Green function $\mathbf{G}(\mathbf{r}, \mathbf{r}'; \omega)$ to arrive at the final design variable $n(\vec{r})$ in Table 5.1.

5.4.3 Computational resource: UQML-Andromeda cluster

The three-dimensional and fully vectorial evaluation of Maxwell's equation is computationally demanding in both time- and frequency-domain. In particular, for PhCWs featuring ultra-high Q-factor, as the decay rate of electric intracavity fields is extremely small, the evaluation of Maxwell's equation in time domain takes very long time. Also, the computation domain must be meshed with reasonably good spatial resolution in order to capture delicate patterns and shapes of the PhCW. Therefore, it is highly desirable to parallize the task to reduce the calculation time.

The parallization must be carefully performed depending on the properties of the computational alogrithm. For example, the MPB calculation may be massively parallized as solving the eigenmodes at one frequency is independent from the computations at other frequencies. In contrast, the parallization of the FDTD simulations requires the interconnection between the distributed tasks because the solution from one computational node depends on the others. Therefore, the parallization for FDTD solvers is often performed with the message-passing interface (MPI). In addition, the interconnects between the nodes for FDTD require an infiniband fabric to reduce the latency for the communication.

In order to speed up and systematize our design process at the UQML, we built a cluster server in heterogeneous achitecture, which we named a UQML-Andromeda cluster, as shown in Figure 5.5(c). The system mainly consists of one master node and two computing nodes. As summarized in Table 5.2, the characteristics of the two computing nodes (CN1 and CN2) are different. The CN1 has a higher CPU performance with less number of cores,

Table 5.2: Specifications of the UQML-Andromeda cluster server used to design and analyze the nanophotonic structure for the proposed waveguide QED system. Note that this information is based on the hardware installed in the very initial version of the system (October 2017). Steve G Weiss provided a fan-mounted server rack.

Acronym	Part number	Description	Task
UPS	APC 3000VA	Uninterrupted power supply	Battery back-up for master node in case of power outage
MN	Dell, R910	32 Core 4 X 2.16 GHz CPU, 128GB RAM 1.2 TB HDD	Master node: user-interface and distribute the tasks over compute nodes
CN1	HP ProLiant, DL580 G7	32 Core Intel E7-4820 CPU, 512GB RAM	Computing node 1: Lumerical FDTD for the Green functions
NS	Mellanox, MSX6036	56Gb/s full bidirectional bandwidth per port	Interconnect the compute node 2.
CN2	HP ProLiant, SL230s Gen8	128 Core 2.20GHz Intel E5-2660, 512GB RAM	Computing node 2: massively parallelized computation, e.g., gradient descent optimization with MPB and MEEP for Casimir-Polder forces.

compared to the CN2. The CN2 consists of eight blades of sub-computing nodes that are linked together by a high-bandwidth network switch (NS) with ethernet cables.

The CN1 was utilized to obtain Green functions for the finite-sized PhCW via Lumerical FDTD Solutions, whereas the CN2 was focused on the calculation for the photonic band diagrams and Casimir Polder potential with MPB and MEEP [226], respectively. As for the Casimir-Polder force, the electric field was calculated at several atomic positions for a unit cell of the designed PhCW with the Bloch boundary condition to reduce the computational space. As the evaluation of the electric field at each position is independent from another, the task was efficiently distributed over the eight nodes of the CN1 without the speed being limited by the bandwidth of the ethernet cables.

Table 5.3: Experimental parameters for realizing universal quantum matter and their energy scale together with the corresponding effective error rates.

Definition	Value	Comments
$g_c = \sqrt{\frac{\omega_b d^2}{2\epsilon_0 A_{\text{eff}} L_c}}$	$\sim 10\,\text{GHz}$	Atom-PhCW interaction
$t \approx \frac{\eta_l^2 f^2 g_c^2}{\Delta}$	$\sim 1\,\text{MHz}$	Mechanical tunneling, Requirement: $f \ll 1, f g_c \ll \Delta$
$J_{\alpha,\beta}^{(i,j)} = 2\,\text{Re}\left[\frac{\tilde{\Omega}_{\alpha,l}^{(i)} \tilde{\Omega}_{\beta,l}^{(i)*}}{\Delta_l}\right]$	$\sim 50\,\text{kHz}$	Spin-spin interaction, Requirement: $\lvert\tilde{\Omega}_{\alpha,l}^{(i)}\rvert \ll \Delta_l \ll \lvert\epsilon_{l\pm1} - \epsilon_l\rvert$
$\kappa = \kappa_0 + \frac{g_c^2}{\Delta^2}\Gamma'$	$\sim 10\,\text{MHz}$	Photon loss
$\gamma_m \approx \frac{\kappa}{\Delta} t$	$\sim 10\,\text{Hz}$	Phonon loss
$\gamma \approx \frac{\gamma_m}{\Delta_l} J^{(i,j)}$	$\sim 0.1\,\text{Hz}$	Spin decoherence
$\mathcal{F} = \frac{t}{\gamma_m} = \frac{\Delta}{\left(\kappa_0 + \frac{g_c^2}{\Delta^2}\Gamma'\right)}$	$> 10^4$	Figure of merit

5.5 Detailed design analysis

In this section, we present the detailed analysis for the designed structure. Starting with investigating the photonic properties of the designed SqPhCW, we evaluate coherent spin-spin interaction rate and collective dissipation rate of the localized Cesium atoms. Also, we describe two trapping schemes and estimate the nearest-neighbor phonon tunneling rate as well as on-site interaction for each cases. The results estimate the coherent spin-spin interaction rate $\sim$50 kHz with the spin decoherence rate $\sim$0.1 Hz as well as the phonon loss$\sim$10 Hz, which shows the feasibility of realizing our proposed waveguide QED system as an analogue universal quantum simulator.

5.5.1 Photonic properties: dispersion relation of the guided modes

The results of dispersion engineering is shown in Figure 5.6(b) for our flat-band silicon nitride SqPhCW slab, with the effective mass m_e =2.1 $\text{Hz}^{-1}\,\text{m}^{-2}$. In the single-band approximation, the localization length is expected to be $L_c \simeq 2a_0$ at Δ_e =0.4 THz. We assume that the atom is confined by the blue-detuned magic-wavelength GM trap ν_t at

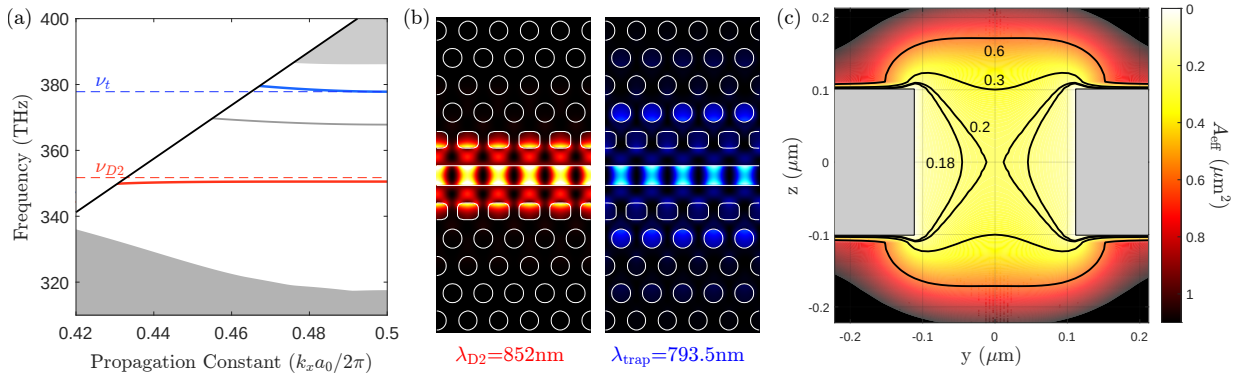

Figure 5.6: Simulation results of optical properties of the designed photonic crystal waveguide. (a) SqPhCW band diagram. The guided modes are depicted as solid lines for both the excitation $\nu_{D2} = \omega_{D2}/(2\pi)$ (red) and trapping modes ν_t (blue). Through our optimization iterations, the guided modes (GM) ν_{D2} and ν_t are flattened around the Cesium D_2–transition and magic-wavelength trapping frequencies. The GM ν_t is defined to operate at the blue-detuned magic-wavelength condition for the D_2–transition at λ_t =793.5 nm. The grey shaded region indicates the presence of slab modes. (b) Contour intensity map of the guided modes at ν_{D2} and ν_t. (c) Effective mode area A_{eff}. We depict the x-cut contour map of A_{eff} for the GM ν_{D2}. We anticipate the sub-wavelength localization $A_{\text{eff}}/\lambda_{D2}^2$ ≈0.18 of the guided field with the effective coupling rate g_c ≈11.5 GHz to the trapped Cs atom. The resulting photonic Lamb shift and localization length are $\Delta_{\text{Lamb}}^{\text{1D}}$ ≈620 MHz and L_c ≈0.77 µm at Δ_e =0.4 THz.

λ_t =793.5 nm (blue line of Figure 5.6(a)) with the intensity represented by blue-coloured contour map in Figure 5.6(b). The excited states of the trapped atom is modified by the vacuum of ν_{D2}-mode (red line of Figure 5.6(a)) as indicated by the red contour map in Figure 5.6(b). At the band edge $k_0 = 0.5$, ν_{D2}-mode is highly localized with the effective mode area $A_{\text{eff}} \simeq 0.18\lambda_{D2}^2$. The resulting photonic Lamb shift is $\Delta_{\text{Lamb}}^{\text{1D}} = \frac{g_c^2}{\Delta_e} \simeq$620 MHz at Δ_e =0.4 THz.

5.5.2 Coherent spin-spin interactions and correlated dissipations

We now turn to the numerical Green function $\mathbf{G}(\mathbf{r}_i, \mathbf{r}_j; \omega)$ of a finite SqPhCW with device length $L_d = 80a_0$ in Figure 5.7. We evaluate the collective decay and the coherent

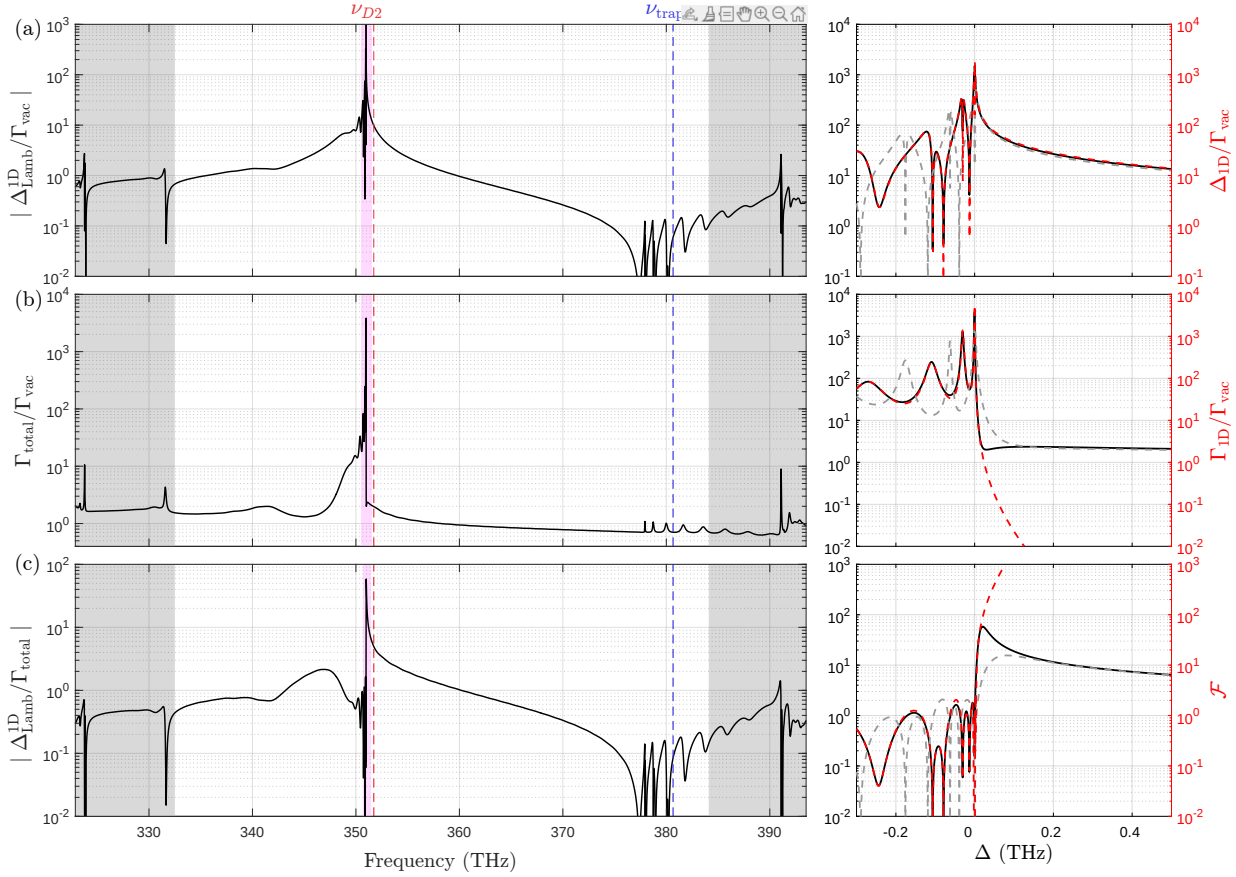

Figure 5.7: Numerical evaluation of coherent spin-exchange coefficients and collective decay rates in 1D photonic crystal waveguide. (a) Photonic Lamb shift $\Delta^{1D}_{\text{Lamb}}$ for electronically excited states normalized by the free-space decay rate Γ_{vac}. The energy shift $\Delta^{1D}_{\text{Lamb}}$ of the excited state $|6P_{3/2}, F = 4\rangle$ of Cesium atoms is computed by numerically evaluating the local scattering Green function $\mathbf{G}_s(\mathbf{r}, \mathbf{r}; \omega)$. We also display the photonic Lamb shift $\Delta^{1D}_{\text{Lamb}}$ under the single-band approximation as red dashed line. (b) The enhancement and inhibition of spontaneous emission in dispersive and reactive regimes. The total decay rate Γ_{total} is strongly enhanced at the band edge, and is exponentially inhibited in the band gap with $\Gamma_{\text{total}} \simeq \Gamma_{1D} \exp(-L_d/L_c)$, where Γ_{1D} is the enhanced decay rate at the resonance closest to the band edge. $L_d = 80a_0$ is the device length for lattice constant a_0, and L_c is the localization length. (c) Lamb shift to decay rate ratio $\Delta^{1D}_{\text{Lamb}}/\Gamma_{\text{total}}$ across a wide detuning range up to $\Delta_e \approx$10 THz. Inset. Figure of merit $\mathcal{F} \gg 1$ (red dashed line). The grey shaded region indicates the presence of slab modes.

interaction

$$\begin{aligned}\Gamma_{\text{total}}^{(i,j)} &= \frac{2\mu_0\omega_A^2}{\hbar}\,\text{Im}\left[\mathbf{d_i}^*\mathbf{G}\left(\mathbf{r}_i,\mathbf{r}_j;\omega\right)\mathbf{d_i}\right],\\ \Delta_{\text{Lamb}}^{(i,j)} &= \frac{\mu_0\omega_A^2}{\hbar}\,\text{Re}\left[\mathbf{d_i}^*\mathbf{G}_s\left(\mathbf{r}_i,\mathbf{r}_j;\omega\right)\mathbf{d_i}\right],\end{aligned} \tag{5.29}$$

where the scattering Green function is $\mathbf{G}_s = \mathbf{G} - \mathbf{G}_0$ with respect to the vacuum $\mathbf{G}_0$. More generally, we also define the waveguide Green function $\mathbf{G}_{wg} = \mathbf{G} - \mathbf{G}_h$ absent the homogeneous (non-guided) contribution $\mathbf{G}_h$ (coupling to the lossy modes beyond the light cone and to the free-space modes), where the waveguide portion $\mathbf{G}_{wg}$ can be estimated from a multimode cavity model [15] under a single-band approximation, with the resulting decay rate

$$\Gamma_{\text{1D}}^{(i,j)} = \frac{2\mu_0\omega_A^2}{\hbar}\,\text{Im}\left[\mathbf{d_i}^*\mathbf{G}_{wg}\left(\mathbf{r}_i,\mathbf{r}_j;\omega\right)\mathbf{d_i}\right] \tag{5.30}$$

into the waveguide GM.

As shown in Figure 5.7, in the dispersive regime [100], the flat band ν_{D2} exhibits extreme slow-light enhancement of the decay rate with group index $n_g \approx 1,000$ near the band edge. As the atom enters the band gap in the reactive regime $\Delta_e > 0$ [121], the waveguide decay rate Γ_{1D} from $\mathbf{G}_{wg}$ is exponentially suppressed (red dashed line in Figure 5.7(b)), while the highly asymmetric Fano-like resonance of $\mathbf{G}_{wg}$ around the band edge gives rise to a photonic Lamb shift $\Delta_{\text{Lamb}}^{\text{1D}} \approx$620 MHz that greatly exceeds $\Gamma_{\text{total}} \approx$60 MHz ($\Gamma_{\text{1D}} \approx$4 kHz) in the band gap with figure of merit $\mathcal{F} > 10^4$ at $\Delta_e =$0.4 THz, indicating significant coherence fraction in the collective motion relative to the correlated phononic dissipation. Deep into the band gap $\Delta_e \gg 0$, the reduction of Γ_{total} is limited by the weakly inhibited homogeneous decay rate $\Gamma' \approx 0.7\Gamma_{\text{vac}}$ that predominantly emits photons out of plane of the slab.

With the close agreement between the numerical Green function $\mathbf{G}$ (black lines) and the waveguide model $\mathbf{G}_{wg}$ (red dashed lines) in Figure 5.7, we can reliably predict Γ_{1D} from $\mathbf{G}_{wg}$ and the mechanical loss factor γ_m from both $\mathbf{G}$ and $\mathbf{G}_{wg}$. Thanks to the large band flatness, we can operate as close as $\Delta =$5 THz ($\Delta \approx$10 THz) and attain short-ranged motional coupling over $L_c \approx 2a_0 \ll L_d$, while maintaining inherent figure of merit $\mathcal{F} \sim 10^{10}$. We remark that $\mathcal{F}$ is defined as the ultimate coherence-to-dissipation ratio for the collective phonon modes, where we only consider the inherent dissipation of the atomic motions in the photonic band gap. In practice, our method will be realistically limited by the phase-noises of Raman sideband lasers and the inhomogeneous hyperfine broadening of the trapped atoms, as well as various uncontrollable surface forces.

For disordered photonic structures, we compute the dyadic Green functions with the Gaussian-random geometric disorder of 1 nm (positions and sizes of holes, thickness of the waveguide) distributed across the entire nanophotonic waveguide. In a single realization, the radiative enhancement factor at the band edge may be hindered by Anderson and weak localization. However, in the reactive regime $\Delta_e > 0$, we observe that the decay rate and the photonic Lamb shift in Figure 5.7, as well as the nonlocal Green function $\mathbf{G}(\mathbf{r}_i, \mathbf{r}_j; \omega)$ are not significantly modified by the structural disorder of 1 nm (grey dashed lines in Figure 5.7). Such nanofabrication tolerances have been demonstrated in reference [101, 121]. Because of the nature of the photonic bandgap, the non-radiative atom-field localized modes are resistant to the degree of structural disorder.

5.5.3 Ground-state potentials and phononic modes

We now turn our attention to the trapping mechanism for the atoms in the SqPhCW. For simplicity, we first consider a single GM trap that combines the repulsive FORT $\hat{H}_{\text{FORT}}$ of the GM at the blue-detuned magic-wavelength condition λ_t =793.5 nm (blue line of Figure 5.6(a)) and the attractive Casimir-Polder (CP) potential $\hat{H}_{\text{CP}}$. The ground-state adiabatic potential is obtained by diagonalizing $\hat{H}_{\text{trap}} = \hat{H}_{\text{FORT}} + \hat{H}_{\text{CP}}$ [132, 165, 169]. $\hat{H}_{\text{FORT}}$ is readily computed by the field profile of the trap GM at λ_t =793.5 nm. $\hat{H}_{\text{CP}}$ is obtained by the method described in Section 5.3.4. As we are only concerned with sub-wavelength distance scales, we neglect bulk material dispersion. For the excited states, we additionally include the Lamb shift $\Delta^{\text{1D}}_{\text{Lamb}}$ in Figure 5.7 associated with the radiative decay Γ_{1D}.

In Figure 5.8, we show the trap temperature for the ground state $|6S_{1/2}\rangle$ of Cesium atom. Repulsive FORT at the band edge confines the external motion along x-y plane, while the CP attraction along z-axis localizes the atom towards the center of the SqPhCW. Due to the tight field localization, we obtain a large trap frequency $\omega_x = 2\pi \times 3.8$MHz along the propagation mode x with Lamb-Dicke parameter $\eta_0^{(x)}$=0.04 and zero-point motion $x_0 = 5$nm. Remarkably, due to the extreme trapping confinement along the y-direction, the trapping frequency is $\omega_y = 2\pi \times 1.9$MHz even for a relatively shallow trap depth 60 µK. Due to the significant $\eta_0^{(y)}$=0.50 and $y_0 = 12$nm, we expect the presence of Mott-insulating phase with strong on-site interaction $U_0 > t$ in the phononic Hubbard model. For z–direction, the trap frequency is $\omega_z = 2\pi \times 197$kHz with $\eta_0^{(0)} = 0.19$ and $z_0 = 40$nm.

With these parameters for the Bose-Hubbard model, we estimate a modest nearest-neighbor phonon tunneling rate $t \simeq 2\pi \times 1.5$kHz and on-site interaction $U_0 \simeq 2\pi \times 9$kHz. The tunneling rate is largely limited by the small zero-point motion x_0, which cannot be

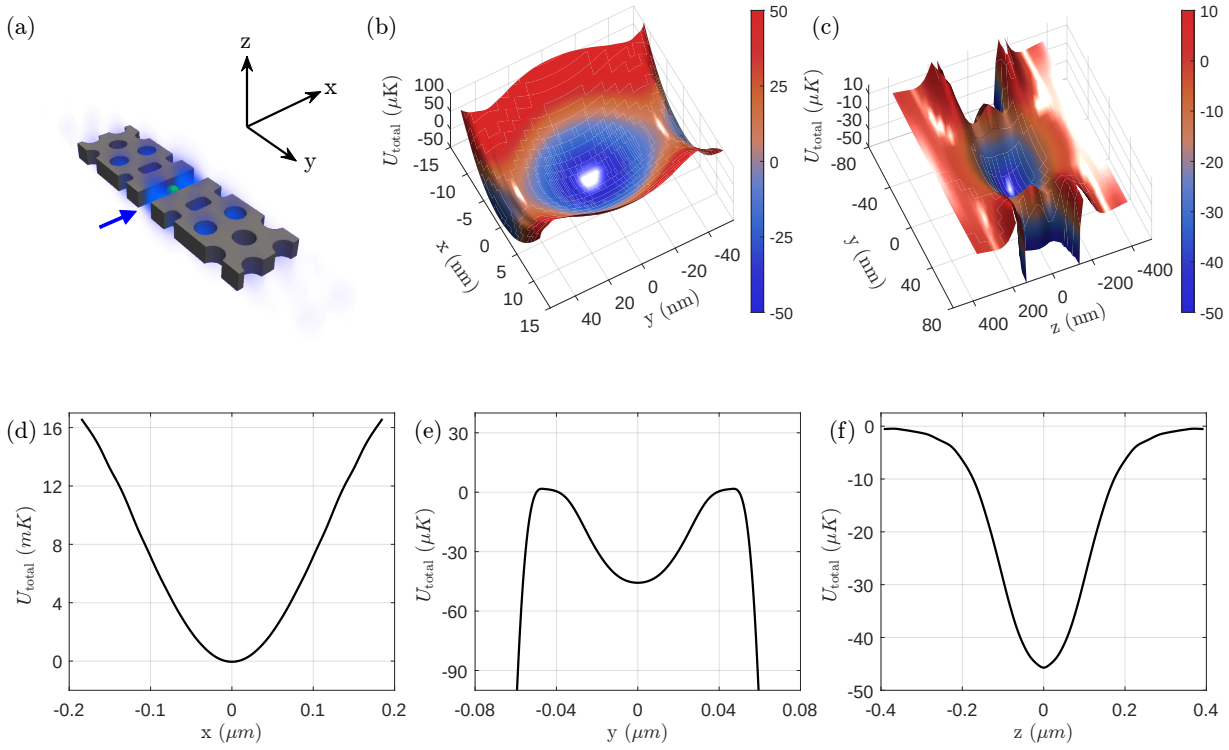

Figure 5.8: Adiabatic ground-state potentials of a Cesium atom with a blue-detuned field in the guided mode. Cesium trapping potential of $|6S_{1/2}\rangle$ for (b) x-y plane and (c) y-z plane with (d) the x-, (e) y-, (f) z-slices. The confinement along z-axis is due to the attractive Casimir-Polder potential that pulls the atom towards the center of the structure, while the double peaks are the effect of repulsive FORT potential that protects the atom from colliding with the surface. We assume that the refracitve index is frequency-independent.

readily improved in a single-beam configuration. In the limit of small total phonon number $\langle n \rangle \ll 1$, we neglect the effect of the later term into the superfluid phonon dispersion. However, for large-scale systems $N \gg 10$, phonon on-site interaction should be included with the dispersion of Bogoliubov excitations. We also remark that the preparation of zero-temperature phonon bath is not necessary, as we virtually populate the phonon dispersion. For instance, it is possible to operate the Equation 5.3 with close to unity filling, whereby phonon "holes" can alternatively play the role of phononic excitations.

An improved method, as shown in Figure 5.9, is to confine the atoms in the y-z plane by two incoherent incoherent side-illumination (SI) beams and localize the x-motion by a weak guided mode trap at 794 nm. With the SI beams near the blue-detuned magic-wavelength

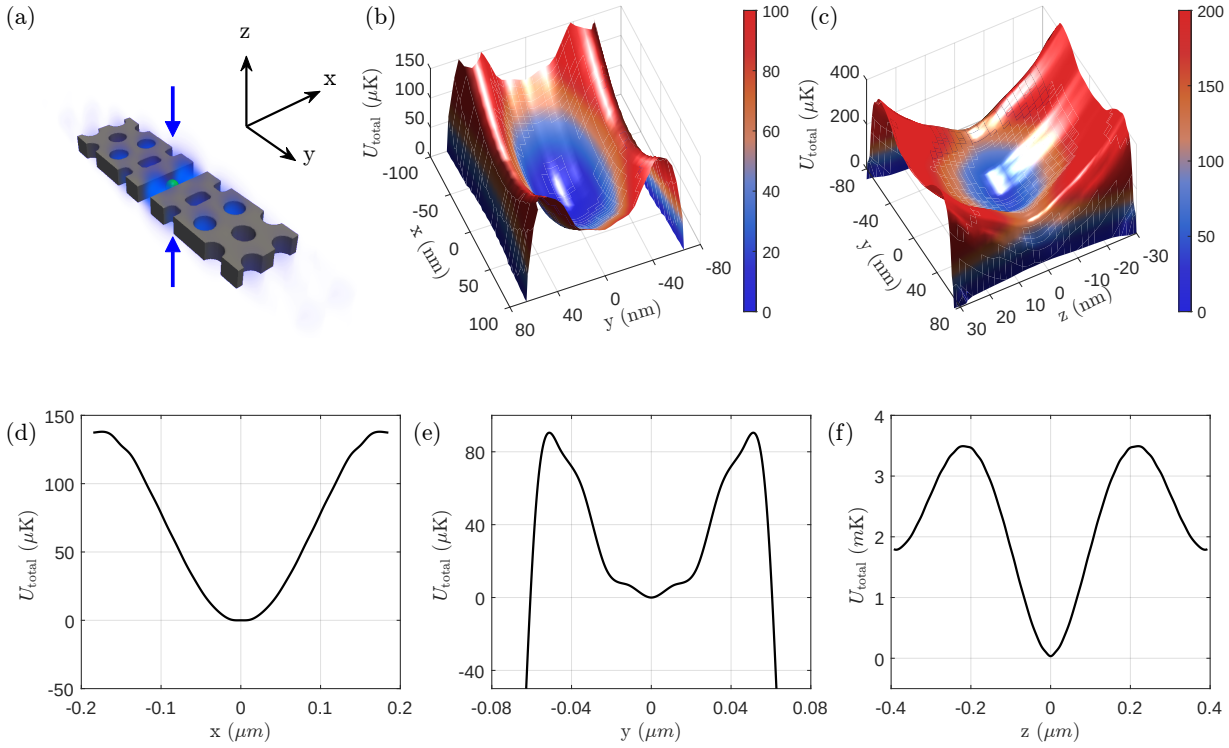

Figure 5.9: Adiabatic ground-state potentials for Cesium atom with side-illumination beams. Cesium trapping potentials of $|6S_{1/2}\rangle$ for (b) x-y plane and (c) y-z plane with (d) the x-, (e) y-, (f) z-slices. We assume that the refractive index of the SqPhCW is frequency-independent.

λ=687 nm in an optical accordion, we anticipate efficient loading into the GM trap. Because the SI beam provides additional confinement along z-direction, we can operate the GM trap away from the band edge at $k_x = 0.48$, thereby reducing the intensity contrast along x-direction. The result is a shallow 3D FORT with trap frequency $\omega_x' = 2\pi \times 260$kHz and zero-point motion $x_0' = 34$nm, yielding a maximum tunneling rate $t' \simeq 2\pi \times 230$kHz.

From the numerical non-local Green function $\mathbf{G}(\mathbf{r}_i, \mathbf{r}_j; \omega)$, we observe that the localization length scales with $L_c = \sqrt{1/2m_e\Delta_e}$ and the effective mass $m_e = 2.1\text{Hz}^{-1}\,\text{m}^{-2}$ up to $\Delta_e \approx 5$ THz. We attribute the deviation of the localization scaling beyond $\Delta_e > 5$ THz to the residual Lamb shift by the off-resonant couplings to the other bands and to the slab modes. Figure 5.10 depicts the local nature of external atom-atom interaction $t_{ij} = \eta_l^2 f^2 \Delta_{\text{Lamb}}(x_i, x_j)$ with $\eta_l = x_0/L_c$ relative to the mechanical decoherence $\gamma_m = \eta_l^2 f^2(\Gamma_{1\text{D}} + |\Delta_{\text{Lamb}}/\Delta_e|^2\Gamma')$, where the homogeneous decay rate $\Gamma' \simeq 0.7\Gamma_{\text{vac}}$ is weakly inhibited. At

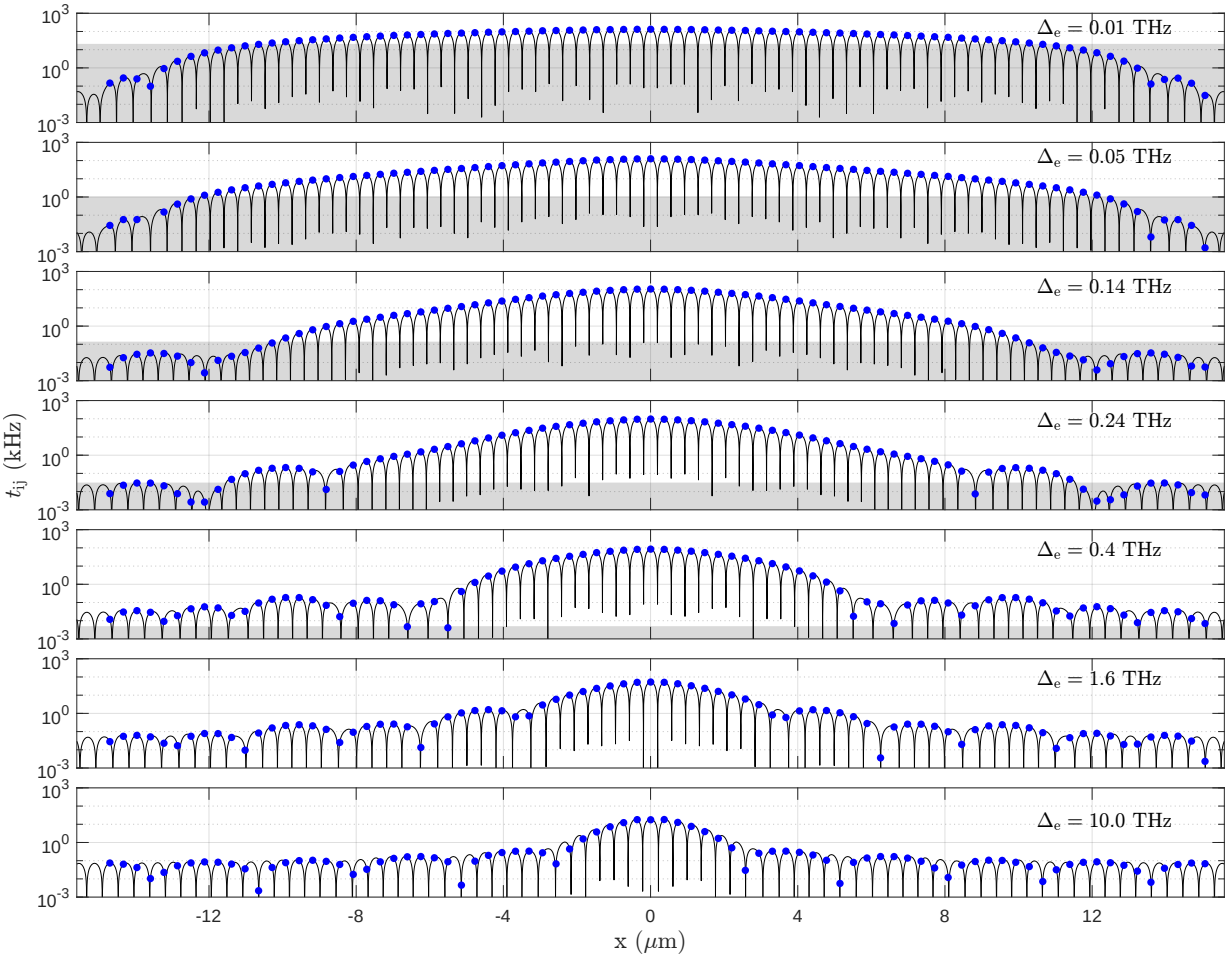

Figure 5.10: Short-ranged atom-atom interaction in a photonic band gap. We numerically evaluate the non-local Green function $\mathbf{G}(\mathbf{r}_i, \mathbf{r}_j; \omega)$ for the SqPhCW and obtain the spin-cooperativity factors for effective detunings $\Delta_e = 0.01$, 0.05, 0.14, 0.24, 0.4, 1.6, 10 THz. Due to the large photon mass m_e, the atoms experience exponentially localized tunneling interactions $t_{ij}/\gamma_m \gg 1$ over lengths L_c. The grey shaded regions depict the dissipative regime with $t_{ij} < \gamma_m$, where collective phononic loss dominates over the coherent tunneling rate. For large Δ_e, the ratio $t_{ij}/\gamma_m \gg 10^4$ is exponentially enhanced at the expense of reduced values $t_{ij} \approx 2\pi \times 20$ kHz and localized length $L_c \approx 2.5 a_0$ at $\Delta_e \approx 10$ THz

Δ_e =0.4 THz, we find tunneling rate $t \approx 2\pi \times 230$ kHz and localization length L_c =0.77 µm and phonon loss rate $\gamma_m \approx 2\pi \times 5$ Hz. Another possible error source could be recoil heating

from the trapping beam. Since we work with FORT in blue detuning, the heating rate can be estimated as $\gamma_{\text{heat}} \approx E_r(\Omega_t/\delta_t)^2\Gamma'/\hbar w_t$ [97], where Ω_t and δ_t are trapping Rabi frequency and laser-atom detuning respectively, and $E_r = 4\pi^2\hbar/2m\lambda_t^2$ is recoil energy. For Cesium atom and our trapping setup, the heating rate is estimated as $\gamma \approx 0.2\,\text{Hz} \ll \gamma_m$, therefore can be neglected safely.

5.6 Toward experimental demonstration: a cluster UHV system for waveguide QED with neutral atoms

The realization of quantum spin networks in our waveguide QED system requires a ultra-high vacuum (UHV) system for cooling and trapping atoms and highly stabilized laser system to control the motion and internal states of atoms. In this section, we present our cluster UHV system designed for various experiments in the Waveguide QED lab at the UQML, including our proposed scheme for universal quantum matter. The designing process began in November 2016 and completed in May 2017 after multiple iterations. The cleaning and air-baking was performed in January 2018.

5.6.1 Design considerations

Designing a UHV system generally requires lots of literature reviews and discussions with experts. This is mainly because vacuum physics is based on a combination of fluid dynamics with surface physics, and there are a set of cautionary design "rules" [161]. In particular, a large and cluster UHV system generally requires a set of well-defined goals and requirements as the system can easily be excessviely complicated and expensive. The goal usually determines a conceptual design and specify the customized parts as well as long-lead items. Furthermore, the designer must pay a great attention to every single joints of the UHV components because one small mistake or missing item would either require a major revision of the design or delay at least one week to procure the replacement. Prof. Kyung Soo Choi and my colleague Hyeran Kong shared their experience and insights with me.

We mainly consider two requirements. First, we must prepare a cold and dense atomic gas trapped in a UHV environment with the ultimate pressure of less than 1×10^{-12} torr where the lifetime of the trapped atoms is estimated to be a few seconds. Preparing a large number of atoms ($N > 10^9$) that are densely trapped in such a low pressure used to be one of the major challenges for the realization of Bose-Einstein condensate in late nineties. Nowadays, this issue can readily be addressed in many AMO physics laboratories

either using the Zeeman slower [235] or preparing the pre-cooled atoms in a separate high-vacuum chamber, namely "Source Chamber" [192]. Both methods aim to prepare a slow and regulated atomic beam to the UHV-maintained "Science Chamber". In the Rydberg Lab at the UQML, former group members have already designed, analyzed, and implemented such a chamber with the latter technique (see reference [161] for the developed system). Here, we applied the same technique for the UHV system in the Waveguide QED Lab. Secondly, as achieving the UHV condition requires considerable manpower with a long pumping time, it is highly desirable to include a loadlock system which enables loading various nanophotonic samples without breaking the vacuum of the Science Chamber. The loadlock system has been used for various deposition and etching systems in many nanofabrication facilities.

In addition to the two major requirements, there are several notable conditions to facilitate waveguide QED experiments. First, the Science Chamber must provide a spacious room to include UHV-compatible optomechanical setups to inject laser fields into a nanophotonic sample. We plan to interface PhCWs with standard optical fibers whose positions are precisely controlled by a UHV-compatible nanopositioner. Also, especially for stainless steel chambers, the number of viewports and their arrangement must be specified according to the number of laser beams and their directions for the conceived cooling and trapping sequences. Furthermore, once a PhCW is loaded in the Science Chamber, the sample is exposed to dense Cesium gases during experiments. We anticipate that metallic Cesium atoms are deposited on the dielectric sample and change the photonic properties, e.g., guided mode frequency. Our solution to this problem is the in-situ plasma cleaning on the metal-deposited silicon nitride sample which has also recently been investigated in trapped-ion community [203].

5.6.2 System architecture

As shown in Figure 5.11(a), our cluster UHV system consists of three chambers: Science Chamber, Source Chamber, and loadlock chambers. Each chamber is supported by three-point contacted aluminum fixtures and the three chambers are connected by stainless steel bellows in order to minimize potential mechanical stress caused by the over-constrained assembly. The separation between the Science Chamber and Source Chamber is made by a differential pumping tube (not shown in Figure 5.11) which maintains the pressure difference by two orders of magnitudes. The loadlock chamber is separated by a gate valve to isolate the pressure of the Science Chamber from outside as it is often exposed to the atmosphere when the nanophotonic sample is loaded. A 60.2 mm–diameter stainless steel

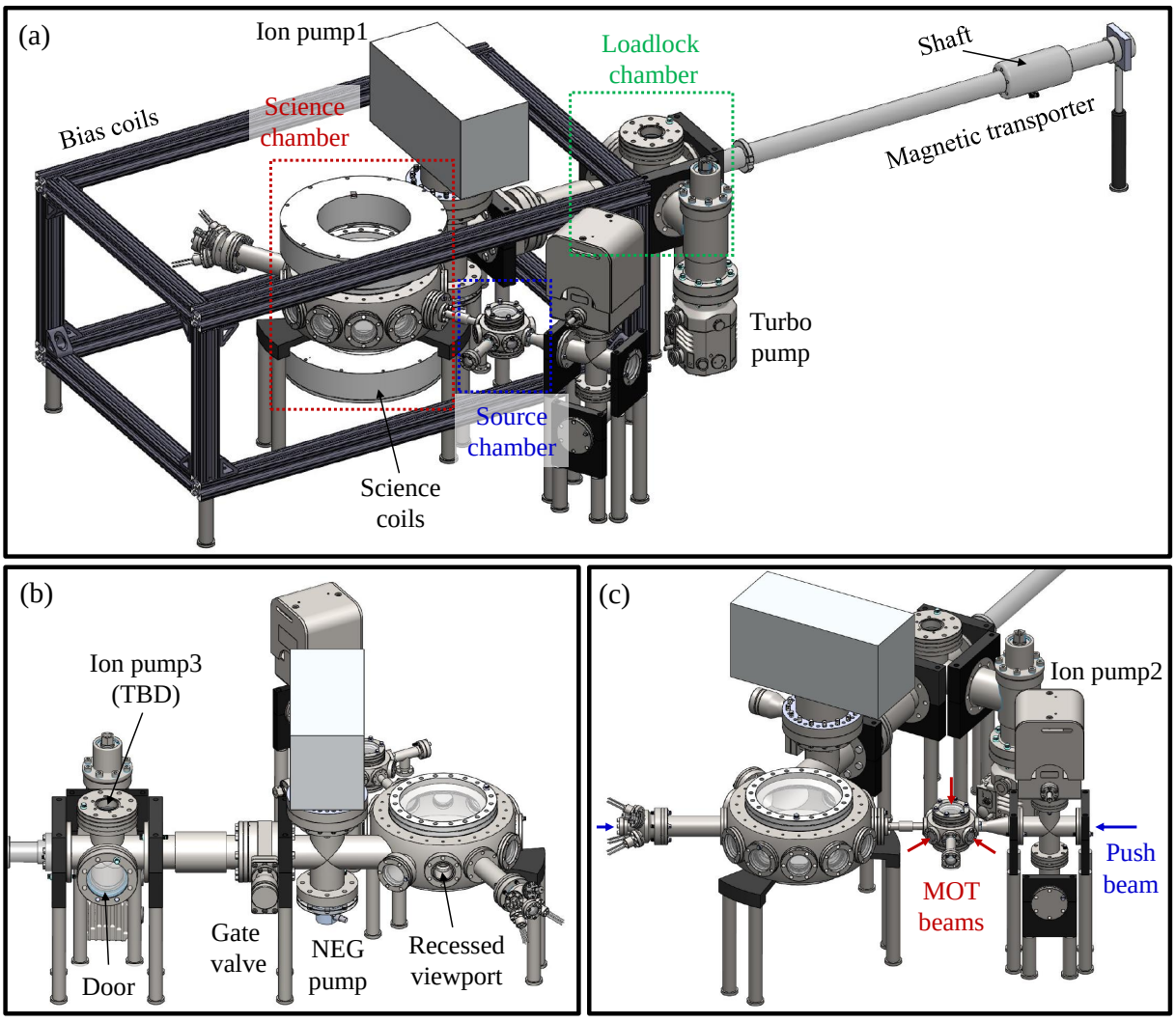

Figure 5.11: 3D CAD drawing of a cluster UHV system designed for the Waveguide QED Lab at the UQML. (a) An overview of the designed system which mainly consists of three chambers: Science Chamber (red deshed line), Source Chamber (blue deshed line), and loadlock chamber (green deshed line). The close-up to (b) the loadlock system and (c) the Source Chamber. See main text for the detailed descriptions.

tube connects the Science Chamber to loadlock chamber, which provides high vacuum conductance for pumps, as discussed later in detail. With the designed architecture, following is the planned experimental procedure.

Loading nanophotonic samples

Figure 5.11(b) shows the close-up to the loadlock system. We close the gate valve, vent the loadlock chamber, and open a viewport to load a sample. Once the sample is mounted on the magnetic transporter, we seal the chamber with the viewport and then pump it down by mechanical pumps, i.e., a roughing pump and turbo pump. After the pressure reaches in a range from 1×10^{-6} torr to 1×10^{-7} torr, a small ion pump (Ion pump3) further reduces the pressure to 1×10^{-10} torr. Then, the gate valve is opened with the non-evaporable getter (NEG) pump (inside the Science Chamber) turned off, and we transport the sample to the docking stage installed inside the Science Chamber. After the sample is secured on the stage, we close the gate valve, and operate the ion pump (Ion pump1) and NEG pump to reduce the pressure in the Science Chamber to 1×10^{-12} torr.

Preparing ultracold atoms

Figure 5.11(c) shows our Source Chamber. The standard magneto-optical trap (MOT) method is utilized to continuously prepare the Doppler-limited cold atomic gas inside the Source Chamber. The three pairs of electromagnet coils are directly mounted on the chamber in order to reduce the number of windings as well as the amount of current flow. Then, a weakly focused laser field (Push beam) delivers the atoms at the well-regulated speed to the Science Chamber where the atoms are re-trapped at the center. The detailed analysis for choosing the beam size and detuning frequency of the Push beam is provided in reference [161].

5.6.3 Subsystem description

Science Chamber

Our Science Chamber is a 27 cm–wide and 9.5 cm–thick stainless steel disk-shaped chamber which is sealed with two 8 inch (20.32 cm) viewports at the top and bottom, ten 2.75 inch (6.985 cm) viewports on the side, and three 4.5 inch (11.43 cm) flanges for the pumps and the sample transportation, as shown in Figure 5.12(a). This large chamber was manufactured the company named VMT. The manufacturing process begins with machining two individual pieces of the main disk-shaped body and the flanges from bulk SS316LN materials. Then, the two parts are welded from both inside and outside. The entire chamber was then electro-polished, ultrasound-cleaned, and vacuum-passivated after the leak-test.

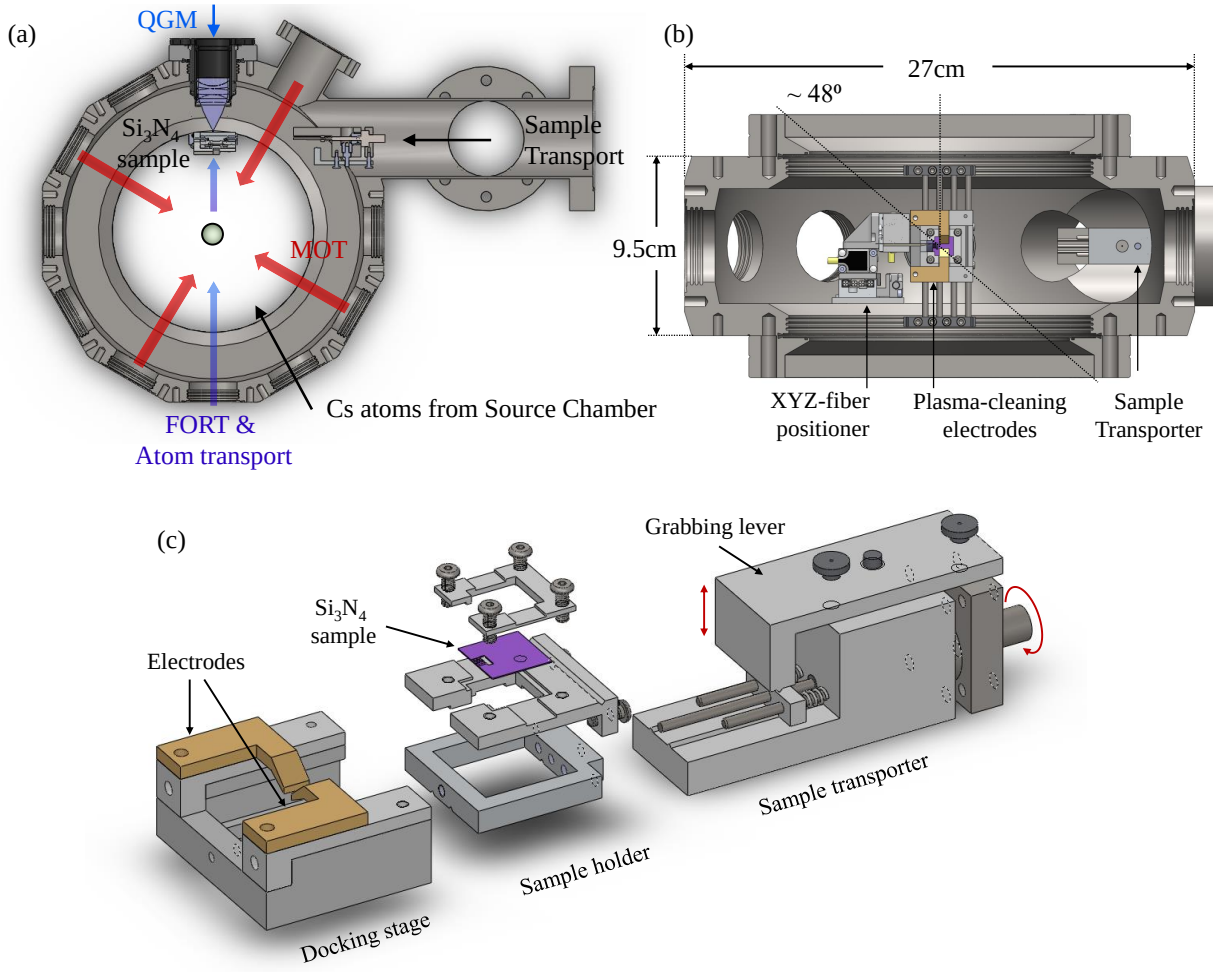

Figure 5.12: 3D CAD drawing of the custom-designed subsystems. (a)–(b) the Science Chamber with a quantum gas microscope (QGM) and XYZ-fiber positioner installed in it. A green sphere represents an atomic cloud that is injected from the Source Chamber and recaptured at the center of the Science Chamber. (c) The docking stage and the sample transporter. The detailed descriptions for each subsystem are provided in the main text.

The chamber provides the wide angle of optical access to the center as well as the sufficient room to install various tools for experiments. The delivered atoms from the Source Chamber are recaptured at the center of the Science Chamber in various optical configurations. The four of the six MOT beams can simply be injected from the four side viewports, as depicted in Figure 5.12(a). Or, if one wants to save the side viewports, then

the four MOT beams could be injected from the top and bottom viewports as the angular field of view is greater than 90°.

Our sample holder is mounted at the docking stage placed in the line-of-sight from the loadlock chamber via the grabber grooves. The UHV-compatible XYZ-nanopositioner is placed next to the sample docking stage in order to selectively couple an optical fiber to one of the several PhCWs fabricated on a Si_3N_4 chip. We plan to use a pair of deformable lenses that are electrically controlled to translate the focal position with the constant spot size [174]. This allows us to transport the atoms from MOT to the optical dipole potential which can then be translated from the center of the Science Chamber to the vicinity of a nanophotonic sample.

As the optimal arrangement of the trapping potential depend on the structures of the samples, we anticipate to use a quantum gas microscope (QGM) with high numerical aperture combined with digital micro-mirror device as a holographic amplitude modulator. Also, we plan to implement a close-loop and real-time rearrangement of the position of the trapped atoms based on images of the atomic lattice through the QGM. This allows us to load a defect-free atomic array in a pseudo-deterministic way, as recently demonstrated with Rydberg atom quantum simulators [43].

Loadlock sample transport and docking stage

The fabricated sample must be precisely and reliably loaded into the Science Chamber. In addition, since PhCWs are suspended in air by tethers attached to the tapered waveguides [313], mechanical vibrations must be minimized during the loading process. We developed a mechanism of transporting and docking the sample. Figure 5.12(c) shows a preliminary design for the sample holder, transporter, and docking stage that may be refined in consideration with the UHV-compatibility in the future.

A brief description of loading procedure is as follows. The fabricated device is first mounted on the Teflon sample holder with the top cover fixed by four UHV-compatiable screws outside the loadlock chamber. The assembled holder is then placed on the sample transporter which is installed in the loadlock chamber. The transporter has a lever whose height is adjusted by the rotation of the magnetic transporter shaft (see Figure 5.11(a)) with respect to the L-shaped main body. This means, if the L-shaped body is not fixed or hold, the rotation of the shaft will freely rotate the whole sample transporter instead of lifting the lever. Therefore, once the holder is properly placed on the transporter, one must hold the body by hands and then rotate the shaft to lower the grabbing lever to hold the sample holder. Once the lever is lowered, the whole transporter stage is freely rotatable,

and therefore the angular alignment can be manually done when the transporter is close to the docking stage inside the Science Chamber. The sample holder can be slided into the docking stage. As this point, we rotate the shaft and lift up the grabbing lever. We can further secure the sample holder on the docking stage by using screws, which completes the loading procedure. The unloading procedure is basically the reverse process of the loading steps.

As briefly mentioned previously, the nanophotonic device may be metalized after its exposure to the Cesium gas. The designed docking stage includes two monolithic titanium blades for in-situ plasma cleaning, as shown in Figure 5.12(c). More sophisticated design analysis will be carried out via finite-element analysis for electric field distribution in the future.

5.6.4 UHV components preparation

We procured all the components including three chambers, viewports, bellows, flanges, oxygen-free coppor gaskets, and silver-plated screws, and so on. Most UHV components are made of SN316LN stainless steel, and the detailed cleaning procedure for this material is well documented in reference [161]. We performed thorough cleaning of the individual components in the acetone-filled ultrasound bath, rinsed them with isopropanol, and let them dried under the Ultra Low Penetration Air (ULPA) filter.

The formation of chromium-oxide layers on surfaces of the individual components is a necessary step to reach the UHV condition. This is because the chromium-oxide layers prevent hydrogen atoms from penetrating into the UHV environment [32]. It can be done by either vacuum-passivation or air-baking process. The manufacturer VMT provided the vacuum-passivation for the Science Chamber. The chromium-oxide layers appear in the interior with gold coloured reflective surface, as shown in Figure 5.13(a). As for the other components, we used our home-made furnace and performed air-baking. Our furnace is made of firebricks covered by the UHV aluminum foil, as shown in Figure 5.13(b). The equipment and the baking recipe were developed in the Rydberg Lab [161]. As shown in Figure 5.13(c) to (f), after the air-baking, we obtained the beautiful gold-coloured components with their reflective metal surfaces well preserved.

5.6.5 Brief summary of other experimental activities

In addition to the UHV system, we implemented lasers and control electronics as well as other prerequisites (e.g., electromagnets and photodetectors) for the Waveguide QED Lab.

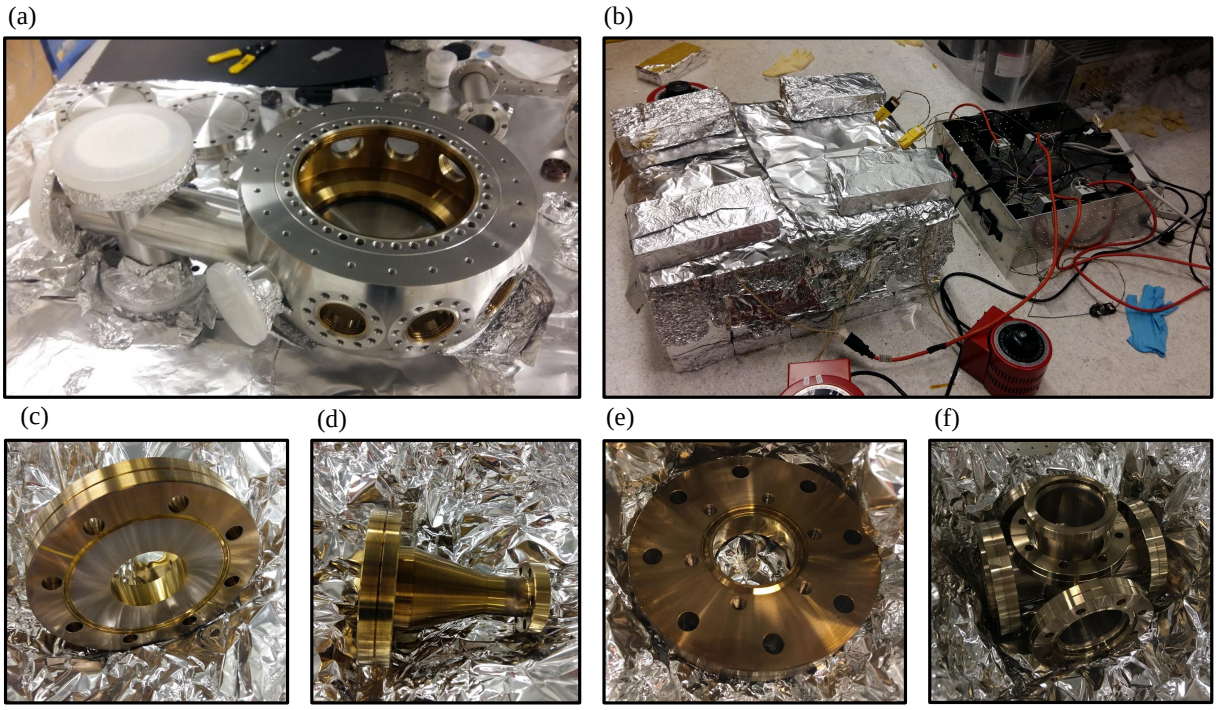

Figure 5.13: Photographs of the UHV components with chromium-oxide layers formed on the surface. (a) Science Chamber after the vacuum-passivation provided by the manufacturer. (b) Home-made furnace for the air-baking process. (c)–(f) The stainless steel (SS316LN) UHV components after the air-baking process.

The accuracy of manipulating atomic internal state and external motion heavily relies on lasers' linewidth and phase noises. The entire laser system must be stable and remote controlled for long data acquisition and analysis.

We designed and implemented three-layer μ–metal enclosures in order to shield external magnetic fields (e.g., Earth magnetic field) for precise spectroscopy with atomic vapour cells, as shown in Figure 5.14(a). We also constructed and tested low-noise power supplies, laser control electronics, a three-channel current source for bias coils, and a twelve-channel acousto-optic modulator (AOM) controller. Circuit diagrams were developed in the Rydberg Lab with the carefully selected electronic components. The mechanical enclosures were machined from Science Machine shop at the University of Waterloo.

The implementation of electromagnetic coils for MOT requires appropriate materials for the coil holder. As it typcially requires several amperes of current flow or greater, the

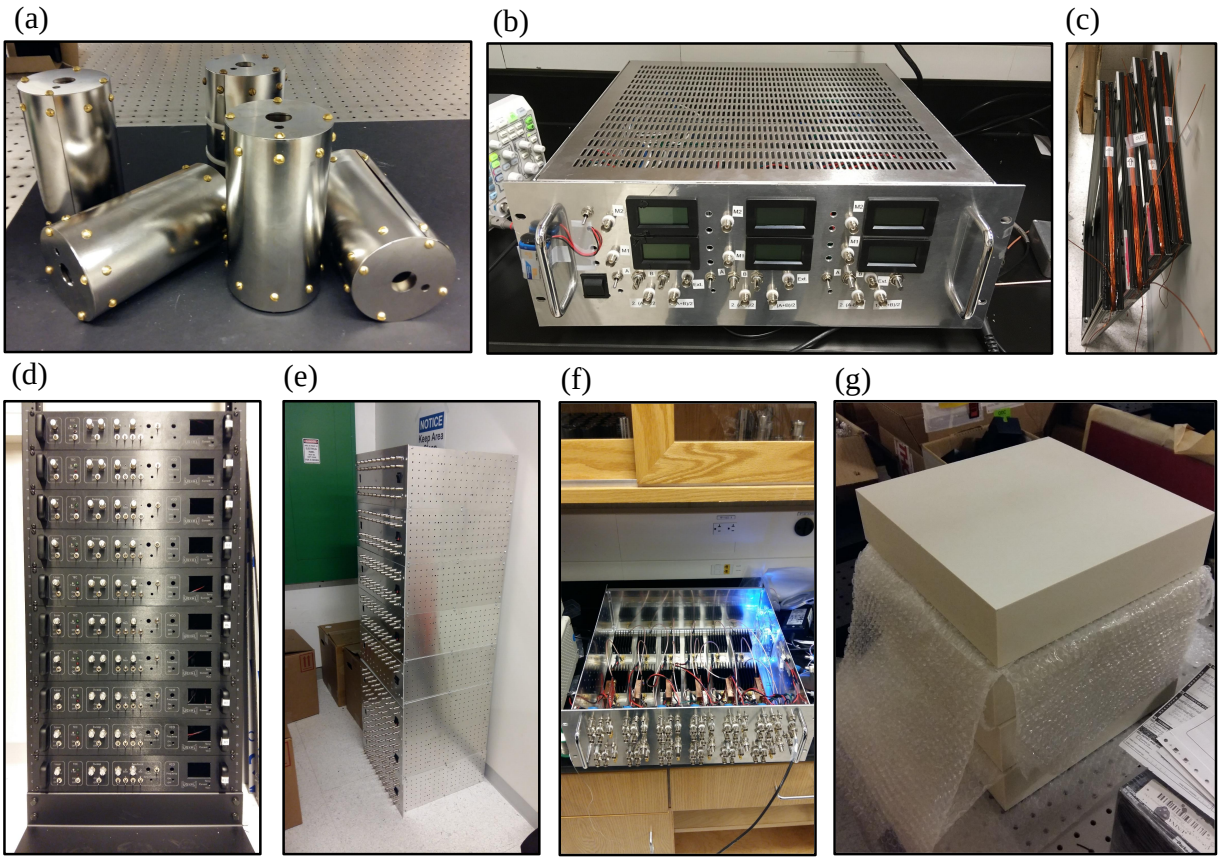

Figure 5.14: Photographs of hardware implemented at UQML. (a) Five three-layer μ–metal enclosures. (b) A stable high-current source for bias coils. (c) Four bias coils. (d) Ten laser control electronics and each of which includes ultra-stable current source, temperature controller, and frequency-locking module. (e) Eight twenty-channel power supplies. (f) A twelve-channel AOM controller. (g) Four laminated $30.5 \times 30.5 \times 7.62\text{cm}^3$ Corian blocks.

material must exhibit good thermal conductivity and high temperature rating. We found a promising candidate of machinable thermoceramic named Corian with the high thermal conductivity $\sim 1.01\,\text{W}\,\text{m}^{-1}\,\text{K}^{-1}$ and good temperature rating $\sim$150°C. One challenge of using it for MOT coils is that this material is not available in blocks. As it is produced for kitchen countertops, the manufacturer DuPont only produces sheets. We found two solutions for this problem. One is to make a block with a stack of the Corian sheets that are glued together so that when they can be machined with no voids present. The other is to thermo-form the sheet to make a cylinder part separately for the coil holder. Then,

the cylinder is glued to the sheet. Both methods would work, but we decided having blocks, as shown in Figure 5.14(g), given that the thermoforming process for individual custom-designed parts with a few quantities was relatively costly.

5.7 Chapter summary

The first part of this chapter described a novel waveguide QED system which allows synthesizing universal quantum matter. An array of atoms are coherently driven under the tailored electromagnetic vacuum, and their correlated photonic Lamb shift generates mechanical interaction between the external motional states of atoms. In turn, the Bogoliubov photons are exploited as a quantum bus for mediating the universal Hamiltonian.

We designed and analyzed a slotted photonic crystal waveguide to support the feasibility of the proposed waveguide QED system. The systematic designing process and optimization yielded a nanophotonic structure tailored to achieve the desired photonic bands for strong photon-mediated mechanical interactions with extremely low dissipations as well as the formation of stable trapping potentials. Based on the Green function formalism, we numerically evaluated the coherent spin-exchange rate between the trapped atoms and the collective decay rate. Also, we presented two possible methods of trapping atoms near the photonic crystal waveguide via far-off resonant traps.

Finally, we presented our progress in the experimental demonstration of the hybrid nanophotonic system with neutral atoms. We designed a cluster UHV system with the detailed plan for experimental procedures. Our UHV system is designed to incorporate a standard loadlock mechanism with the continuous loading of pre-cooled atoms. Our preliminary design of the UHV-compatible sample transporter and docking stage described a full sequence of experimental procedure to load and unload nanophotonic samples. We summarized the preparation of some of equipment to turn our Waveguide QED Lab into a functional AOM laboratory.

Chapter 6

Conclusion and outlook

6.1 Conclusion

The work presented in this thesis demonstrates several advances towards satellite-assisted quantum networks. We discussed the development of three devices, i.e., polarization-entangled photon sources, photon transceivers, and quantum frequency transducers, specifically designed to support the QEYSSat mission. We also described theoretical investigations and experimental progress to realize a fully programmable spin-network as a device for quantum nodes which interface photonic quantum channels with matter qubits and process quantum information.

In Chapter 2, polarization-entangled photon sources were developed to enable concurrent entanglement distributions where one photon is compatiable with ground-based fiber-optic networks while the other photon is compatible with ground-to-satellite free-space channels. We showed a novel beam-displacement Sagnac-interferometer which is the first design to allow using various optical nonlinear media without customizing (and hard to manufacture) polarization optics. Also, the direct generation of entangled photon-pairs from optical fibers via dual-pump four-wave mixing was analyzed to show the feasibility of experimental demonstrations. These research outcomes contribute to practical implementations of polarization-entangled photon sources and to improving the stability of the sources.

In Chapter 3, two dedicated characterization platforms were developed for assessments of aberrations and polarization effects of large scale optical components used for satellite quantum communications, including lenses and telesocpes. Our new aberration test system

for lenses, reflective or refractive telescopes can perform the wavefront measurement at a precision which is an order of magnitude better than conventional Shack-Hartmann wavefront sensors. Also, we built a unique robotized polarization-test system which allows analyzing polarization states at desired positions and angles, which enables characterizing a variety of optical components at consistent precision. Both measurement systems produced test results which closely matched results from theoretical models. Two telescopes and their primary elements, e.g., the 20.3 cm achromatic doublet and the curved primary mirror, were tested to show the fitness of optical transceivers in the QEYSSat mission.

In Chapter 4, an optical microring resonator was designed and numerically simulated for quantum frequency translations, with the goal to interface quantum-dot-based photon emitters with ground-to-satellite quantum links in the QEYSSat mission. The designed device is predicted to tranlsate the wavelength from 985 nm to 785 nm with the conversion efficiency of 80 % including the 0.05 $\mathrm{dB\,cm^{-1}}$ propagation loss at the single-pump powers of 15 mW. The potential integrability of the designed ring resonators with quantum-dot-based photon emitters provides the first step toward performing single-photon quantum key distributions with satellites. As an alternative approach a photonic-crystal fiber system was studied and experimental data was generated to show that the desired phase-matching conditions indeed exist.

In Chapter 5, a many-body waveguide QED system was developed with an array of atoms trapped in the vicinity of a photonic crystal waveguide. We proposed a novel scheme to simulate universal Hamiltonians by utilizing strong interactions between atoms and the guided photons under vacuum of the nanophotonic structure. The correlated motions of atoms, which arises from a strong photonic Lamb shift, can mediate an arbitrary SU(2) spin-spin interactions between any sites of atoms. The interactions can then be programmed by the Raman sideband engineering, thereby constructing a universal and analogue quantum simulator. We designed a slotted photonic crystal waveguide to realize the proposed many-body QED system. The spin-spin interactions and collective dissipations of the Cesium atoms were numerically computed to show strong and long-live coherent dynamics over the dissipations. We also showed two different approaches to form stable trapping potentials of atoms in the vicinity of the dielectric. We presented our experimental progresses toward the realization of the proposed scheme.

The work in this thesis covered a wide range of theories of light from classical linear and nonlinear optics to advanced quantum optics with dielectrics. Our polarimeters in Chapter 3 were modeled in a Mueller matrix formalism based on classical fields interacting with linear optical media. The theory of quantum frequency translations was formulated from classical nonlinear optics in Chapter 4. The coupling between discretized cavity modes and continuous waveguide modes was treated in a purterbative approach, and the

system dynamics was described by a mean-field theory of driven-dissipative open quantum system. The generation of entangled photon pairs in Chapter 2 was described in standard quantum optics theory with the electromagnetic vacuum as a resource of creating photons. In Chapter 5, the vacuum was a medium engineered by quantum and classical dielectrics. Atoms dressed by photonic fields under the modified vacuum formed a nanoscopic quantum network, and the system dynamics was fully described by driven-dissipative open quantum systems based on the Green function formalism. Various numerical techniques based on the forementioned physical theories were developed to analyze various components in the devices presented in this thesis. We share several source codes in the appendices and the UQML Github https://github.com/Quantum-Matter-and-Light/waveguideQEDcodes.

The work presented in this thesis has been publicised as follows:

1. Youn Seok Lee, Mengyu Xie, Ramy Tannous, and Thomas Jennewein. Sagnac-type entangled photon source using only conventional polarization optics. Quantum Sci. Technol., **6** 025004 (2021) [308]

2. Mengyu Xie, Youn Seok Lee, Ramy Tannous, Guilu Long, and Thomas Jennewein. Roles of fiber birefringence and Raman scattering in spontaneous four-wave mixing process through birefringent fiber. Opt. Express **29**(20), 31348-31363 (2021) [171]

3. Youn Seok Lee, Kimia Mohammadi, and Thomas Jennewein. Practical wavefront measurement with scanning pentaprism for optical terminals in free-space quantum communication. *In preparation*

4. Youn Seok Lee, Kimia Mohammadi, Lindsay Babcock, Brendon Higgins, Hugh Podmore, and Thomas Jennewein. Robotized polarization characterization platform for free-space quantum communications. arXiv:2109.01984 (2021) [170]

5. Hugh Podmore, Ian D'Souza, Jeffrey Cain, Thomas Jennewein, Brendon Higgins, Youn Seok Lee, Alex Koujelev, Danya Hudson, Ashley McColgan. QKD Terminal for Canada's Quantum Encryption and Science Satellite (QEYSSat). Proc. SPIE 11851, International Conference on Space Optics — ICSO 2020, 118520H (2021) [237]

6. Ying Dong, Jacob Taylor, Youn Seok Lee, Hyeran Kong, and Kyung Soo Choi. Waveguide QED toolboxes for universal quantum matter. arXiv:1712.02020v4 (2021) [76]

6.2 Outlook

6.2.1 Polarization-entangled photon sources

Development of entangled photon sources for the QEYSSat mission

Section 2.4 presented the conceptual baseline of a polarization-entangled photon source suitable for the QEYSSat mission, and currently a new source is under construction. This new source will be mainly focused on the generation of entangled photon-pairs, namely signal and idler, with the brightness greater than 100 MHz and fiber-coupling efficiency above 90 %. We fully expect that the signal photons at 790 nm are sent to the satellite and the idlers at 1552 nm are measured on the ground to perform quantum key distributions between ground and space. The development of such ultra-bright, narrow-band, and low-noise sources of entangled photons is technically challenging. In Section 2.4, we mainly discussed optimizing the experimental parameters to achieve the high brightness and fiber-coupling efficiency.

Another important consideration is the photon detections on the ground. Assuming that the photons on the ground do not experience high losses, the photon detection and the data acquisition must be performed at a similar rate to the production. This requires single-photon detectors that are capable of detecting the idlers at the 100 MHz detection rate without being saturated. Also, the time of arrival must be recorded by a high-speed time tagger, which is then efficiently stored in a computer for the post-processing. In the Quantum Photonics Laboratory (QPL) group, we recently acquired a six-channel superconducting nanowire single-photon detector whose maximum photon-detection rate of each channel is greater than 20 MHz. The distribution of the idlers over the six channels can reduce the overhead of high-rate photon detection at each channel. This multiplexed detection scheme can be further used to perform reference-frame-independent quantum key distributions, namely 6-4 state protocol, where the polarization states of the idler is fully characterized by the measurements with six tomographically complete polarization states [281]. Our group also acquired a high-speed time-tagging system which has a 15.625 ps timing resolution with 64 independent input channels. Data transfer to the host computer is via external-PCI-express interface, enabling a high-speed data transfer up to a total of 800 MHz continous events for all inputs combined. The complete entangled photon source will be installed in the QEYSSat Science Operating Center located at University of Waterloo.

Polarization-entangled photon-triplets via third-order parametric down conversions

Our beam-displacement Sagnac-type entangled photon source can be adapted for various optical media at a wide range of wavelengths. The direct production of photon triplets has been known for an interesting subject owing to its non-Gaussianity of the generated fields which is in general a resource of photonic universal quantum computing [112]. So far, photon triplets at optical frequencies have been realized only by cascaded second-order parametric down conversion processes [128]. Its direct generation via third-order parametric down-conversion has been a long-standing goal, and several fiber media have been proposed as promising cadidates [54]. By placing a photon-triplet source in the Sagnac-loop, one can produce polarization-entangled photon triplets such as Greenberger–Horne–Zeilinger state. Interestingly, when the third-order nonlinear process is fully seeded by lasers, genuine tripartite continuous-variable entanglement is generated, which appears to be robust to photon losses [103].

6.2.2 Characterization of optical terminals and optical components for satellite quantum communications

We demonstrated two unique instruments for characterization of polarization and wavefront aberration of large optical systems. Our characterization systems can be further upgraded in the future. For instance, The precision of our imaging polarimeter is mainly limited by the dynamic range and noise of the camera being used. This is indicated by the interquartile range of the measured QBERs that are greater than the median values. Also, note that the linearity of the camera's exposure time showed uncertainty from 0.1 % to 1.6 %. Since our AOI measurements verified the reliable control of the position and orientation of the polarimeter, the replacement of the camera with two photomultiplier-tube (PMT) modules may be considered in future to improve polarization measurement precision [22].

In the near future, we will upgrade our aberration characterization system by extending our linear measurement setup to two-dimensional measurement of wavefronts, which may identify correctable aberrations such as coma aberration. The two-dimensional topography of optical surfaces has been obtained in scanning pentaprism deflectometries [275, 10, 245]. One could perform additional linear measurements in different scanning directions, and reconstruct wavefronts using similar methods. For example, wavefronts can be expanded in terms of Zernike polynomials, and its gradient in the scanning directions can be fit to the measured slopes via a least-squares method, as discussed in [245]. Also, the measurement precision may be further improved by more precise alignment of the pentaprism. The

quadratic response of centroid position shifts caused by the pentaprism rotation around the scanning direction can be minimized by the alignment of the pentaprism to the normal incident angle. This can be experimentally tested by centroid position measurements as a function of pentaprism rotation angles in both scanning and cross-scanning directions. The detailed description of the test method is provided in [95].

The two characterization systems will continue to support the development of optical terminals in the QEYSSat mission. Kimia Mohammadi in the QPL is currently responsible for developing a fine-pointing module, and the assembly of the quantum optical transmitter will be characterized in terms of aberrations and polarizations. Also, our industry partner, Honeywell Canada Aerospace, recently reported the development of the optical terminal for the receiver to be placed at the satellite [237]. The quantum link between the two systems will be tested before launching the QETSSat satellite, currently expected in late 2022.

6.2.3 Integration of silicon nitride nanophotonic devices with quantum-dot photon emitters

One challenge of using quantum-dot-based photon emitters for quantum communication tasks is to alter polarizations and frequencies of the emitted photons at high repetition rates. Our numerical designing and analysis tools can be utilized to develop on-chip quantum light sources emitting photons with structured characteristics. For example, wavelength superposition states of single photons can be generated by frequency translation processes in the ring resonators. Also, one could enhance photon emission rates with time-multiplexed pump pulses by embedding multiple quantum emitters. Moreover, as recently demonstrated by Loredo *et al.* [188], the photon number states could be selectively populated or even superposed by transferring coherence of pump fields to multiple quantum dot sources.

The integration of the silicon nitride ring resonators with quantum-dot photon emitters requires a technological capability of operating the device in a cryogenic temperature. The optical properties of silicon nitride films must be characterized in low temperatures. The characterization results will then be used to design ring resonators or other devices to perform the desired quantum optical tasks. Recently, Kartik Srinivasan's group at the National Institute of Standards and Technology demonstrated soliton frequency combs at cryogenic temperatures using a silicon nitride miroring resonator [215]. Their measurement was performed at around 10 K and showed a thermorefractive coefficient two orders of magnitude smaller than the room-temperature value, which leads to the strong suppression

of optical frequency fluctuations. Also, it was shown that the Lugiato-Lefever equation with a simple thermal model reproduces their experimental results. In the future, our numerical solver for the generalized nonlinear Schrödinger equation with the Ikeda map could be incorporated with the thermal model to further support the design of ring resonators at cryogenic temperatures.

6.2.4 Interfacing quantum matter with satellite quantum communication links

Our quantum frequency transducers and our analogue quantum simulator can be integrated on a silicon nitride chip. The D_1–transition frequency of Cesium atoms (λ_{D_1} =894 nm) can be translated to the wavelength for free-space quantum channels (λ_{D_1} =785 nm). Then, two or more quantum matter at distant locations, each of which can be arbitrarily designed at local, can be efficiently linked and potentially entangled by free-space channels. One interesting experiment would be the investigation of entanglement between two quantum matter, one of which is placed in an orbiting satellite. According to the discussions in reference [44], it is expected that the entanglement is degraded due to the change of the gravitational field. If so, one might ask a question "can we find and realize quantum states of matter that can protect nonlocal correlations from gravity-induced decoherence?". This question is just a speculation, and future experiments may provide the answers.

The large-scale quantum network with long-range links and the small-scale spin network with complex connectivity will continue to be pursued and involve many different physical realizations. The research and results demonstrated in this thesis will provide important steps towards this long-term vision of a global quantum network for both scientific advances and practical applications.

References

[1] Corning smf-28e+ optical fiber data sheet. https://www.corning.com/media/worldwide/coc/documents/Fiber/PI-1463-AEN.pdf.

[2] *Beam Optics*, chapter 3, pages 80–107. John Wiley & Sons, Ltd, 1991.

[3] *Optical Microresonator Theory*, pages 71–103. Springer New York, New York, NY, 2008.

[4] G. S. Agarwal. Quantum electrodynamics in the presence of dielectrics and conductors. iv. general theory for spontaneous emission in finite geometries. *Phys. Rev. A*, 12:1475–1497, Oct 1975.

[5] Imad Agha, Marcelo Davanço, Bryce Thurston, and Kartik Srinivasan. Low-noise chip-based frequency conversion by four-wave-mixing bragg scattering in sinx waveguides. *Opt. Lett.*, 37(14):2997–2999, Jul 2012.

[6] G.-P. Agrawal. *Nonlinear Fiber Optics*. Academic Press, Boston, Massachusetts, 1995.

[7] Brian F. Alexander and Kim Chew Ng. Elimination of systematic error in subpixel accuracy centroid estimation [also Letter 34(11)3347-3348(Nov1995)]. *Optical Engineering*, 30(9):1320 – 1331, 1991.

[8] D. W. Allan. Statistics of atomic frequency standards. *Proceedings of the IEEE*, 54(2):221–230, 1966.

[9] R Alléaume, F Treussart, G Messin, Y Dumeige, J-F Roch, A Beveratos, R Brouri-Tualle, J-P Poizat, and P Grangier. Experimental open-air quantum key distribution with a single-photon source. *New Journal of Physics*, 6:92–92, jul 2004.

[10] Richard Allen, Peng Su, James H. Burge, Brian Cuerden, and Hubert M. Martin. Scanning pentaprism test for the GMT 8.4-m off-axis segments. In Eli Atad-Ettedgui and Dietrich Lemke, editors, *Modern Technologies in Space- and Ground-based Telescopes and Instrumentation*, volume 7739, pages 340 – 351. International Society for Optics and Photonics, SPIE, 2010.

[11] J. Sánches Almeida, V. Martínez pillet, and A. D. Wittmann. The instrumental polarization of a gregory-coudé telescope. *Solar Physics*, 134:1–13, 1991.

[12] J.B. Altepeter, E.R. Jeffrey, and P.G. Kwiat. Photonic state tomography. volume 52 of *Advances In Atomic, Molecular, and Optical Physics*, pages 105–159. Academic Press, 2005.

[13] Luigi Amico, Rosario Fazio, Andreas Osterloh, and Vlatko Vedral. Entanglement in many-body systems. *Rev. Mod. Phys.*, 80:517–576, May 2008.

[14] M. Anderson, T. Müller, J. Skiba-Szymanska, A. B. Krysa, J. Huwer, R. M. Stevenson, J. Heffernan, D. A. Ritchie, and A. J. Shields. Gigahertz-clocked teleportation of time-bin qubits with a quantum dot in the telecommunication c band. *Phys. Rev. Applied*, 13:054052, May 2020.

[15] Gerasimos Angelatos. *Theory and applications of light-matter interactions in quantum dot nanowire photonic crystal systems*. PhD thesis, Queen's University, 2015.

[16] Shin Arahira, Naoto Namekata, Tadashi Kishimoto, Hiroki Yaegashi, and Shuichiro Inoue. Generation of polarization entangled photon pairs at telecommunication wavelength using cascaded $\chi(2)$ processes in a periodically poled linbo3 ridge waveguide. *Opt. Express*, 19(17):16032–16043, Aug 2011.

[17] Frank Arute, Kunal Arya, Ryan Babbush, Dave Bacon, Joseph C. Bardin, Rami Barends, Rupak Biswas, Sergio Boixo, Fernando G. S. L. Brandao, David A. Buell, Brian Burkett, Yu Chen, Zijun Chen, Ben Chiaro, Roberto Collins, William Courtney, Andrew Dunsworth, Edward Farhi, Brooks Foxen, Austin Fowler, Craig Gidney, Marissa Giustina, Rob Graff, Keith Guerin, Steve Habegger, Matthew P. Harrigan, Michael J. Hartmann, Alan Ho, Markus Hoffmann, Trent Huang, Travis S. Humble, Sergei V. Isakov, Evan Jeffrey, Zhang Jiang, Dvir Kafri, Kostyantyn Kechedzhi, Julian Kelly, Paul V. Klimov, Sergey Knysh, Alexander Korotkov, Fedor Kostritsa, David Landhuis, Mike Lindmark, Erik Lucero, Dmitry Lyakh, Salvatore Mandrà, Jarrod R. McClean, Matthew McEwen, Anthony Megrant, Xiao Mi, Kristel Michielsen, Masoud Mohseni, Josh Mutus, Ofer Naaman, Matthew Neeley, Charles

Neill, Murphy Yuezhen Niu, Eric Ostby, Andre Petukhov, John C. Platt, Chris Quintana, Eleanor G. Rieffel, Pedram Roushan, Nicholas C. Rubin, Daniel Sank, Kevin J. Satzinger, Vadim Smelyanskiy, Kevin J. Sung, Matthew D. Trevithick, Amit Vainsencher, Benjamin Villalonga, Theodore White, Z. Jamie Yao, Ping Yeh, Adam Zalcman, Hartmut Neven, and John M. Martinis. Quantum supremacy using a programmable superconducting processor. *Nature*, 574(7779):505–510, Oct 2019.

[18] M. Aspelmeyer, T. Jennewein, M. Pfennigbauer, W.R. Leeb, and A. Zeilinger. Long-distance quantum communication with entangled photons using satellites. *IEEE Journal of Selected Topics in Quantum Electronics*, 9(6):1541–1551, 2003.

[19] David D. Awschalom, Ronald Hanson, Jörg Wrachtrup, and Brian B. Zhou. Quantum technologies with optically interfaced solid-state spins. *Nature Photonics*, 12(9):516–527, Sep 2018.

[20] R. M. A. Azzam. Stokes-vector and mueller-matrix polarimetry. *J. Opt. Soc. Am. A*, 33(7):1396–1408, Jul 2016.

[21] Eyal Bahar, Xiaoyue Ding, Asaf Dahan, Haim Suchowski, and Jeffrey Moses. Adiabatic four-wave mixing frequency conversion. *Opt. Express*, 26(20):25582–25601, Oct 2018.

[22] J. Bailey, L. Kedziora-Chudczer, D. V. Cotton, K. Bott, J. H. Hough, and P. W. Lucas. A high-sensitivity polarimeter using a ferro-electric liquid crystal modulator. *Monthly Notices of the Royal Astronomical Society*, 449:3064–3073, 2015.

[23] Stéphane Balac and Arnaud Fernandez. Spip: A computer program implementing the interaction picture method for simulation of light-wave propagation in optical fibre. *Computer Physcis Communications*, 199:139–152, 2016.

[24] Christoph Baune, Jan Gniesmer, Axel Schönbeck, Christina E. Vollmer, Jaromír Fiurášek, and Roman Schnabel. Strongly squeezed states at 532 nm based on frequency up-conversion. *Opt. Express*, 23(12):16035–16041, Jun 2015.

[25] Christoph Baune, Axel Schönbeck, Aiko Samblowski, Jaromír Fiurášek, and Roman Schnabel. Quantum non-gaussianity of frequency up-converted single photons. *Opt. Express*, 22(19):22808–22816, Sep 2014.

[26] Jared F. Bauters, Martijn J. R. Heck, Demis John, Daoxin Dai, Ming-Chun Tien, Jonathon S. Barton, Arne Leinse, René G. Heideman, Daniel J. Blumenthal, and

John E. Bowers. Ultra-low-loss high-aspect-ratio si3n4 waveguides. *Opt. Express*, 19(4):3163–3174, Feb 2011.

[27] C. Beck, R. Schlichenmaier, M. Collados, L. B. Rubio, and T. Kentischer. A polarization model for the german vacuum tower telescope from in situ and laboratory measurements. *Astronomy and Astrophysics*, 443:1047–1053, 2005.

[28] Robert Bedington, Juan Miguel Arrazola, and Alexander Ling. Progress in satellite quantum key distribution. *npj Quantum Information*, 3(1):30, Aug 2017.

[29] Charles H. Bennett and Gilles Brassard. Quantum cryptography: Public key distribution and coin tossing. *Theoretical Computer Science*, 560:7–11, Dec 2014.

[30] Charles H. Bennett, Gilles Brassard, and N. David Mermin. Quantum cryptography without bell's theorem. *Phys. Rev. Lett.*, 68:557–559, Feb 1992.

[31] Ryan S. Bennink. Optimal collinear gaussian beams for spontaneous parametric down-conversion. *Phys. Rev. A*, 81:053805, May 2010.

[32] M. Bernardini, S. Braccini, R. De Salvo, A. Di Virgilio, A. Gaddi, A. Gennai, G. Genuini, A. Giazotto, G. Losurdo, H. B. Pan, A. Pasqualetti, D. Passuello, P. Popolizio, F. Raffaelli, G. Torelli, Z. Zhang, C. Bradaschia, R. Del Fabbro, I. Ferrante, F. Fidecaro, P. La Penna, S. Mancini, R. Poggiani, P. Narducci, A. Solina, and R. Valentini. Air bake-out to reduce hydrogen outgassing from stainless steel. *Journal of Vacuum Science & Technology A*, 16(1):188–193, 1998.

[33] Immanuel Bloch, Jean Dalibard, and Wilhelm Zwerger. Many-body physics with ultracold gases. *Rev. Mod. Phys.*, 80:885–964, Jul 2008.

[34] Daniel J. Blumenthal, René Heideman, Douwe Geuzebroek, Arne Leinse, and Chris Roeloffzen. Silicon nitride in silicon photonics. *Proceedings of the IEEE*, 106(12):2209–2231, 2018.

[35] J. Bochmann, M. Mücke, C. Guhl, S. Ritter, G. Rempe, and D. L. Moehring. Lossless state detection of single neutral atoms. *Phys. Rev. Lett.*, 104:203601, May 2010.

[36] K. Boone, J.-P. Bourgoin, E. Meyer-Scott, K. Heshami, T. Jennewein, and C. Simon. Entanglement over global distances via quantum repeaters with satellite links. *Phys. Rev. A*, 91:052325, May 2015.

[37] Bruno Boulbry, Jessica C. Ramella-Roman, and Thomas A. Germer. Improved method for calibrating a stokes polarimeter. *Appl. Opt.*, 46(35):8533–8541, Dec 2007.

[38] J.-P. Bourgoin, E. Meyer-Scott, B. L. Higgins, B. Helou, C. Erven, H. Hübel, R. Laflamme, T. Jennewein, B. Kumar, D. Hudson, I. D'Souza, and R. Girard. A comprehensive design and performance analysis of low earth orbit satellite quantum communication. *New Journal of Physics*, 15(2):35, 2013.

[39] Katherine Bourzac. 4 tough chemistry problems that quantum computers will solve [news]. *IEEE Spectrum*, 54(11):7–9, 2017.

[40] Dik Bouwmeester, Jian-Wei Pan, Klaus Mattle, Manfred Eibl, Harald Weinfurter, and Anton Zeilinger. Experimental quantum teleportation. *Nature*, 390(6660):575–579, Dec 1997.

[41] Robert W. Boyd. *Nonlinear Optics, Third Edition*. Academic Press, Inc., USA, 3rd edition, 2008.

[42] Samuraí Brito, Askery Canabarro, Daniel Cavalcanti, and Rafael Chaves. Satellite-based photonic quantum networks are small-world. *PRX Quantum*, 2:010304, Jan 2021.

[43] Antoine Browaeys and Thierry Lahaye. Many-body physics with individually controlled rydberg atoms. *Nature Physics*, 16(2):132–142, Feb 2020.

[44] David Edward Bruschi, Carlos Sabín, Angela White, Valentina Baccetti, Daniel K L Oi, and Ivette Fuentes. Testing the effects of gravity and motion on quantum entanglement in space-based experiments. *New Journal of Physics*, 16(5):053041, may 2014.

[45] Stefan Yoshi Buhmann, Ludwig Knöll, Dirk-Gunnar Welsch, and Ho Trung Dung. Casimir-polder forces: A nonperturbative approach. *Phys. Rev. A*, 70:052117, Nov 2004.

[46] Stefan Yoshi Buhmann and Dirk-Gunnar Welsch. Dispersion forces in macroscopic quantum electrodynamics. *Progress in Quantum Electronics*, 31(2):51–130, 2007.

[47] Iulia Buluta and Franco Nori. Quantum simulators. *Science*, 326(5949):108–111, 2009.

[48] A. S. Cacciapuoti, M. Caleffi, F. Tafuri, F. S. Cataliotti, S. Gherardini, and G. Bianchi. Quantum internet: Networking challenges in distributed quantum computing. *IEEE Network*, 34(1):137–143, 2020.

[49] Raymond Y Q Cai and Valerio Scarani. Finite-key analysis for practical implementations of quantum key distribution. *New Journal of Physics*, 11(4):045024, apr 2009.

[50] Giuseppe Calajó, Francesco Ciccarello, Darrick Chang, and Peter Rabl. Atom-field dressed states in slow-light waveguide qed. *Phys. Rev. A*, 93:033833, Mar 2016.

[51] Marcello Caleffi, Angela Sara Cacciapuoti, and Giuseppe Bianchi. Quantum internet: From communication to distributed computing. In *Proceedings of the 5th ACM International Conference on Nanoscale Computing and Communication*, NANOCOM '18, New York, NY, USA, 2018. Association for Computing Machinery.

[52] Yuan Cao, Yu-Huai Li, Kui-Xing Yang, Yang-Fan Jiang, Shuang-Lin Li, Xiao-Long Hu, Maimaiti Abulizi, Cheng-Long Li, Weijun Zhang, Qi-Chao Sun, Wei-Yue Liu, Xiao Jiang, Sheng-Kai Liao, Ji-Gang Ren, Hao Li, Lixing You, Zhen Wang, Juan Yin, Chao-Yang Lu, Xiang-Bin Wang, Qiang Zhang, Cheng-Zhi Peng, and Jian-Wei Pan. Long-distance free-space measurement-device-independent quantum key distribution. *Phys. Rev. Lett.*, 125:260503, Dec 2020.

[53] Yuan Cao, Yu-Huai Li, Wen-Jie Zou, Zheng-Ping Li, Qi Shen, Sheng-Kai Liao, Ji-Gang Ren, Juan Yin, Yu-Ao Chen, Cheng-Zhi Peng, and Jian-Wei Pan. Bell test over extremely high-loss channels: Towards distributing entangled photon pairs between earth and the moon. *Phys. Rev. Lett.*, 120:140405, Apr 2018.

[54] Andrea Cavanna, Jonas Hammer, Cameron Okoth, Erasto Ortiz-Ricardo, Hector Cruz-Ramirez, Karina Garay-Palmett, Alfred B. U'Ren, Michael H. Frosz, Xin Jiang, Nicolas Y. Joly, and Maria V. Chekhova. Progress toward third-order parametric down-conversion in optical fibers. *Phys. Rev. A*, 101:033840, Mar 2020.

[55] Poompong Chaiwongkhot, Sara Hosseini, Arash Ahmadi, Brendon L. Higgins, Dan Dalacu, Philip J. Poole, Robin L. Williams, Michael E. Reimer, and Thomas Jennewein. Enhancing secure key rates of satellite qkd using a quantum dot single-photon source, 2020.

[56] D. E. Chang, J. S. Douglas, A. González-Tudela, C.-L. Hung, and H. J. Kimble. Colloquium: Quantum matter built from nanoscopic lattices of atoms and photons. *Rev. Mod. Phys.*, 90:031002, Aug 2018.

[57] D. E. Chang, L. Jiang, A. V. Gorshkov, and H. J. Kimble. Cavity QED with atomic mirrors. *New Journal of Physics*, 14(6):063003, jun 2012.

[58] M. Imran Cheema and Andrew G. Kirk. Accurate determination of the quality factor and tunneling distance of axisymmetric resonators for biosensing applications. *Opt. Express*, 21(7):8724–8735, Apr 2013.

[59] Xie Chen, Zheng-Cheng Gu, and Xiao-Gang Wen. Local unitary transformation, long-range quantum entanglement, wave function renormalization, and topological order. *Phys. Rev. B*, 82:155138, Oct 2010.

[60] Yan Chen, Jiaxiang Zhang, Michael Zopf, Kyubong Jung, Yang Zhang, Robert Keil, Fei Ding, and Oliver G. Schmidt. Wavelength-tunable entangled photons from silicon-integrated iii–v quantum dots. *Nature Communications*, 7(1):10387, Jan 2016.

[61] Jae-yoon Choi, Sebastian Hild, Johannes Zeiher, Peter Schauß, Antonio Rubio-Abadal, Tarik Yefsah, Vedika Khemani, David A. Huse, Immanuel Bloch, and Christian Gross. Exploring the many-body localization transition in two dimensions. *Science*, 352(6293):1547–1552, 2016.

[62] J. I. Cirac, P. Zoller, H. J. Kimble, and H. Mabuchi. Quantum state transfer and entanglement distribution among distant nodes in a quantum network. *Phys. Rev. Lett.*, 78:3221–3224, Apr 1997.

[63] John F. Clauser, Michael A. Horne, Abner Shimony, and Richard A. Holt. Proposed experiment to test local hidden-variable theories. *Phys. Rev. Lett.*, 23:880–884, Oct 1969.

[64] Stéphane Clemmen, Alessandro Farsi, Sven Ramelow, and Alexander L. Gaeta. Ramsey interference with single photons. *Phys. Rev. Lett.*, 117:223601, Nov 2016.

[65] Stéphane Coen, Hamish G. Randle, Thibaut Sylvestre, and Miro Erkintalo. Modeling of octave-spanning kerr frequency combs using a generalized mean-field lugiato–lefever model. *Opt. Lett.*, 38(1):37–39, Jan 2013.

[66] Daniel C. Cole, Erin S. Lamb, Pascal Del'Haye, Scott A. Diddams, and Scott B. Papp. Soliton crystals in kerr resonators. *Nature Photonics*, 11(10):671–676, Oct 2017.

[67] Van Vlack Cole Percy. *Dyadic Green Functions and their applications in Classical and Quantum Nanophotonics*. PhD thesis, Queen's University, 2012.

[68] R. Colella, A. W. Overhauser, and S. A. Werner. Observation of gravitationally induced quantum interference. *Phys. Rev. Lett.*, 34:1472–1474, Jun 1975.

[69] A. N. Craddock, J. Hannegan, D. P. Ornelas-Huerta, J. D. Siverns, A. J. Hachtel, E. A. Goldschmidt, J. V. Porto, Q. Quraishi, and S. L. Rolston. Quantum interference between photons from an atomic ensemble and a remote atomic ion. *Phys. Rev. Lett.*, 123:213601, Nov 2019.

[70] Toby S. Cubitt, Ashley Montanaro, and Stephen Piddock. Universal quantum hamiltonians. *Proceedings of the National Academy of Sciences*, 115(38):9497–9502, 2018.

[71] Dan Dalacu, Philip J Poole, and Robin L Williams. Nanowire-based sources of nonclassical light. *Nanotechnology*, 30(23):232001, mar 2019.

[72] J.N. Damask. *Polarization Optics in Telecommunications*. Springer Series in Optical Sciences. Springer, 2004.

[73] Marcelo Davanco, Jin Liu, Luca Sapienza, Chen-Zhao Zhang, José Vinícius De Miranda Cardoso, Varun Verma, Richard Mirin, Sae Woo Nam, Liu Liu, and Kartik Srinivasan. Heterogeneous integration for on-chip quantum photonic circuits with single quantum dot devices. *Nature Communications*, 8(1):889, Oct 2017.

[74] Xiaoyue Ding, Dylan Heberle, Kerrianne Harrington, Noah Flemens, Wei-Zung Chang, Tim A. Birks, and Jeffrey Moses. Observation of rapid adiabatic passage in optical four-wave mixing. *Phys. Rev. Lett.*, 124:153902, Apr 2020.

[75] J. A. Dobrowolski. Optical properties of films and coatings. *Handbook of Optics I*, pages 42.3–130, 1995.

[76] Y. Dong, J. Taylor, Y. S. Lee, H. R. Kong, and K. S. Choi. Waveguide qed toolboxes for universal quantum matter, 2021.

[77] Audrey Dot, Evan Meyer-Scott, Raja Ahmad, Martin Rochette, and Thomas Jennewein. Converting one photon into two via four-wave mixing in optical fibers. *Phys. Rev. A*, 90:043808, Oct 2014.

[78] J. S. Douglas, H. Habibian, C.-L. Hung, A. V. Gorshkov, H. J. Kimble, and D. E. Chang. Quantum many-body models with cold atoms coupled to photonic crystals. *Nature Photonics*, 9(5):326–331, May 2015.

[79] S. V. Drabek, V. V. Komarov, S. A. Potanin, A. D. Savvin, A. S. Moskvitin, and O. I. Spiridonova. Study of the quality of the zeiss-1000 telescope optical system using the shack–hartmann wavefront sensor. *Astrophysical Bulletin*, 72(2):206–216, Apr 2017.

[80] Ho Trung Dung, Ludwig Knöll, and Dirk-Gunnar Welsch. Three-dimensional quantization of the electromagnetic field in dispersive and absorbing inhomogeneous dielectrics. *Phys. Rev. A*, 57:3931–3942, May 1998.

[81] James F. Dynes, Winci W-S. Tam, Alan Plews, Bernd Fröhlich, Andrew W. Sharpe, Marco Lucamarini, Zhiliang Yuan, Christian Radig, Andrew Straw, Tim Edwards, and Andrew J. Shields. Ultra-high bandwidth quantum secured data transmission. *Scientific Reports*, 6(1):35149, Oct 2016.

[82] H. El Dirani, M. Casale, S. Kerdiles, C. Socquet-Clerc, X. Letartre, C. Monat, and C. Sciancalepore. Crack-free silicon-nitride-on-insulator nonlinear circuits for continuum generation in the C -band. *IEEE Photonics Technology Letters*, 30(4):355–358, 2018.

[83] Houssein El Dirani, Ayman Kamel, Marco Casale, Sébastien Kerdiles, Christelle Monat, Xavier Letartre, Minhao Pu, Leif Katsuo Oxenløwe, Kresten Yvind, and Corrado Sciancalepore. Annealing-free si3n4 frequency combs for monolithic integration with si photonics. *Applied Physics Letters*, 113(8):081102, 2018.

[84] P. G. Evans, R. S. Bennink, W. P. Grice, T. S. Humble, and J. Schaake. Bright source of spectrally uncorrelated polarization-entangled photons with nearly single-mode emission. *Phys. Rev. Lett.*, 105:253601, Dec 2010.

[85] J. Fan, M. D. Eisaman, and A. Migdall. Bright phase-stable broadband fiber-based source of polarization-entangled photon pairs. *Phys. Rev. A*, 76:043836, Oct 2007.

[86] Bin Fang, Offir Cohen, and Virginia O. Lorenz. Polarization-entangled photon-pair generation in commercial-grade polarization-maintaining fiber. *J. Opt. Soc. Am. B*, 31(2):277–281, Feb 2014.

[87] U. Fano. Atomic theory of electromagnetic interactions in dense materials. *Phys. Rev.*, 103:1202–1218, Sep 1956.

[88] Alessandro Farsi. *Coherent Manipulation Of Light In The Classical And Quantum Regimes Via Four-Wave Mixing Bragg Scattering*. PhD thesis, Cornell University, 2015.

[89] Matthias Fink, Ana Rodriguez-Aramendia, Johannes Handsteiner, Abdul Ziarkash, Fabian Steinlechner, Thomas Scheidl, Ivette Fuentes, Jacques Pienaar, Timothy C. Ralph, and Rupert Ursin. Experimental test of photonic entanglement in accelerated reference frames. *Nature Communications*, 8(1):15304, May 2017.

[90] Marco Fiorentino and Raymond G. Beausoleil. Compact sources of polarization-entangled photons. *Opt. Express*, 16(24):20149–20156, Nov 2008.

[91] Marco Fiorentino, Gaétan Messin, Christopher E. Kuklewicz, Franco N. C. Wong, and Jeffrey H. Shapiro. Generation of ultrabright tunable polarization entanglement without spatial, spectral, or temporal constraints. *Phys. Rev. A*, 69:041801, Apr 2004.

[92] Craig R. Forest, Claude R. Canizares, Daniel R. Neal, Michael McGuirk, and Mark Lee Schattenburg. Metrology of thin transparent optics using Shack-Hartmann wavefront sensing. *Optical Engineering*, 43(3):742 – 753, 2004.

[93] Yunfei Fu, Tong Ye, Weijie Tang, and Tao Chu. Efficient adiabatic silicon-on-insulator waveguide taper. *Photon. Res.*, 2(3):A41–A44, Jun 2014.

[94] Jérémie Fulconis, Olivier Alibart, Jeremy L. O'Brien, William J. Wadsworth, and John G. Rarity. Nonclassical interference and entanglement generation using a photonic crystal fiber pair photon source. *Phys. Rev. Lett.*, 99:120501, Sep 2007.

[95] Ralf D Geckeler. Optimal use of pentaprisms in highly accurate deflectometric scanning. *Measurement Science and Technology*, 18(1):115–125, nov 2006.

[96] Ralf D. Geckeler and Ingolf Weingaertner. Sub-nm topography measurement by deflectometry: flatness standard and wafer nanotopography. In Angela Duparré and Bhanwar Singh, editors, *Advanced Characterization Techniques for Optical, Semiconductor, and Data Storage Components*, volume 4779, pages 1 – 12. International Society for Optics and Photonics, SPIE, 2002.

[97] Fabrice Gerbier and Yvan Castin. Heating rates for an atom in a far-detuned optical lattice. *Phys. Rev. A*, 82:013615, Jul 2010.

[98] Marissa Giustina, Marijn A. M. Versteegh, Sören Wengerowsky, Johannes Handsteiner, Armin Hochrainer, Kevin Phelan, Fabian Steinlechner, Johannes Kofler, Jan-Åke Larsson, Carlos Abellán, Waldimar Amaya, Valerio Pruneri, Morgan W. Mitchell, Jörn Beyer, Thomas Gerrits, Adriana E. Lita, Lynden K. Shalm, Sae Woo Nam, Thomas Scheidl, Rupert Ursin, Bernhard Wittmann, and Anton Zeilinger. Significant-loophole-free test of bell's theorem with entangled photons. *Phys. Rev. Lett.*, 115:250401, Dec 2015.

[99] Roy J. Glauber and M. Lewenstein. Quantum optics of dielectric media. *Phys. Rev. A*, 43:467–491, Jan 1991.

[100] A. Goban, C.-L. Hung, J. D. Hood, S.-P. Yu, J. A. Muniz, O. Painter, and H. J. Kimble. Superradiance for atoms trapped along a photonic crystal waveguide. *Phys. Rev. Lett.*, 115:063601, Aug 2015.

[101] A. Goban, C.-L. Hung, S.-P. Yu, J. D. Hood, J. A. Muniz, J. H. Lee, M. J. Martin, A. C. McClung, K. S. Choi, D. E. Chang, O. Painter, and H. J. Kimble. Atom–light interactions in photonic crystals. *Nature Communications*, 5(1):3808, May 2014.

[102] Yun-Hong Gong, Kui-Xing Yang, Hai-Lin Yong, Jian-Yu Guan, Guo-Liang Shentu, Chang Liu, Feng-Zhi Li, Yuan Cao, Juan Yin, Sheng-Kai Liao, Ji-Gang Ren, Qiang Zhang, Cheng-Zhi Peng, and Jian-Wei Pan. Free-space quantum key distribution in urban daylight with the spgd algorithm control of a deformable mirror. *Opt. Express*, 26(15):18897–18905, Jul 2018.

[103] E. A. Rojas González, A. Borne, B. Boulanger, J. A. Levenson, and K. Bencheikh. Continuous-variable triple-photon states quantum entanglement. *Phys. Rev. Lett.*, 120:043601, Jan 2018.

[104] A. González-Tudela, C.-L. Hung, D. E. Chang, J. I. Cirac, and H. J. Kimble. Subwavelength vacuum lattices and atom–atom interactions in two-dimensional photonic crystals. *Nature Photonics*, 9(5):320–325, May 2015.

[105] Daniel Gottesman, Thomas Jennewein, and Sarah Croke. Longer-baseline telescopes using quantum repeaters. *Phys. Rev. Lett.*, 109:070503, Aug 2012.

[106] Davide Grassani, Stefano Azzini, Marco Liscidini, Matteo Galli, Michael J. Strain, Marc Sorel, J. E. Sipe, and Daniele Bajoni. Micrometer-scale integrated silicon source of time-energy entangled photons. *Optica*, 2(2):88–94, Feb 2015.

[107] Federico Grasselli and Marcos Curty. Practical decoy-state method for twin-field quantum key distribution. *New Journal of Physics*, 21(7):073001, jul 2019.

[108] Markus Greiner, Olaf Mandel, Tilman Esslinger, Theodor W. Hänsch, and Immanuel Bloch. Quantum phase transition from a superfluid to a mott insulator in a gas of ultracold atoms. *Nature*, 415(6867):39–44, Jan 2002.

[109] Christian Gross and Immanuel Bloch. Quantum simulations with ultracold atoms in optical lattices. *Science*, 357(6355):995–1001, 2017.

[110] T. Gruner and D.-G. Welsch. Green-function approach to the radiation-field quantization for homogeneous and inhomogeneous kramers-kronig dielectrics. *Phys. Rev. A*, 53:1818–1829, Mar 1996.

[111] H. Gu, X. Chen, C. Zhang, H. Jiang, and S. Liu. Study of the retardance of a birefringent waveplate at tilt incidence by mueller matrix ellipsometer. *Journal of Optics*, 20:015401, 2018.

[112] Mile Gu, Christian Weedbrook, Nicolas C. Menicucci, Timothy C. Ralph, and Peter van Loock. Quantum computing with continuous-variable clusters. *Phys. Rev. A*, 79:062318, Jun 2009.

[113] M. Gullans, T. G. Tiecke, D. E. Chang, J. Feist, J. D. Thompson, J. I. Cirac, P. Zoller, and M. D. Lukin. Nanoplasmonic lattices for ultracold atoms. *Phys. Rev. Lett.*, 109:235309, Dec 2012.

[114] Laszlo Gyongyosi and Sandor Imre. A survey on quantum computing technology. *Computer Science Review*, 31:51–71, 2019.

[115] X. Han, H.-L. Yong, P. Xu, K.-X. Yang, S.-L. Li, W.-Y. Wang, H.-J. Xue, F.-Z. Li, J.-G. Ren, C.-Z. Peng, and J.-W. Pan. Polarization design for ground-to-satellite quantum entanglement distribution. *Optics Express*, 28:369–378, 2020.

[116] T. Hasegawa, K. Inoue, and K. Oda. Polarization independent frequency conversion by fiber four-wave mixing with a polarization diversity technique. *IEEE Photonics Technology Letters*, 5(8):947–949, 1993.

[117] M. Heiblum and J. Harris. Analysis of curved optical waveguides by conformal transformation. *IEEE Journal of Quantum Electronics*, 11(2):75–83, 1975.

[118] Tobias Heindel, Christian A Kessler, Markus Rau, Christian Schneider, Martin Fürst, Fabian Hargart, Wolfgang-Michael Schulz, Marcus Eichfelder, Robert Roßbach, Sebastian Nauerth, Matthias Lermer, Henning Weier, Michael Jetter, Martin Kamp, Stephan Reitzenstein, Sven Höfling, Peter Michler, Harald Weinfurter, and Alfred Forchel. Quantum key distribution using quantum dot single-photon emitting diodes in the red and near infrared spectral range. *New Journal of Physics*, 14(8):083001, aug 2012.

[119] Michael Hentschel, Hannes Hübel, Andreas Poppe, and Anton Zeilinger. Three-color sagnac source of polarization-entangled photon pairs. *Opt. Express*, 17(25):23153–23159, Dec 2009.

[120] D. H. Höhn. Depolarization of a laser beam at 6328 å due to atmospheric transmission. *Appl. Opt.*, 8(2):367–369, Feb 1969.

[121] Jonathan D. Hood, Akihisa Goban, Ana Asenjo-Garcia, Mingwu Lu, Su-Peng Yu, Darrick E. Chang, and H. J. Kimble. Atom–atom interactions around the band edge of a photonic crystal waveguide. *Proceedings of the National Academy of Sciences*, 113(38):10507–10512, 2016.

[122] Jonathan David Hood. *Atom-light Interactions in a Photonic Crystal Waveguide*. PhD thesis, California Institute of Technology, 2017.

[123] Rolf Horn and Thomas Jennewein. Auto-balancing and robust interferometer designs for polarization entangled photon sources. *Opt. Express*, 27(12):17369–17376, Jun 2019.

[124] Ehsan Shah Hosseini, Siva Yegnanarayanan, Amir Hossein Atabaki, Mohammad Soltani, and Ali Adibi. Systematic design and fabrication of high-q single-mode pulley-coupled planar silicon nitride microdisk resonators at visible wavelengths. *Opt. Express*, 18(3):2127–2136, Feb 2010.

[125] He-Liang Huang, Dachao Wu, Daojin Fan, and Xiaobo Zhu. Superconducting quantum computing: a review. *Science China Information Sciences*, 63(8):180501, Jul 2020.

[126] Jianming Huang and Prem Kumar. Observation of quantum frequency conversion. *Phys. Rev. Lett.*, 68:2153–2156, Apr 1992.

[127] Yu-Ping Huang, Vesselin Velev, and Prem Kumar. Quantum frequency conversion in nonlinear microcavities. *Opt. Lett.*, 38(12):2119–2121, Jun 2013.

[128] Hannes Hübel, Deny R. Hamel, Alessandro Fedrizzi, Sven Ramelow, Kevin J. Resch, and Thomas Jennewein. Direct generation of photon triplets using cascaded photon-pair sources. *Nature*, 466(7306):601–603, Jul 2010.

[129] Hannes Hübel, Michael R. Vanner, Thomas Lederer, Bibiane Blauensteiner, Thomas Lorünser, Andreas Poppe, and Anton Zeilinger. High-fidelity transmission of polarization encoded qubits from an entangled source over 100 km of fiber. *Opt. Express*, 15(12):7853–7862, Jun 2007.

[130] Johan Hult. A fourth-order runge-kutta in the interaction picture method for simulating supercontinuum generation in optical fibers. *Journal of lightwave technology*, 25:3770–3775, 2007.

[131] C.-L. Hung, Alejandro González-Tudela, J. Ignacio Cirac, and H. J. Kimble. Quantum spin dynamics with pairwise-tunable, long-range interactions. *Proceedings of the National Academy of Sciences*, 113(34):E4946–E4955, 2016.

[132] C.-L. Hung, S. M. Meenehan, D. E. Chang, O. Painter, and H. J. Kimble. Trapped atoms in one-dimensional photonic crystals. *New Journal of Physics*, 15(8):083026, aug 2013.

[133] B. Huttner, S. Serulnik, and Y. Ben-Aryeh. Quantum analysis of light propagation in a parametric amplifier. *Phys. Rev. A*, 42:5594–5600, Nov 1990.

[134] Bruno Huttner and Stephen M. Barnett. Quantization of the electromagnetic field in dielectrics. *Phys. Rev. A*, 46:4306–4322, Oct 1992.

[135] K. Ichimoto, B. Lites, D. Elmore, Y. Suematsu, S. Tsuneta, Y. Katsukawa, T. Shimizu, R. Shine, T. Tarbell, A. Title, J. Kiyohara, K. Shinoda, G. Card, A. Lecinski, K. Streander, M. Nakagiri, M. Miyashita, M. Noguchi, C. Hoffmann, and T. Cruz. *Polarization Calibration of the Solar Optical Telescope onboard Hinode*, pages 179–207. Springer New York, New York, NY, 2008.

[136] Rikizo Ikuta, Hiroshi Kato, Yoshiaki Kusaka, Shigehito Miki, Taro Yamashita, Hirotaka Terai, Mikio Fujiwara, Takashi Yamamoto, Masato Koashi, Masahide Sasaki, Zhen Wang, and Nobuyuki Imoto. High-fidelity conversion of photonic quantum information to telecommunication wavelength with superconducting single-photon detectors. *Phys. Rev. A*, 87:010301, Jan 2013.

[137] Rikizo Ikuta, Toshiki Kobayashi, Tetsuo Kawakami, Shigehito Miki, Masahiro Yabuno, Taro Yamashita, Hirotaka Terai, Masato Koashi, Tetsuya Mukai, Takashi Yamamoto, and Nobuyuki Imoto. Polarization insensitive frequency conversion for an atom-photon entanglement distribution via a telecom network. *Nature Communications*, 9(1):1997, May 2018.

[138] Rikizo Ikuta, Toshiki Kobayashi, Kenichiro Matsuki, Shigehito Miki, Taro Yamashita, Hirotaka Terai, Takashi Yamamoto, Masato Koashi, Tetsuya Mukai, and Nobuyuki Imoto. Heralded single excitation of atomic ensemble via solid-state-based telecom photon detection. *Optica*, 3(11):1279–1284, Nov 2016.

[139] Rikizo Ikuta, Toshiki Kobayashi, Shuto Yasui, Shigehito Miki, Taro Yamashita, Hirotaka Terai, Mikio Fujiwara, Takashi Yamamoto, Masato Koashi, Masahide Sasaki, Zhen Wang, and Nobuyuki Imoto. Frequency down-conversion of 637 nm light to the

telecommunication band for non-classical light emitted from nv centers in diamond. *Opt. Express*, 22(9):11205–11214, May 2014.

[140] J. M. Jauch and K. M. Watson. Phenomenological quantum-electrodynamics. *Phys. Rev.*, 74:950–957, Oct 1948.

[141] T. Jennewein. Towards quantum communications with satellites. In *2018 IEEE Photonics Society Summer Topical Meeting Series (SUM)*, pages 217–218, 2018.

[142] T. Jennewein, J. P. Bourgoin, B. Higgins, C. Holloway, E. Meyer-Scott, C. Erven, B. Heim, Z. Yan, H. Hübel, G. Weihs, E. Choi, I. D'Souza, D. Hudson, and R. Laflamme. QEYSSAT: a mission proposal for a quantum receiver in space. In Zameer U. Hasan, Philip R. Hemmer, Hwang Lee, and Charles M. Santori, editors, *Advances in Photonics of Quantum Computing, Memory, and Communication VII*, volume 8997, pages 21 – 27. International Society for Optics and Photonics, SPIE, 2014.

[143] Xingchen Ji, Felippe A. S. Barbosa, Samantha P. Roberts, Avik Dutt, Jaime Cardenas, Yoshitomo Okawachi, Alex Bryant, Alexander L. Gaeta, and Michal Lipson. Ultra-low-loss on-chip resonators with sub-milliwatt parametric oscillation threshold. *Optica*, 4(6):619–624, Jun 2017.

[144] Jeongwan Jin, Jean-Philippe Bourgoin, Ramy Tannous, Sascha Agne, Christopher J. Pugh, Katanya B. Kuntz, Brendon L. Higgins, and Thomas Jennewein. Genuine time-bin-encoded quantum key distribution over a turbulent depolarizing free-space channel. *Opt. Express*, 27(26):37214–37223, Dec 2019.

[145] Warren Jin, Ronald G. Polcawich, Paul A. Morton, and John E. Bowers. Piezoelectrically tuned silicon nitride ring resonator. *Opt. Express*, 26(3):3174–3187, Feb 2018.

[146] John D. Joannopoulos, Steven G. Johnson, Joshua N. Winn, and Robert D. Meade. *Photonic Crystals: Molding the Flow of Light (Second Edition)*. Princeton University Press, 2 edition, 2008.

[147] Sajeev John and Tran Quang. Quantum optical spin-glass state of impurity two-level atoms in a photonic band gap. *Phys. Rev. Lett.*, 76:1320–1323, Feb 1996.

[148] Sajeev John and Jian Wang. Quantum electrodynamics near a photonic band gap: Photon bound states and dressed atoms. *Phys. Rev. Lett.*, 64:2418–2421, May 1990.

[149] Steven G. Johnson and J. D. Joannopoulos. Block-iterative frequency-domain methods for maxwell's equations in a planewave basis. *Opt. Express*, 8(3):173–190, Jan 2001.

[150] Chaitali Joshi, Alessandro Farsi, Avik Dutt, Bok Young Kim, Xingchen Ji, Yun Zhao, Andrew M. Bishop, Michal Lipson, and Alexander L. Gaeta. Frequency-domain quantum interference with correlated photons from an integrated microresonator. *Phys. Rev. Lett.*, 124:143601, Apr 2020.

[151] Dieter H. Jundt. Temperature-dependent sellmeier equation for the index of refraction, ne, in congruent lithium niobate. *Opt. Lett.*, 22(20):1553–1555, Oct 1997.

[152] Keiji Kataoka. Estimation of coupling efficiency of optical fiber by far-field method. *Optical Review*, 17(5):476–480, Sep 2010.

[153] Andrei Khrennikov. After bell. *Fortschritte der Physik*, 65(6-8):1600044, 2017.

[154] Craig Kiikka, Daniel R. Neal, John Kincade, Robert Bernier, Tony Hull, David Chaney, Steve Farrer, John Dixson, Avery Causey, and Steve Strohl. The JWST infrared Scanning Shack Hartman System: a new in-process way to measure large mirrors during optical fabrication at Tinsley. In John C. Mather, Howard A. MacEwen, and Mattheus W. M. de Graauw, editors, *Space Telescopes and Instrumentation I: Optical, Infrared, and Millimeter*, volume 6265, pages 1107 – 1117. International Society for Optics and Photonics, SPIE, 2006.

[155] Taehyun Kim, Marco Fiorentino, and Franco N. C. Wong. Phase-stable source of polarization-entangled photons using a polarization sagnac interferometer. *Phys. Rev. A*, 73:012316, Jan 2006.

[156] H. J. Kimble. The quantum internet. *Nature*, 453(7198):1023–1030, Jun 2008.

[157] Junko Kiyohara, Satoru Ueno, Reizaburo Kitai, Hiroki Kurokawa, Mitsugu Makita, and Kiyoshi Ichimoto. Calibration of the instrumental polarization of the domeless solar telescope at the hida observatory. volume 5492, pages 1778 – 1785. International Society for Optics and Photonics, SPIE, 2004.

[158] Masato Koashi and John Preskill. Secure quantum key distribution with an uncharacterized source. *Phys. Rev. Lett.*, 90:057902, Feb 2003.

[159] Toshiki Kobayashi, Rikizo Ikuta, Shuto Yasui, Shigehito Miki, Taro Yamashita, Hirotaka Terai, Takashi Yamamoto, Masato Koashi, and Nobuyuki Imoto. Frequency-domain hong–ou–mandel interference. *Nature Photonics*, 10(7):441–444, Jul 2016.

[160] P. Kómár, E. M. Kessler, M. Bishof, L. Jiang, A. S. Sørensen, J. Ye, and M. D. Lukin. A quantum network of clocks. *Nature Physics*, 10(8):582–587, Aug 2014.

[161] Kong, Hyeran. Towards many-body physics with rydberg-dressed cavity polaritons. Master's thesis, 2018.

[162] Prem Kumar. Quantum frequency conversion. *Opt. Lett.*, 15(24):1476–1478, Dec 1990.

[163] Gershon Kurizki. Two-atom resonant radiative coupling in photonic band structures. *Phys. Rev. A*, 42:2915–2924, Sep 1990.

[164] Paul G. Kwiat, Edo Waks, Andrew G. White, Ian Appelbaum, and Philippe H. Eberhard. Ultrabright source of polarization-entangled photons. *Phys. Rev. A*, 60:R773–R776, Aug 1999.

[165] C. Lacroûte, K. S. Choi, A. Goban, D. J. Alton, D. Ding, N. P. Stern, and H. J. Kimble. A state-insensitive, compensated nanofiber trap. *New Journal of Physics*, 14(2):023056, feb 2012.

[166] Nicholas J. Lambert, Alfredo Rueda, Florian Sedlmeir, and Harald G. L. Schwefel. Coherent conversion between microwave and optical photons—an overview of physical implementations. *Advanced Quantum Technologies*, 3(1):1900077, 2020.

[167] Fabian Laudenbach, Sebastian Kalista, Michael Hentschel, Philip Walther, and Hannes Hübel. A novel single-crystal & single-pass source for polarisation- and colour-entangled photon pairs. *Scientific Reports*, 7(1):7235, Aug 2017.

[168] Fam Le Kien and A. Rauschenbeutel. Spontaneous emission of a two-level atom with an arbitrarily polarized electric dipole in front of a flat dielectric surface. *Phys. Rev. A*, 93:043828, Apr 2016.

[169] Fam Le Kien, Philipp Schneeweiss, and Arno Rauschenbeutel. Dynamical polarizability of atoms in arbitrary light fields: general theory and application to cesium. *The European Physical Journal D*, 67(5):92, May 2013.

[170] Youn Seok Lee, Kimia Mohammadi, Lindsay Babcock, Brendon L. Higgins, Hugh Podmore, and Thomas Jennewein. Robotized polarization characterization platform for free-space quantum communication optics, 2021.

[171] Youn Seok Lee, Mengyu Xie, Ramy Tannous, and Thomas Jennewein. Sagnac-type entangled photon source using only conventional polarization optics. *Quantum Science and Technology*, 6(2):025004, jan 2021.

[172] Simon Lefrancois, Alex S. Clark, and Benjamin J. Eggleton. Optimizing optical bragg scattering for single-photon frequency conversion. *Phys. Rev. A*, 91:013837, Jan 2015.

[173] G. W. R. Leibbrandt, G. Harbers, and P. J. Kunst. Wave-front analysis with high accuracy by use of a double-grating lateral shearing interferometer. *Appl. Opt.*, 35(31):6151–6161, Nov 1996.

[174] Julian Léonard, Moonjoo Lee, Andrea Morales, Thomas M Karg, Tilman Esslinger, and Tobias Donner. Optical transport and manipulation of an ultracold atomic cloud using focus-tunable lenses. *New Journal of Physics*, 16(9):093028, sep 2014.

[175] Qing Li, Marcelo Davanço, and Kartik Srinivasan. Efficient and low-noise single-photon-level frequency conversion interfaces using silicon nanophotonics. *Nature Photonics*, 10(6):406–414, Jun 2016.

[176] Xiaoying Li, Paul L. Voss, Jay E. Sharping, and Prem Kumar. Optical-fiber source of polarization-entangled photons in the 1550 nm telecom band. *Phys. Rev. Lett.*, 94:053601, Feb 2005.

[177] Chuang Liang, Kim Fook Lee, Todd Levin, Jun Chen, and Prem Kumar. Ultra stable all-fiber telecom-band entangled photon-pair source for turnkey quantum communication applications. *Opt. Express*, 14(15):6936–6941, Jul 2006.

[178] Long-Yue Liang, Jun-Sheng Liang, Quan Yao, Ming-Yang Zheng, Xiu-Ping Xie, Hong Liu, Qiang Zhang, and Jian-Wei Pan. Compact all-fiber polarization-independent up-conversion single-photon detector. *Optics Communications*, 441:185–189, 2019.

[179] Sheng-Kai Liao, Wen-Qi Cai, Wei-Yue Liu, Liang Zhang, Yang Li, Ji-ang Ren, Juan Yin, Qi Shen, Yuan Cao, Zheng-Ping Li, Feng-Zhi Li, Xia-Wei Chen, Li-Hua Sun, Jian-Jun Jia, Jin-Cai Wu, Xiao-Jun Jiang, Jian-Feng Wang, Yong-ei Huang, Qiang Wang, Yi-Lin Zhou, Lei Deng, Tao Xi, Lu Ma, Tai Hu, Qiang Zhang, Yu-Ao Chen, Nai-Le Liu, Xiang-Bin Wang, Zhen-Cai Zhu, Chao-Yang Lu, Rong Shu, Cheng-Zhi Peng, Jian-Yu Wang, and Jian-Wei Pan. Satellite-to-ground quantum key distribution. *Nature*, 549(7670):43–47, Sep 2017.

[180] Han Chuen Lim, Akio Yoshizawa, Hidemi Tsuchida, and Kazuro Kikuchi. Stable source of high quality telecom-band polarization-entangled photon-pairs based on a single, pulse-pumped, short ppln waveguide. *Opt. Express*, 16(17):12460–12468, Aug 2008.

[181] Q. Lin, F. Yaman, and Govind P. Agrawal. Photon-pair generation in optical fibers through four-wave mixing: Role of raman scattering and pump polarization. *Phys. Rev. A*, 75:023803, Feb 2007.

[182] Qiang Lin and Govind P. Agrawal. Vector theory of four-wave mixing: polarization effects in fiber-optic parametric amplifiers. *J. Opt. Soc. Am. B*, 21(6):1216–1224, Jun 2004.

[183] Alexander Ling, Antía Lamas-Linares, and Christian Kurtsiefer. Absolute emission rates of spontaneous parametric down-conversion into single transverse gaussian modes. *Phys. Rev. A*, 77:043834, Apr 2008.

[184] Seth Lloyd. Universal quantum simulators. *Science*, 273(5278):1073–1078, 1996.

[185] Hoi-Kwong Lo, Xiongfeng Ma, and Kai Chen. Decoy state quantum key distribution. *Phys. Rev. Lett.*, 94:230504, Jun 2005.

[186] Peter Lodahl, Sahand Mahmoodian, and Søren Stobbe. Interfacing single photons and single quantum dots with photonic nanostructures. *Rev. Mod. Phys.*, 87:347–400, May 2015.

[187] Alexander Lohrmann, Chithrabhanu Perumangatt, Aitor Villar, and Alexander Ling. Broadband pumped polarization entangled photon-pair source in a linear beam displacement interferometer. *Applied Physics Letters*, 116(2):021101, Jan 2020.

[188] J. C. Loredo, C. Antón, B. Reznychenko, P. Hilaire, A. Harouri, C. Millet, H. Ollivier, N. Somaschi, L. De Santis, A. Lemaître, I. Sagnes, L. Lanco, A. Auffèves, O. Krebs, and P. Senellart. Generation of non-classical light in a photon-number superposition. *Nature Photonics*, 13(11):803–808, Nov 2019.

[189] Rodney. Loudon. *The quantum theory of light / Rodney Loudon.* Clarendon Press Oxford, 1973.

[190] J.D. Love. Tapered single-mode fibres and devices. part 1: Adiabaticity criteria. *IEE Proceedings J (Optoelectronics)*, 138:343–354(11), October 1991.

[191] Xiyuan Lu, Gregory Moille, Ashutosh Rao, and Kartik Srinivasan. Proposal for noise-free visible-telecom quantum frequency conversion through third-order sum and difference frequency generation. *Opt. Lett.*, 46(2):222–225, Jan 2021.

[192] Z. T. Lu, K. L. Corwin, M. J. Renn, M. H. Anderson, E. A. Cornell, and C. E. Wieman. Low-velocity intense source of atoms from a magneto-optical trap. *Phys. Rev. Lett.*, 77:3331–3334, Oct 1996.

[193] L. A. Lugiato and R. Lefever. Spatial dissipative structures in passive optical systems. *Phys. Rev. Lett.*, 58:2209–2211, May 1987.

[194] K. Luke, Y. Okawach, M.-R.-E. Lamont, A.-L. Gaeta, and M. Lipson. Broadband mid-infrared frequency comb generation in a si_3n_4 microresonator. *Optics Letters*, 40:4823–4826, 2015.

[195] Fei Ma, Long-Yue Liang, Jiu-Peng Chen, Yang Gao, Ming-Yang Zheng, Xiu-Ping Xie, Hong Liu, Qiang Zhang, and Jian-Wei Pan. Upconversion single-photon detectors based on integrated periodically poled lithium niobate waveguides. *J. Opt. Soc. Am. B*, 35(9):2096–2101, Sep 2018.

[196] Xiongfeng Ma, Chi-Hang Fred Fung, and Hoi-Kwong Lo. Quantum key distribution with entangled photon sources. *Phys. Rev. A*, 76:012307, Jul 2007.

[197] S. Machida, J. Sakai, and T. Kimura. Polarisation conservation in single-mode fibres. *Electronics Letters*, 17(14):494–495, 1981.

[198] I.-H. Malitson. Interspecimen comperison of the refracitve index of fused silica. *Journal of the optical society of america*, 55:1205–1209, 1965.

[199] P.-V. Mamyshev and S.-V. Chernikov. Ultrashort-pulse propagation in optical fibers. *Optics Letter*, 15:1076–1078, 1990.

[200] D. Marcuse, American Telephone, and Telegraph Company. *Theory of Dielectric Optical Waveguides*. OPTICS AND PHOTONICS SERIES. Academic Press, 1991.

[201] Nicolas Maring, Pau Farrera, Kutlu Kutluer, Margherita Mazzera, Georg Heinze, and Hugues de Riedmatten. Photonic quantum state transfer between a cold atomic gas and a crystal. *Nature*, 551(7681):485–488, Nov 2017.

[202] Nicolas Maring, Dario Lago-Rivera, Andreas Lenhard, Georg Heinze, and Hugues de Riedmatten. Quantum frequency conversion of memory-compatible single photons from 606 to the telecom c-band. *Optica*, 5(5):507–513, May 2018.

[203] Robert McConnell, Colin Bruzewicz, John Chiaverini, and Jeremy Sage. Reduction of trapped-ion anomalous heating by in situ surface plasma cleaning. *Phys. Rev. A*, 92:020302, Aug 2015.

[204] C. J. McKinstrie, J. D. Harvey, S. Radic, and M. G. Raymer. Translation of quantum states by four-wave mixing in fibers. *Opt. Express*, 13(22):9131–9142, Oct 2005.

[205] Kevin M. McPeak, Sriharsha V. Jayanti, Stephan J. P. Kress, Stefan Meyer, Stelio Iotti, Aurelio Rossinelli, and David J. Norris. Plasmonic films can easily be better: Rules and recipes. *ACS Photonics*, 2(3):326–333, Mar 2015.

[206] C. Menyuk. Nonlinear pulse propagation in birefringent optical fibers. *IEEE Journal of Quantum Electronics*, 23(2):174–176, 1987.

[207] Evan Meyer-Scott, Nidhin Prasannan, Christof Eigner, Viktor Quiring, John M. Donohue, Sonja Barkhofen, and Christine Silberhorn. High-performance source of spectrally pure, polarization entangled photon pairs based on hybrid integrated-bulk optics. *Opt. Express*, 26(25):32475–32490, Dec 2018.

[208] Evan Meyer-Scott, Vincent Roy, Jean-Philippe Bourgoin, Brendon L. Higgins, Lynden K. Shalm, and Thomas Jennewein. Generating polarization-entangled photon pairs using cross-spliced birefringent fibers. *Opt. Express*, 21(5):6205–6212, Mar 2013.

[209] Michal Mičuda, Ester Doláková, Ivo Straka, Martina Miková, Miloslav Dušek, Jaromír Fiurášek, and Miroslav Ježek. Highly stable polarization independent mach-zehnder interferometer. *Review of Scientific Instruments*, 85(8):083103, 2014.

[210] Farokh Mivehvar, Francesco Piazza, Tobias Donner, and Helmut Ritsch. Cavity qed with quantum gases: New paradigms in many-body physics, 2021.

[211] Khaled Mnaymneh, Dan Dalacu, Joseph McKee, Jean Lapointe, Sofiane Haffouz, John F. Weber, David B. Northeast, Philip J. Poole, Geof C. Aers, and Robin L. Williams. On-chip integration of single photon sources via evanescent coupling of tapered nanowires to sin waveguides. *Advanced Quantum Technologies*, 3(2):1900021, 2020.

[212] Kimia Mohammadi. Design and characterization of a transceiver telescope for quantum communications with satellites. Master's thesis, University of Waterloo, 2021.

[213] Gregory Moille, Qing Li, Travis C. Briles, Su-Peng Yu, Tara Drake, Xiyuan Lu, Ashutosh Rao, Daron Westly, Scott B. Papp, and Kartik Srinivasan. Broadband

resonator-waveguide coupling for efficient extraction of octave-spanning microcombs. *Opt. Lett.*, 44(19):4737–4740, Oct 2019.

[214] Gregory Moille, Qing Li, Xiyuan Lu, and Kartik Srinivasan. pylle: a fast and user friendly lugiato-lefever equation solver, 2019-05-24 2019.

[215] Gregory Moille, Xiyuan Lu, Ashutosh Rao, Qing Li, Daron A. Westly, Leonardo Ranzani, Scott B. Papp, Mohammad Soltani, and Kartik Srinivasan. Kerr-microresonator soliton frequency combs at cryogenic temperatures. *Phys. Rev. Applied*, 12:034057, Sep 2019.

[216] Christopher Monroe, Michael G. Raymer, and Jacob Taylor. The u.s. national quantum initiative: From act to action. *Science*, 364(6439):440–442, 2019.

[217] Galan Moody, Volker J. Sorger, Paul W. Juodawlkis, William Loh, Cheryl Sorace-Agaskar, Marcelo Davanco, Lin Chang, John E. Bowers, Niels Quack, Christophe Galland, Igor Aharonovich, M. A. Wolff, C. Schuck, Neil Sinclair, Marko Lončar, Tin Komljenovic, David Weld, Shayan Mookherjea, Sonia Buckley, Marina Radulaski, Stephan Reitzenstein, Benjamin Pingault, Bartholomeus Machielse, Debsuvra Mukhopadhyay, Alexey Akimov, Aleksei Zheltikov, Girish S. Agarwal, Kartik Srinivasan, Juanjuan Lu, Hong X. Tang, Wentao Jiang, Timothy P. McKenna, Amir H. Safavi-Naeini, Stephan Steinhauer, Ali W. Elshaari, Val Zwiller, Paul S. Davids, Nicholas Martinez, Michael Gehl, John Chiaverini, Karan K. Mehta, Jacquiline Romero, Navin B. Lingaraju, Andrew M. Weiner, Daniel Peace, Robert Cernansky, Mirko Lobino, Eleni Diamanti, Luis Trigo Vidarte, and Ryan M. Camacho. Roadmap on integrated quantum photonics, 2021.

[218] C.-E. Morosanu. The preparation, characterization and applications of silicon nitride thin films. *Thin Solid Films*, 65(2):171 – 208, 1980.

[219] Christopher L. Morrison, Markus Rambach, Zhe Xian Koong, Francesco Graffitti, Fiona Thorburn, Ajoy K. Kar, Yong Ma, Suk-In Park, Jin Dong Song, Nick G. Stoltz, Dirk Bouwmeester, Alessandro Fedrizzi, and Brian D. Gerardot. A bright source of telecom single photons based on quantum frequency conversion. *Applied Physics Letters*, 118(17):174003, 2021.

[220] Daniel R. Neal, Paul Pulaski, Thomas D. Raymond, David A. Neal, Quandou Wang, and Ulf Griesmann. Testing highly aberrated large optics with a Shack-Hartmann wavefront sensor. In John D. Gonglewski, Mikhail A. Vorontsov, and Mark T.

Gruneisen, editors, *Advanced Wavefront Control: Methods, Devices, and Applications*, volume 5162, pages 129 – 138. International Society for Optics and Photonics, SPIE, 2003.

[221] C. T. Nguyen, D. D. Sukachev, M. K. Bhaskar, B. Machielse, D. S. Levonian, E. N. Knall, P. Stroganov, R. Riedinger, H. Park, M. Lončar, and M. D. Lukin. Quantum network nodes based on diamond qubits with an efficient nanophotonic interface. *Phys. Rev. Lett.*, 123:183602, Oct 2019.

[222] M. Avenda no Alejo. Analysis of the refraction of the extraordinary ray in a plane-parallel uniaxial plate with an arbitrary orientation of the optical axis. *Opt. Express*, 13(7):2549–2555, Apr 2005.

[223] Yoshitomo Okawachi, Kasturi Saha, Jacob S. Levy, Y. Henry Wen, Michal Lipson, and Alexander L. Gaeta. Octave-spanning frequency comb generation in a silicon nitride chip. *Opt. Lett.*, 36(17):3398–3400, Sep 2011.

[224] Laurent Olislager, Jassem Safioui, Stéphane Clemmen, Kien Phan Huy, Wim Bogaerts, Roel Baets, Philippe Emplit, and Serge Massar. Silicon-on-insulator integrated source of polarization-entangled photons. *Opt. Lett.*, 38(11):1960–1962, Jun 2013.

[225] A. Osada, Y. Ota, R. Katsumi, M. Kakuda, S. Iwamoto, and Y. Arakawa. Strongly coupled single-quantum-dot–cavity system integrated on a cmos-processed silicon photonic chip. *Phys. Rev. Applied*, 11:024071, Feb 2019.

[226] Ardavan F. Oskooi, David Roundy, Mihai Ibanescu, Peter Bermel, J.D. Joannopoulos, and Steven G. Johnson. Meep: A flexible free-software package for electromagnetic simulations by the fdtd method. *Computer Physics Communications*, 181(3):687–702, 2010.

[227] Mark Oxborrow. Traceable 2-d finite-element simulation of the whispering-gallery modes of axisymmetric electromagnetic resonators. *IEEE Transactions on Microwave Theory and Techniques*, 55(6):1209–1218, 2007.

[228] E. D. Palik and G. Ghosh. *Handbook of Optical Constants of Solids: Handbook of Thermo-Optic Coefficients of Optical Materials with Applications*. Elsevier Science & Technology Books, 1997.

[229] Jiho Park, Heonoh Kim, and Han Seb Moon. Polarization-entangled photons from a warm atomic ensemble using a sagnac interferometer. *Phys. Rev. Lett.*, 122:143601, Apr 2019.

[230] J. S. Pelc, Paulina S. Kuo, Oliver Slattery, Lijun Ma, Xiao Tang, and M. M. Fejer. Dual-channel, single-photon upconversion detector at 1.3 μm. *Opt. Express*, 20(17):19075–19087, Aug 2012.

[231] J. S. Pelc, L. Ma, C. R. Phillips, Q. Zhang, C. Langrock, O. Slattery, X. Tang, and M. M. Fejer. Long-wavelength-pumped upconversion single-photon detector at 1550 nm: performance and noise analysis. *Opt. Express*, 19(22):21445–21456, Oct 2011.

[232] Jason S. Pelc, Leo Yu, Kristiaan De Greve, Peter L. McMahon, Chandra M. Natarajan, Vahid Esfandyarpour, Sebastian Maier, Christian Schneider, Martin Kamp, Sven Höfling, Robert H. Hadfield, Alfred Forchel, Yoshihisa Yamamoto, and M. M. Fejer. Downconversion quantum interface for a single quantum dot spin and 1550-nm single-photon channel. *Opt. Express*, 20(25):27510–27519, Dec 2012.

[233] Matthew Pelton, Philip Marsden, Daniel Ljunggren, Maria Tengner, Anders Karlsson, Anna Fragemann, Carlota Canalias, and Fredrik Laurell. Bright, single-spatial-mode source of frequency non-degenerate, polarization-entangled photon pairs using periodically poled ktp. *Opt. Express*, 12(15):3573–3580, Jul 2004.

[234] N. L. Petrov, A. A. Voronin, A. B. Fedotov, and A. M. Zheltikov. Ultrahigh-contrast cross-polarized entangled photon pairs from a strongly birefringent photonic-crystal fiber. *Applied Physics B*, 125(3):54, Mar 2019.

[235] William D. Phillips and Harold Metcalf. Laser deceleration of an atomic beam. *Phys. Rev. Lett.*, 48:596–599, Mar 1982.

[236] Ben C Platt and Roland Shack. History and principles of shack-hartmann wavefront sensing. *Journal of Refractive Surgery*, 17(5):S573–S577, 2001.

[237] H. Podmore, I. D'Souza, J. Cain, T. Jennewein, B. L. Higgins, Y. S. Lee, A. Koujelev, D. Hudson, and A. McColgan. QKD terminal for Canada's Quantum Encryption and Science Satellite (QEYSSat). In Bruno Cugny, Zoran Sodnik, and Nikos Karafolas, editors, *International Conference on Space Optics — ICSO 2020*, volume 11852, pages 203 – 212. International Society for Optics and Photonics, SPIE, 2021.

[238] H. Podmore, I. D'Souza, D. Hudson, T. Jennewin, J. Cain, B. Higgins, C. Midwinter, A. Scott, A. McColgan, D. Caldwell, and S. H. Zheng. Optical terminal for canada's

quantum encryption and science satellite (qeyssat). In *2019 IEEE International Conference on Space Optical Systems and Applications (ICSOS)*, pages 1–5, 2019.

[239] C. D. Poole and R. E. Wagner. Phenomenological approach to polarisation dispersion in long single-mode fibres. *Electronics Letters*, 22(19):1029–1030, 1986.

[240] C.D. Poole, N.S. Bergano, R.E. Wagner, and H.J. Schulte. Polarization dispersion and principal states in a 147-km undersea lightwave cable. *Journal of Lightwave Technology*, 6(7):1185–1190, 1988.

[241] S. A. Potanin. Shack-hartmann wavefront sensor for testing the quality of the optics of the 2.5-m sai telescope. *Astronomy Reports*, 53(8):703–709, Aug 2009.

[242] John Preskill. Quantum Computing in the NISQ era and beyond. *Quantum*, 2:79, August 2018.

[243] Christopher J Pugh, Sarah Kaiser, Jean-Philippe Bourgoin, Jeongwan Jin, Nigar Sultana, Sascha Agne, Elena Anisimova, Vadim Makarov, Eric Choi, Brendon L Higgins, and Thomas Jennewein. Airborne demonstration of a quantum key distribution receiver payload. *Quantum Science and Technology*, 2(2):024009, jun 2017.

[244] Christopher J. Pugh, Jean-Francois Lavigne, Jean-Philippe Bourgoin, Brendon L. Higgins, and Thomas Jennewein. Adaptive optics benefit for quantum key distribution uplink from ground to a satellite. *Advanced Optical Technologies*, 9(5):263–273, 2020.

[245] E. Qi, H. Hu, and X. Luo. Study on low-order aberration measurements of large-aperture flats based on scanning pentaprism technology. *Applied Optics*, 58:787–793, 2019.

[246] A. G. Radnaev, Y. O. Dudin, R. Zhao, H. H. Jen, S. D. Jenkins, A. Kuzmich, and T. A. B. Kennedy. A quantum memory with telecom-wavelength conversion. *Nature Physics*, 6(11):894–899, Nov 2010.

[247] Thomas D. Raymond, Daniel R. Neal, Daniel M. Topa, and Tony L. Schmitz. High-speed noninterferometric nanotopographic characterization of Si wafer surfaces. In Guozhong Cao and Wiley P. Kirk, editors, *Nanoscale Optics and Applications*, volume 4809, pages 208 – 216. International Society for Optics and Photonics, SPIE, 2002.

[248] Andreas Reiserer, Norbert Kalb, Gerhard Rempe, and Stephan Ritter. A quantum gate between a flying optical photon and a single trapped atom. *Nature*, 508(7495):237–240, Apr 2014.

[249] Ji-Gang Ren, Ping Xu, Hai-Lin Yong, Liang Zhang, Sheng-Kai Liao, Juan Yin, Wei-Yue Liu, Wen-Qi Cai, Meng Yang, Li Li, Kui-Xing Yang, Xuan Han, Yong-Qiang Yao, Ji Li, Hai-Yan Wu, Song Wan, Lei Liu, Ding-Quan Liu, Yao-Wu Kuang, Zhi-Ping He, Peng Shang, Cheng Guo, Ru-Hua Zheng, Kai Tian, Zhen-Cai Zhu, Nai-Le Liu, Chao-Yang Lu, Rong Shu, Yu-Ao Chen, Cheng-Zhi Peng, Jian-Yu Wang, and Jian-Wei Pan. Ground-to-satellite quantum teleportation. *Nature*, 549(7670):70–73, 2017.

[250] David Rideout, Thomas Jennewein, Giovanni Amelino-Camelia, Tommaso F Demarie, Brendon L Higgins, Achim Kempf, Adrian Kent, Raymond Laflamme, Xian Ma, Robert B Mann, Eduardo Martín-Martínez, Nicolas C Menicucci, John Moffat, Christoph Simon, Rafael Sorkin, Lee Smolin, and Daniel R Terno. Fundamental quantum optics experiments conceivable with satellites—reaching relativistic distances and velocities. *Classical and Quantum Gravity*, 29(22):224011, oct 2012.

[251] WJ Riley. Handbook of frequency stability analysis. *NIST*, 1065:1–123, 01 2007.

[252] Alejandro W. Rodriguez, Alexander P. McCauley, John D. Joannopoulos, and Steven G. Johnson. Casimir forces in the time domain: Theory. *Phys. Rev. A*, 80:012115, Jul 2009.

[253] Aiko Samblowski, Christina E. Vollmer, Christoph Baune, Jaromír Fiurášek, and Roman Schnabel. Weak-signal conversion from 1550 to 532 nm with 84% efficiency. *Opt. Lett.*, 39(10):2979–2981, May 2014.

[254] K. Sankarasubramanian, V. P. A. Samson, and P. Venkatakrishnan. Measurement of instrumental polarisation of the kodaikanal tunnel tower telescope. *Solar Polarization*, pages 313–320, 1999.

[255] Yoichi Sato and Takunori Taira. Highly accurate interferometric evaluation of thermal expansion and dn/dt of optical materials. *Opt. Mater. Express*, 4(5):876–888, May 2014.

[256] S. Sauge, M. Swillo, M. Tengner, and A. Karlsson. A single-crystal source of path-polarization entangled photons at non-degenerate wavelengths. *Opt. Express*, 16(13):9701–9707, Jun 2008.

[257] Valerio Scarani, Helle Bechmann-Pasquinucci, Nicolas J. Cerf, Miloslav Dušek, Norbert Lütkenhaus, and Momtchil Peev. The security of practical quantum key distribution. *Rev. Mod. Phys.*, 81:1301–1350, Sep 2009.

[258] Otto Schwelb. Transmission, group delay, and dispersion in single-ring optical resonators and add/drop filters - a tutorial overview. *J. Lightwave Technol.*, 22(5):1380, May 2004.

[259] A. Scott, T. Jennewein, J. Cain, I. D'Souza, B. Higgins, D. Hudson, H. Podmore, and W. Soh. The QEYSSAT mission: on-orbit demonstration of secure optical communications network technologies. In Karin Stein and Szymon Gladysz, editors, *Environmental Effects on Light Propagation and Adaptive Systems III*, volume 11532, pages 71 – 76. International Society for Optics and Photonics, SPIE, 2020.

[260] Lynden K. Shalm, Evan Meyer-Scott, Bradley G. Christensen, Peter Bierhorst, Michael A. Wayne, Martin J. Stevens, Thomas Gerrits, Scott Glancy, Deny R. Hamel, Michael S. Allman, Kevin J. Coakley, Shellee D. Dyer, Carson Hodge, Adriana E. Lita, Varun B. Verma, Camilla Lambrocco, Edward Tortorici, Alan L. Migdall, Yanbao Zhang, Daniel R. Kumor, William H. Farr, Francesco Marsili, Matthew D. Shaw, Jeffrey A. Stern, Carlos Abellán, Waldimar Amaya, Valerio Pruneri, Thomas Jennewein, Morgan W. Mitchell, Paul G. Kwiat, Joshua C. Bienfang, Richard P. Mirin, Emanuel Knill, and Sae Woo Nam. Strong loophole-free test of local realism. *Phys. Rev. Lett.*, 115:250402, Dec 2015.

[261] Lijiong Shen, Jianwei Lee, Le Phuc Thinh, Jean-Daniel Bancal, Alessandro Cerè, Antia Lamas-Linares, Adriana Lita, Thomas Gerrits, Sae Woo Nam, Valerio Scarani, and Christian Kurtsiefer. Randomness extraction from bell violation with continuous parametric down-conversion. *Phys. Rev. Lett.*, 121:150402, Oct 2018.

[262] Tao Shi, Ying-Hai Wu, A. González-Tudela, and J. I. Cirac. Bound states in boson impurity models. *Phys. Rev. X*, 6:021027, May 2016.

[263] Jasminder S. Sidhu, Siddarth K. Joshi, Mustafa Gundogan, Thomas Brougham, David Lowndes, Luca Mazzarella, Markus Krutzik, Sonali Mohapatra, Daniele Dequal, Giuseppe Vallone, Paolo Villoresi, Alexander Ling, Thomas Jennewein, Makan Mohageg, John Rarity, Ivette Fuentes, Stefano Pirandola, and Daniel K. L. Oi. Advances in space quantum communications, 2021.

[264] Maria C. Simon. Wollaston prism with large split angle. *Appl. Opt.*, 25(3):369–376, Feb 1986.

[265] Anshuman Singh, Qing Li, Shunfa Liu, Ying Yu, Xiyuan Lu, Christian Schneider, Sven Höfling, John Lawall, Varun Verma, Richard Mirin, Sae Woo Nam, Jin Liu, and Kartik Srinivasan. Quantum frequency conversion of a quantum dot single-photon source on a nanophotonic chip. *Optica*, 6(5):563–569, May 2019.

[266] Alicia Sit, Frédéric Bouchard, Robert Fickler, Jérémie Gagnon-Bischoff, Hugo Larocque, Khabat Heshami, Dominique Elser, Christian Peuntinger, Kevin Günthner, Bettina Heim, Christoph Marquardt, Gerd Leuchs, Robert W. Boyd, and Ebrahim Karimi. High-dimensional intracity quantum cryptography with structured photons. *Optica*, 4(9):1006–1010, Sep 2017.

[267] James D. Siverns, John Hannegan, and Qudsia Quraishi. Neutral-atom wavelength-compatible 780 nm single photons from a trapped ion via quantum frequency conversion. *Phys. Rev. Applied*, 11:014044, Jan 2019.

[268] Slaman, Sebstian. Understanding polarization distortions for real-world quantum key distribution. Master's thesis, 2020.

[269] Brian J. Smith, P. Mahou, Offir Cohen, J. S. Lundeen, and I. A. Walmsley. Photon pair generation in birefringent optical fibers. *Opt. Express*, 17(26):23589–23602, Dec 2009.

[270] A.W. Snyder and J. Love. *Optical Waveguide Theory*. Springer US, 2012.

[271] Mohammad Soltani. *Novel integrated silicon nanophotonic structures using ultra-high Q resonators*. PhD thesis, Georgia Institute of Technology, 12 2009.

[272] W.H. Southwell. Wave-front estimation from wave-front slope measurements. *J. Opt. Soc. Am.*, 70(8):998–1006, Aug 1980.

[273] Fabian Steinlechner, Pavel Trojek, Marc Jofre, Henning Weier, Daniel Perez, Thomas Jennewein, Rupert Ursin, John Rarity, Morgan W. Mitchell, Juan P. Torres, Harald Weinfurter, and Valerio Pruneri. A high-brightness source of polarization-entangled photons optimized for applications in free space. *Opt. Express*, 20(9):9640–9649, Apr 2012.

[274] Terence E. Stuart, Joshua A. Slater, Félix Bussières, and Wolfgang Tittel. Flexible source of nondegenerate entangled photons based on a two-crystal sagnac interferometer. *Phys. Rev. A*, 88:012301, Jul 2013.

[275] P. Su, J. H. Burge, B. Cuerden, J. Sasian, and H. M. Martin. Scanning pentaprism measurements of off-axis aspherics. *Frontiers in Optics 2008/Laser Science XXIV/-Plasmonics and Metamaterials/Optical Fabrication and Testing*, page JWD7, 2008.

[276] Bogdan Szafraniec, Bernd Nebendahl, and Todd Marshall. Polarization demultiplexing in stokes space. *Opt. Express*, 18(17):17928–17939, Aug 2010.

[277] Masao Takamoto, Feng-Lei Hong, Ryoichi Higashi, and Hidetoshi Katori. An optical lattice clock. *Nature*, 435(7040):321–324, May 2005.

[278] Kazuya Takemoto, Yoshihiro Nambu, Toshiyuki Miyazawa, Kentaro Wakui, Shinichi Hirose, Tatsuya Usuki, Motomu Takatsu, Naoki Yokoyama, Ken'ichiro Yoshino, Akihisa Tomita, Shinichi Yorozu, Yoshiki Sakuma, and Yasuhiko Arakawa. Transmission experiment of quantum keys over 50 km using high-performance quantum-dot single-photon source at 1.5 μm wavelength. *Applied Physics Express*, 3(9):092802, sep 2010.

[279] Takuo Tanemura, Kazuhiro Katoh, and Kazuro Kikuchi. Polarization-insensitive asymmetric four-wave mixing using circularly polarized pumps in a twisted fiber. *Opt. Express*, 13(19):7497–7505, Sep 2005.

[280] Zhongkan Tang, Rakhitha Chandrasekara, Yue Chuan Tan, Cliff Cheng, Kadir Durak, and Alexander Ling. The photon pair source that survived a rocket explosion. *Scientific Reports*, 6(1):25603, May 2016.

[281] Ramy Tannous, Zhangdong Ye, Jeongwan Jin, Katanya B. Kuntz, Norbert Lütkenhaus, and Thomas Jennewein. Demonstration of a 6 state-4 state reference frame independent channel for quantum key distribution. *Applied Physics Letters*, 115(21):211103, 2019.

[282] J. D. Thompson, T. G. Tiecke, N. P. de Leon, J. Feist, A. V. Akimov, M. Gullans, A. S. Zibrov, V. Vuletić, and M. D. Lukin. Coupling a single trapped atom to a nanoscale optical cavity. *Science*, 340(6137):1202–1205, 2013.

[283] T. G. Tiecke, J. D. Thompson, N. P. de Leon, L. R. Liu, V. Vuletić, and M. D. Lukin. Nanophotonic quantum phase switch with a single atom. *Nature*, 508(7495):241–244, Apr 2014.

[284] Abderrahmen Trichili, Mitchell A. Cox, Boon S. Ooi, and Mohamed-Slim Alouini. Roadmap to free space optics. *J. Opt. Soc. Am. B*, 37(11):A184–A201, Nov 2020.

[285] Haohua Tu, Yuan Liu, Xiaomin Liu, Dmitry Turchinovich, Jesper Lægsgaard, and Stephen A. Boppart. Nonlinear polarization dynamics in a weakly birefringent all-normal dispersion photonic crystal fiber: toward a practical coherent fiber supercontinuum laser. *Opt. Express*, 20(2):1113–1128, Jan 2012.

[286] R. Ulrich, S. C. Rashleigh, and W. Eickhoff. Bending-induced birefringence in single-mode fibers. *Opt. Lett.*, 5(6):273–275, Jun 1980.

[287] Ravitej Uppu, Freja T. Pedersen, Ying Wang, Cecilie T. Olesen, Camille Papon, Xiaoyan Zhou, Leonardo Midolo, Sven Scholz, Andreas D. Wieck, Arne Ludwig, and Peter Lodahl. Scalable integrated single-photon source. *Science Advances*, 6(50), 2020.

[288] R. Ursin, F. Tiefenbacher, T. Schmitt-Manderbach, H. Weier, T. Scheidl, M. Lindenthal, B. Blauensteiner, T. Jennewein, J. Perdigues, P. Trojek, B. Ömer, M. Fürst, M. Meyenburg, J. Rarity, Z. Sodnik, C. Barbieri, H. Weinfurter, and A. Zeilinger. Entanglement-based quantum communication over 144 km. *Nat. Phys.*, 3:481–486, 2007.

[289] Giuseppe Vallone, Daniele Dequal, Marco Tomasin, Francesco Vedovato, Matteo Schiavon, Vincenza Luceri, Giuseppe Bianco, and Paolo Villoresi. Interference at the single photon level along satellite-ground channels. *Phys. Rev. Lett.*, 116:253601, Jun 2016.

[290] R. Van Meter and S. J. Devitt. The path to scalable distributed quantum computing. *Computer*, 49(9):31–42, 2016.

[291] Aaron P. Vandevender and Paul G. Kwiat. High efficiency single photon detection via frequency up-conversion. *Journal of Modern Optics*, 51(9-10):1433–1445, 2004.

[292] P. Vergyris, F. Kaiser, E. Gouzien, G. Sauder, T. Lunghi, and S. Tanzilli. Fully guided-wave photon pair source for quantum applications. *Quantum Science and Technology*, 2(2):024007, June 2017.

[293] Z. Vernon, M. Liscidini, and J. E. Sipe. Quantum frequency conversion and strong coupling of photonic modes using four-wave mixing in integrated microresonators. *Phys. Rev. A*, 94:023810, Aug 2016.

[294] Aitor Villar, Alexander Lohrmann, Xueliang Bai, Tom Vergoossen, Robert Bedington, Chithrabhanu Perumangatt, Huai Ying Lim, Tanvirul Islam, Ayesha Reezwana, Zhongkan Tang, Rakhitha Chandrasekara, Subash Sachidananda, Kadir Durak,

Christoph F. Wildfeuer, Douglas Griffin, Daniel K. L. Oi, and Alexander Ling. Entanglement demonstration on board a nano-satellite. *Optica*, 7(7):734–737, Jul 2020.

[295] C. Van Vlack and S. Hughes. Finite-difference time-domain technique as an efficient tool for calculating the regularized green function: applications to the local-field problem in quantum optics for inhomogeneous lossy materials. *Opt. Lett.*, 37(14):2880–2882, Jul 2012.

[296] Thomas Walker, Koichiro Miyanishi, Rikizo Ikuta, Hiroki Takahashi, Samir Vartabi Kashanian, Yoshiaki Tsujimoto, Kazuhiro Hayasaka, Takashi Yamamoto, Nobuyuki Imoto, and Matthias Keller. Long-distance single photon transmission from a trapped ion via quantum frequency conversion. *Phys. Rev. Lett.*, 120:203601, May 2018.

[297] Herbert Walther, Benjamin T H Varcoe, Berthold-Georg Englert, and Thomas Becker. Cavity quantum electrodynamics. *Reports on Progress in Physics*, 69(5):1325–1382, apr 2006.

[298] Noel H. Wan, Sara Mouradian, and Dirk Englund. Two-dimensional photonic crystal slab nanocavities on bulk single-crystal diamond. *Applied Physics Letters*, 112(14):141102, 2018.

[299] Hui Wang, Yu-Ming He, T.-H. Chung, Hai Hu, Ying Yu, Si Chen, Xing Ding, M.-C. Chen, Jian Qin, Xiaoxia Yang, Run-Ze Liu, Z.-C. Duan, J.-P. Li, S. Gerhardt, K. Winkler, J. Jurkat, Lin-Jun Wang, Niels Gregersen, Yong-Heng Huo, Qing Dai, Siyuan Yu, Sven Höfling, Chao-Yang Lu, and Jian-Wei Pan. Towards optimal single-photon sources from polarized microcavities. *Nature Photonics*, 13(11):770–775, Nov 2019.

[300] Jian-Yu Wang, Bin Yang, Sheng-Kai Liao, Liang Zhang, Qi Shen, Xiao-Fang Hu, Jin-Cai Wu, Shi-Ji Yang, Hao Jiang, Yan-Lin Tang, Bo Zhong, Hao Liang, Wei-Yue Liu, Yi-Hua Hu, Yong-Mei Huang, Bo Qi, Ji-Gang Ren, Ge-Sheng Pan, Juan Yin, Jian-Jun Jia, Yu-Ao Chen, Kai Chen, Cheng-Zhi Peng, and Jian-Wei Pan. Direct and full-scale experimental verifications towards ground–satellite quantum key distribution. *Nature Photonics*, 7(5):387–393, May 2013.

[301] Jianwei Wang, Fabio Sciarrino, Anthony Laing, and Mark G. Thompson. Integrated photonic quantum technologies. *Nature Photonics*, 14(5):273–284, May 2020.

[302] Stephanie Wehner, David Elkouss, and Ronald Hanson. Quantum internet: A vision for the road ahead. *Science*, 362(6412), 2018.

[303] W. Weinstein. Computations in thin film optics. *Vacuum*, 4(1):3–19, 1954.

[304] Byron M. Welsh, Brent L. Ellerbroek, Michael C. Roggemann, and Timothy L. Pennington. Fundamental performance comparison of a hartmann and a shearing interferometer wave-front sensor. *Appl. Opt.*, 34(21):4186–4195, Jul 1995.

[305] R. N. Wilson. 'Matching error' (spherical aberration) in the Hubble Space Telescope (HST) - Some technical comments. *The Messenger*, 61:22–24, September 1990.

[306] J. Wu, Z. He, L. Zhang, L. Yuan, T. Wang, J. Jia, R. Shu, and J. Wang. Polarization study about a telescope-based transmitter for quantum communication. *Applied Optics*, 56:8501–8506, 2017.

[307] Jincai Wu, Liang Zhang, JianJun Jia, Tianhong Wang, Rong Shu, Zhiping He, and Jianyu Wang. Polarization-maintaining design for satellite-based quantum communication terminals. *Opt. Express*, 28(8):10746–10759, Apr 2020.

[308] Mengyu Xie, Youn Seok Lee, Ramy Tannous, Gui-Lu Long, and Thomas Jennewein. Roles of fiber birefringence and raman scattering in the spontaneous four-wave mixing process through birefringent fibers. *Opt. Express*, 29(20):31348–31363, Sep 2021.

[309] Julius Yellowhair and James H. Burge. Analysis of a scanning pentaprism system for measurements of large flat mirrors. *Appl. Opt.*, 46(35):8466–8474, Dec 2007.

[310] Juan Yin, Yuan Cao, Yu-Huai Li, Sheng-Kai Liao, Liang Zhang, Ji-Gang Ren, Wen-Qi Cai, Wei-Yue Liu, Bo Li, Hui Dai, Guang-Bing Li, Qi-Ming Lu, Yun-Hong Gong, Yu Xu, Shuang-Lin Li, Feng-Zhi Li, Ya-Yun Yin, Zi-Qing Jiang, Ming Li, Jian-Jun Jia, Ge Ren, Dong He, Yi-Lin Zhou, Xiao-Xiang Zhang, Na Wang, Xiang Chang, Zhen-Cai Zhu, Nai-Le Liu, Yu-Ao Chen, Chao-Yang Lu, Rong Shu, Cheng-Zhi Peng, Jian-Yu Wang, and Jian-Wei Pan. Satellite-based entanglement distribution over 1200 kilometers. *Science*, 356(6343):1140–1144, 2017.

[311] Juan Yin, Yuan Cao, Yu-Huai Li, Ji-Gang Ren, Sheng-Kai Liao, Liang Zhang, Wen-Qi Cai, Wei-Yue Liu, Bo Li, Hui Dai, Ming Li, Yong-Mei Huang, Lei Deng, Li Li, Qiang Zhang, Nai-Le Liu, Yu-Ao Chen, Chao-Yang Lu, Rong Shu, Cheng-Zhi Peng, Jian-Yu Wang, and Jian-Wei Pan. Satellite-to-ground entanglement-based quantum key distribution. *Phys. Rev. Lett.*, 119:200501, Nov 2017.

[312] Juan Yin, Yu-Huai Li, Sheng-Kai Liao, Meng Yang, Yuan Cao, Liang Zhang, Ji-Gang Ren, Wen-Qi Cai, Wei-Yue Liu, Shuang-Lin Li, Rong Shu, Yong-Mei Huang, Lei Deng, Li Li, Qiang Zhang, Nai-Le Liu, Yu-Ao Chen, Chao-Yang Lu, Xiang-Bin

Wang, Feihu Xu, Jian-Yu Wang, Cheng-Zhi Peng, Artur K. Ekert, and Jian-Wei Pan. Entanglement-based secure quantum cryptography over 1,120 kilometres. *Nature*, 582(7813):501–505, Jun 2020.

[313] Su-Peng Yu. *Nano-Photonic Platform for Atom-Light Interaction*. PhD thesis, California Institute of Technology, 2017.

[314] Yong Yu, Fei Ma, Xi-Yu Luo, Bo Jing, Peng-Fei Sun, Ren-Zhou Fang, Chao-Wei Yang, Hui Liu, Ming-Yang Zheng, Xiu-Ping Xie, Wei-Jun Zhang, Li-Xing You, Zhen Wang, Teng-Yun Chen, Qiang Zhang, Xiao-Hui Bao, and Jian-Wei Pan. Entanglement of two quantum memories via fibres over dozens of kilometres. *Nature*, 578(7794):240–245, Feb 2020.

[315] Garam Yun, Karlton Crabtree, and Russell A. Chipman. Three-dimensional polarization ray-tracing calculus i: definition and diattenuation. *Appl. Opt.*, 50(18):2855–2865, Jun 2011.

[316] Iman Esmaeil Zadeh, Ali W. Elshaari, Klaus D. Jöns, Andreas Fognini, Dan Dalacu, Philip J. Poole, Michael E. Reimer, and Val Zwiller. Deterministic integration of single photon sources in silicon based photonic circuits. *Nano Letters*, 16(4):2289–2294, Apr 2016.

[317] Zhongxi Zhang, Liang Chen, and Xiaoyi Bao. A fourth-order runge-kutta in the interaction picture method for numerically solving the coupled nonlinear schrödinger equation. *Opt. Express*, 18(8):8261–8276, Apr 2010.

[318] Manjin Zhong, Morgan P. Hedges, Rose L. Ahlefeldt, John G. Bartholomew, Sarah E. Beavan, Sven M. Wittig, Jevon J. Longdell, and Matthew J. Sellars. Optically addressable nuclear spins in a solid with a six-hour coherence time. *Nature*, 517(7533):177–180, Jan 2015.

[319] Zhi-Yuan Zhou, Shi-Long Liu, Shi-Kai Liu, Yin-Hai Li, Dong-Sheng Ding, Guang-Can Guo, and Bao-Sen Shi. Superresolving phase measurement with short-wavelength noon states by quantum frequency up-conversion. *Phys. Rev. Applied*, 7:064025, Jun 2017.

[320] Tiecheng Zhu, Yiwen Hu, Pradip Gatkine, Sylvain Veilleux, Joss Bland-Hawthorn, and Mario Dagenais. Ultrabroadband high coupling efficiency fiber-to-waveguide coupler using si $_3$n$_4$ /sio$_2$ waveguides on silicon. *IEEE Photonics Journal*, 8(5):1–12, 2016.

[321] Magdalena Zych, Fabio Costa, Igor Pikovski, and Časlav Brukner. Quantum interferometric visibility as a witness of general relativistic proper time. *Nature Communications*, 2(1):505, Oct 2011.

APPENDICES

Appendix A

Material refractive indices

Periodically poled lithium niobate (PPLN)

Sellmeier equation used for the PPLN crystal in Section 2.4 is from the reference [151]

$$\begin{aligned} n_e^2 &= 5.756 + 2.860 \times 10^{-6} f \\ &\quad + \frac{(0.0983 + 4.700 \times 10^{-8} f)}{\lambda^2 - (0.2020 + 6.113 \times 10^{-8} f)^2} + \frac{(189.32 + 1.516 \times 10^{-4} f)}{\lambda^2 - 12.52 f^2} - 1.32 \times 10^{-2} \lambda^2 \\ n_o^2 &= 5.653 + 7.941 \times 10^{-7} f \\ &\quad + \frac{(0.1185 + 3.134 \times 10^{-8} f)}{\lambda^2 - (0.2091 - 4.6413 \times 10^{-9} f)^2} + \frac{(89.61 - 2.188 \times 10^{-6} f)}{\lambda^2 - 10.85^2} + 1.97 \times 10^{-2} \lambda^2, \end{aligned} \tag{A.1}$$

with $f = (T - 24.5) \times (T + 570.82)$. The thermal expansion of the crystal is described by

$$L = L_0 \times \left(1 + \alpha(T - 25) + \beta(T - 25)^2\right), \tag{A.2}$$

where L_0 is the crystal length at 25°C with $\alpha = 1.54 \times 10^{-5}$ and $\beta = 5.3 \times 10^{-9}$.

Silicon nitride

Sellmeier equation used for the Si_3N_4 ring resonator in Chapter 4 is from the reference [194].

$$n_{SiN}^2 = 1 + \frac{3.0249 \lambda^2}{\lambda^2 - 135.3406^2} + \frac{40314 \lambda^2}{\lambda^2 - 1239842^2} \tag{A.3}$$

Silicon dioxide

Sellmeier equation used for the SiO_2 buffer layer of the ring resonator in Chapter 4 is from the reference [198].

$$n^2_{SiO_2} = 1 + \frac{0.6961663\lambda^2}{\lambda^2 - 0.0684043^2} + \frac{0.4079426\lambda^2}{\lambda^2 - 0.1162414^2} + \frac{0.8974794\lambda^2}{\lambda^2 - 9.896161^2} \tag{A.4}$$

Appendix B

C code: coupled nonlinear Schrödinger equation via fourth-order Runge-Kutta interaction picture method

```
/*
2020 Nov.
Youn Seok Lee, University of Waterloo.

Matlab Mexfunction
[UoutfH,UoutfV] = mex_CNLSE_RK4IP(UinfH,UinfV,dz,alpha,beta,gamma,Bbeta,Bvec,N_roundtrip)
:Solve Coupled Nonlinear Schrodinger Equations.

INPUT:
U0H (double array [N X 2]): pumps/signal/idler power in frequency domain
U0V (double array [N X 2]): pumps/signal/idler power in frequency domain
dz  (double scaler [1 X 1]): roundtrip length of ring cavity
alpha (double scaler [1 X 1]): material propagation loss
beta (double array [N X 1]): propagation constant of ring cavity
gamma (double array [N X 1]): nonlinear coefficient
Bbeta (double array [N X M]): fiber birefringence, N: number of frequency grid, M: number
    of waveplates
Btheta (double array [1 X M]): waveplate orientation/angle
Nt (int scaler [1 X 1]): number of iterations

OUTPUT:
U_hatH (complex array [N X 2]): electric field spectrum at pass port
U_hatV (complex array [N X 2]): electric field spectrum inside cavity
*/

#include stdlib.h
#include stdio.h
```

```c
#include math.h
#include fftw3.h
#include mex.h

/* Macros for real and imaginary parts */
#define REAL 0
#define IMAG 1

/* Function declaration */
void mexFunction(int nlhs, mxArray *plhs[], int nrhs, const mxArray *prhs[]);
void doublevector2complexarray(double *in, double out[][2], int array_length);
void complexarray2doublevector(double in[][2], double *out, int array_length);
void run_RK4IP(double *UinfH, double *UinfV, double length, double alpha, double *beta,
    double *gamma, double *Bbeta, double *Btheta, int N_roundtrip, int M_plate, int N_freq
    , double *UoutfH_RE, double *UoutfH_IM, double *UoutfV_RE, double *UoutfV_IM);

/*--------------------------------*/
/****** MATLAB MEX GATEWAY *******/
/*--------------------------------*/
void mexFunction(int nlhs, mxArray *plhs[], int nrhs, const mxArray *prhs[])
  {
    /* input parameters */
  double *UinfH;
  double *UinfV;
  double dz;
  double alpha;
  double *beta;
  double *gamma;
  double *Bbeta;
  double *Btheta;
  int N_roundtrip;
  mwSize M_plate;
  mwSize N_freq;

  UinfH = mxGetPr(prhs[0]);   /* complex array: double [N X 2] */
  UinfV = mxGetPr(prhs[1]);   /* complex array: double [N X 2] */
  dz = *mxGetPr(prhs[2]);     /* scalar       */
  alpha = *mxGetPr(prhs[3]);      /* scalar       */
  beta = mxGetPr(prhs[4]);      /* real array: double [N X 1]   */
  gamma = mxGetPr(prhs[5]);     /* real array: double [N X 1]   */
  Bbeta = mxGetPr(prhs[6]);   /* real array: double [N X M] */
  Btheta = mxGetPr(prhs[7]);    /*  real array: double [1 X M]  */
  N_roundtrip = *mxGetPr(prhs[8]);  /* scalar       */

  M_plate = mxGetM(prhs[7]);
  N_freq = mxGetM(prhs[0]);

  plhs[0] = mxCreateDoubleMatrix(N_freq, N_roundtrip, mxREAL);
  plhs[1] = mxCreateDoubleMatrix(N_freq, N_roundtrip, mxREAL);
  plhs[2] = mxCreateDoubleMatrix(N_freq, N_roundtrip, mxREAL);
  plhs[3] = mxCreateDoubleMatrix(N_freq, N_roundtrip, mxREAL);

  run_RK4IP(UinfH, UinfV, dz, alpha, beta, gamma, Bbeta, Btheta, N_roundtrip, M_plate,
      N_freq,  mxGetPr(plhs[0]), mxGetPr(plhs[1]),mxGetPr(plhs[2]),mxGetPr(plhs[3]));
  }
/*--------------------------------*/
/******** END GATEWAY *************/
```

```
81  /*--------------------------------*/
82
83  /*--------------------------------*/
84  /******* RK4IP for CNLSE  *********/
85  /*--------------------------------*/
86
87  void run_RK4IP(double *UinfH, double *UinfV, double dz, double alpha, double *beta, double
        *gamma, double *Bbeta, double *Btheta, int N_roundtrip, int M_plate, int N_freq,
      double *UoutfH_RE, double *UoutfH_IM, double *UoutfV_RE, double *UoutfV_IM)
88    {
89    double (*m_matrix)[M_plate][4][2] = malloc(N_freq*sizeof(double[M_plate][4][2]));
90    double (*halfprop)[2] = malloc(N_freq * sizeof(double[2]));
91    double (*U_hatH)[2] = malloc(N_freq * sizeof(double[2]));
92    double (*U_hatV)[2] = malloc(N_freq * sizeof(double[2]));
93    double (*Uip_hatH)[2] = malloc(N_freq * sizeof(double[2]));
94    double (*Uip_hatV)[2] = malloc(N_freq * sizeof(double[2]));
95    double (*U1H)[2] = malloc(N_freq * sizeof(double[2]));
96    double (*U2H)[2] = malloc(N_freq * sizeof(double[2]));
97    double (*U3H)[2] = malloc(N_freq * sizeof(double[2]));
98    double (*U4H)[2] = malloc(N_freq * sizeof(double[2]));
99    double (*k1H)[2] = malloc(N_freq * sizeof(double[2]));
100   double (*k2H)[2] = malloc(N_freq * sizeof(double[2]));
101   double (*k3H)[2] = malloc(N_freq * sizeof(double[2]));
102   double (*U1V)[2] = malloc(N_freq * sizeof(double[2]));
103   double (*U2V)[2] = malloc(N_freq * sizeof(double[2]));
104   double (*U3V)[2] = malloc(N_freq * sizeof(double[2]));
105   double (*U4V)[2] = malloc(N_freq * sizeof(double[2]));
106   double (*k1V)[2] = malloc(N_freq * sizeof(double[2]));
107   double (*k2V)[2] = malloc(N_freq * sizeof(double[2]));
108   double (*k3V)[2] = malloc(N_freq * sizeof(double[2]));
109
110   double (*Uf_RE_H)[N_roundtrip] = malloc(N_freq * sizeof(double[N_roundtrip]));
111   double (*Uf_IM_H)[N_roundtrip] = malloc(N_freq * sizeof(double[N_roundtrip]));
112   double (*Uf_RE_V)[N_roundtrip] = malloc(N_freq * sizeof(double[N_roundtrip]));
113   double (*Uf_IM_V)[N_roundtrip] = malloc(N_freq * sizeof(double[N_roundtrip]));
114
115   double normfactor = 1.0 / N_freq;
116
117   /* FFT in-plane (input = output) */
118   fftw_plan FFTplan_ip = fftw_plan_dft_1d(N_freq, U1H, U1H, FFTW_BACKWARD, FFTW_MEASURE);
119   /* IFFT in-plane (input = output) */
120   fftw_plan IFFTplan_ip = fftw_plan_dft_1d(N_freq, U1H, U1H, FFTW_FORWARD, FFTW_MEASURE);
121   /* FFT out-plane (input ~= output) */
122   fftw_plan FFTplan_op = fftw_plan_dft_1d(N_freq, U_hatH, U1H, FFTW_BACKWARD, FFTW_MEASURE
          );
123   /* FFT out-plane (input ~= output) */
124   fftw_plan IFFTplan_op = fftw_plan_dft_1d(N_freq, U1H, U_hatH, FFTW_FORWARD, FFTW_MEASURE
          );
125
126   int i;
127   int j;
128
129   /* initialize the complex vector variables and prepare M-matrix */
130   for (i = 0; i < N_freq; i++)
131     {
132     U_hatH[i][REAL] = 0.0; U_hatH[i][IMAG] = 0.0;
133     U_hatV[i][REAL] = 0.0; U_hatV[i][IMAG] = 0.0;
```

```
134
135     halfprop[i][REAL] = exp(-1.0*alpha*0.5*dz*0.5)*cos(-1.0*beta[i]*dz*0.5);
136     halfprop[i][IMAG] = exp(-1.0*alpha*0.5*dz*0.5)*sin(-1.0*beta[i]*dz*0.5);
137     }
138
139   /* double vector to complex array */
140   doublevector2complexarray(UinfH, U_hatH, N_freq);
141   doublevector2complexarray(UinfV, U_hatV, N_freq);
142
143   /* M-matrix */
144   for (i = 0; i < N_freq; i++)
145     for (j = 0; j < M_plate; j++)
146     {
147       {
148       /* M-matrix 1 X 1 component */
149       m_matrix[i][j][0][REAL] = cos(-1.0 * Bbeta[i+(j*N_freq)] * 0.5 * dz * 0.5) * cos(
              Btheta[j]) * cos(Btheta[j]) + cos(1.0 * Bbeta[i+(j*N_freq)] * 0.5 * dz * 0.5) *
              sin(Btheta[j]) * sin(Btheta[j]);
150       m_matrix[i][j][0][IMAG] = sin(-1.0 * Bbeta[i+(j*N_freq)] * 0.5 * dz * 0.5) * cos(
              Btheta[j]) * cos(Btheta[j]) + sin(1.0 * Bbeta[i+(j*N_freq)] * 0.5 * dz * 0.5) *
              sin(Btheta[j]) * sin(Btheta[j]);
151
152       /* M-matrix 1 X 2 component */
153       m_matrix[i][j][1][REAL] = cos(-1.0 * Bbeta[i+(j*N_freq)] * 0.5 * dz * 0.5) * cos(
              Btheta[j]) * sin(Btheta[j]) - cos(1.0 * Bbeta[i+(j*N_freq)] * 0.5 * dz * 0.5) *
              cos(Btheta[j]) * sin(Btheta[j]);
154       m_matrix[i][j][1][IMAG] = sin(-1.0 * Bbeta[i+(j*N_freq)] * 0.5 * dz * 0.5) * cos(
              Btheta[j]) * sin(Btheta[j]) - sin(1.0 * Bbeta[i+(j*N_freq)] * 0.5 * dz * 0.5) *
              cos(Btheta[j]) * sin(Btheta[j]);
155
156       /* M-matrix 2 X 1 component */
157       m_matrix[i][j][2][REAL] = cos(-1.0 * Bbeta[i+(j*N_freq)] * 0.5 * dz * 0.5) * cos(
              Btheta[j]) * sin(Btheta[j]) - cos(1.0 * Bbeta[i+(j*N_freq)] * 0.5 * dz * 0.5) *
              cos(Btheta[j]) * sin(Btheta[j]);
158       m_matrix[i][j][2][IMAG] = sin(-1.0 * Bbeta[i+(j*N_freq)] * 0.5 * dz * 0.5) * cos(
              Btheta[j]) * sin(Btheta[j]) - sin(1.0 * Bbeta[i+(j*N_freq)] * 0.5 * dz * 0.5) *
              cos(Btheta[j]) * sin(Btheta[j]);
159
160       /* M-matrix 2 X 2 component */
161       m_matrix[i][j][3][REAL] = cos(-1.0 * Bbeta[i+(j*N_freq)] * 0.5 * dz * 0.5) * sin(
              Btheta[j]) * sin(Btheta[j]) + cos(1.0 * Bbeta[i+(j*N_freq)] * 0.5 * dz * 0.5) *
              cos(Btheta[j]) * cos(Btheta[j]);
162       m_matrix[i][j][3][IMAG] = sin(-1.0 * Bbeta[i+(j*N_freq)] * 0.5 * dz * 0.5) * sin(
              Btheta[j]) * sin(Btheta[j]) + sin(1.0 * Bbeta[i+(j*N_freq)] * 0.5 * dz * 0.5) *
              cos(Btheta[j]) * cos(Btheta[j]);
163       }
164     }
165
166   /* RK4IP starts! */
167   for (j = 0; j < N_roundtrip; j++)
168     {
169     /* Matlab code:  u1 = ifft(u_cav_hat); */
170     fftw_execute_dft(IFFTplan_op,U_hatH,U1H);
171     fftw_execute_dft(IFFTplan_op,U_hatV,U1V);
172
173     /* Matlab code:  uip_hat = halfstep.*M1.*u_cav_hat; u1 = u1*abs(u1).^2; */
174     for (i = 0; i < N_freq; i++)
```

```
175         {
176         double tmpRE_H = U_hatH[i][REAL];
177         double tmpIM_H = U_hatH[i][IMAG];
178         double tmpRE_V = U_hatV[i][REAL];
179         double tmpIM_V = U_hatV[i][IMAG];
180         /* M1.*U_hat */
181         U_hatH[i][REAL] = (m_matrix[i][j][0][REAL]*tmpRE_H - m_matrix[i][j][0][IMAG]*tmpIM_H
                ) + (m_matrix[i][j][1][REAL]*tmpRE_V - m_matrix[i][j][1][IMAG]*tmpIM_V);
182         U_hatH[i][IMAG] = (m_matrix[i][j][0][REAL]*tmpIM_H + m_matrix[i][j][0][IMAG]*tmpRE_H
                ) + (m_matrix[i][j][1][REAL]*tmpIM_V + m_matrix[i][j][1][IMAG]*tmpRE_V);
183         U_hatV[i][REAL] = (m_matrix[i][j][2][REAL]*tmpRE_H - m_matrix[i][j][2][IMAG]*tmpIM_H
                ) + (m_matrix[i][j][3][REAL]*tmpRE_V - m_matrix[i][j][3][IMAG]*tmpIM_V);
184         U_hatV[i][IMAG] = (m_matrix[i][j][2][REAL]*tmpIM_H + m_matrix[i][j][2][IMAG]*tmpRE_H
                ) + (m_matrix[i][j][3][REAL]*tmpIM_V + m_matrix[i][j][3][IMAG]*tmpRE_V);
185
186         Uip_hatH[i][REAL] = halfprop[i][REAL]*U_hatH[i][REAL] - halfprop[i][IMAG]*U_hatH[i][
                IMAG];
187         Uip_hatH[i][IMAG] = halfprop[i][REAL]*U_hatH[i][IMAG] + halfprop[i][IMAG]*U_hatH[i][
                REAL];
188
189         Uip_hatV[i][REAL] = halfprop[i][REAL]*U_hatV[i][REAL] - halfprop[i][IMAG]*U_hatV[i][
                IMAG];
190         Uip_hatV[i][IMAG] = halfprop[i][REAL]*U_hatV[i][IMAG] + halfprop[i][IMAG]*U_hatV[i][
                REAL];
191
192         tmpRE_H = U1H[i][REAL];
193         tmpIM_H = U1H[i][IMAG];
194         tmpRE_V = U1V[i][REAL];
195         tmpIM_V = U1V[i][IMAG];
196
197         double abs_squareH = tmpRE_H * tmpRE_H + tmpIM_H * tmpIM_H;
198         double abs_squareV = tmpRE_V * tmpRE_V + tmpIM_V * tmpIM_V;
199
200         double squareHreal = tmpRE_H * tmpRE_H - tmpIM_H * tmpIM_H;
201         double squareHimag = 2.0 * tmpRE_H * tmpIM_H;
202
203         double squareVreal = tmpRE_V * tmpRE_V - tmpIM_V * tmpIM_V;
204         double squareVimag = 2.0 * tmpRE_V * tmpIM_V;
205
206         U1H[i][REAL] = (tmpRE_H * abs_squareH + (2.0/3.0) * tmpRE_H * abs_squareV +
                (1.0/3.0) * (tmpRE_H * squareVreal + tmpIM_H * squareVimag)) * normfactor *
                normfactor * normfactor;
207         U1H[i][IMAG] = (tmpIM_H * abs_squareH + (2.0/3.0) * tmpIM_H * abs_squareV +
                (1.0/3.0) * (tmpRE_H * squareVimag - tmpIM_H * squareVreal)) * normfactor *
                normfactor * normfactor;
208
209         U1V[i][REAL] = (tmpRE_V * abs_squareV + (2.0/3.0) * tmpRE_V * abs_squareH +
                (1.0/3.0) * (tmpRE_V * squareHreal + tmpIM_V * squareHimag)) * normfactor *
                normfactor * normfactor;
210         U1V[i][IMAG] = (tmpIM_V * abs_squareV + (2.0/3.0) * tmpIM_V * abs_squareH +
                (1.0/3.0) * (tmpRE_V * squareHimag - tmpIM_V * squareHreal)) * normfactor *
                normfactor * normfactor;
211         }
212
213       /* Matlab code:  u1 = fft(u1); */
214       fftw_execute_dft(FFTplan_ip,U1H,U1H);
215       fftw_execute_dft(FFTplan_ip,U1V,U1V);
```

```
216
217     /* Matlab code: k1 = halfstep.*M1*(1i*gamma.*u1); */
218     /*         U2 = uip_hat + k1*dz/2  */
219     for (i = 0; i < N_freq; i++)
220       {
221       double tmpRE_H = U1H[i][REAL];
222       double tmpIM_H = U1H[i][IMAG];
223       double tmpRE_V = U1V[i][REAL];
224       double tmpIM_V = U1V[i][IMAG];
225       /* M1.*U_hat */
226       U1H[i][REAL] = (m_matrix[i][j][0][REAL]*tmpRE_H - m_matrix[i][j][0][IMAG]*tmpIM_H) +
                (m_matrix[i][j][1][REAL]*tmpRE_V - m_matrix[i][j][1][IMAG]*tmpIM_V);
227       U1H[i][IMAG] = (m_matrix[i][j][0][REAL]*tmpIM_H + m_matrix[i][j][0][IMAG]*tmpRE_H) +
                (m_matrix[i][j][1][REAL]*tmpIM_V + m_matrix[i][j][1][IMAG]*tmpRE_V);
228       U1V[i][REAL] = (m_matrix[i][j][2][REAL]*tmpRE_H - m_matrix[i][j][2][IMAG]*tmpIM_H) +
                (m_matrix[i][j][3][REAL]*tmpRE_V - m_matrix[i][j][3][IMAG]*tmpIM_V);
229       U1V[i][IMAG] = (m_matrix[i][j][2][REAL]*tmpIM_H + m_matrix[i][j][2][IMAG]*tmpRE_H) +
                (m_matrix[i][j][3][REAL]*tmpIM_V + m_matrix[i][j][3][IMAG]*tmpRE_V);
230
231       k1H[i][REAL] = halfprop[i][REAL]*(-1.0*gamma[i]*U1H[i][IMAG]) - halfprop[i][IMAG]*(
              gamma[i]*U1H[i][REAL]);
232       k1H[i][IMAG] = halfprop[i][REAL]*(gamma[i]*U1H[i][REAL]) + halfprop[i][IMAG]*(-1.0*
              gamma[i]*U1H[i][IMAG]);
233
234       k1V[i][REAL] = halfprop[i][REAL]*(-1.0*gamma[i]*U1V[i][IMAG]) - halfprop[i][IMAG]*(
              gamma[i]*U1V[i][REAL]);
235       k1V[i][IMAG] = halfprop[i][REAL]*(gamma[i]*U1V[i][REAL]) + halfprop[i][IMAG]*(-1.0*
              gamma[i]*U1V[i][IMAG]);
236
237       U2H[i][REAL] = Uip_hatH[i][REAL] + k1H[i][REAL]*dz*0.5;
238       U2H[i][IMAG] = Uip_hatH[i][IMAG] + k1H[i][IMAG]*dz*0.5;
239
240       U2V[i][REAL] = Uip_hatV[i][REAL] + k1V[i][REAL]*dz*0.5;
241       U2V[i][IMAG] = Uip_hatV[i][IMAG] + k1V[i][IMAG]*dz*0.5;
242       }
243
244     /* Matlab code:  u2 = ifft(u2); */
245     fftw_execute_dft(IFFTplan_ip,U2H,U2H);
246     fftw_execute_dft(IFFTplan_ip,U2V,U2V);
247
248     /* Matlab code:  u2 = u2*abs(u2).^2; */
249     for (i = 0; i < N_freq; i++)
250       {
251       double tmpRE_H = U2H[i][REAL];
252       double tmpIM_H = U2H[i][IMAG];
253       double tmpRE_V = U2V[i][REAL];
254       double tmpIM_V = U2V[i][IMAG];
255
256       double abs_squareH = tmpRE_H * tmpRE_H + tmpIM_H * tmpIM_H;
257       double abs_squareV = tmpRE_V * tmpRE_V + tmpIM_V * tmpIM_V;
258
259       double squareHreal = tmpRE_H * tmpRE_H - tmpIM_H * tmpIM_H;
260       double squareHimag = 2.0 * tmpRE_H * tmpIM_H;
261
262       double squareVreal = tmpRE_V * tmpRE_V - tmpIM_V * tmpIM_V;
263       double squareVimag = 2.0 * tmpRE_V * tmpIM_V;
264
```

```
265       U2H[i][REAL] = (tmpRE_H * abs_squareH + (2.0/3.0) * tmpRE_H * abs_squareV +
              (1.0/3.0) * (tmpRE_H * squareVreal + tmpIM_H * squareVimag)) * normfactor *
              normfactor * normfactor;
266       U2H[i][IMAG] = (tmpIM_H * abs_squareH + (2.0/3.0) * tmpIM_H * abs_squareV +
              (1.0/3.0) * (tmpRE_H * squareVimag - tmpIM_H * squareVreal)) * normfactor *
              normfactor * normfactor;
267
268       U2V[i][REAL] = (tmpRE_V * abs_squareV + (2.0/3.0) * tmpRE_V * abs_squareH +
              (1.0/3.0) * (tmpRE_V * squareHreal + tmpIM_V * squareHimag)) * normfactor *
              normfactor * normfactor;
269       U2V[i][IMAG] = (tmpIM_V * abs_squareV + (2.0/3.0) * tmpIM_V * abs_squareH +
              (1.0/3.0) * (tmpRE_V * squareHimag - tmpIM_V * squareHreal)) * normfactor *
              normfactor * normfactor;
270       }
271
272     /* Matlab code:  u2 = fft(u2); */
273     fftw_execute_dft(FFTplan_ip,U2H,U2H);
274     fftw_execute_dft(FFTplan_ip,U2V,U2V);
275
276     /* Matlab code:  k2 = 1i*gamma.*u2; */
277     /*        u3 = uip_hat + k2*dz/2; */
278     for (i = 0; i < N_freq; i++)
279       {
280       k2H[i][REAL] = -1.0*gamma[i]*U2H[i][IMAG];
281       k2H[i][IMAG] = gamma[i]*U2H[i][REAL];
282
283       k2V[i][REAL] = -1.0*gamma[i]*U2V[i][IMAG];
284       k2V[i][IMAG] = gamma[i]*U2V[i][REAL];
285
286       U3H[i][REAL] = Uip_hatH[i][REAL] + k2H[i][REAL]*dz*0.5;
287       U3H[i][IMAG] = Uip_hatH[i][IMAG] + k2H[i][IMAG]*dz*0.5;
288
289       U3V[i][REAL] = Uip_hatV[i][REAL] + k2V[i][REAL]*dz*0.5;
290       U3V[i][IMAG] = Uip_hatV[i][IMAG] + k2V[i][IMAG]*dz*0.5;
291       }
292
293     /* Matlab code:  u3 = ifft(u3);  */
294     fftw_execute_dft(IFFTplan_ip,U3H,U3H);
295     fftw_execute_dft(IFFTplan_ip,U3V,U3V);
296
297     /* Matlab code:  u3 = u3*abs(u3).^2; */
298     for (i = 0; i < N_freq; i++)
299       {
300       double tmpRE_H = U3H[i][REAL];
301       double tmpIM_H = U3H[i][IMAG];
302       double tmpRE_V = U3V[i][REAL];
303       double tmpIM_V = U3V[i][IMAG];
304
305       double abs_squareH = tmpRE_H * tmpRE_H + tmpIM_H * tmpIM_H;
306       double abs_squareV = tmpRE_V * tmpRE_V + tmpIM_V * tmpIM_V;
307
308       double squareHreal = tmpRE_H * tmpRE_H - tmpIM_H * tmpIM_H;
309       double squareHimag = 2.0 * tmpRE_H * tmpIM_H;
310
311       double squareVreal = tmpRE_V * tmpRE_V - tmpIM_V * tmpIM_V;
312       double squareVimag = 2.0 * tmpRE_V * tmpIM_V;
313
```

```
314       U3H[i][REAL] = (tmpRE_H * abs_squareH + (2.0/3.0) * tmpRE_H * abs_squareV +
              (1.0/3.0) * (tmpRE_H * squareVreal + tmpIM_H * squareVimag)) * normfactor *
              normfactor * normfactor;
315       U3H[i][IMAG] = (tmpIM_H * abs_squareH + (2.0/3.0) * tmpIM_H * abs_squareV +
              (1.0/3.0) * (tmpRE_H * squareVimag - tmpIM_H * squareVreal)) * normfactor *
              normfactor * normfactor;
316
317       U3V[i][REAL] = (tmpRE_V * abs_squareV + (2.0/3.0) * tmpRE_V * abs_squareH +
              (1.0/3.0) * (tmpRE_V * squareHreal + tmpIM_V * squareHimag)) * normfactor *
              normfactor * normfactor;
318       U3V[i][IMAG] = (tmpIM_V * abs_squareV + (2.0/3.0) * tmpIM_V * abs_squareH +
              (1.0/3.0) * (tmpRE_V * squareHimag - tmpIM_V * squareHreal)) * normfactor *
              normfactor * normfactor;
319       }
320
321     /* Matlab code:  u3 = fft(u3); */
322     fftw_execute_dft(FFTplan_ip,U3H,U3H);
323     fftw_execute_dft(FFTplan_ip,U3V,U3V);
324     /* Matlab code:  k3 = 1i*gamma.*u3; u4 = halfstep.*(uip_hat + k3*dz); */
325     for (i = 0; i < N_freq; i++)
326       {
327       k3H[i][REAL] = -1.0*gamma[i]*U3H[i][IMAG];
328       k3H[i][IMAG] = gamma[i]*U3H[i][REAL];
329
330       k3V[i][REAL] = -1.0*gamma[i]*U3V[i][IMAG];
331       k3V[i][IMAG] = gamma[i]*U3V[i][REAL];
332
333       double tmpRE_H = Uip_hatH[i][REAL] + k3H[i][REAL]*dz;
334       double tmpIM_H = Uip_hatH[i][IMAG] + k3H[i][IMAG]*dz;
335       double tmpRE_V = Uip_hatV[i][REAL] + k3V[i][REAL]*dz;
336       double tmpIM_V = Uip_hatV[i][IMAG] + k3V[i][IMAG]*dz;
337       /* M1.*U_hat */
338       double tmptmpRE_H;
339       double tmptmpIM_H;
340       double tmptmpRE_V;
341       double tmptmpIM_V;
342       tmptmpRE_H = (m_matrix[i][j][0][REAL]*tmpRE_H - m_matrix[i][j][0][IMAG]*tmpIM_H) + (
              m_matrix[i][j][1][REAL]*tmpRE_V - m_matrix[i][j][1][IMAG]*tmpIM_V);
343       tmptmpIM_H = (m_matrix[i][j][0][REAL]*tmpIM_H + m_matrix[i][j][0][IMAG]*tmpRE_H) + (
              m_matrix[i][j][1][REAL]*tmpIM_V + m_matrix[i][j][1][IMAG]*tmpRE_V);
344       tmptmpRE_V = (m_matrix[i][j][2][REAL]*tmpRE_H - m_matrix[i][j][2][IMAG]*tmpIM_H) + (
              m_matrix[i][j][3][REAL]*tmpRE_V - m_matrix[i][j][3][IMAG]*tmpIM_V);
345       tmptmpIM_V = (m_matrix[i][j][2][REAL]*tmpIM_H + m_matrix[i][j][2][IMAG]*tmpRE_H) + (
              m_matrix[i][j][3][REAL]*tmpIM_V + m_matrix[i][j][3][IMAG]*tmpRE_V);
346
347       U4H[i][REAL] = halfprop[i][REAL]*(tmptmpRE_H) - halfprop[i][IMAG]*(tmptmpIM_H);
348       U4H[i][IMAG] = halfprop[i][REAL]*(tmptmpIM_H) + halfprop[i][IMAG]*(tmptmpRE_H);
349
350       U4V[i][REAL] = halfprop[i][REAL]*(tmptmpRE_V) - halfprop[i][IMAG]*(tmptmpIM_V);
351       U4V[i][IMAG] = halfprop[i][REAL]*(tmptmpIM_V) + halfprop[i][IMAG]*(tmptmpRE_V);
352       }
353
354     /* Matlab code:  u4 = ifft(u4); */
355     fftw_execute_dft(IFFTplan_ip,U4H,U4H);
356     fftw_execute_dft(IFFTplan_ip,U4V,U4V);
357
358     /* Matlab code:  u4 = u2*abs(u4).^2; */
```

```
359     for (i = 0; i < N_freq; i++)
360       {
361       double tmpRE_H = U4H[i][REAL];
362       double tmpIM_H = U4H[i][IMAG];
363       double tmpRE_V = U4V[i][REAL];
364       double tmpIM_V = U4V[i][IMAG];
365
366       double abs_squareH = tmpRE_H * tmpRE_H + tmpIM_H * tmpIM_H;
367       double abs_squareV = tmpRE_V * tmpRE_V + tmpIM_V * tmpIM_V;
368
369       double squareHreal = tmpRE_H * tmpRE_H - tmpIM_H * tmpIM_H;
370       double squareHimag = 2.0 * tmpRE_H * tmpIM_H;
371
372       double squareVreal = tmpRE_V * tmpRE_V - tmpIM_V * tmpIM_V;
373       double squareVimag = 2.0 * tmpRE_V * tmpIM_V;
374
375       U4H[i][REAL] = (tmpRE_H * abs_squareH + (2.0/3.0) * tmpRE_H * abs_squareV +
              (1.0/3.0) * (tmpRE_H * squareVreal + tmpIM_H * squareVimag)) * normfactor *
              normfactor * normfactor;
376       U4H[i][IMAG] = (tmpIM_H * abs_squareH + (2.0/3.0) * tmpIM_H * abs_squareV +
              (1.0/3.0) * (tmpRE_H * squareVimag - tmpIM_H * squareVreal)) * normfactor *
              normfactor * normfactor;
377
378       U4V[i][REAL] = (tmpRE_V * abs_squareV + (2.0/3.0) * tmpRE_V * abs_squareH +
              (1.0/3.0) * (tmpRE_V * squareHreal + tmpIM_V * squareHimag)) * normfactor *
              normfactor * normfactor;
379       U4V[i][IMAG] = (tmpIM_V * abs_squareV + (2.0/3.0) * tmpIM_V * abs_squareH +
              (1.0/3.0) * (tmpRE_V * squareHimag - tmpIM_V * squareHreal)) * normfactor *
              normfactor * normfactor;
380       }
381
382     /* Matlab code:  u4 = fft(u4); */
383     fftw_execute_dft(FFTplan_ip,U4H,U4H);
384     fftw_execute_dft(FFTplan_ip,U4V,U4V);
385
386     /* Matlab code:  u_cav_hat = halfstep.*(uip_hat + k1*dz/6 + k2*dz/3 + k3*dz/3) + 1i*
          gamma.*u4*dz/6; */
387     for (i = 0; i < N_freq; i++)
388       {
389       double tmp_RE_H = Uip_hatH[i][REAL] + k1H[i][REAL]*dz*(1.0/6.0) + k2H[i][REAL]*dz
              *(1.0/3.0) + k3H[i][REAL]*dz*(1.0/3.0);
390       double tmp_IM_H = Uip_hatH[i][IMAG] + k1H[i][IMAG]*dz*(1.0/6.0) + k2H[i][IMAG]*dz
              *(1.0/3.0) + k3H[i][IMAG]*dz*(1.0/3.0);
391       double tmp_RE_V = Uip_hatV[i][REAL] + k1V[i][REAL]*dz*(1.0/6.0) + k2V[i][REAL]*dz
              *(1.0/3.0) + k3V[i][REAL]*dz*(1.0/3.0);
392       double tmp_IM_V = Uip_hatV[i][IMAG] + k1V[i][IMAG]*dz*(1.0/6.0) + k2V[i][IMAG]*dz
              *(1.0/3.0) + k3V[i][IMAG]*dz*(1.0/3.0);
393
394       double tmptmpRE_H;
395       double tmptmpIM_H;
396       double tmptmpRE_V;
397       double tmptmpIM_V;
398       tmptmpRE_H = (m_matrix[i][j][0][REAL]*tmp_RE_H - m_matrix[i][j][0][IMAG]*tmp_IM_H) +
               (m_matrix[i][j][1][REAL]*tmp_RE_V - m_matrix[i][j][1][IMAG]*tmp_IM_V);
399       tmptmpIM_H = (m_matrix[i][j][0][REAL]*tmp_IM_H + m_matrix[i][j][0][IMAG]*tmp_RE_H) +
               (m_matrix[i][j][1][REAL]*tmp_IM_V + m_matrix[i][j][1][IMAG]*tmp_RE_V);
```

```
400       tmptmpRE_V = (m_matrix[i][j][2][REAL]*tmp_RE_H - m_matrix[i][j][2][IMAG]*tmp_IM_H) +
               (m_matrix[i][j][3][REAL]*tmp_RE_V - m_matrix[i][j][3][IMAG]*tmp_IM_V);
401       tmptmpIM_V = (m_matrix[i][j][2][REAL]*tmp_IM_H + m_matrix[i][j][2][IMAG]*tmp_RE_H) +
               (m_matrix[i][j][3][REAL]*tmp_IM_V + m_matrix[i][j][3][IMAG]*tmp_RE_V);
402
403       U_hatH[i][REAL] = (halfprop[i][REAL]*tmptmpRE_H - halfprop[i][IMAG]*tmptmpIM_H) -
              gamma[i]*U4H[i][IMAG]*dz*(1.0/6.0);
404       U_hatH[i][IMAG] = (halfprop[i][REAL]*tmptmpIM_H + halfprop[i][IMAG]*tmptmpRE_H) +
              gamma[i]*U4H[i][REAL]*dz*(1.0/6.0);
405
406       U_hatV[i][REAL] = (halfprop[i][REAL]*tmptmpRE_V - halfprop[i][IMAG]*tmptmpIM_V) -
              gamma[i]*U4V[i][IMAG]*dz*(1.0/6.0);
407       U_hatV[i][IMAG] = (halfprop[i][REAL]*tmptmpIM_V + halfprop[i][IMAG]*tmptmpRE_V) +
              gamma[i]*U4V[i][REAL]*dz*(1.0/6.0);
408
409       Uf_RE_H[i][j] = U_hatH[i][REAL];
410       Uf_IM_H[i][j] = U_hatH[i][IMAG];
411       Uf_RE_V[i][j] = U_hatV[i][REAL];
412       Uf_IM_V[i][j] = U_hatV[i][IMAG];
413       }
414     }
415
416   /* double vector to complex array */
417   for (i = 0; i < N_freq; i++)
418     {
419     for (j = 0; j < N_roundtrip; j++)
420       {
421       UoutfH_RE[i+N_freq*j] = Uf_RE_H[i][j];
422       UoutfH_IM[i+N_freq*j] = Uf_IM_H[i][j];
423       UoutfV_RE[i+N_freq*j] = Uf_RE_V[i][j];
424       UoutfV_IM[i+N_freq*j] = Uf_IM_V[i][j];
425       }
426     }
427
428   /* Clear space */
429   fftw_destroy_plan(FFTplan_ip);
430   fftw_destroy_plan(IFFTplan_ip);
431   fftw_destroy_plan(FFTplan_op);
432   fftw_destroy_plan(IFFTplan_op);
433   fftw_cleanup();
434
435   free(m_matrix);
436   free(halfprop);
437   free(Uip_hatH);
438   free(Uip_hatV);
439   free(U_hatH);
440   free(U_hatV);
441   free(U1H);
442   free(U2H);
443   free(U3H);
444   free(U4H);
445   free(k1H);
446   free(k2H);
447   free(k3H);
448   free(U1V);
449   free(U2V);
450   free(U3V);
```

```
  free(U4V);
  free(k1V);
  free(k2V);
  free(k3V);
  free(Uf_RE_H);
  free(Uf_IM_H);
  free(Uf_RE_V);
  free(Uf_IM_V);
  }

void doublevector2complexarray(double *in, double out[][2], int array_length)
  {
  int i;
  for (i = 0; i < array_length; i++) {
    out[i][0] = in[i];
    out[i][1] = in[i+array_length];
    }
  }

void complexarray2doublevector(double in[][2], double *out, int array_length)
  {
  int i;
  for (i = 0; i < array_length; i++) {
    out[i] = in[i][0];
    out[i+array_length] = in[i][1];
    }
  }
```

Appendix C

Matlab code: optimal focal conditions in spontaneous parametric down-conversion process

```
function [R_CC, R_SSC, R_ISC]=Absolute_emission_rate (LightParam, MediumParam)
%%%% Input variables
% LightParam.waist_p: beam waist of pump light
% LightParam.waist_s: beam waist of signal light
% LightParam.waist_i: beam waist of idler light
% LightParam.k_p: wavevector of pump light
% LightParam.k_s: wavevector of signal light
% LightParam.k_i: wavevector of idler light
% LightParam.Pp: pump power
% LightParam.deltak: wavevector-mismatch
% LightParam.design_signal: signal wavelength
% LightParam.design_idler: idler wavelength
% LightParam.dLambda_s: wavelength steps for numerical
% integration of signal photons
% LightParam.dLambda_i: wavelength steps for numerical
% integration of idler photons

% MediumParam.z: spatial grid
% MediumParam.np: refractive index at pump wavelength
% MediumParam.ns: refractive index at signal wavelength
% MediumParam.ni: refractive index at idler wavelength
% MediumParam.xi2: periodic poling function, e.g., periodic square function.

%%%% Ouput variables
% R_CC: coincident counting rate
% R_SSC: single counting rate (signal)
% R_ISC: single counting rate (idler)

%% Constant
clight = 299792458;         % m/s
```

```
eps0 = 8.85418782e-12;  % s^4 A^2 / m^3 / kg

deff = 15.9e-12; % Effective nonlinear coefficient of Lithium niobate (Type-0) [m^-1*V^-1]
Ep0 = sqrt(2*LightParam.Pp/eps0/MediumParam.np/clight);

q_p = LightParam.waist_p^2 + 2*1i*MediumParam.z ./ LightParam.k_p;
q_s = LightParam.waist_s^2 + 2*1i*MediumParam.z ./ LightParam.k_s;
q_i = LightParam.waist_i^2 + 2*1i*MediumParam.z ./ LightParam.k_i;

%% Absolute emission rate
denom = (conj(q_s).*conj(q_i)+q_p.*conj(q_i)+q_p.*conj(q_s));
dz = MediumParam.z(2)-MediumParam.z(1);

% Coincidence rate
PhizCC = sqrt(8/pi) * LightParam.waist_p * LightParam.waist_s * LightParam.waist_i * sum(
    dz * exp(-1i * LightParam.deltak' * MediumParam.z) .* repmat(MediumParam.xi2,[length(
    LightParam.deltak),1]) ./ repmat(denom,[length(LightParam.deltak),1]),2);
Phi_integratedCC = sum(abs(PhizCC).^2 .* (2 * pi * clight * MediumParam.ns / (LightParam.
    design_signal * 1e-6)^2) * (LightParam.dLambda_s * 1e-6));
R_CC = (deff*Ep0/clight)^2 * (2 * pi * clight / LightParam.design_signal / 1e-6)*(2 * pi *
     clight / LightParam.design_idler / 1e-6) / (MediumParam.ns * MediumParam.ni * 2 * pi)
     * Phi_integratedCC;

% Single rate
Laguerre_S = (conj(q_s).* q_i + q_p.*q_i - q_p.*conj(q_s)) ./ (conj(q_s).*conj(q_i) + q_p
    .*conj(q_i) + q_p.*conj(q_s));
Laguerre_I = (conj(q_i).*q_s + q_p.*q_s - q_p.*conj(q_i)) ./ (conj(q_s).*conj(q_i) + q_p.*
    conj(q_i) + q_p.*conj(q_s));
Laguerre_order = 20;

R_SSC = 0;
R_ISC = 0;

for qq = 0:Laguerre_order
    PhizSSC =  sqrt(8/pi) * LightParam.waist_p * LightParam.waist_s * LightParam.waist_i *
         sum(dz * exp(-1i * LightParam.deltak' * MediumParam.z) .* repmat(MediumParam.xi2
        ,[length(LightParam.deltak),1]) ./ repmat(denom,[length(LightParam.deltak),1]) .*
        repmat(Laguerre_S.^(qq),[length(LightParam.deltak),1]),2);
    PhizISC =  sqrt(8/pi) * LightParam.waist_p * LightParam.waist_s * LightParam.waist_i *
         sum(dz * exp(-1i * LightParam.deltak' * MediumParam.z) .* repmat(MediumParam.xi2
        ,[length(LightParam.deltak),1]) ./ repmat(denom,[length(LightParam.deltak),1]) .*
        repmat(Laguerre_I.^(qq),[length(LightParam.deltak),1]),2);
    Phi_integratedSSC = sum(abs(PhizSSC).^2 .* (2 * pi * clight * MediumParam.ns / (
        LightParam.design_signal * 1e-6)^2) * (LightParam.dLambda_s * 1e-6));
    Phi_integratedISC = sum(abs(PhizISC).^2 .* (2 * pi * clight * MediumParam.ni / (
        LightParam.design_idler * 1e-6)^2) * (LightParam.dLambda_i * 1e-6));
    R_SSC = R_SSC + (deff * Ep0 / clight)^2 * (2 * pi * clight / LightParam.design_signal
        / 1e-6) * (2 * pi * clight / LightParam.design_idler / 1e-6) / (MediumParam.ns *
        MediumParam.ni * 2 * pi) * Phi_integratedSSC;
    R_ISC = R_ISC + (deff * Ep0 / clight)^2 * (2 * pi * clight / LightParam.design_signal
        / 1e-6) * (2 * pi * clight / LightParam.design_idler / 1e-6) / (MediumParam.ns *
        MediumParam.ni * 2 * pi) * Phi_integratedISC;
end
```

Appendix D

Matlab code: coherent spin-exchange rate and collective dissipation using Green function

```
% contants
clight=299792458;
a=374*10^-9;      % Lattice constant in m
eps0=8.85e-12;
hbar=1.05457148e-34;
mu0=4*pi*10^(-7);
h=2*pi*hbar;
fcs_d1=335.116*10^12;
fcs_d2=351.725*10^12; % Units in Hz
omega_d1=2*pi*fcs_d1;
omega_d2=2*pi*fcs_d2;
ec=1.6022*10^-19;
a0=5.291*10^-11;
JdJD1=4.489*ec*a0; % Jonathan's thesis (A.19)
JdJD2=6.324*ec*a0; % Jonathan's thesis (A.20) : already includes jj_factor
jj_factor=0.5; % D2 transition

%% Data load
% Local Green function
load('muresulty.mat')
load('GreenNf2D.mat')
load('GreenN2D.mat')
load('Green0f2D.mat')
load('Green02D.mat')

% FDTD result
load('GFresulty.mat')
ffieldy=GFresult.f;
Efieldy=GFresult.E;
X=GFresult.x;
```

```
load('GFresult0y.mat')
Efield0y=GFresult0.E;
ffield0y=GFresult0.f;
X0=GFresult0.x;

% Linear interpolation (not necessary)
Xplot=linspace(X(1),X(end),100000);
ffield=linspace(ffieldy(1),ffieldy(end),100000);
InG0f=interp1(ffield0y,squeeze(G0f(2,2,:)),ffield,'linear');
InGNfyy=interp1(ffieldy,squeeze(GNf(2,2,:)),ffield,'linear');
InG0=interp1(X0,squeeze(G0(2,2,:)),Xplot,'linear');
InGNyy=interp1(X,squeeze(GN(2,2,:)),Xplot,'linear');

% Find the frequency at the band edge
[M I]=max(squeeze(imag(GNf(2,2,:))));
fg=ffieldy(I);
delta=(ffieldy-fg);
deltav=(ffield0y-fg);
[m0 q0]=min(abs(delta));
[mv0 qv0]=min(abs(deltav));

% Detuning
delta1=0.1*10^12;
[m1 q1]=min(abs(delta-delta1));
[mv1 qv1]=min(abs(deltav-delta1));

w0=2*pi*ffieldy(q0); wv0=2*pi*ffield0y(qv0);
w1=2*pi*ffieldy(q1); wv1=2*pi*ffield0y(qv1);

q=[q0 q1];
qv=[qv0 qv1];
w=[w0 w1];
wv=[wv0 wv1];

% Calculate nonlocal Green function
for j=1:length(q)
    Gyy(:,j)=squeeze((Efieldy(:,2,q(j))))*clight^2*eps0/w(j)^2/mu;
    Gyy0(:,j)=squeeze((Efield0y(:,2,qv(j))))*clight^2*eps0/wv(j)^2/mu;
end

% Linear interpolation (not necessary)
for i=1:length(q)
    InGyy(:,i)=interp1(X,squeeze(Gyy(:,i)),Xplot);
    InGyy0(:,i)=interp1(X0,squeeze(Gyy0(:,i)),Xplot);
end

% Gamma (decay rate) & Jij (spin-exchange coefficient)
Gamma_yy=(JdJD2*jj_factor)^2*(2*omega_d2^2/(hbar*eps0*clight^2))*(imag(InGNfyy));
Jij_yy=(JdJD2*jj_factor)^2*(omega_d2^2/(hbar*eps0*clight^2))*(real(InGNfyy));
Gamma0=(JdJD2*jj_factor)^2*(2*omega_d2^2/(hbar*eps0*clight^2))*(imag(InG0f));
Jij0=(JdJD2*jj_factor)^2*(omega_d2^2/(hbar*eps0*clight^2))*(real(InG0f));
Gamma1D=Gamma_yy-Gamma_yy(34000);

NLoGamma=(JdJD2*jj_factor)^2*(2*omega_d2^2/(hbar*eps0*clight^2))*(imag(InGyy));
NLoJij=(JdJD2*jj_factor)^2*(omega_d2^2/(hbar*eps0*clight^2))*(real(InGyy));
NLoGamma0=(JdJD2*jj_factor)^2*(2*omega_d2^2/(hbar*eps0*clight^2))*(imag(InGyy0));
NLoJij0=(JdJD2*jj_factor)^2*(omega_d2^2/(hbar*eps0*clight^2))*(real(InGyy0));
```

Appendix E

Scheme MEEP code: Casimir-Polder force

```
;; 2017.08.23 Youn Seok Lee
;; This CTL file is to calculate Casimir-Polder potential for the ground
;; state of Cesium atom near the "Si3N4 Squircle W1 waveguide
;; structure" by MEEP. "filename_xyr" is for the calculation of
;; CP potential in xy-plane at z=0, and "filename_zr" is
;; for the z-direction at x=y=0.

;; Structure parameters :
;;        (1) Lattice constant : a
;;        (2) Air-hole radius (r1: Squircle size)
;;                (r2: Second-line holes)
;;                (r3: all the other holes)
;;        (3) Structure thickness : thk
;;        (4) Width of air-line-slot: wid
;;        (5) Ellipcity of squircles : Alpha
;; (the larger value: more elongated squircle in x-direction)
;;        (6) Shift of the squircles in y-direction : s1
;;        (7) Shift of the second line of holes in y-direction : s2
;;        (8) offset : Additional dielectric slap
;;          between the first line squircles and air line-slot
;;        (9) Squareness : Nsq
;;        (*) Sinusoidal modulation of the edge of th air
;;          line-slot (Alligator structrue) : Amplitude

;; distance units in (um) and unity speed of light (c=1) ;;

;(include "/usr/share/meep/casimir.scm")
(include "/home/uqml/apps/meep-1.3/share/meep/parallel.scm")

;; constant;;
(define pi (* 2 (acos 0)))  ; pi
(define Si3N4 1.9935)    ; index of Si3N4
(define-param myvacuum 1)
```

```
(define-param Sigma 1)

;; PhC dimensions (um);;
(define-param Nsq 4)    ; Only even number:  2 -> Circle, 4 -> Squircle
(define-param amp 0)
(define-param wid 114)
(define-param thk 200)
(define-param a 373)   ; lattice constant
(define-param y 8)    ; the number of unitcell in y-direction
(define-param r1 110)   ; radius of the 1st air-holes (Squircles)
(define-param r2 110)   ; radius of the 2nd air-holes
(define-param r3 110)    ; radius of all the other air-holes
(define-param s1 -20)    ; minimum distance between air hole and air slot
(define-param s2 -20)    ; minimum distance between 1st air hole and 2nd air hole
(define-param offset 120)
(define-param slot (* 2 (+ amp wid)))
(define-param alpha 1.15)    ; ellipcity of the 2nd holes
(define-param buffer 500) ; distance between the edge of structure and PML layer

;; define unit conversion function ;;
(define (simUnits x) (/ x a))   ; units of length in (um)

;; Unit conversion ;;
(define-param MEEPthk (simUnits thk))
(define-param MEEPa (simUnits a))
(define-param MEEPr1 (simUnits r1))
(define-param MEEPr2 (simUnits r2))
(define-param MEEPr3 (simUnits r3))
(define-param MEEPs1 (simUnits s1))
(define-param MEEPs2 (simUnits s2))
(define-param MEEPslot (simUnits slot))
(define-param MEEPoffset (simUnits offset))
(define-param MEEPbuffer (simUnits buffer))
(define-param elpta (* alpha r1))
(define-param elptb (/ r1 alpha))
(define-param MEEPelpta (simUnits elpta))
(define-param MEEPelptb (simUnits elptb))

;; Define perfecty-matched-layer thickness ;;
(define-param dpml 1)

;; Define computational cell dimension ;;
(define supercell-x MEEPa) ; width of blocks in x-direction
; distance between central line and the center of 1st air hole (squircle)
(define L1 (+ MEEPs1 MEEPoffset (* (/ (sqrt 3) 2) MEEPa)))
; distance between central line and the center of 2nd air hole
(define L2 (+ MEEPs2 MEEPoffset (* (sqrt 3) MEEPa)))
; width of blocks in y-direction
(define wY (+ (* (sqrt 3) MEEPa y) (* 2 L2)))
; the computational size in y-axis
(define supercell-y (+ wY (* 2 MEEPbuffer) (* 2 dpml)))
(define supercell-z (+ MEEPthk (* 2 MEEPbuffer) (* 2 dpml)))

;; AUX Settings ;;
(define-param res 32)
(define-param crnt 0.5)
(set-param! resolution res)
```

```
(set-param! Courant crnt)
(define-param endtime 10)
(define-param kpt (* 0.5 (/ 1 MEEPa)))
(define dx (/ 1 res 10))

;; Create geometry ;;
(define (drawBlock x)
  (let ((dy (+ wid (* amp (cos (* 2 pi x))))))
       (let ((cy (/ dy 2)))
            (list
              (make block
                (center x (simUnits cy) 0)
                (size (* 1.1 dx) (simUnits dy) (simUnits thk))
                (material (make dielectric (index myvacuum)))
              )
              (make block
                (center x (* -1 (simUnits cy)) 0)
                (size (* 1.1 dx) (simUnits dy) (simUnits thk))
                (material (make dielectric (index myvacuum)))
              )
            )
        )
))

(define (drawSquircle x)
  (let ((dy (* 2 MEEPelptb (expt (- 1 (/ (expt x Nsq) (expt MEEPelpta 4))) (/ 1 Nsq)))))
       (list
   (make block
    (center x L1 0)
    (size (* 1.1 dx) dy MEEPthk)
    (material (make dielectric (index myvacuum)))
   )
   (make block
    (center x (* -1 L1) 0)
    (size (* 1.1 dx) dy MEEPthk)
    (material (make dielectric (index myvacuum)))
   )
       )
))

(define (makeModule x)
        (if (>= x 1)
            '()
            (begin (set! geometry (append geometry (drawBlock x)))
             (makeModule (+ x dx))
            )
      ))
(define (makeSquircle x)
        (if (>= x MEEPelpta)
             '()
            (begin (set! geometry (append geometry (drawSquircle x)))
             (makeSquircle (+ x dx))
            )
      ))


;; Sources ;;
```

```
(define-param fcen (/ 1 0.852))      ; unit in (c/a=1/(lambda/a))
(define-param df 1)

;; position of interest ;;
(define-param xbgn 0)
(define-param ybgn 0)
(define-param zbgn 0)
(define-param r-min -0.2)
(define-param r-max (+ -0.2 (/ 20 res)))
(define-param dr (/ 1 res))
(define r-list (parallel-make-list r-min r-max dr))
(define eps-list (list Si3N4 myvacuum))

(define pol-list (list Ex Ey Ez))

(define Ext-list (list r-list eps-list))
(define Int-list (list pol-list))

(define param-info (make-param-list Ext-list Int-list))
(print param-info)
(define param-list (first param-info))
(define Next (second param-info))
(define Nint (third param-info))
(define Nsims (* Next Nint))

(define gamma-list (make-list Next 0))
(print "Number of simulations: "Nsims"\n")

;%%%%% LOCAL COMMUNICATION

;(define nproc (meep-count-processors))
;(define ngroups (min Nsims nproc))
;(define mygroup (meep-divide-parallel-processes ngroups))

;(print "nproc = "nproc"\n")
;(print "ngroups = "ngroups"\n")
;(print "mygroup = "mygroup"\n")
; a list of simulations for the group
;(define my-sims (get-indices Nsims nproc mygroup))
;(print "Total: my-sims = "my-sims"\n")

(define polstring "xyddz")
(define xstring "")
(define rstring "")
(define prev-r r-min)

(define (run-sim current-sim)
  (let* (  (index-info (get-ie-indices current-sim Next Nint))
      (i-internal (first index-info))
      (i-external (second index-info))
     ;%%%%% Get current simulation parameters
     (curr-params (list-ref param-list current-sim))
     (curr-r (first curr-params))
     (curr-eps (second curr-params))
     (curr-pol (third curr-params))
     (ft (meep-type curr-pol))
     (dt (/ Courant resolution))
```

```
     )
(print "index-info "index-info", i-internal "i-internal",
i-external "i-external", curr-params "curr-params"\n")

  (set! pml-layers (list
                 (make pml (direction Z) (thickness dpml))
                 (make pml (direction Y) (thickness dpml))
                 ;(make pml (direction X) (thickness dpml))
          )
  )

  (set! ensure-periodicity true)
  (set! geometry-lattice (make lattice
    (size supercell-x supercell-y supercell-z)))
  ;Bloch perioodicity
  (set-param! k-point (vector3 kpt 0 0))
  (set! geometry '())
  (set! geometry
   (append
    (list
     (make block (center 0 0 0) (size infinity infinity infinity)
       (material (make dielectric (index myvacuum))))
      (make block (center 0 0 0) (size MEEPa wY MEEPthk)
        (material (make dielectric (index curr-eps)))) ; dielectric Block
      ; First air holes
       (make cylinder (center (* 0.5 MEEPa) L2 0) (radius MEEPr2)
         (height MEEPthk) (material (make dielectric (index myvacuum))))
       (make cylinder (center (* -0.5 MEEPa) L2 0) (radius MEEPr2)
         (height MEEPthk) (material (make dielectric (index myvacuum))))
      (make cylinder (center (* 0.5 MEEPa) (* -1 L2) 0) (radius MEEPr2)
        (height MEEPthk) (material (make dielectric (index myvacuum))))
       (make cylinder (center (* -0.5 MEEPa) (* -1 L2) 0) (radius MEEPr2)
         (height MEEPthk) (material (make dielectric (index myvacuum))))
      )
      (geometric-object-duplicates
        (vector3 0 (* (sqrt 3) MEEPa) 0) 0 (/ (- y 2) 2)
       (make cylinder (center 0 (+ (* (/ (sqrt 3) 2) MEEPa) L2) 0)
       (radius MEEPr3) (height MEEPthk)
       (material (make dielectric (index myvacuum))))
     )
      (geometric-object-duplicates
        (vector3 0 (* -1 (* (sqrt 3) MEEPa)) 0) 0 (/ (- y 2) 2)
      (make cylinder (center 0 (- (* (/ (sqrt 3) -2) MEEPa) L2) 0)
      (radius MEEPr2) (height MEEPthk)
        (material (make dielectric (index myvacuum))))
      )
      (geometric-object-duplicates
        (vector3 0 (* (sqrt 3) MEEPa) 0) 0 (/ (- y 2) 2)
       (make cylinder (center (* 0.5 MEEPa) (+ (* (sqrt 3) MEEPa) L2) 0)
       (radius MEEPr2) (height MEEPthk)
        (material (make dielectric (index myvacuum))))
      )
      (geometric-object-duplicates
        (vector3 0 (* (sqrt 3) MEEPa) 0) 0 (/ (- y 2) 2)
       (make cylinder (center (* -0.5 MEEPa) (+ (* (sqrt 3) MEEPa) L2) 0)
       (radius MEEPr2) (height MEEPthk)
        (material (make dielectric (index myvacuum))))
```

```
        )
        (geometric-object-duplicates
          (vector3 0 (* -1 (* (sqrt 3) MEEPa)) 0) 0 (/ (- y 2) 2)
         (make cylinder (center (* 0.5 MEEPa) (- (* -1 (* (sqrt 3) MEEPa)) L2) 0)
         (radius MEEPr2) (height MEEPthk)
          (material (make dielectric (index myvacuum)))) ; First middle hole below
        )
        (geometric-object-duplicates
          (vector3 0 (* -1 (* (sqrt 3) MEEPa)) 0) 0 (/ (- y 2) 2)
         (make cylinder (center (* -0.5 MEEPa) (- (* -1 (* (sqrt 3) MEEPa)) L2) 0)
         (radius MEEPr2) (height MEEPthk)
          (material (make dielectric (index myvacuum)))) ; First middle hole below
        )
    ))

    (makeModule 0)
    (makeSquircle (* -1 MEEPelpta))
    (if (= ft E-stuff) (begin
          (set! global-D-conductivity Sigma)
          (set! global-B-conductivity 0)))
    (set! sources (list (make source ( src
               (make custom-src
               (src-func (lambda (t) (/ 1 dt)))
               (start-time (* -.25 dt))
               (end-time (* .75 dt))
               (width dt)
               (is-integrated? false))
               ;(make gaussian-src (frequency fcen) (fwidth df))
              )
              (component curr-pol)
              (center xbgn curr-r 0)
              (size 0 0 0))
          )
    )

(print "Current polarization: "curr-pol"\n")
(print (string (string-ref polstring curr-pol))"\n")
(print "Current dielectric constant: "curr-eps"\n")
(print "Current position: "curr-r"\n")

  (reset-meep)
  (init-fields)
  (if (= curr-eps myvacuum) (use-output-directory
    (string-append "out_vac_xyr_xp" (number->string xbgn) "_kx"
    (number->string kpt))) (use-output-directory
    (string-append "out_xyr_xp" (number->string xbgn) "_kx"
    (number->string kpt))))
  (if (not (= curr-r prev-r)) (begin (set! rstring (string-append rstring "r"))
  (set! prev-r curr-r)))
;  (if (not (= xbgn 0)) (begin (set! xstring (string-append xstring "x"))
;  (set! xbgn 0)))
;  (get-filename-prefix "kpt")
        (run-until endtime
    (at-beginning output-epsilon)
                (after-time 0 (to-appended (string-append (string #\e #\x)
                  (string (string-ref polstring curr-pol)) (string #\k #\x)
                  (number->string kpt) (string #\r) rstring)
```

```
                  (at-every dt (in-point (vector3 xbgn curr-r 0) output-efield-x))))
                (after-time 0 (to-appended (string-append (string #\e #\y)
                  (string (string-ref polstring curr-pol)) (string #\k #\x)
                  (number->string kpt) (string #\r) rstring)
                  (at-every dt (in-point (vector3 xbgn curr-r 0) output-efield-y))))
                (after-time 0 (to-appended (string-append (string #\e #\z)
                  (string (string-ref polstring curr-pol)) (string #\k #\x)
                  (number->string kpt) (string #\r) rstring)
                  (at-every dt (in-point (vector3 xbgn curr-r 0) output-efield-z))))
      )
  )
)

(do ((j 0 (1+ j))) ((= j Nsims)) (run-sim j))
```

Appendix F

Scheme MPB code: photonic bands

```
;; This CTL file is to calculate the dispersion relation for "Si3N4 Squircle W1 waveguide structure" by MPB
;; Structure parameters : (1) Lattice constant : a
;;        (2) Air-hole radius (r1: Squircle size) (r2: Second-line holes) (r3: all the other holes)
;;        (3) Structure thickness : thk
;;        (4) Width of air-line-slot: wid
;;        (5) Ellipcity of squircles : Alpha (larger value gives more elongated squircle in x-direction)
;;        (6) Shift of the squircles in y-direction : s1
;;        (7) Shift of the second line of holes in y-direction : s2
;;        (8) offset : Additional dielectric slap between the first line squircles and air line-slot
;;        (9) Squareness : Nsq
;;        (*) Sinusoidal modulation of the edge of th air line-slot (Alligator structrue) : Amplitude

;; W1 waveguide structure parameters ;;
(define pi (* 2 (acos 0)))  ; pi
(define ix_SiN 1.9935)    ; index of Si3N4
(define myvacuum 1)
;(define-param kst 0.42)
;(define-param ked 0.47)
(define-param kstart 0.4)
(define-param kend 0.4997)
;; PhC dimensions ;;
(define-param Nsq 4)  ; (Only even number) Nsq = 2 -> Circle // Nsq = 4 -> Squircle
(define-param amp 0)
(define-param wid 114)
(define-param thk 200)
(define-param a 373)
(define-param y 8) ; the number of unitcell in y-direction
(define-param r1 110) ; radius of the 1st air-holes
(define-param r2 110) ; radius of the 2nd air-holes
(define-param r3 110) ; radius of all the other air-holes
(define-param s1 0) ;minimum distance between air hole and air slot
(define-param s2 0) ; minimum distance between 1st air hole and 2nd air hole
(define-param offset 100)
(define-param slot (* 2 (+ amp wid)))
(define-param alpha 1.15) ; ellipcity of the 2nd holes

;; define unit conversion function ;;
```

```
(define (simUnits x) (/ x a))

;; Unit conversion ;;
(define-param MPBthk (simUnits thk))
(define-param MPBa (simUnits a))
(define-param MPBr1 (simUnits r1))
(define-param MPBr2 (simUnits r2))
(define-param MPBr3 (simUnits r3))
(define-param MPBs1 (simUnits s1))
(define-param MPBs2 (simUnits s2))
(define-param MPBslot (simUnits slot))
(define-param MPBoffset (simUnits offset))

(define-param elpta (* alpha r1))
(define-param elptb (/ r1 alpha))
(define-param MPBelpta (simUnits elpta))
(define-param MPBelptb (simUnits elptb))

; width of blocks in x-direction
(define-param wX 1)
; distance between central line and the center of 1st air hole (squircle)
(define-param L1 (+ MPBs1 MPBoffset (/ (sqrt 3) 2)))
; distance between central line and the center of 2nd air hole
(define-param L2 (+ MPBs2 MPBoffset (sqrt 3)))
(define-param wY (+ (* (sqrt 3) y) (* 2 L2))) ; width of blocks in y-direction
(define-param sy wY) ; the computational size in y-axis

;; AUX Setting ;;
;; AUX settings ;;
(define-param res 20)
(set-param! resolution res)
(define dx (/ 1 res 10))
(define-param kpts 10)
(define-param nbands 24)

;; Cell dimensions ;;
(define sx wX)
(define-param sz 10)
(set! geometry-lattice (make lattice (size sx sy sz)))

;; Create geometry ;;
(define (drawBlock x)
  (let ((dy (+ wid (* amp (cos (* 2 pi x))))))
       (let ((cy (/ dy 2)))
            (list
              (make block
                (center x (simUnits cy) 0)
                (size (* 1.1 dx) (simUnits dy) (simUnits thk))
                (material (make dielectric (index myvacuum)))
              )
              (make block
                (center x (* -1 (simUnits cy)) 0)
                (size (* 1.1 dx) (simUnits dy) (simUnits thk))
                (material (make dielectric (index myvacuum)))
              )
            )
       )
```

```
))

(define (drawSquircle x)
  (let ((dy (* 2 MPBelptb (expt (- 1 (/ (expt x 4) (expt MPBelpta 4))) (/ 1 4)))))
       (list
   (make block
    (center (- x 0.5) L1 0)
    (size (* 1.1 dx) dy MPBthk)
    (material (make dielectric (index myvacuum)))
   )
   (make block
    (center (- x 0.5) (* -1 L1) 0)
    (size (* 1.1 dx) dy MPBthk)
    (material (make dielectric (index myvacuum)))
   )
   (make block
    (center (+ x 0.5) L1 0)
    (size (* 1.1 dx) dy MPBthk)
    (material (make dielectric (index myvacuum)))
   )
   (make block
    (center (+ x 0.5) (* -1 L1) 0)
    (size (* 1.1 dx) dy MPBthk)
    (material (make dielectric (index myvacuum)))
   )
       )
))

(set! geometry '())
(set! geometry
 (append
  (list
   (make block (center 0 0 0) (size sx sy MPBthk) (material (make dielectric (index ix_SiN)))) ; dielectric Block
   ;(make cylinder (center 0.5 L1 0) (radius MPBr1) (height MPBthk)
   ;  (material (make dielectric (index myvacuum))))  ; First air hole right above
   ;(make cylinder (center -0.5 L1 0) (radius MPBr1) (height MPBthk)
   ;  (material (make dielectric (index myvacuum)))) ; First air hole left above
   ;(make cylinder (center 0.5 (* -1 L1) 0) (radius MPBr1) (height MPBthk)
   ;  (material (make dielectric (index myvacuum)))) ; First air hole right below
   ;(make cylinder (center -0.5 (* -1 L1) 0) (radius MPBr1) (height MPBthk)
   ;  (material (make dielectric (index myvacuum)))) ; First air hole left below
   (make cylinder (center 0 L2 0) (radius MPBr2) (height MPBthk)
   ;  (material (make dielectric (index myvacuum))))  ; First air hole right above
   (make cylinder (center 0 (* -1 L2) 0) (radius MPBr2) (height MPBthk)
   ;  (material (make dielectric (epsilon 1)))) ; First air hole left above
  )
  (geometric-object-duplicates (vector3 0 (sqrt 3) 0) 0 (/ y 2)
   (make cylinder (center 0.5 (+ (/ (sqrt 3) 2) L2) 0) (radius MPBr3) (height MPBthk)
    (material (make dielectric (index myvacuum))))
  )
  (geometric-object-duplicates (vector3 0 (sqrt 3) 0) 0 (/ y 2)
   (make cylinder (center -0.5 (+ (/ (sqrt 3) 2) L2) 0) (radius MPBr2) (height MPBthk)
    (material (make dielectric (index myvacuum))))
  )
  (geometric-object-duplicates (vector3 0 (sqrt 3) 0) 0 (/ y 2)
   (make cylinder (center 0 (+ (sqrt 3) L2) 0) (radius MPBr2) (height MPBthk)
    (material (make dielectric (index myvacuum))))
```

```
  )
  (geometric-object-duplicates (vector3 0 (* -1 (sqrt 3)) 0) 0 (/ y 2)
   (make cylinder (center 0.5 (- (/ (sqrt 3) -2) L2) 0) (radius MPBr2) (height MPBthk)
    (material (make dielectric (index myvacuum))))
  )
  (geometric-object-duplicates (vector3 0 (* -1 (sqrt 3)) 0) 0 (/ y 2)
   (make cylinder (center -0.5 (- (/ (sqrt 3) -2) L2) 0) (radius MPBr2) (height MPBthk)
    (material (make dielectric (index myvacuum))))
  )
  (geometric-object-duplicates (vector3 0 (* -1 (sqrt 3)) 0) 0 (/ y 2)
   (make cylinder (center 0 (- (* -1 (sqrt 3)) L2) 0) (radius MPBr2) (height MPBthk)
    (material (make dielectric (index myvacuum)))) ; First middle hole below
  )
))

(define (makeModule x)
  (if (>= x 1)
        '()
      (begin
        (set! geometry (append geometry (drawBlock x)))
  (makeModule (+ x dx))
      )
  )
)
(define (makeSquircle x)
  (if (>= x MPBelpta)
        '()
      (begin
  (set! geometry (append geometry (drawSquircle x)))
  (makeSquircle (+ x dx))
      )
  )
)

(makeModule 0)
(makeSquircle (* -1 MPBelpta))

(define pork (vector3 0.4998 0 0))
(define chicken (vector3 0.4999 0 0))
(define beef (vector3 0.5 0 0))
(define Delicacy (list pork chicken beef))
(define Gamma (vector3 kstart 0 0))
(define M (vector3 kend 0 0))
(define Normal (interpolate kpts (list Gamma M)))
(set! k-points (append Normal Delicacy))
(set! num-bands nbands)
(set! tolerance 1e-9)
;(run-tm display-group-velocities fix-efield-phase output-efield)
(run-zeven display-group-velocities
  (output-at-kpoint beef fix-efield-phase output-efield-x output-efield-y output-efield-z ))
```